Electrical Control Of Magnetism From Group Theoretical And Quantum Mechanical Calculations

CAMERON ANTHONY MATTHEW SCOTT

Electrical Control Of Magnetism From Group Theoretical And Quantum Mechanical Calculations

Cameron Scott

Abstract

Volatile memory devices, with their constant power requirement, are a source of energy inefficiency in today's digitised world. Using ferroically ordered materials, which retain a ferroic state in the absence of any applied field, is one route towards alleviating this issue. For example, ferroelectric materials are those with spontaneous and switchable macroscopic polarisations. One direction of polarisation could represent a "1" and the other a "0". Alternatively, ferromagnetic materials have a switchable macroscopic magnetisation. It is typically cheap to switch the polarisation in ferroelectrics but the read operation is destructive and requires a rewrite stage. In contrast, reversing the magnetisation in a ferromagnet is energetically costly because of the large external fields needed, but reading is cheap as non-destructive magnetoresistive effects can be used. Allowing for both of these ferroic order parameters in a single-phase material might allow for cross couplings permitting writing with electric fields but reading using magnetoresistive effects. In order for this to be true, the information written in the polarisation must be transmitted to the magnetic degrees of freedom.

This thesis approaches this problem from a theoretical point of view. I analysed the symmetry of multiferroic materials and constructed Landau expansions to determine how order parameters are coupled. Through this process, I determined whether the reversal of the polarisation necessitates the reversal of magnetisation. After the symmetry was analysed, I investigated candidate materials in more detail through the application of quantum mechanical simulation. I find that certain perovskite materials do show the necessary couplings to enable electric field control of magnetism. Single perovskites under mild epitaxial strains are shown to possess a universal polar instability which, when coupled to an external electric field, induces a transition from an antiferromagnetic state to a ferromagnetic one. Additionally, the symmetry analysis identifies that improper ferroelectrics are most likely to host the desired couplings and that cation ordering, such as in $CeBaMn_2O_6$, is the easiest route to achieve them. Future work would focus on stabilising the important cation orderings and investigating the detailed switching dynamics of candidate materials.

Supervisors: Dr. Nicholas Bristowe and Prof. Stewart Clark

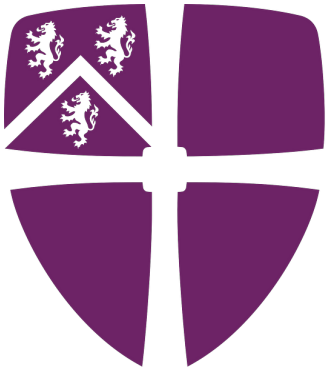

Durham University

Electrical Control Of Magnetism From Group Theoretical And Quantum Mechanical Calculations

Cameron Scott

A thesis presented for the degree of

Doctor of Philosophy

Condensed Matter Physics

Durham University

Durham, United Kingdom

March 2025

Contents

Declaration

The work in this thesis is based on research carried out at the Department of Physics, University of Durham, United Kingdom. No part of this thesis has been submitted elsewhere for any other degree or qualification, and it is the sole work of the author unless referenced to the contrary in the text. Some of the work presented in this thesis has been published in journals and conference proceedings - the relevant publications are listed below.

Relevant Publications

1. **Scott, Cameron AM,** and Nicholas C. Bristowe. "Universal Polar Instability in Highly Orthorhombic Perovskites." Journal of the American Chemical Society 146.43 (2024): 29735-29741. (This work forms the basis of Chapter 6.)

2. Simpson, Struan, **Cameron AM Scott**, Fernando Pomiro, Jeremiah P. Tidey, Urmimala Dey, Fabio Orlandi, Pascal Manuel et al. "Symmetry-informed design of magnetoelectric coupling in the manganite perovskite $CeBaMn_2O_6$." Journal of Materials Chemistry C 12, no. 37 (2024): 15058-15069. (This work forms the basis of Chapter 7.)

Auxiliary Publications

1. Crawford, Catriona A., Craig I. Hiley, **Cameron AM Scott**, Clemens Ritter, Martin R. Lees, Nicholas C. Bristowe, Richard I. Walton, and Mark S. Senn. "The Interplay of Electronic Configuration and Anion Ordering on the Magnetic Behavior of Hydroxyfluoride Diaspores." Inorganic Chemistry (2024). (This work is an example of using density functional theory to calculate the magnetic exchange constants, as described in Chapters 2 and 5.)

Statement Of Copyright

Acknowledgements

"No man is an island, entire of itself." wrote the poet John Donne. Nowhere is this more true than a PhD thesis. Although it is my name that is printed in large letters on the cover of this thesis, this belies the contributions of so many others without whom I would never have completed this work. For those who bother to read acknowledgements, permit me two pages to declare my heartfelt thanks.

First and foremost, I'd like to thank my supervisor Nicholas Bristowe who has skillfully guided me through the PhD process. He has been unfailingly insightful throughout my time in his group and is solely responsible for the development of my confidence as a scientist. Most importantly, he has achieved all this through being good-humoured and congenial. He has been a delight to work with and will continue to be so in the future. Maybe we can finally work on some of the "low-hanging fruit" that always seems tantalisingly out of reach.

In addition, I would like to also thank The Leverhulme Foundation, through which I have received funding for the work contained in this thesis.

Next, I want to thank all the other academics who've played a part in the work I've conducted during my PhD. Stewart Clark, Emma McCabe, Nikitas Gidopolous, Mark Senn, Finlay Morrison, Jorge Iniguez-Gonzalez, Del Atkinson, Miro Cafolla, Marek Szablewski, Tom Lancaster, Struan Simpson, Catriona Crawford, Ben Tragheim and Evie Ladbrook have all been fantastic to work with over the last three years. Whether through scientific collaboration or through close proximity at Durham University, they have made coming to work an experience to treasure. Every single interaction with them has been special and I've learned a lot from them.

People often overlook the vital role played by the administrative staff but Lisa, Joanne, Helen, Samuel and all the ARC team have drastically reduced the stress of the completing a PhD. They have also been instrumental in my quest to make Durham CMP a more cohesive community. I am positive that they will continue to help others with as much dilligence that they

have shown me.

Next up in the parade of thanks are the members of the Bristowe group. Urmimala, Alex, Paul and Pierre-Louis must have done something terrible in previous lives to have to share an office with me but I thank them wholeheartedly for making Ph301 such a productive place and for filling it with humour and helpful distractions. PhDs are hard, so I'm thankful I had such supportive people around me to help.

This brings me to the other PhDs and postdocs who weren't consigned to sharing an office with me - it really is a fate worse than death. Glen, Areesha, Kaviya, Ali, Michael and Emma all started at the same time as me and have been great sources of friendship since day one. The same can be said for Visigan, Lucy, Ben, Faisal, Sam, Vanessa and so many others who have appeared in the department over the years. I wish to give special thanks to Amy, who has been frustratingly easy to talk to and has a remarkable ability to make me laugh, no matter the circumstances. She has no idea how much these conversations cheer me up.

Faye has been a constant friend ever since I turned up at the University Of Birmingham to begin studying physics. Despite not being in Durham, she has a remarkable ability of always being close when I need her. She's proving very difficult to ditch.

I sometimes think it is surprising that I have ended up where I am after reminiscing about the paralysingly shy boy I used to be. I owe everything to my family for pushing me to be ambitious and determined, for inspiring my interests, for generating my sense of humour and for producing the kind loving family environment that every child deserves.

Finally, I need to thank Charlotte for all of her love, support and unending laughter. In order to do this properly, I'd have to write a second thesis.

All these people, and many others I'm sure I've missed, deserve their names on the front cover of this thesis, and probably in larger letters than my own.

To Charlotte Rose,

Cheers dude.

Perovskite Distortions

Distortion	Γ	X	M	R
Strain	$\Gamma_3^+;\Gamma_5^+$			
Cation Order (A Sites)		X_1^+	M_1^+	R_1^+
Cation Order (B Sites)		X_3^-	M_4^+	R_2^-
Anion Order (X Sites)		X_1^+	$M_4^+;M_5^-$	R_5^+
(Anti-) Polar (A Sites)	Γ_4^-	X_3^-	$M_3^-;M_5^-$	R_4^-
(Anti-) Polar (B Sites)	Γ_4^-	X_1^+	$M_2^-;M_5^-$	R_5^+
Jahn-Teller Modes	Γ_3^+	X_3^-	M_3^+	R_3^-
Octahedral Tilt Modes			M_2^+	R_5^-
Magnetic Order (A Sites)	$m\Gamma_4^+$	$mX_3^+;mX_5^+$	$mM_3^+;mM_5^+$	mR_4^+
Magnetic Order (B Sites)	$m\Gamma_4^+$	$mX_1^-;mX_5^-$	$mM_2^+;mM_5^+$	mR_5^-

Table 1: The main distortions and their corresponding irreducible representations in perovskite materials. The irreducible representation labels are given assuming a $Pm\bar{3}m$ parent cell with the A site at $[0, 0, 0]$.

Chapter 1

Introduction - The Need For Magnetoelectric Multiferroics

1.1 The Energy Requirements Of The 21st Century

Quantum mechanics, one of the most extraordinary advances of 20th century physics, is nearing its 100th birthday. The complementary development of matrix mechanics (1925) and wave mechanics (1926) revealed an entirely new way to understand the properties and dynamics of microscopic objects. Of particular importance was how quantum mechanics enabled better comprehension of the behaviour of electrons in materials - the so called *electronic structure* of a material. With this enormous shift in understanding, solid state theorists and experimentalists were now able to design bespoke, functional materials to address particular needs. Conductors, semiconductors and insulators are some prominent examples of materials whose electronic structures are well understood and whose properties are routinely tuned to fit a particular function. As the eminent scientists responsible for developing the central tenets of the theory were dotting their is and crossing their $\hbar$s, they could not have possibly foreseen the enormous impact their work would have over the next century.

Perhaps the most consequential innovation enabled by the quantum mechanical understanding of semiconductors was the creation of the transistor. First created by John Bardeen and

Walter Brattain in 1948 [1] from a crystal of germanium*, it forms the central component of all modern electronics. Its ability to amplify and switch electric currents makes it the ideal device to implement logic and memory circuits and the vacuum tube, the bulkier analogue counterpart to the transistor, was quickly supplanted. Continued research and development in the semiconductor industry resulted in silicon-based field effect transistors (FETs) and also in decreasing size and costs. Along with resistors, capacitors, and other electrical devices, transistors were incorporated into the new integrated circuits of the 1960s. The microprocessors and memory devices that are so central to contemporary computing are constructed from these integrated circuits, which themselves include a huge number of transistors. As the size of an individual transistor was reduced, the number of transistors on an integrated circuit of a given dimension has also increased, leading to a steady increase in computer complexity and speed. This seemingly unstoppable march of progress is perhaps best typified by an observation by Gordon Moore of IBM that the density of transistors on an integrated circuit should double roughly every two years. "Moore's Law" has remained remarkably robust for the last sixty [3] years although it is now showing signs of slowing because quantum mechanics, the physical law whose discovery kickstarted the whole process, becomes important once again. Transistors are becoming so small that they are reaching atomic dimensions - a fundamental limit - and scaling becomes much more complicated.

Semiconductor applications are obviously not restricted to transistors. Optical devices such as light emitting diodes and lasers are also created by fine-tuning semiconductor material properties, as are photovoltaic solar cells and other sensors designed to respond to mechanical, thermal, magnetic or chemical stimuli [4].

The increasing versatility of semiconductor devices has substantially increased consumer demand so that semiconductors can now be found in almost every aspect of modern life. Here lies the problem - all these devices need power. How to source this power is a problem of tantamount scientific importance in the 21st century. It is also a question with important societal, political and ecological ramifications as continuing to choose the high energy density but non-renewable, polluting sources such as fossil fuels will hasten climatic breakdown and

*A field effect transistor was first patented by Julius Edgar Lilienfeld in 1927 [2] but was never created.

produce irrevocable changes to our biosphere.

In the above, I focused on transistors, as it is these that form the backbone of the logic and memory circuits that are so essential to any form of computer technology. Recent studies [5, 6, 7] have estimated that the global electricity demand was about 20,000 TWh in 2010 and seems to be growing at an annual rate of about 3%. Of this electricity usage, about 20% is expected to be taken up by computer technology. Subdividing this further, electricity usage from personal devices is expected to fall due to increasing efficiency whereas that from data centres facilitating the transfer of information will grow - potentially consuming almost half of all electricity demanded for computer technology in the worst case scenarios. In these centres, about half of the energy goes to processing and storage functions whilst most of the rest is responsible for cooling. Combining all of these rough approximations, it is plausible that the energy requirements of computing in data centres alone could reach about 5% of global energy usage. Indeed, data centres in 2012 were estimated to use about 1.35% of global electricity [8], and with a predicted yearly rise of 4.4%, it's clear that data centres will take an increasingly large share of electricity usage in the future, especially if these centres are used to train and implement modern artificial intelligence programs.

With the energy usage of computing increasing, energy efficiency becomes more important. Wastage occurs at every single stage of the life-cycle of a computing device and each of these must be addressed if we are to reduce our gluttonous energy requirements. Interestingly, quantum ideas will be (and already are) important in designing new materials that can help us escape the energy dependency that quantum ideas helped to cause in the first place! For example, Joule heating is the energy loss to heat as an electrical current flows through a conductor. It is caused by the scattering of electrons off atoms in the conducting material and the energy of collision is radiated away as heat. The quantum idea of superconductivity alleviates this issue [9]. When temperature is low enough in some materials, electrons do not scatter randomly from atoms. Instead, the coordinated motion of the atoms and electrons result in electrons pairing up, requiring an inaccessibly high energy to break them apart again. When the electrons are paired, they do not scatter but instead flow interrupted and Joule heating is completely eliminated. Using quantum mechanical ideas to construct a room-temperature, ambient pressure

superconductor is therefore an incredibly important field of research which, if successful, would be truly revolutionary.

This is just one aspect in which quantum mechanics can be used to design the energy-efficient materials of tomorrow. Others include the construction of new energy storage materials like batteries and supercapacitors [10] which are essential in the transition toward electric vehicles. The coupling of electrons to photons of light is also an incredibly important idea already in use in the photovoltaic industry but a greater understanding of how to maximise this effect in any given material will help to develop the next generation of solar panels and reduce the reliance on non-renewable fossil fuels.

More prosaically, but still equally important, is to try to reduce the energy usage of the electrical components that are hidden away within data centers and inside our smart devices. For example, any memory device must continually retain its data in the form of 1s and 0s. Traditionally, this is done by maintaining a high and a low voltage state to represent a 1 and a 0 respectively. However, this can only be achieved if the device is constantly supplied with power. This is not only desirable because of the extra energy required but also because of the evolving preference towards portable, ultra-low power devices [11]. In addition, current CPUs are developing at a faster rate than memory devices so that the memory becomes a bottleneck. This problem has been called the "memory wall" [12]. We therefore arrive at the central question to be addressed in this thesis: "Can quantum mechanics be used to understand, design and realise novel materials for more energy efficient memory devices?"

1.2 The Ultimate Memory Device

In principle, anything that can be programmed into two stable states can be used as memory for binary computation. In practice, it is almost always stable states in semiconductor devices that are used for the obvious reasons of microscopic scale and sub-microsecond read and write speeds. However, this still allows for a wide variety of possible implementations. Here I review some of these possibilities, assessing their advantages and disadvantages, and culminating in the exposition of *multiferroic memories*. These are often touted as the "ultimate memory device"

permitting previously impossible functionalities. The identification and theoretical understanding of novel materials that can enable this revolutionary technology forms the central theme of this thesis.

1.2.1 Volatile Memories

Volatile memory is only capable of data retention if the device is also provided with a source of power. Once that power is removed, data is lost. To achieve this on an integrated circuit, there are two main approaches.

Static random access memory (SRAM) [13] has one of the highest frequency read/write cycles of all memory devices but to accomplish this, considerably more transistors must be used. A typical SRAM circuit element involves six transistors, four of which are paired off into inverters. These take a high voltage input and produce a low voltage output and vice versa. Importantly, the inverters are coupled so that an output from either acts as input to the other and consequently, there are two stable states - shown in Figure 1.1.

The basic design of the SRAM circuits highlights an important issue with the technology - it requires multiple transistors to store a single bit of information. This results in significantly higher costs and reduced data density which offset the attractive high read/write speeds. Typically, it is used in the cache memory of a CPU where it is speed and not volume which is critical. As the technology has progressed, new issues have arisen. The requirement of a constant supply of power leads to non-negligible leakage currents with this effect strengthening with decreasing circuit size.

Dynamic random access memory (DRAM) [4] greatly reduces the size of a memory circuit. It does this by using a single transistor to control the charge stored on a connected capacitor (Figure 1.2). A charged and discharged capacitor maps onto the logical 1 and 0 state necessary for computation. These two states are therefore incredibly simple. However, the reliance of a capacitor (which will always have some leakage of charge) requires the continual pulsing of voltage, usually at a frequency of around 100Hz, to continue to retain data. Nevertheless, DRAM

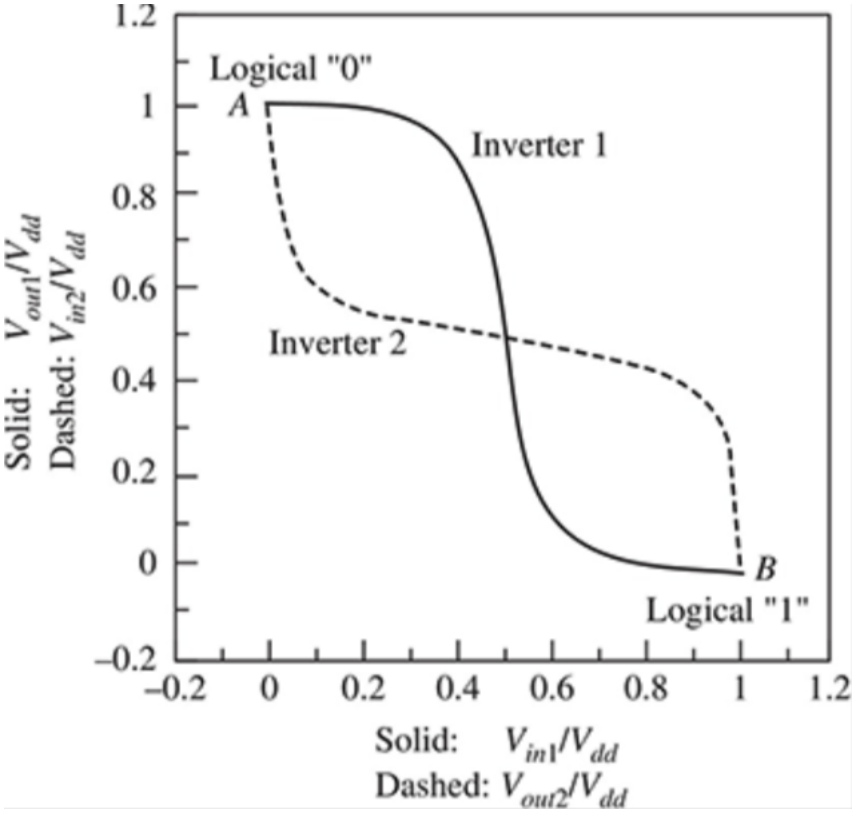

Figure 1.1: The "butterfly plot" obtained by operating an SRAM circuit. The two stable voltage states constitute the two necessary configurations for a memory device. V_dd is the voltage of the attached power supply. Taken from Reference [13].

remains the cheapest and most ubiquitous memory device whose small circuit design leads to much greater data density than SRAM.

Despite the cheapness of DRAM and the speed of SRAM, both are energy inefficient. Future memory technologies must find a way around the requirement for a constant supply of energy. In future, memory devices must be non-volatile.

1.2.2 Non-Volatile Memories

Non-volatile memory, in contrast to volatile memory, does not require any external power source to retain data and subsequently, has become an enormously attractive avenue in the design of novel energy efficient memory devices.

The most commercially successful, approach to non-volatile memory is Flash memory [13, 14].

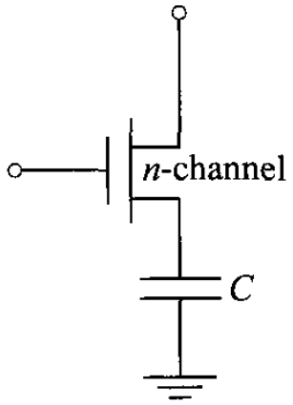

Figure 1.2: DRAM circuit diagram showing the controlling p-type transistor - the "access device" and the connected capacitor. Taken from [4]

Here the injection of additional charge into the *floating gate* of a transistor alters the threshold voltage. Once the charge has been injected it can be retained for many years within the gate without the need for any periodic refreshing or external power supply. A floating gate transistor with injected charge and a transistor without the charge become the two stable states. The whole array of transistors can then be erased with a "flash" of ultraviolet radiation, hence the name. Due to the high energy barriers that must be overcome to inject charge, Flash memory is typically used in a read-only storage role and forms the basis of the solid state drive (SSDs) found in most modern computers.

Flash is not the only way to implement a non-volatile memory. As all that is necessary is a material that can be switched between two stable and distinguishable states, materials science plays an important role towards finding and understanding these states. Just as H_2O transform between a liquid and solid states via the application or removal of heat, every other material can exist in a huge variety of state or *phases*. The study of the phase transitions [15] of materials is an incredibly rich discipline of materials science and well suited to looking for stable states that are accessible enough to be suitable representations of the 1s and 0s of computer logic.

The scientific literature is replete with exotic material phases that have been proposed for this exact purpose. The skyrmion, meron, hopfion, hedgehog, bubble and vortex phases found in magnetic and dielectric materials are just some of the jargon routinely attached to the study of

memory materials [16] and new ideas are always emerging, including using the thermal properties of different phases of materials for computation [17].

My research has focused on ferroic phase transitions. This is a transition that takes a material from an initial phase to one of at least two equivalent phases. Importantly, for the ferroic classification to apply, it must be possible to switch between the two phases. To illustrate this point, imagine a rod holding up a heavy weight [18]. As the weight increases, the rod must eventually buckle either to the left or to the right (in a 2D world). Is this a ferroic transition? If you are strong enough to bend a rod deformed to the left into a rod deformed to the right, then yes, this is a ferroic transition. If you are not strong enough to do this, and cannot find anyone or anything who can, then it is not a ferroic transition. Maybe the rod could be deformed with an applied force slightly greater than the maximum you could provide, but until that transition to the reversed state is observed, it is not a ferroic transition. This highlights the point that the classification is more empirical than fundamental. However, the hypothetical existence of both states is not up for dispute. If the rod could bend to the left, the initial symmetry of the situation ensures that it could also bend to the right. I shall show later that symmetry provides an essential tool in the physics of phase transitions, and will prove invaluable. If the transition does prove to be ferroic, then "left" and "right" become faithful representations of "1" and "0" in some strange analog computer: both states are clearly distinguishable from each other and, being a ferroic transition, it is switchable. In order for this kind of phase transition to be useful as non-volatile *memory device, it must be a ferroic phase transition.

Enough with the academic allegories! In the three sections below, I explore various examples of real ferroic phase transitions that may result in the next generation of memory devices. In these sections, I introduce the concepts of ferroelectricity, magnetism, and multiferroicism.

1.2.2.1 Ferroelectricity and Ferroelectric Memories

Dielectric materials are the class of insulating materials which have the property that, on the application of an electric field, the positive and negative charges in the material separate, result-

*The rod analogy would certainly be non-volatile as removing the weight does not cause the rod to become straight again

ing in net electrical polarisation [19, 20]. It is critically important that the material is insulating because without this proviso, free charges redistribute themselves within the material and create an opposite, depolarising field that cancels that created by the external field.

Only a subset of dielectrics can have their polarisation changed with external strains, as well as with electric fields. These are termed *piezoelectric* materials.

A subset of piezoelectrics, and thus an even smaller of all dielectrics have a net polarisation even in the absence of any field or strain. These are known as *polar materials* and polarisation arises because the anions and cations that make up the crystal structure are positioned in such a way that there is a surplus of positive charge in one direction and a deficit in another. As I describe in Chap 3, this is a consequence of the symmetry of the crystal structure - polar materials lack centrosymmetry. An increase in temperature begins to randomise the positions of the ions in these materials, lowering the strong spatial correlations between them and reducing the polarisation, and consequently polar materials are also known as *pyroelectric*[*].

Upon the application of an electric field to a pyroelectric, it is sometimes possible to reverse the polarisation from P to $-P$. If this is the case, the material is denoted as *ferroelectric*. This emphasises the point that the "ferroelectric" classification is not fundamental but can only be applied by doing some experiments. The reversal of polarisation must be observed for a material to be properly described as a ferroelectric. Nevertheless, many polar materials are frequently described as ferroelectric materials without this observation. The subdivision of dielectric materials into piezoelectric, pyroelectric and ferroelectric is schematically illustrated in Figure 1.3.

First discovered at the end of the 19^{th} century in a class of materials known as Rochelle salts [21], ferroelectricity can be determined by observing a *hysteresis loop* in the $P - E$ plot. This can be explained by imagining the ferroelectric material as a mosaic of domains, each with a randomly oriented polarisation. Applying a field in the direction of one of these polarisations causes that domain to grow whilst others shrink. Continued increase of the electric field results in a single, monodomain sample with a saturated polarisation P_S. Reducing the field, to zero

[*]Temperature would also effect the positions of ions in non-polar crystals but the effect of temperature is always random and so no net polarisation is created because of changes in temperature.

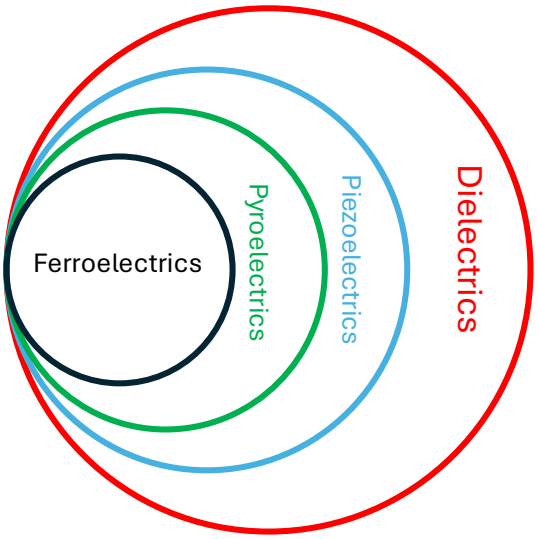

Figure 1.3: Schematic illustration of the hierarchy of dielectric materials.

will now leave a net polarisation because the interactions between dipoles is strong enough to persist without this external influence. The remaining polarisation in zero electric field is the *remanent polarisation*. Reversing the field makes the originally polarisation direction unfavourable and the polarisation is completely destroyed at the *coercive field*, $-E_C$. Continuing to increase the field in the opposite direction reaches the opposite saturation polarisation $-P_S$*. Observing ferroelectricity is occasionally difficult because the coercive field is larger than the breakdown field (the field when it ceases to be insulating) of the material and so the reversal of the polarisation is an impossibility - metallicity destroys ferroelectricity†.

A transition to a ferroelectric phase happens below a ferroelectric Curie temperature T_C from a high temperature *paraelectric* phase - a phase without a polarisation. Right at T_C, an infinitesimally small electric field can trigger the transition to a phase with a finite, non-zero polarisation. Therefore, the electric susceptibility χ diverges at T_C.

Perovskites - materials with a ABO_3 chemical formula and formed of a three-dimensional

*Another class of materials with distinctive *P-E* plots are *antiferroelectrics*. This is a poorly defined concept but is best described as any material displaying a *double* hysteresis loop. This would be a material in which a small E field changes the polarisation linearly as the material is initially non-polar. With increasing field, the system transitions to a ferroelectric phase with a miniature hysteresis loop at end of the linear portion of the *P-E* plot. There is another small hysteresis plot for the reversed field, hence the "double hysteresis" descriptor. If a polar material transitions to a different polar phase with field, the linear portion would be replaced with a regular hysteresis loop and you would observe a triple hysteresis loop!

†It does seem possible to have polar crystal structures that are metals but it is not possible to switch these. The external fields are screened.

network of corner sharing BO_6 octahedra - possess a great deal of chemical and structural flexibility. It is in this class of materials that ferroelectricity is perhaps best understood and a ferroelectric transition is typically ascribed to either "condensation of a zone-centred soft phonon" (Chapter 2) or a "coupling between symmetry adapted distortions" (Chapter 3).

Whatever the origin of ferroelectricity, the (at least) two polar states map nicely onto "1" and "0" states needed for ferroelectric RAM (FeRAM) [22, 23, 24]. FeRAMS have read and write cycles faster than alternative nonvolatile memories like FLASH and also have faster access times. The huge downside to FeRAM is that the read operation is destructive because in order to find out the polarisation state of a ferroelectric, the polarisation must be switched and the resulting current measured. This requires an additional application of a field to rewrite the data, which leads to a slightly higher energy cost and undercutting the energy-saving promise that FeRAMs bring.

1.2.2.2 Magnetism and Magnetic Memories

Magnetism is a uniquely quantum phenomenon with no classical description [18]. The magnetic dipoles present on atoms and ions are caused by spin and orbital degrees of freedom of the electrons. The sizeable magnetic dipole on an Fe 3^+ ion is caused by five such electron spins each organised into different orbitals so that the spins do not pair up and compensate each other.

Bringing a number of magnetic ions together and lowering the temperature can lead to a magnetic phase transition below a critical temperature T_C. Above this transition, the material is said to be *paramagnetic*. Below the transition, the combined spin on each ion could align with the spins on its neighbours - this is a *ferromagnet*. Alternatively, the spin could align oppositely with its neighbours to produce an *antiferromagnet*.

As could be guessed from the similarity between the terms *ferroelectric* and *ferromagnet*, the phenomenology of ferromagnetism and ferroelectricity is similar despite the very different origins of the effects [24]. Ferromagnets show hysteresis loops with associated remanent and saturation magnetisations as well as coercive magnetic fields. The magnetic susceptibility also diverges at T_C. The similarity between the two suggest that they are both different manifestations of the

same overarching concept. This is indeed the case: both are examples of phase transitions with the magnetisation or polarisation being just two examples of *order parameters*. The theory of phase transitions is summarised in Chapter 3.

The origin of the magnetic phase transitions is different depending on whether the material is insulating or metallic. Metallic materials usually become magnetic due to the *Stoner criterion* (There are other mechanisms - see [18, 25]). This states that, after the magnetic interaction between neighbouring dipoles becomes strong enough, it becomes energetically favourable to populate the quantum states of the electrons in a spin-polarized manner. One spin channel becomes favoured over another and the metal becomes a ferromagnetic.

Magnetic insulators adopt magnetic states because it is possible to lower the energy of the material if the electrons are allowed to jump between different atomic sites [20], in the same way that the energy of an electron in a well is reduced if the well is made wider. These *exchange interactions* are allowed only if the spins on the neighboring atoms are oriented oppositely to each other. This is a consequence of the Pauli Exclusion Principle - the jumping of electrons would not be permissible if they both had the same spin, as this would doubly occupy the same state with two electrons with the same quantum number. This rough heuristic means that insulators tend to be antiferromagnets [26]. However, as will be discussed later, these antiferromagnetically coupled spins can still cant in a cooperative manner so that a ferromagnetic moment can appear perpendicular to the magnetisation of any particular spin.

Anticipating my need to combine ferromagnetism with ferroelectricity, which requires insulating materials, I ignore the first mechanism of magnetism and instead focus on the second. The chemical flexibility of ABO_3 perovskite materials allows either the A or B site to be a magnetic ion [27]. Chapter 2 explores the magnetic properties of perovskite materials and includes a more detailed description of the exchange mechanism producing the magnetic structures.

As I will explore in Chapter 3, from the point of view of symmetry, it is immaterial whether the material is ferromagnetic or antiferromagnetic with a canted ferromagnetic moment. This is because a ferromagnet and a canted moment both transform in the same way, and therefore couple in the same way to other modes in the system. For the purposes of creating a purely

magnetic memory device, it is also not particularly important that the material is insulating*. All that is necessary is a net magnetisation M, which can be switched to the reversed state $-M$ with a magnetic field H. This allows ferromagnets to map themselves onto "1" and "0".

One realization of magnetic materials in memory devices are magnetoresistive RAMs (MRAM) which operate on a wholly different principle to FeRAMs. MRAMS consist of two ferromagnets separated by a spacer forming a magnetic tunnel junction (MTJ). One of these ferromagnets has its direction of magnetisation fixed and the other is free to reorient with an applied magnetic field. If the two ferromagnets have aligned magnetisations, the resistance of the MTJ is substantially reduced due to tunneling magnetoresistance. This effect describes how the resistance of electrons flowing through stacked ferromagnets changes depending on the relative spin of the electron and the ferromagnetic layer. This low resistance state can be considered to be the "1" of a memory device. Applying a current to produce a magnetic field can reverse the free ferromagnetic and increases the resistance of the MTJ. This state becomes the "0".

The great advantage of MRAMS over FeRAMs is that the read operation is not destructive. In fact, the state of the MTJ can be determined by passing current through the MTJ and recording the current out. A large current would indicate a 1 and a small current would be a 0.

However, the difference in the energy scales of magnetic and electric fields is the main disadvantage of magnetic memories [28]. If a MTJ needs a field of 0.1 T to reverse the direction of the free ferromagnetic layer (as appears to be the case in MTJs constructed from CoFeB [29]), and this field is produced at the edge of a 1μm wire then the require current through this wire would be

$$I = \frac{2\pi r B}{\mu_0} = 1.6\text{A}, \tag{1.1}$$

and such a high current through such a thin wire would produce Joule heating that both endangers the structure of the wire and also becomes a significant drain on energy, especially if used in a portable device.

*There are some magnetic memory devices which actually require metallic behaviour.

In contrast, the coercive field required to switch the polarisation in $BaTiO_3$ ranges from between 10-100 kV/cm [30] which, for a thin film 100nm in thickness, can be achieved with the application of 0.01-0.1V. In fact, as the film size gets smaller, the necessary voltage also decreases for the same field. These voltages are routinely achieved in semiconductor physics and would pose no technical challenge.

Therefore, MRAMS have an advantageous non-destructive read operation but are hindered by large Joule heating whereas FeRAMs can be operated using cheap electric fields but require a rewrite after every read due to the destructive nature of the read operation. Wouldn't it be nice to combine the beneficial features of both and ditch the downsides?

1.2.2.3 Multiferroics and Multiferroic Memories

Multiferroics [31, 32] are materials combining two or more of these ferroic phase transitions. There are four categories of primary ferroic materials [33]; ferroelectrics which couple to electric fields and break inversion symmetry, ferromagnets which couple to magnetic fields and break time reversal symmetry, ferroelastics which couple to strain fields and do not break time or inversion symmetry and finally ferrotoroidics which couple to the vector product of electric and magnetic fields $\mathbf{E} \times \mathbf{H}$ and break both inversion and time reversal symmetry.

A multiferroic is therefore any material which has two or more of these ferroic properties. In this thesis, I am concerned with the magnetoelectric properties of ferromagnetic-ferroelectric multiferroics. This describes materials that possess both a magnetisation that is switchable by coupling to an external magnetic field and also a polarisation that is switchable by coupling to an external electric field. For this reason, I use the term multiferroic to mean a ferromagnetic-ferroelectric multiferroic material.

Having established what is meant by "multiferroic materials", the category can be further subdivided by a classification introduced by Daniel Khomskii [34]. It could be the case that the ferromagnetic and ferroelectric transitions occur at different temperatures, resulting in a *Type I* multiferroic material. Alternatively, the two transitions could occur simultaneously giving a

Type II multiferroic*.

With the introduction of two ferroic phase transitions, we have the potential for a four-state logic system with $(+P,+M),(+P,-M),(-P,+M)$ and $(-P,-M)$ which, if achieved could greatly increase the data density of memory devices.

However, polarisation and magnetisation are coupled by magnetoelectricity [37] . This is the change in magnetisation with an electric field or the change in polarisation by a magnetic field. For a multiferroic, this is most easily described by employing the free energy expansion

$$\begin{aligned}\mathcal{F}(\mathbf{E},\mathbf{H}) =& \mathcal{F}_0 - P_i^S E_i - M_i^S H_i - \frac{1}{2}\epsilon_0\epsilon_{ij}E_iE_j - \frac{1}{2}\mu_0\mu_{ij}H_iH_j \\ &- \alpha_{ij}E_iH_j - \frac{1}{2}\beta ijkE_iH_jH_k - \frac{1}{2}\gamma_{ijk}H_iE_jE_k - ...\end{aligned} \tag{1.2}$$

so that the polarisation and magnetisation can be obtained by finding the minimum of the free energy ie. by differentation so that

$$P_i(\mathbf{E},\mathbf{H}) = -\frac{\partial\mathcal{F}}{\partial E_i} = P_i^S + \epsilon_0\epsilon_{ij}E_j + \alpha_{ij}H_j + \frac{1}{2}\beta_{ijk}H_iH_k + \frac{1}{2}\gamma_{ijk}H_iE_j - ... \tag{1.3}$$

and

$$M_i(\mathbf{E},\mathbf{H}) = -\frac{\partial\mathcal{F}}{\partial H_i} = M_i^S + \mu_0\mu_{ij}H_j + \alpha_{ij}E_j + \frac{1}{2}\beta_{ijk}E_iH_j + \frac{1}{2}\gamma_{ijk}E_jE_k - ... \tag{1.4}$$

where in these equations E_i and H_i are the components of the $\mathbf{E}$ and $\mathbf{H}$ respectively. P_i^S and M_i^S are the components of the spontaneous polarisations and magnetisations found in multiferroics. Repeated indices in a term are summed over. The interpretation of the coefficients α_{ij},β_{ijk} and γ_{ijk} is obtained from Equations 1.3 and 1.4. α_{ij} describes the change in polarisation (magnetisation) from the first power of magnetic (electric) field. Therefore, it quantifies the

*There has recently been discussion in the literature of *Type III* multiferroics [35, 36]. These are materials in which an ordering of ions in the materials breaks the symmetry and produces ferroelectricity. Therefore, there is no non-polar to polar transition. However, I believe that this is really just a Type I multiferroic as the cations have to order at some temperature even if this is quite high. In the language of Chapter 3, I would call this an improper ferroelectric driven by the cation ordering.

linear magnetoelectric effect. The remaining coefficients describe higher-order magnetoelectric effects. If we wish to access all the states of a four-state memory - for example, changing from the state $(+P, +M)$ to $(+P, -M)$ with an electric field - we would require a material with extremely large magnetoelectric coefficients. To illustrate this, imagine applying a sizeable electric field to the state $(+P_x, +M_x)$ in the hope of switching M to $-M$. I assume that both the polarisations and the magnetisatons are along the x direction only for simplicity and that second order effects are negligible. An electric field in the opposite direction to the the polarisation would change this state to $(P_x^S - \epsilon_0 \epsilon_{xx} E_x, M_x^S - \alpha_{xx} E_x)$. The magnetisation could only be reversed completely if $\alpha_{xx} = \frac{2M_x^S}{E_x}$ which is unrealistically large for reasonable electric fields, especially for the large saturation magnetisations found in Fe compounds. It could potentially be achieved with large electric fields, but then this would also reverse the polarisation and make a four-state memory unattainable.

Instead, consider a multiferroic where the spontaneous polarisation and magnetisation were strongly coupled together so that reversing one necessarily reverses the other. We can now only access two states* $(+\mathbf{P}_i^S, +\mathbf{M}_i^S)$ and $(-\mathbf{P}_i^S, -\mathbf{M}_i^S)$ but would describe a type of strong magnetoelectricity not easily obtained from Equations 1.3 and 1.4.

Such two-state memory devices would have significant advantages over ferroelectric or ferromagnetic memories. Firstly, the data storage would come from the spontaneous polarisation or magnetisation which would retain data without external power and is accordingly non-volatile. Secondly, information could be written with an electric field and read with a magnetic field. Figure 1.4 shows that this combines the best features of ferroelectric and ferromagnetic memories while discarding the worst. We have seen that writing with electric fields is fast and cheap but attempting to read the polarisation state is a necessarily destructive operation. On the other hand, writing with a magnetic field is expensive but reading through the magnetoresistive effect does not destroy the information and require a rewriting phase. The two-state memory with strongly coupled polarisations and magnetisation would circumvent this; the information would be written into the polarisation, instantly transferred to the magnetisation and then is able to be read by a magnetic field.

*Alternatively,$(+\mathbf{P}_i^S, -\mathbf{M}_i^S)$ and $(-\mathbf{P}_i^S, +\mathbf{M}_i^S)$

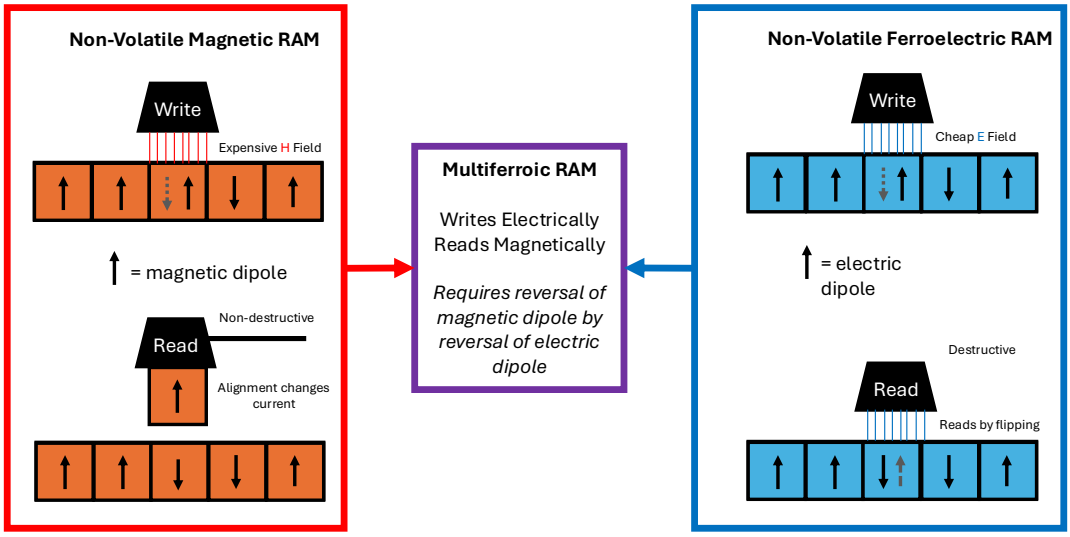

Figure 1.4: Comparison of the properties of magnetic RAM (MRAM) and ferroelectric RAM (FeRAM). Magnetoelectric multiferroics combine the best properties of both.

Although the coupling of magnetisation and polarisation in a multiferroic was first observed in boracites [38], the majority of research has focused on perovskite-related materials. This is due to the deep understanding of ferroelectricity in this structure, the ability to incorporate a wide range of magnetic cations, and also the huge number of distortions available to the perovskites that may play the role of the intermediary transferring information from the polarisation to the magnetisation.

$BiFeO_3$ is the perovskite that has received the most attention [39, 40]. It has room temperature polarisation and magnetisation, and, when grown in a film, can have a magnetic structure that is simple and has a weak ferromagnetic component. The reversal of the magnetisation with electric field has been observed in this material [41] but, by using symmetry arguments similar to those in Chapter 4, the direct reversal of magnetisation after the reversal of polarisation is impossible and instead, switching takes place through a complicated "two-step" process which requires large electric fields. Furthermore, it was not possible to carry out more than a couple of complete switching cycles before device breakdown. Despite the appealing room-temperature polarisation and magnetisation, single crystals of $BiFeO_3$ are also difficult to synthesise, often show large leakage currents and are not easily compatible with existing CMOS technologies [42].

Some degree of electric field control of magnetism has also been observed or predicted in other multiferroic perovskites [43] but the reversal appears to be difficult to achieve. There is still a lot to discover about $BiFeO_3$, but a range of possible perovskite materials is vast and alternatives may be out there. The goal of this thesis is to find these alternatives and to identify those in which it is possible to switch the magnetisation directly with reversing polarisation.

Multiferroic materials are in principle easy to achieve. The stacking of a magnetic material on top of a ferroelectric material would be one. However, getting strong interactions between the magnetic and ferroelectric dipoles, and observing the electric field reversal of magnetisation in particular, is much more difficult. Obtaining this effect in a single phase material, above room temperature and ambient pressure, so that an effective multiferroic memory could be created, would be a much lauded feat in condensed matter.

1.3 Outline and Aims

I can now refine the question I posed at the end of the first section of this chapter: "Can quantum mechanics be used to understand, design and realise novel perovskite-based multiferroics in which the electric field control of magnetism is possible?". Materials in which this is possible would surely find applications in future memory devices and possibly form the basis of "the ultimate memory device". It is therefore the purpose of this thesis to describe my efforts in identifying perovskite based materials in which the electric field reversal is possible and then to explore promising candidates with further quantum-mechanical simulation.

In order to achieve this, some preliminary understanding of the perovskite structure is necessary. This is presented in Chapter 2. The basics of ferroelectrics, magnets and multiferroics were briefly explored above, but in Chapter 2, the details of these phenomena in perovskites specifically are explored. Despite its seemingly simple chemistry, the perovskite structure can become incredibly complex, and some method of systematizing the many possibilities is required. This is provided by group theory and crystallography which is explored in detail in Chapter 3. Group theory becomes an invaluable predictive tool when combined with the Landau Theory of phase transitions. Chapter 3, examines the power of this theory to predict new phases of mater-

ials that could host the necessary simultaneous ordering of electric and magnetic dipoles. The chapter also identifies how these dipoles must be coupled in order to achieve electric field control of the magnetic dipoles. Group theory is incredibly powerful, and Chapter 4 takes these ideas and applies them, predicting new perovskite materials in which the desired coupling between electric and magnetic dipoles is present.

Identification of promising candidate materials is not the end of the story. Group theory can only get one so far. It can tell you whether a particular structure allows for a polarisation but it can say nothing about what the magnitude of the polarisation will be or even if the structure is stable. To have any understanding of the size of physical properties and the stability of matter, group theory must be supplemented with a tool that is capable of calculating the energetics of the structure. As the fundamental building block is of roughly atomic dimensions, it should come as no surprise that this tool is quantum mechanics! Chapter 5 details density functional theory (DFT), an exact reformulation of quantum mechanics that allows for the fully quantum mechanical treatment of crystal structures. With this tool, I can calculate the energy levels of electrons in a crystal, the forces on atoms, and the stable crystal structures. Also explored in this chapter are other quantum mechanical concepts that allow for the computation of important physical properties: the modern theory of polarisation for calculating polarisation, band structures to determine insulating or conducting behaviour, and the Hubbard Model to incorporate the correlation of electrons occupying the same atomic site.

Chapters 6 and 7 combines the group theoretical analysis with quantum mechanical calculation in a series of perovskite materials with increasing complexity. We support the group theoretical identification of materials in which electric field control of magnetism is possible with calculations of their energetics. If the desired structural phase does not appear to be thermodynamically stable (ie. the most stable) but is instead metastable (ie. stable with respect to small perturbations only)*, we explore how external stimuli like strain can change the energy landscape and lead to novel multiferroic phases.

Electric field control of magnetism in which the reversal of the electric dipole necessarily reverses the magnetic dipole, is the central principle behind the next generation of memory devices

*These terms will be more rigorously defined later.

and the quest to identify materials in which it is possible has been a deeply gratifying journey. The physics is simple enough to be easily understandable, rare enough to be exciting when found and general enough to send me flying all over the Periodic Table in my quest for coupled dipoles. More than anything, this project has irrevocably cemented my belief that science works best as an interconnected discipline and as my research into multiferroics sits squarely at the intersection between physics, chemistry, engineering, material science and computing, I have been exposed to ideas, and been able to meet people, that I would never have expected to encounter when I began my undergraduate degree in theoretical physics almost eight years ago. Just as electric dipoles are indirectly connected to magnetic dipoles, condensed matter physics provides the glue that connects people from disparate fields. I hope that my enthusiasm for the subject remains evident in the ensuing pages.

Chapter 2

Multiferroicism In Perovskite Based Materials

Having identified perovskite-based materials as candidates for accomodating the necessary ferroelectric and magnetic distortions which could enable the electric field control of magnetism, this chapter reviews the essential physics and chemistry of this structure type. I aim to define terms that will frequently appear in the remainder of the thesis, explore the origins of ferroelectricity and magnetism in perovskites, and the difficulty in getting both to appear in the same phase. This chapter ends by discussing some methods to overcome this difficulty.

2.1 The Perovskite Structure

The perovskite structure ABO_3 [44, 45, 26] has a simplistic chemical formula that disguises an enormous amount of complexity. The unit cell of the highest symmetry phase[†] contains five atoms; the A-site in the corners of the unit cell, the B-site in the center and the three O atoms in the face centers. This cubic structure, when expanded using the translational symmetry of crystals, can be thought of as describing a three-dimensional network of corner-sharing, rigid octahedra with A-site ions inserted in the middle of the cubo-octahedral gaps left by the octahedral network.

[†]The symmetry of perovskite materials will be discussed in some detail in subsequent chapters

The ABO_3 formula suggests substantial compositional flexibility, but there are, of course, certain restrictive conditions. Obviously, the overall charge in an unit cell must be neutral, so that perovskites typically have A/B elements with I/V, II/IV or III/III oxidation states. The second condition is that the A-site must fit in the cubo-octahedral gap. If it is to do this and maintain a perfect cubic structure then, by Pythagoras' theorem, the edge distance $2(r_B + r_O)$ must be equal the face diagonal distance $2(r_A + r_O)$ divided by $\sqrt{2}$. This can be used to define a quantity

$$t = \frac{(r_A + r_O)}{\sqrt{2}(r_B + r_O)} \tag{2.1}$$

which is known as the Goldschmidt Tolerance Factor and r_A, r_B and r_O are the radii of the A-, B- and O-sites respectively. If $t \approx 1$, then this gives confidence that the cubic structure is stable. If $t < 1$, this suggests that the A-site is too small for its site and conversely if $t > 1$, the A-site is too big. The opposite conclusions apply for B-sites.

How does the perovskite deal with non-ideal tolerance factors? The structure allows for various distortions that may reduce the high electrostatic forces that develop from having cations that are too large or too small to fit into their sites. Alternatively, there may be other sources of structural instability, not related to cation size, which are also accommodated by distortions. The wide range of distortions available to perovskite materials gives them a great deal of structural flexibility which enables their chemical flexibility. This is why perovskites are such useful materials to work with and exhibit such a wide range of material properties [44]. I enumerate these distortions in the following subsections and all of them are displayed schematically in Fig 2.1.

2.1.1 Octahedral Tilts

The most important distortion available to perovskites are the rigid motions of the BO_6 octahedra that maintain the bond distances between the B and O sites. The octahedra can tilt and rotate to change the size of the cubo-octahedral gap inhabited by the A-site and reduce the electrostatic penalty of cation size mismatches. As the BO_6 octahedra are connected by the O

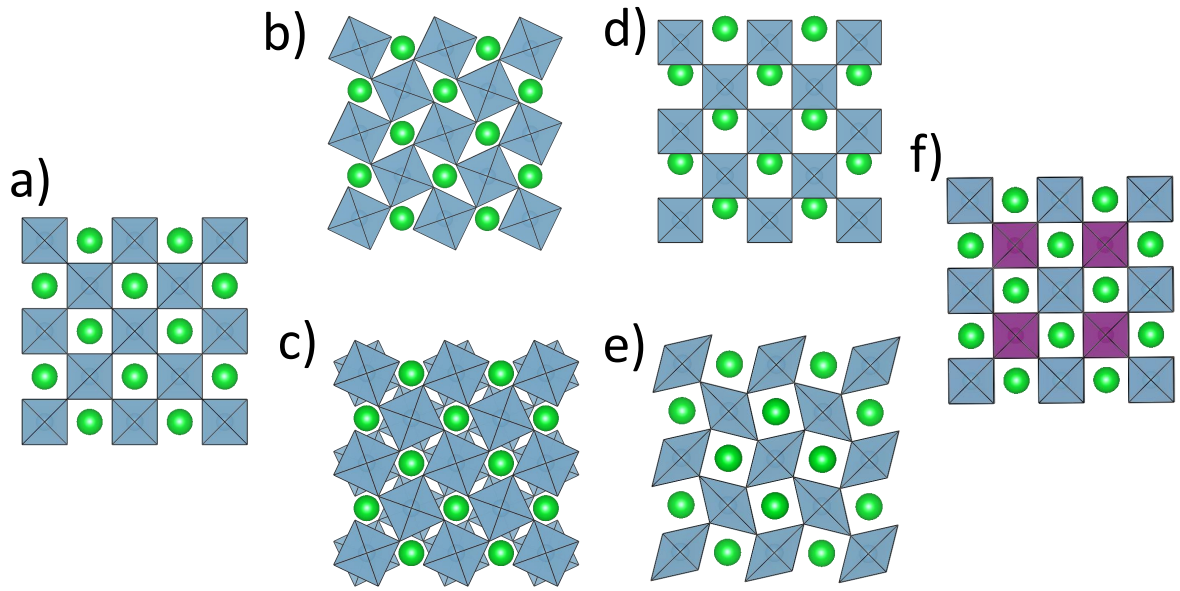

Figure 2.1: Various distortions available to the perovskite to resolve size mismatches, electronic effects or high Coulomb interactions a) The undistorted perovskite b) In-phase octahedral rotations about one axis ($a^+a^0a^0$). c) Anti-phase octahedral tilts about one axis ($a^-a^0a^0$) d) Polar distortion e) Cooperative Jahn-Teller distortion f) Nearest-neighour cation ordering.

anions at the vertices, the tilt or rotation of one cation necessarily affects the entire network. For a single layer of corner-connected octahedra, a rotation about an axis perpendicular to the layer and through one octahedra rotates all the neigbouring octahedra in the opposite direction. There is an addition degree of freedom describing the pattern of rotations in the layers above and below. Either these layers can rotate in the same direction as the one in the middle (an *in-phase pattern*), or they can rotate in the opposite sense (an *anti-phase* pattern). Being a three-dimensional network, it is possible to rotate around any of the axes of the octahedra. The complete rotation pattern is thus a combination of in-phase and anti-phase rotations about each axis. A convenient notation to describe this was invented by Glazer [46, 47] in which the relative magnitudes and tilts are described using three symbols.

A tilt pattern in which there are equal magnitude, in-phase tilts about all three axes is described by the symbol $a^+a^+a^+$. If the magnitude is different along the third axis, the symbol becomes $a^+a^+c^+$. The change from a to c denotes a change in relative magnitude, but provides no information at all on the absolute magnitude; you cannot tell if the tilts around the third axis

are larger or smaller than the tilts around the other axes. Glazer's approach was an attempt to describe the different symmetries of perovskites and so the absolute magnitude did not matter. If the tilts around the third axis are instead anti-phase, the symbol becomes $a^+a^+c^-$. Different magnitudes about all axes would have the symbol $a^+b^+c^-$. There are 22 possible tilt patterns that can be enumerated in this manner, although only 15 are actually symmetry inequivalent - see Chapter 4 and Reference [48]*.

2.1.2 Ferrodistortive and Antiferrodistortive Displacements

Rigid octahedral distortions are an example of antiferrodistortive displacements of anions. Considering each ion I to be a point charge of charge Z_I, then a distortion that moves each cation by an amount $\mathbf{u}_I$ would produce a net polarisation of

$$\Delta\mathbf{P} = \frac{e}{V}\sum_I Z_I\mathbf{u}_I \tag{2.2}$$

where V is the volume of the cell containing all I ions. If the result of all ionic distortions is a state with $P = 0$, then that set of distortions is antiferrodistortive. Octahedral rotations are one example. A motion where a cation moves in one direction and neighbouring cations move oppositely would also be an antiferrodistortive displacement and is occasionally called an antipolar distortion.

If instead the sum of distortions leads to $P \neq 0$, then that motion is *ferrodistortive* or *polar*. The collective off-centering of cations is the most important example and leads to the breaking of the centre-of-symmetry and the formation of a net polarisation in ferroelectric perovskites such as $BaTiO_3$. A net polarisation in an insulating material leads to a build up of charge at the surface and the subsequent formation of a depolarising field directed oppositely to the polarisation [49]. This provides a force that suppresses polar distortions in thin film materials, unless the surface charge is screened through contact with conducting electrodes [50]. However, no screening is perfect and as a result, there tends to be a critical thickness for perovskites

*These are the simple tilt patterns that can be formed. There are also tilt patterns that are formed by superpositions of in-phase and anti-phase rotations about the same axis. These are rare and I don't mention them further.

below which the remaining depolarising field is large enough to suppress the ferrodistortive displacement [51].

In order to be ferroelectric, this distortion should be able to be switched by an external field. Clearly this is not possible in a metal because free charges screen all electric fields from the inside of a conductor. However, there is nothing in principle stopping a material from containing ferrodistortive displacements and being a metal. These materials are termed *polar metals* [52, 53] which are extremely interesting in their own right but I will not discuss them further because they are impossible to switch through the traditional method of applying electric fields.

Equation 2.2 can be generalized into an integral for more realistic continuous charge densities $\rho(\mathbf{r})$. There is however, a serious flaw in this approach to calculating the polarisation in using Equation 2.2 or its continuous generalisation. The problem arises from ambiguity in choosing the unit cell, different choices lead to different values of the polarisation. The solution is to recognize that the polarisation is not a uniquely defined quantity in bulk materials. The formal mathematics behind this discovery is relegated to Chapter 5, but one immediate consequence of the Modern Theory of Polarisation [54, 55, 56] that is useful here is the concept of effective charge. As electronic charge is a continuous quantity, the motion of the positively charge nucleus disturbs this charge field. The negative charge due to electrons may move independently of the nuclei, especially if the electrons are involved in covalent bonds. More specifically, the distribution of electrons associated with the orbitals of each ions are centered at the *Wannier centre*. When the nuclei of the ion is displaced, the Wannier centre may displace in the opposite direction, creating a larger dipole than would be obtained if the centres of negative charge were assumed to be fixed.

This introduces the concept of the *Born effective charge*

$$Z^*_{ij} = \frac{V}{e}\frac{\partial P_i}{\partial u_j} \tag{2.3}$$

which measures the change in polarisation with changing ionic displacement u_j. This can be reworked into

$$\Delta P_i = \frac{e}{V} \sum_j Z^*_{ij} u_j \tag{2.4}$$

which is equivalent to Equation 2.2 if Z is replaced with the effective charge Z^*. This replacement of charge with effective charge reminds us that the polarisation can be affected by the electronic degrees of freedom (as in the lone-pair mechanism discussed below) as well as ionic displacements.

2.1.3 Jahn-Teller Distortions

Another important class of antiferrodistortive displacements are Jahn-Teller distortions [57, 44]. These are caused by degeneracies in the electronic structure of cations in certain anion environments. In perovskites, the BO_6 octahedra are the important anion structure. The crystal field produced by the octahedra splits the five-fold degeneracy of d orbitals into two levels [58]; the lower energy, three-fold degenerate t_{2g} orbitals and the higher energy, two-fold degenerate e_g orbitals.

Depending on the occupancy of the d levels, the energy can be further lowered. For example, if the B-site has a d^4 electronic structure, then the three t_{2g} levels are singly occupied and, because of a Hund's coupling favouring parallel spins, the final electron must go into the higher e_g orbitals with the same spin orientation. Due to the two-fold degeneracy, the electron can go into either e_g orbital with each choice giving the same energy. The e_g orbitals d_{z^2} and $d_{x^2-y^2}$ are directed along the B-O bonds; a displacement of anions that extends the bond parallel to d_{z^2} would lower this orbital's energy with respect to $d_{x^2-y^2}$. The two other bonds can expand so that the average of the t_{2g} energies stays constant. However, the single e_g electron can now occupy the lower d_{z^2} orbital and so the total free energy of the system has been reduced. This distortion - the Jahn-Teller distortion - is therefore favourable when such an electronic degeneracy exists. The process is illustrated in Figure 2.2

The splitting in the e_g orbitals would be proportional to the distortion u away from the undistorted octahedra, so that $\Delta E = \pm gu + \frac{1}{2}ku^2$ where the second term is the elastic cost of the distortion and g is a coupling constant. The linear term always ensures that a distortion

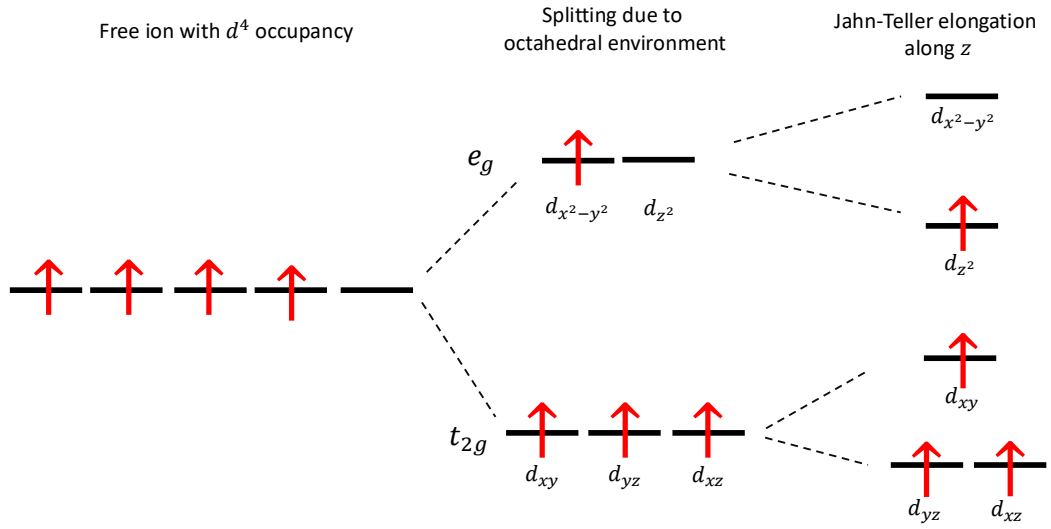

Figure 2.2: Lowering of total energy with a Jahn-Teller distortion that extends the B-O bond parallel to the z axis. The free ion with d^4 occupancy has fully degenerate d orbitals, the octahedral environment splits these into e_g and t_{2g} orbitals. The Jahn-Teller distortion further splits the e_g and t_{2g}

is preferred and so for high-spin d^4 and d^9 occupancies, the Jahn-Teller distorions are aways important*.

2.1.4 Ion Ordering

The final distortion worth mentioning is ion ordering. For perovskites containing multiple ions that could occupy any particular site, they may take up an ordered arrangement to minimise the electrostatic repulsion of different ordered ions. For example, a perovskite with disordered B-sites $A(B^{3+}, B'^{5+})O_3$ may order the B-sites below a certain temperature to minimise the electrostatic repulsion of the B^{3+} and B'^{5+} cations. The most common arrangement is one in which every neighbouring cation is of the opposite kind, the *rocksalt* arrangement [59]. Alternatively, the cations can be ordered in layers along a certain direction or in columns, although these are much rarer for B sites.

*Jahn-Teller distortions are also important for other occupancies but these involve degeneracies in the t_{2g} levels - a weaker effect.

The same cation orderings could potentially be achieved by the A-site although experimentally it is only the layered arrangement that is typically observed [60]. This is due to the fundamentally different environment of the A-sites compared the B-sites and the breaking of symmetry permitted by each kind of ordering. It is also possible to order both the A and the B sites simultaneously [61, 62].

The above cation orderings produce *double perovskites* because the chemical formula becomes $AA'BB'O_6$ - one formula unit contains ten atoms rather than the five atoms of ABO_3*. This can be extended to include cation orderings in larger perovskite cells. There are triple perovskites [64, 65] with 15 atoms in the formula unit and also quadruple perovskites [66, 67, 68] with 20 atoms. Contained within the quadruple perovskite umbrella are separate subfamilies. There are the $AA'_3B_4O_{12}$ perovskites as well as the $A_2A'A''B_4O_{12}$ perovskites with columnar order of the A-sites [69]. Each cation ordering changes the symmetry of the structure, with consequences for the allowed physical properties. Chapter 4 investigates the symmetry of some of these orderings to see whether any of them create the conditions necessary to allow for the electric field control of magnetism.

Finally, ordering on the anion sites is also a powerful tool to break symmetries and is a field which is still in its infancy. The O^{2-} site can also be occupied by halide (F^{3-},Cl^{3-}), chalcogenide (O^{2-},S^{2-}) and pnictide (N^{1-}) anions [70, 71, 72, 73, 74, 75, 76]. It appears that it is extremely difficult to control anion ordering, but it could open up a wide range of perovskite phases, some of which would be polar [74].

Importantly, the inclusion of multiple cations or anions in the perovskite structure also changes the tolerance factor so that now the *average* radii must be used and so

$$t = \frac{(< r_A > + < r_X >)}{\sqrt{2}(< r_B > + < r_X >)}. \tag{2.5}$$

This increases the chemical flexibility for a particular tolerance factor. In addition, the change in the anion oxidation state through anion order (or through complete replacement like

*Some authors describe $AA'BB'O_6$ with ordered A and B sites as a "double-double" perovskite [63]. I avoid this term because I think it can be easily mixed up with "quadruple" perovskites.

in fluoride perovskite) changes the charge balance and would allow for new cations to take up the A and B site that were not permissible in purely oxide perovskites.

2.2 Soft Mode Theory

There are clearly many distortions available to the perovskite structure yet they can all conveniently be described within the context of *soft mode* theory. If the force on each atom is known in the high-symmetry phase (Chapter 5 describes how these can be calculated) then the dynamics of each atom can be determined by solving a set of coupling differential equations. This can be done using methods from linear algebra [77] and involves the diagonalisation of the force constant matrix. The resulting eigenvalues and eigenvectors are the vibrational frequencies ω^2 and normal modes respectively. Each of these vibrations has an energy proportional to its frequency and so, when quantised, can be interpreted as energy levels occupied by a certain number of particles - phonons. Each phonon has a frequency and a crystal momentum.

The central idea of soft-mode theory [19, 78] is to associate each distortion in a material to a normal mode (phonon). For example, the ferrodistortive displacement u, which involves the displacement of some atoms against others, is clearly an optical phonon [79] of a certain frequency ω obeying the equation

$$\ddot{u} = -\omega^2 u \tag{2.6}$$

with a dot denoting differentiation with respect to time. This simple harmonic oscillator equation is solved by $u \propto e^{i\omega t}$ suggesting that the ferrodistortive displacement oscillates between positive and negative amplitudes with time.

Sometimes diagonalising the force constant matrix results in an eigenvalue $\omega^2 < 0$, or alternatively, an imaginary frequency. This is the case when the force constant matrix of $BaTiO_3$ in the cubic symmetry is diagonalised. It that case, the phonon associated with the ferrodistortive vibrational mode has an imaginary frequency. The consequences of this are easy to ascertain. The exponential dependence changes to $u \propto e^{-\omega t}$ which no longer describes an oscillating phonon. A phonon with an imaginary frequency becomes fixed in time so that the corresponding distor-

tion is fixed or frozen. In $BaTiO_3$, the frozen phonon results in a permanent distortion and a macroscopic polarisation.

The phase transition happens at a particular temperature T_C and therefore a temperature dependence of $\omega^2 \propto (T - T_C)$ would successfully model the transition to the polar phase as a function of temperature. The reduction of ω^2 with temperature (or other fields) is known as phonon mode softening. It can be used to describe all of the above distortions (except ion ordering). It should be remembered that phonon softening is a useful description once the forces are known, but the forces themselves always have a microscopic mechanism such as the electronic instability for Jahn-Teller distortions.

In perovskites with non-ideal tolerance factors, it is usually the tilt modes which appear first when lowering temperature. In the context of soft-mode theory, we can say that with decreasing temperature, the tilts are the first modes to obtain an imaginary frequency.

2.3 Ferroelectricity In Perovskites

There are several microscopic mechanisms for producing a macroscopic polarisation in perovskites and here I briefly review the most important ones below.

2.3.1 Lone Pair Stereochemistry

Cations such as Bi^{3+} and Pb^{2+} contain outer s electrons that do not participate in the formation of bonds. For example, the $6s^2$ electrons in Pb^{2+} actually occupy an orbital formed through the hybridisation of the $6s$ and $6p$ orbitals, leaving them chemically inert and unavailable for bonding [80]. However, these lone pairs can take a range of orientations and such a directed charge clearly forms an electric dipole moment. Below a ferroelectric transition temperature, these disordered dipoles can align cooperatively, leading to a net polarisation. The transition from disordered dipoles to ordered dipoles is, quite naturally, called an *order-disorder* transition.

The prototypical examples of perovskite ferroelectrics, antiferroelectrics and multiferroics, $PbTiO_3$, $PbZrO_3$ and $BiFeO_3$ respectively, all have their ferroelectric origin in this lone-pair

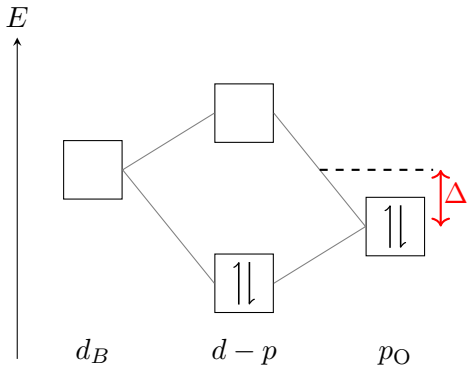

Figure 2.3: Simplified molecular orbital diagram of a covalent bond between the B cation and one of the surrounding O anions in a perovskite.

mechanism. In multiferroic $BiFeO_3$, the lone-pair dipoles align along the body diagonal of the 5-atom perovskite cell.

2.3.2 Second Order Jahn-Teller Effect

The image of polarisation being due to a ferrodistortive displacement of cations is realized in $BaTiO_3$; a cooperative displacement of all Ti^{4+} cations towards one of the O^{2-} anions to which it is covalently bonded. What causes a motion of this kind? A somewhat loose, but extremely intuitive description, is due to Khomskii [26].

To begin, picture the molecular orbital diagram for a covalent bond between the d orbitals on a B cation and the fully occupied p orbital on the neighbouring O^{2-} ion. This is shown in Figure 2.3. The bonding and antibonding orbitals are caused by the occurence of non-zero matrix elements $t = \langle p|H|d\rangle$ between the p and d orbitals where H is the Hamiltonian operator to be defined in Chapter 5 [81]. The greater the overlap of p and d orbitals, the larger this matrix element becomes.

Its possible to model the hybridisation between p and d as a jumping of electrons from the filled p into the empty d and back again. This delocalises the electrons, lowering their energy in a manner akin to an electron in a box with increasing dimensions. The probability to hop between p and d is proportional to t, so that the probability to hop back to the starting place is proportional to t^2. However, the electrons must also increase their energy by Δ (the energy

difference between the anion p and cation d orbitals) to complete the first hop which reduces the total energy savings obtained through delocalisation. Finally, the total energy is proportional to $-\frac{t^2}{\Delta}$.

Now suppose that the B site moves a distance u towards the O on the right, then the hopping probability is changed by an amount $\delta t = \gamma u$ where γ is just a constant of proportionality. The new probability to hop to the right is $(t + \delta t)$ and the probability to hop to the left is $(t - \delta t)$. The energy of the whole system is therefore

$$E_{right} + E_{left} \propto -\frac{(t+\delta t)^2}{\Delta} - \frac{(t-\delta t)^2}{\Delta} = \frac{2t^2}{\Delta} - \frac{2\delta t^2}{\Delta} = \frac{2t^2}{\Delta} - \frac{2\gamma^2 u^2}{\Delta} \tag{2.7}$$

where the first term in the final expression is just the energy that the system would have without this additional B site distortion. It appears that a polar displacement of the B site will therefore always further lower the energy by an amount $-\frac{2\gamma^2 u^2}{\Delta}$, so why are most oxides not polar? It is because this distortion has to also contend against quadratic restoring forces of the form $\Delta E = +\frac{1}{2}ku^2$. Only when the lowering due to a displacement is greater than this restoring force, is this particular mechanism effective at producing polar crystal structures.

The same analysis can be performed much more rigourously [82, 83, 84] by expanding the Hamiltonian in a power series of the displacement u and then by using standard quantum mechanical perturbation theory. This calculation reveals that the first order term of the form gu is the familiar Jahn-Teller mode that I have already described. This new effect based on increased electron delocalisation is quadratic in the displacement u, and is therefore termed the *second-order Jahn-Teller effect* (SOJT). For illustrative reasons, I prefer Khomskii's presentation.

If the SOJT effect leads to a cooperative displacement of all B-sites in the same direction, that leads to a polar crystal structure. On the other hand, if different B-sites displace in different directions, this is an antipolar distortion and results in zero net polarisation. If it were the case that lowering temperature causes a transition from the non-distorted crystal structure to the distorted one, this is a *displacive* transition, and if instead the lowering of temperature leads from a phase in which the SOJT distortions are present but uncorrelated to one where they are all correlated, this is an *order-disorder* transition.

2.3.3 Geometric Ferroelectricity

Occasionally, a combination of antiferrodistortive modes can combine to give a net ferrodistortive displacement. The prototypical example of this *geometric* ferroelectricity is $YMnO_3$ (which is not strictly a perovskite because it formed from layers of trigonal bipyramids instead of octahedra) where an antipolar motion of Y cations and tilts of the bipyramids, both effects are caused by soft phonons, leads to a net polarisation [85, 86].

Similar behaviour occurs in the $a^-a^-c^+$ tilt pattern in perovskites wherein local dipoles form as the tilts bring O anions close to A-sites. Unfortunately, there are an equal number of dipoles directed opppositely and so no net polarisation develops [34]. Methods to stop these anti-polar motions from cancelling exactly is an effective method to engineer large polarisations, and is the method adopted in Chapter 7.

As the polarisation appears from the symmetry of the structure, rather than due to any kind of electronic instability, the Born effective charges remain nominal in a geometric transition.

2.3.4 Cooperative Interactions

$LiNbO_3$ and $ZnSnO_3$ are examples of low-tolerance factor perovskite materials with $a^-a^-a^-$ tilt patterns. Due to the non-ideal tolerance factor, the magnitude of these tilts is extremely large. Previous work, such as Reference [87], has shown that almost all distortions act to suppress the polar distortion. These are known as competitive interactions.

This tilt pattern by itself does not break inversion symmetry and so there is no reason to suppose the $LiNbO_3$ should be polar. However, in this situation, the tilts are so large that they are actually destabilizing the material and producing large forces on the cations. Only through a secondary distortion, in this case it is a polar distortion, can the forces be reduced. When one distortion favours another, this is a cooperative interaction. Very low tolerance factor perovskites often become polar in this manner. Without the possibility of cooperative interaction, these materials would be centrosymmetric*. In Chapter 6, I explore another way to

*There is another reason while the polar mode is favoured in the $a^-a^-a^-$. This particular tilt pattern does

circumvent competitive effects by controlling the strength of cooperative interactions.

2.3.5 Ferroelectricity Due To Ion Or Charge Ordering

Similar to geometric ferroelectricity, charge ordering or ion ordering can break the centre of inversion of a crystal and therefore enforce a polarisation. Thin films of magnetite (Fe_3O_4) are known to show ferroelectricity below its charge ordering temperature (the Verwey transition) because the centrosymmetry is broken [88].

In perovskites, a charge or ion ordering, in combination with various antiferrodistortive modes could be enough to produce polar distortions. This appears to be the case in the doped manganite material $Pr_{0.6}Ca_{0.4}MnO_3$ [89].

Whether any particular order allows for a polarisation is a question that is best tackled through a thorough analysis of the symmetry of materials. This is the goal of Chapters 3 and and 4.

2.3.6 Strain

Epitaxial strain strongly couples to and softens the zone-centered optical phonons that cause polar distortions in perovskites. Tensile strain increases the length of the unit vectors parallel to the epitaxial substrate and decreases the vectors perpendicular to the surface. This preferentially softens the zone-centered phonons corresponding to polar phonons directed along the in-plane direction. Conversely, compressive strain decreases the lattice vectors in the plane and increases the vector perpendicular to the surface. This softens the out-of-plane polar phonons. This effect has frequently been used to predict polar transitions in a variety of perovskite materials [90, 91, 92, 93].

not allow for any secondary modes to appear, each of which would be another source of competitive interaction with the polar mode. Therefore, the cooperative interaction favouring polarisation due to large tilts has fewer competitive interactions to contend with.

2.4 Magnetism In Perovskites

Having described various mechanisms for how perovskites gain their ferroelectric properties, we now discuss the other necessary component for a multiferroic and explore how perovskites can become magnetic. As mentioned in Chapter 1, it is ferromagnetic-ferroelectric multiferroics that are the ultimate goal of this project because of their intrinsic utility to memory devices. This requires the material to be insulating so that a macroscopic polarisation can arise. As a result, I will not mention mechanisms responsible for magnetism in metals (such as the Stoner criterion mentioned in the introduction or the RKKY interaction [18]) but instead focus wholly on mechanisms that are relevant to insulators.

2.4.1 Exchange Interactions

Any ion with unpaired spins possesses a magnetic moment $\boldsymbol{\mu}$. From basic magnetostatics [49], two magnetic moments, seperated by $\boldsymbol{r}$ can interact with each other through a dipolar interaction

$$E = \frac{\mu_0}{4\pi r^3}\left[\boldsymbol{\mu}_1 \cdot \boldsymbol{\mu}_2 - \frac{3}{r^2}(\boldsymbol{\mu}_1 \cdot \boldsymbol{r})(\boldsymbol{\mu}_2 \cdot \boldsymbol{r})\right] \tag{2.8}$$

but plugging in representative values for the magnetic moments ($\approx 1\mu_B$) and separations (≈ 1Å) leads to an interaction energy equivalent to about 1K. If this was the only mechanism to create long-range magnetic order, the magnetic structure would be destroyed by thermal fluctations for anything above 1K. We cannot describe the high temperature magnetism of a perovskite like $BiFeO_3$ using this mechanism.

Instead, the concept of exchange becomes essential. This arises from the fermionic statistics of the electron and dictates that the quantum mechanical state must be antisymmetric with respect to exchange of any two electrons. This fundamental tenet of quantum mechanics leads to the Pauli Exclusion Principle but, more appositely, to mechanisms enabling long-range magnetic order at high temperatures.

The central idea behind *direct exchange* can be understood from a model of two electrons distributed over two atoms. The combined electronic state can be decomposed into a product

of spatial and a spin states. The spatial part can either be symmetric or antisymmetric, and then to ensure the antisymmetry of the full state, the spin symmetry must be of the opposite symmetry. Therefore, for a symmetric spatial wavefunction, we obtain the antisymmetric spin state (the singlet) whereas for the antisymmetric spatial wavefunction we get the symmetric spin state (the triplet). Even without considering any kind of dipolar interactions, there is a dependence of the energy on the spin state, because a particular spin state is inextricably linked to a spatial state. The triplet and singlet states arise from the standard quantum mechanical rules for combining angular momenta. The combination of two electrons with $S = 1/2$ results in a state with either $S = 0$ or $S = 1$. Alternatively, we can relate the total spin to the product of the spins on each individual electron because

$$\boldsymbol{S}_{\text{total}} = \boldsymbol{S}_1 + \boldsymbol{S}_2 \tag{2.9}$$

so that

$$\boldsymbol{S}_1 \cdot \boldsymbol{S}_2 = \frac{1}{2}\left[\boldsymbol{S}^2_{\text{total}} - \boldsymbol{S}^2_1 - \boldsymbol{S}^2_2\right]. \tag{2.10}$$

As the eigenvalue of the square of a spin operator $\boldsymbol{S}^2$ is $S(S+1)$, then $\boldsymbol{S}_1 \cdot \boldsymbol{S}_2 = \frac{1}{4}$ for triplet states and $\boldsymbol{S}_1 \cdot \boldsymbol{S}_2 = -\frac{3}{4}$ for singlet states. We can therefore parameterize the energy of the system via this scalar product as

$$E = -J_{ex}\boldsymbol{S}_1 \cdot \boldsymbol{S}_2 \tag{2.11}$$

where J_{ex}, known as the exchange integral. The model can be extended to the Heisenberg Model

$$H = -\frac{1}{2}\sum_{ij} J_{ij}\boldsymbol{S}_i \cdot \boldsymbol{S}_j \tag{2.12}$$

describing the magnetism of larger systems by considering similar interactions between all pairs of spins. The factor of $\frac{1}{2}$ accounts for the double counting of each spin pair.

This model effectively describes all magnetic interactions in solids but is not just a simple extension of the direct exchange mechanism described above. This is because J_{ij} can describe

much more general interactions [27]. In direct exchange, J_{ex} describes the difference in the Coulomb energies of the symmetric and antisymmetric states

$$J_{ex} = \int \psi_1^*(\boldsymbol{r})\psi_2^*(\boldsymbol{r}')\frac{e^2}{4\pi\epsilon_0|\boldsymbol{r}-\boldsymbol{r}'|}\psi_1(\boldsymbol{r}')\psi_2(\boldsymbol{r})d^3\boldsymbol{r}d^3\boldsymbol{r}' \tag{2.13}$$

which is is only sizeable if there is considerable overlap between the two electron states. Because of this restriction, direct exchange is also too small to account for the magnetic properties of magnetic insulators.

Instead, we turn to *superexchange* interactions which describe how the hopping of electrons between sites can favour one kind of magnetic structure over another. In a simple model of a one-dimensional* chain of antiferromagnetically aligned atoms, an excited state E_1 would be attained through an electron hopping from one site and doubly occupying the next site. The difference in energy between the ground state and this excited state is $U = E_1 - E_0$ and comes from the Coulomb repulsion of having two electrons on the same atom. Using second-order quantum mechanical perturbation theory, the change in energy is

$$\Delta E = \frac{|\langle 0|H'|1\rangle|^2}{E_1 - E_0} = -\frac{t^2}{U} \tag{2.14}$$

where I have defined $t = \langle 0|H'|1\rangle$ to be hopping element. Physically, the energy is reduced by $\frac{t^2}{U}$ because the electron can now hop between sites, increasing its kinetic energy in the same way that the energy of an electron in a box is reduced if the box is made wider. The process is known as virtual hopping because it involves hopping to a neighbouring site and then back, which is equivalent to doing nothing at all. This is related to the mathematical fact that a second order perturbation always results in a lowering of the energy.

However, this hopping is not permissible for a ferromagnetically aligned spin chain because a single hopping would doubly occupy a site with parallel spins, violating the Pauli exclusion principle. For a ferromagnetic chain, $t = 0$. Therefore, superexchange results in energies that are dependent on the magnetic structure and so can be incorporated into the Heisenberg model by

*This model is just for illustrative purposes. Magnetic order cannot exist in 1D systems as codified in the Mermin-Wagner theorem.

setting $J = +\frac{t^2}{U}$. The positive sign is important because then the antiferromagnetic configuration becomes favourable.

In many magnetic oxides, such as the antiferromagnetic MnO or the perovskites $BiFeO_3$, $LaFeO_3$ or $LaMnO_3$, each magnetic cation is seperated from its neighbour by O anions. The superexchange mechanism still applies here and is in fact the primary mechanism for long-range magnetic order in the magnetic insulators. Instead of hopping directly to the neigbouring cation, an electron (virtually) hops from the filled oxygen p orbitals to either of the half filled magnetic d orbitals on neighbouring cations. With an antiferromagnetic configuration of spins, a greater number of excited states can be mixed in with the ground state without falling foul of the Pauli exclusion principle*.

In real materials, we need to contend with all three dimensions. Magnetic cations in a BO_6 octahedral environment have many d-orbitals and it may be the case that the orbital that overlaps with the intermediate oxygen is actually empty whilst the other d orbital in the B-O-B chain is either half-filled or filled. One can work though the number of allowed excited states in this case and find that it is actually the ferromagnetic state that is stabilised so that $J < 0$. However, this ferromagnetic interaction is weaker than the antiferromagnetic coupling due to two half-filled orbitals.

Which magnetic interaction exists is neatly summarised by the Goodenough-Kanamori-Anderson (GKA) rules [94, 95, 96, 97] which can be succinctly stated that, for 180° B-O-B chains, "superexchange interactions are antiferromagnetic where the virtual electron transfer is between overlapping orbitals that are each half-filled, but they are ferromagnetic where the virtual electron transfer is from a half-filled to an empty orbital or from a filled to a half-filled orbital" [94]. If instead the bond is closer to 90°, the conclusions are reversed.

Usually the GKA rules can give some quantitative idea about the magnetic structure but in perovskites, the various distortions do make things quite difficult; the tilts distort the bonds away

*Some authors, most notably Goodenough[94], use the term semi-covalent exchange to describe a interaction involving an intermediate anion and restricts the use of the term superexchange to hopping mechanisms that do not involve an intermediate anion. On the other hand, Blundell [18] uses the term superexchange to describe the anion-mediated mechanism. The term *kinetic exchange* is often used [26], which I believe is a better term because it encapsulates the mechanism in which energy is lowered. However, the literature appears to have settled on "superexchange" to describe the virtual hopping mechanism irrespective of whether there is an anion present, and so I use this term.

from simple 180° or 90° angles making it hard to decide what the strength of each interaction should be. Nevertheless, it is possible to calculate exchange constants numerically [98], and they often agree well with what you would expect from a naive application of GKA. I use the GKA rules to predict a magnetic structure in Chapter 7 and find that it agrees well with calculations.

Allowing for antiferromagnetic and ferromagnetic couplings in perovskites, there are four main collinear magnetic structures. In the smallest 5-atom cell, the only allowed magnetic structure is ferromagnetic. In the larger cell containing a $a^-a^-c^+$ tilt pattern, there are three other structures. *A*-type magnetism is formed by ferromagnetic couplings within layers that are perpendicular to the in-phase tilt and antiferromagnetic couplings between layers. *C*-type describes a structure with antiferromagnetic spins within layers and ferromagnetic interactions between. Finally, *G*-type magnetism involves antiferromagnetic interactions between all nearest neighbours. These are shown in Figure 2.4. There are more complicated magnetic structures available in larger cells, such as the *E* and *CE*-types found in doped manganite perovskites [99, 100].

2.4.2 Non-Collinear Magnetism

We have seen how superexchange controls the coupling between neighbouring spins in real materials but this mechanism alone is still not capable of describing real magnetic structures in perovskite materials. Real perovskites have a certain amount of non-collinearity in their magnetic structure.

The small deviation from perfect collinearity is captured by Bertault's notation - a concept best described through an illustrative example. The full magnetic structure of $LaFeO_3$ is $\mathbf{G}_x\mathrm{A}_y\mathrm{F}_z$ - the bold $\mathbf{G}_x$ denotes that the main magnetic structure is collinear *G*-type with each moment directed either parallel or antiparallel to the *x*-axis. The next terms $\mathrm{A}_y\mathrm{F}_z$ state that there is also a small amount of canting included in the structure too. A_y suggests that there is *A*-type canting where layers perpendicular [010] direction alternate their canting towards [010]. F_z means that all spins also cant along the [001] direction. This canting is coordinated so that the material ends up with a small net magnetisation along this same direction - this is called *weak*

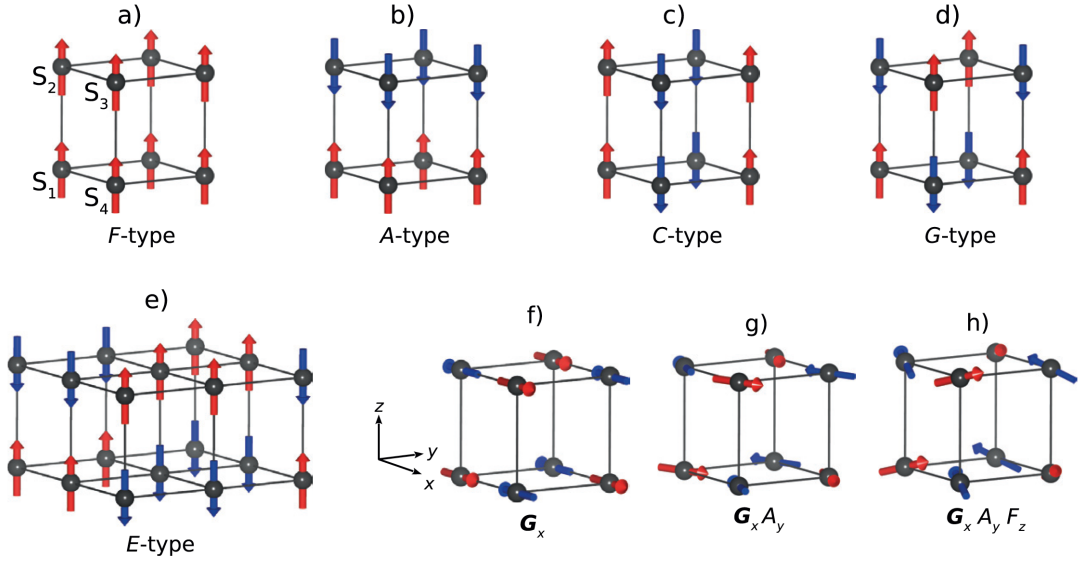

Figure 2.4: Magnetic structures in perovskites. a) Ferromagnetic b)*A*-type AFM c) *C*-type AFM, d) *G*-type AFM e) *E*-type AFM found in doped manganite perovskites f) g) and h) illustrations of Bertaut's notation and the accompanying non-collinear structure. Taken from Reference [27].

ferromagnetism.

The concept of weak ferromagnetism in antiferromagnetic perovskites is absolutely central to this thesis. As we shall see, the small ferromagnetic canting is often linked to other distortions in the material so that a reversal of these distortions can lead to the reversal of this weak ferromagnetic moment.

The Bertault notation raises two important questions. The first is "Why does $LaFeO_3$ want to have *G*-type spins along the x-axis rather than, say, the y-axis?" and the second is "What mechanism causes the non-collinearity in the first place?". The first question is answered through the concept of magnetic anisotropy. The Heisenberg Hamiltonian in Equation 2.12 needs to be adapted with another term that describes how the electric field produced by the ions in the vicinity of the magnetic charge, change the atomic orbitals and then, through the relativistic spin-orbit coupling that naturally emerges from the Dirac equation, alters the direction of the spin. This sounds complicated but can neatly be incorporated with an additional term of the form

$$H = -\sum_i K_i(\boldsymbol{S}_i \cdot \hat{\boldsymbol{n}})^2. \tag{2.15}$$

This equation lowers the energy if the spin is aligned either parallel or antiparallel to the *easy axis* $\hat{\boldsymbol{n}}$. In $LaFeO_3$, the easy axis is the x-axis. The constant K measures the strength of this anisotropy and could in principle be deduced from the Dirac equation, or extracted from a first-principles calculation with spin-orbit coupling enabled.

That resolves the first question. The additional antiferromagnetic and ferromagnetic cantings also find their origins through relativistic quantum mechanics. They are produced by the *Dzyaloshinski-Moriya interaction* [18, 27, 101, 102] which takes the form

$$H = \boldsymbol{D} \cdot (\boldsymbol{S}_1 \times \boldsymbol{S}_2). \tag{2.16}$$

This energy encourages the two neighbouring spins to be perpendicular (maximising $\boldsymbol{S}_1 \times \boldsymbol{S}_2$) and also mutually perpendicular to the Dzyaloshinsky-Moriya vector $\boldsymbol{D}$ (to minimise the energy). $\boldsymbol{D}$ controls the strength of this interaction. The superexchange constant J aligns spins in a parallel manner whereas $\boldsymbol{D}$ encourages a perpendicular alignment - the result is a canted structure. The ratio of the two constants determines the magnitude of the the canting.

As $\boldsymbol{D}$ is so central to this interaction, Moriya devised a set of rules, imposed by the symmetry of the material, to determine various properties of $\boldsymbol{D}$ [101]. The most important is that $\boldsymbol{D} = 0$ if the centre of the line joining the two magnetic cations is also a centre of inversion of the material. This may occur for lots of non-polar materials but it is not true that non-polar materials cannot have a significant canting. Perovskites like $LaFeO_3$ are proof of this.

If there aren't any centres of inversion, then there is the additional possibility of spiral magnetism in which the spins rotate continuously with position with an associated wave vector. This is the case in $BiFeO_3$ (although a small amount of strain changes the magnetic structure to largely collinear) and the rare-earth manganite materials. I will not discuss this further in my thesis, mostly because they are almost impossible to simulate with the ab-initio methods I am using (see Chapter 5).

2.5 The Contraindication Of Magnetism And Ferroelecticity

Although there are clearly several mechanisms for creating ferroelectric perovskites and also multiple ways to produce ferromagnetism, observing both in the same material is challenging. As a result, controlling the magnetism through interacting with the electric dipole of the material seems out of reach, as both of these must be present by definition.

There are several reasons why ferromagnetism and ferroelectricity are contraindicated in perovskites and all find their origin in the mechanisms discussed above.

Firstly, $3d$, $4d$ and $5d$ transition metal cations needed for unpaired spins and magnetic dipoles typically only occupy the B-sites of the perovskite, and they are slightly too large for this position. This lowers the tolerance factor and encourages the appearance of octahedral tilts and antipolar motions which we have seen have a strong competitive nature with ferrodistortive displacements. In short, steric effects caused by inserting magnetic cations causes additional distortions unfavourable to polar modes [87].

Secondly, the second order Jahn-Teller effect is known to drive ferrodistortive displacements but a closer look at Figure 2.3 reveals that it may be much more difficult if the d orbital is occupied. In this simplified model of just one d level and one p level, the electron in the d orbital will need to sit in the antibonding orbital, eliminating some of the energy savings from the bonding orbital. The higher level of theory [84], also discusses the importance of hopping integrals that are zero by symmetry. Many oxide materials with d occupancy have their highest energy states and their lowest energy unoccupied states formed mainly by d-orbitals. When second-order perturbation theory is applied to polar distortions in these materials, the distortion is more favourable if integrals like $\langle \Psi_1 | H' | \Psi_0 \rangle$ are non-zero where Ψ_1 and Ψ_0 are the ground state and excited states, and H' is the perturbation to the Hamiltonian caused by the polar distortion. If both the ground and excited states have similar d symmetry, this integral is zero.

Finally, strong ferromagnetism typically arises through the unequal occupancy of the spin-up and spin-down bands. This is this content of the Stoner theory of ferromagnetism. This mechanism only works in metals, which we have seen do not permit a macroscopic polarisation.

Without this mechanism, we are left trying to engineer ferromagnetism through direct or superexchange mechanism, which typically result in antiferromagnetic structures, or by searching for magnetic structures that allow for ferromagnetic canting of an antiferromagnetically ordered structure.

2.6 Multiferroic Perovskites

Despite the difficulty in combining ferroelectricity and magnetism, various perovskite materials do show both properties.

Most prominently is $BiFeO_3$ [42] which shows a large polarisation and is also antiferromagnetically ordered with a non-collinear spin spiral. The polarisation is caused through the lone-pair mechanism and occurs at a different (higher) temperature than the magnetic ordering and so, following Khomskii [34], this is a Type-I multiferroic. Applying a small amount of strain changes the magnetic structure to a collinear one that allows for a small weak ferromagnetic canting. Other magnetic materials are also polar* through this same lone pair mechanism, namely $BiMnO_3$ [103] and $PbVO_3$ [104].

For magnetic materials that do not make use of Bi or Pb, strain is often useful. $CaMnO_3$ and $SrMnO_3$ have been predicted [105, 91] to be ferroelectric and thus multiferroic under tensile strain. These predictions were later confirmed with experiments [106, 107]. Similarly, the fluoride perovskites like $NaMnF_3$ have also been shown to become polar with tensile strain [108, 109].

$TbMnO_3$ [110, 111] is the classic example of a Type-II multiferroic in which it is the magnetic structure itself that breaks the symmetry and leads to a polarisation. $TbMnO_3$ has two magnetic phase transition, the first at 41K and the second at 23K where a spin cycloid forms which removes the centre of inversion.

It is also possible that collinear spin structures can break the centre of symmetry. For example, the rare-earth nickelate materials $R\mathrm{NiO}_3$ first undergo a rocksalt charge ordering of Ni^{2+} and Ni^{4+} and then obtains a collinear magnetic structure in which planes of spins along the

*I hesitate to use the term ferroelectric here as not all of them have been switched

body diagonal are ordered in an up-up-down-down fashion. The combination of the charge-order and the magnetic structure removes the centre-of-symmetry and produces a polarisation [89].

This common feature of all of these multiferroics is the crucial role of symmetry. The inversion symmetry is broken in some way, either through crystallographic distortions, magnetic distortions or combinations of both.

2.7 Summary

Perovskite materials clearly present an enormous amount of flexibility. It is a simple task to use symmetry to hypothesise combinations of distortions, orderings and magnetic structures that allow for both ferroelectricity and magnetism. It is a much harder task to identify combinations of *realistic* distortions and magnetic structures that permit the electric field control of magnetism wherein the reversal of the polarisation necessitates the reversal of the ferromagnetic structure. This is the goal of Chapter 4.

Instead of trying every possible combination of distortions, Chapter 4 will take the common distortions in perovskites in the hope that the resulting structures will be synthesisable. For example, the $a^-a^-c^+$ tilt pattern is the most common structure and so introducing ferroelectric distortions to this is a promising avenue. There are also only certain cation orders that have actually been observed and so those are the ones that garner special attention for now.

It is often said that type-II multiferroics are more promising for the electric field control of magnetism because the ferroelectricity and magnetism are coupled together by definition. However, the mechanism that I explore at the end of Chapter 3 and seek in Chapter 4, results in a situation where the reversal of the polarisation must reverse the magnetisation - this is an incredibly strong kind of coupling. We shall see that the mechanism does not depend at all on whether we are dealing with a Type-I or a Type-II multiferroic. In some sense, whether the multiferroic ends up being a Type-I or Type-II is completely immaterial. All that matters is that there are large enough transition temperatures, the correct couplings between polarisation and magnetisation, and large enough coercive fields to prevent dielectric breakdown.

Chapter 3

Symmetry, Phase Transitions And Landau Theory

The previous chapter demonstrated that perovskite based materials can take a multitude of forms each with differing physical properties. Some have octahedral tilts and some have polar distortions. Some undergo octahedral Jahn-Teller distortions and orbital orderings. The cations in some perovskites possess unpaired electrons leading to magnetic dipoles and these dipoles can subsequently order into a myriad of magnetic structures. The simplicity of the perovskite structure imbues it with a flexibility that leads to a confusing complexity. How do we classify a distorted perovskite? How does one type of distortion affect the others? What kind of interactions are possible between distortions?

These are the questions that will be answered in the present chapter. I will describe how it is the *symmetry* of a material that leads to a convenient classification scheme. It is also symmetry that enables us to determine which distortions are present and how those distortions couple. Analysing the symmetry of a material is not only a powerful *descriptive* tool but also functions as a surprisingly effective *predictive* tool. I shall demonstrate how understanding the symmetry of a material allows the determination of the possible phase transitions in a material and therefore, we can use symmetry to predict new phases of materials with technologically useful properties - the electric field control of magnetism being the specific property that I focus on here.

Unfortunately, a symmetry analysis is not a panacea capable of curing all the woes of materials physics. It is not possible for a symmetry analysis to give a quantitative description of a material. It cannot give an answer to the question "What is the polarisation of $BaTiO_3$?" but it can answer the question "Does $BaTiO_3$ have a polarisation?". To obtain the details necessary to answer the former question, we need experiment or computational simulation. As a theorist, I do not know very much about experiments and so when I wish to answer the former question, I turn to simulation. How this has been done for my thesis is described in Chapter 5.

For now, I ignore the precise details and focus on the qualitative picture. To do this, I use this chapter to formulate the ideas necessary to describe the symmetry of a material - *crystallography* and *group theory* - and build up until it is possible to predict whether a particular material* is capable of displaying the electric field control of magnetism.

3.1 Crystallographic And Group Theoretical Ideas

3.1.1 The Space Group

It's necessary to introduce some mathematical concepts to describe crystallographic symmetries. A Bravais lattice [20, 79, 58] is defined as a set of identical points in which any point $\mathbf{R}$ can be reached by a combination of translations of lattice vectors $\mathbf{a}$, $\mathbf{b}$ and $\mathbf{c}$ such as

$$\mathbf{R} = n_a\mathbf{a} + n_b\mathbf{b} + n_c\mathbf{c} \tag{3.1}$$

where n_a, n_b and n_c are integers. The environment of every lattice point must be the same as every other lattice point. The volume enclosed by $\mathbf{a}$, $\mathbf{b}$ and $\mathbf{c}$ form one possible choice of the *unit cell* which, when translated by lattice vectors, can tesselate all space. There is no unambiguous way to define the unit cell. However, there is a smallest possible volume for the unit cell - termed the *primitive unit cell*. One possible choice of the primitive cell is to form the parallelopiped of the three lattice vectors which has volume

*It does not necessarily have to be a perovskite but will be for most of this thesis.

$$V_{prim} = \mathbf{a} \cdot (\mathbf{b} \times \mathbf{c}) \tag{3.2}$$

and any other choice of cell with the same volume is also a primitive cell. The primitive cell can only contain a single lattice point.

The lattice vectors **a**, **b** and **c** do not have to be of equal length nor do the angles α (between **b** and **c**), β (between **a** and **c**) and γ (between **a** and **b**) need to be right angles. This leads to considerable flexibility and results in seven qualitatively different crystal systems:

1. Triclinic (a) : $a \neq b \neq c, \alpha \neq \beta \neq \gamma$
2. Monoclinic (m) : $a \neq b \neq c, \alpha = \gamma = 90^\circ \neq \beta$
3. Orthorhombic (o) : $a \neq b \neq c, \alpha = \beta = \gamma = 90^\circ$
4. Tetragonal (t) : $a = b \neq c, \alpha = \beta = \gamma = 90^\circ$
5. Hexagonal (h) :
    a) Rhombohedral : $a = b = c, \alpha = \beta = \gamma$
    b) Hexagonal : $a = b \neq c, \alpha = \beta = 90^\circ, \gamma = 120^\circ$
6. Cubic (c) : $a = b = c, \alpha = \beta = \gamma = 90^\circ$

The sequence from cubic → tetragonal → orthorhombic → monoclinic → triclinic can be seen as progressively distorting a perfect cube, relaxing one constraint at each step. The rhombohedral phase can be thought of as distorting a cube along the body diagonal whereas the hexagonal lattice stands alone.

It is often advantageous to describe crystal systems with respect to conventional, rather than primitive cells. For example, the face-centered and body-centered cubic lattices are obviously within the cubic class, but the shape of the primitive cell does not make this fact evident. Instead, these lattices are often described using non-primitive cubic cells in which either the faces or the intersection of body diagonals are populated with additional lattice points. The ability to add lattice points to a conventional cell to create new Bravais lattices is called *centering*.

Enumerating the crystal systems with the possible centerings leads to 14 different Bravais lattices. These are the only ways to tile space in three dimensions with lattice vectors obeying Equation 3.1.

It is not enough to know the underlying Bravais lattice to understand the symmetries of the crystal structure. The lattice, a set of mathematical points, must be populated with a *basis* of atoms. The basis could consist of identical, spherically symmetric atoms positioned at the corner of the primitive cells. If this were the only option possible, then there would only be 14 possible crystal structures. Obviously this is not the case, and the possible choices for bases is very large indeed. NaCl for example has the a face-centred cubic Bravais lattice but with a basis of two ions - one at the lattice points and another of the opposite charge displaced by $[1/2, 1/2, 1/2]a$, where a is the cubic lattice vector* [112].

The well studied antiferromagnet MnO mentioned in Chapter 2 also has a face-centered cubic Bravais lattice and an identical basis to NaCl [113]. The two crystal structures have an identical *space group*. A space group is the set of all *symmetry operations* that leave the entire crystal unchanged or *invariant*. Note that these symmetry operations are applied to infinite crystal structures because Equation 3.1 describes an infinite lattice. A surface of any kind in the crystal would destroy translational symmetry and irregular surfaces may also destroy rotational symmetry. Real crystals are not infinite in extent but have dimensions much larger than the lattice parameter a. Therefore the infinite crystal approximation is a good one.

There are many different classes of symmetry operations [58] starting with the trivial symmetry operation of doing nothing at all. This is the identity operation and must be included in the space group in order for it to form a proper mathematical group. Secondly, translation by a vector of the Bravais lattice is equally trivial as it is built in to the definition of Equation 3.1.

The non-trivial operations begin with n-fold rotation axes. This is an axis about which a rotation through integral multiples of $\frac{2\pi}{n}$ leaves the entire crystal invariant.

Reflections through a mirror plane are also important operations to crystal symmetries.

*There are of course other choices for the basis such as having one ion at the lattice points and another at $[1/2, 0, 0]a$. The original choice is conventional as it makes it clear that there is nothing special about any particular direction in a cubic crystal

Inversions, in which the crystal remains unchanged when passed through a point, is another operation. If this point is the origin, then the act of inversion can be represented by the transformation $\mathbf{r} \rightarrow -\mathbf{r}$.

These operations can be combined to give new operations. Sometimes, a rotation is not a symmetry operation but a rotation followed by an inversion is, even though both individual operations may not be by themselves.

The symmetry elements above are all obtained via combinations of translations by vectors in the Bravais lattice or elements in which a single lattice point is kept fixed. This latter subset is known as the *point group*. Space groups that contain only these types of elements are known as *symmorphic*. By considering all possible bases populating the primitive Bravais lattices, crystallographers have enumerated 73 such space groups in three dimensions. However, there are two new classes of symmetry of elements that can be introduced if the restriction to Bravais lattice translations is lifted. These are *screw axes*, in which a crystal structure remains invariant upon a translation through a vector *not* in the Bravais lattice followed by a rotation about that vector, and the *glide plane*, in which the crystal structure remains invariant upon translation by a vector *not* in the Bravais lattice and then a reflection a plane containing the vector. Space groups that involve these elements are known as as *nonsymmorphic* space groups and in three dimensions there are 157 of them, resulting in 230 space groups in total.

To keep track of such a large number of crystal symmetries, there are many notational systems in use. To maintain consistency with the majority of literature on crystal structures, ferroelectrics and multiferroics, I use the Hermann-Mauguin (HM) notation. This is often referred to as the International Notation because of its adoption by the IUCr for the International Tables Of Crystallography [114, 115]. These tables lists the 230 space groups in order of ascending number of symmetry operations and assigns each material a label describing the most prominent symmetry elements. For example, NaCl and MnO both belong to the 225^{th} space group with 192 space group elements and space group symbol "$F\ 4/m\ \bar{3}\ 2/m$". The initial letter F denotes the face-centering of the conventional cubic Bravais lattice. The $4/m$ denotes the presence of a 4-fold rotation axis with a mirror plane perpendicular, the $\bar{3}$ signals the existence of a three-fold rotation-inversion axis and the final $2/m$ indicates a 2-fold rotation-reflection

axis perpendicular to the first. The full notation is cumbersome and so is often compacted to $Fm\bar{3}m$.

The highest symmetry perovskite structure obtained by $SrTiO_3$ at room temperature or other ABO_3 perovskites at elevated temperature has the 221st space group, $Pm\bar{3}m$ [116]. This has a primitive centering, indicated by the P, and has 48 symmetry operations. Having three distinct elements in the chemical formula, it obviously has a basis with more that one atom: the A-site at (0,0,0)a, the B-site at $(1/2, 1/2, 1/2)a$ and the three O-sites at $(1/2, 1/2, 0)a$, $(1/2, 0, 1/2)a$ and $(0, 1/2, 1/2)a$.

3.1.2 Neumann's Principle

In practice, the space group of a crystal structure is determined via experiment or by analysing the result of a simulated geometry optimization (Chapter 5). Once the space group has been determined, we can classify materials according to their symmetry. We immediately sense that there should be something similar between $SrTiO_3$ and $BaTiO_3$ if they both have the $Pm\bar{3}m$ space group. Indeed, the allowed material properties can be obtained directly from the symmetry if the symmetry is known.

This follows from Neumann's Principle [117, 118] which states that:

> "The symmetry of any physical property of a crystal must include the symmetry elements of the point group of the crystal."

As a reminder, the point group is the subset of symmetry elements in the space group in which one point is kept fixed. For symmorphic space groups like $Pm\bar{3}m$, this can be obtained by dropping the intial letter, which describes translations, so that the point group of $Pm\bar{3}m$ is $m\bar{3}m$.

Given the space group (and the point group subgroup) and using this principle, we can determine whether a particular property is permitted. For example, the high temperature crystal structure of $BaTiO_3$ is $Pm\bar{3}m$ with the $m\bar{3}m$ point group. Does this allow for a polarisation? Does it allow for piezoelectricity?

To solve, we turn to basic concepts from linear algebra [77] and define a vector $\mathbf{V}$ to be any object that can be transformed into a different vector $\mathbf{V}'$ via the application of a matrix (or second rank tensor) like

$$V_i' = A_{ij}V_j \tag{3.3}$$

where A_{ij} is the transforming matrix. The polarisation $\mathbf{P}$ is a vector (also known as a first rank tensor) with three components P_1, P_2 and P_3 which must necessarily transform like

$$P_i' = A_{ij}P_j. \tag{3.4}$$

What is the interpretation of the matrix $\mathbf{A}$? Neumann's Principle gives the answer. The polarisation is a physical property of the crystal and so must transform under the symmetry elements of the point group of the crystal. The crystal is left invariant under these operations and so the polarisation must be invariant too. Therefore, if $\mathbf{A}$ is a symmetry element of the point group, we must have

$$P_i' = P_i = A_{ij}P_j, \tag{3.5}$$

with the simple interpretation that the polarisation remains invariant under a symmetry element of the crystal.

The form of $\mathbf{A}$ for any individual symmetry element of the point group is easy to work out. For example, a counter clockwise rotation in a Cartesian basis by an angle ϕ about the c axis would be

$$A_{ij,rot} = \begin{pmatrix} \cos\phi & \sin\phi & 0 \\ -\sin\phi & \cos\phi & 0 \\ 0 & 0 & 1 \end{pmatrix} \tag{3.6}$$

and the inversion symmetry element would be

$$A_{ij,inv} = \begin{pmatrix} -1 & 0 & 0 \\ 0 & -1 & 0 \\ 0 & 0 & -1 \end{pmatrix}. \tag{3.7}$$

The matrix representation of the inversion element allows for a fundamental result to be easily proved. If a crystal contains the inversion element, then it must be true that

$$\begin{pmatrix} P_1 \\ P_2 \\ P_3 \end{pmatrix} = A_{ij,inv} \begin{pmatrix} P_1 \\ P_2 \\ P_3 \end{pmatrix} = \begin{pmatrix} -1 & 0 & 0 \\ 0 & -1 & 0 \\ 0 & 0 & -1 \end{pmatrix} \begin{pmatrix} P_1 \\ P_2 \\ P_3 \end{pmatrix} = \begin{pmatrix} -P_1 \\ -P_2 \\ -P_3 \end{pmatrix}, \tag{3.8}$$

which can only be satisfied if $\mathbf{P} = 0$ ie. crystal structures containing inversion as a symmetry element (known as *centrosymmetric* structures) cannot have a polarisation. Therefore, $BaTiO_3$ in the crystallographic phase with $Pm\bar{3}m$ symmetry cannot be polar because the $m\bar{3}m$ point group contains the inversion element.

$BaTiO_3$ has a phase transition to a phase with $P4mm$ symmetry at 130°C [119]. Applying all the symmetry operations to the polarisation in the same way reveals that the polarisation must exist in this structural polymorph. The point group $4mm$ does not contain the inversion element and the other symmetry elements of the point group do not force the polarisation to be zero. Importantly, Neumann's principle does not dictate whether the the polarisation of the crystal should be $+\mathbf{P}$ or $-\mathbf{P}$; both are permitted. Applying an external field can switch $BaTiO_3$ between these two so that, following the definition of Chapter 1, $BaTiO_3$ is a ferroelectric below 130°C.

The same process can be performed for other physical properties. Piezoelectricity - the changing of polarisation with applied strains - can also be analysed in the same way. The analysis is more complicated as piezoelectricity coefficients transform as a third rank tensor but thankfully the analysis only needs to be done once for any particular point group. Crystallographers of the past have done this and revealed that, 21 of the 32 possible point groups allow for piezoelectricity. The presence of the inversion element in the point group also eliminates the piezoelectric coefficients. A point group can be piezoelectric without being polar. This is the

case in quartz which contains a 2-fold rotation axis along c and a 3-fold rotation about a. In that case, Neumann's principle dictates that the piezoelectric coefficients are non-zero, but the polarisation is zero. This is a result of the rotations and not due to the presence of an inversion element.

With these results, we can reproduce the Venn diagram presented in Chapter 1. The result that all ferroelectrics are pyroelectrics* is an empirical classification but that all pyroelectrics are piezoelectrics is nothing more than a result of symmetry.

This principle can be extended to magnetic symmetries and magnetic point groups. The major difference between magnetic point groups and crystallographic point groups is the consideration of the time reversal element. A ferromagnetic crystal does not obey time-reversal symmetry as magnetic dipoles are reversed under this operation. The greater complexity introduced by allowing time-reversal into the point group results in 90 magnetic point groups and 1651 magnetic space groups† [120, 121].

Neumann's Principle can still be applied and can be used to describe the magnetic easy axes of crystals, predict whether piezomagnetism is permitted or illustrate the magneto-optical activity of a particular crystal.

The concept of a space group classifies materials into sets that have the same symmetry elements. Neumann's Principle allows the description of these materials and can immediately determine, without the need of experiment or simulation, what is possible in any particular material. It is often the case that the size of any individual effect is of secondary importance and symmetry remains the most powerful descriptive tool available.

3.1.3 Reciprocal Space

The crystallographic lattice is mirrored by the *reciprocal lattice* which, in some ways, is the more useful concept than the real space crystal lattice. Like the real space lattice, vectors in the reciprocal lattice also obey a similar equation

*Another term for a material with a non-switchable polarisation synonymous with "polar". Specifically, it means that the polarisation can be changed by varying the temperature. See Chapter 1

†Sometimes called Shubnikov groups.

$$\mathbf{G} = m_a\mathbf{k}_a + m_b\mathbf{k}_b + m_c\mathbf{k}_c, \tag{3.9}$$

where m_a, m_b and m_c are integers and the $\mathbf{k}_i$ are the basis vectors. These basis vectors are obtained from the real space basis vectors through

$$\mathbf{k}_a = 2\pi\frac{\mathbf{b}\times\mathbf{c}}{\mathbf{a}\cdot\mathbf{b}\times\mathbf{c}}, \quad \mathbf{k}_b = 2\pi\frac{\mathbf{c}\times\mathbf{a}}{\mathbf{a}\cdot\mathbf{b}\times\mathbf{c}}, \quad \text{and} \quad \mathbf{k}_c = 2\pi\frac{\mathbf{a}\times\mathbf{b}}{\mathbf{a}\cdot\mathbf{b}\times\mathbf{c}}. \tag{3.10}$$

We can also define a primitive unit cell that tesselates the whole of reciprocal space. Like the real space lattice, there is ambiguity in this choice but typically the Wigner-Seitz cell is constructed. This is the volume of space that is closer to a particular lattice point than any other point. It quite obviously only contains a single reciprocal lattice point. The Wigner-Seitz cell of the reciprocal lattice is known as the first Brillioun zone; a central concept for describing the excitation spectra in materials. Only points inside the Brillioun Zone are significant because of the periodicity of the reciprocal lattice. Any two reciprocal points differing by a reciprocal lattice vector are physically equivalent.

The interpretation of the reciprocal space as the dual to real space becomes easier when we associate each point $\mathbf{k}$ in reciprocal space with a wave $e^{i\mathbf{k}\cdot\mathbf{r}}$ in real space; any distortion propagating in real space in a periodic, wavelike manner can be mapped onto a single point in reciprocal space. For example, a modulation in the density of a one dimensional crystal structure (like a cation ordering) that oscillates with twice the period of the original, un-modulated density would be conveniently described as a wave $e^{\frac{2\pi}{2a}r}$. This is because it is now necessary to travel twice as far in real space to reach an equivalent point. This is all demonstrated in Figure 3.1.

The entire wave is therefore associated with the reciprocal space point (or *wavenumber*) $k = \pi/a$. It should be noted that this density modulation necessarily doubles the size of the unit cell in real space. The denominator common to all terms in Equation 3.10 is in fact the volume of the real space cell $V = \mathbf{a}\cdot\mathbf{b}\times\mathbf{c}$ and so doubling this volume consequently halves the volume of the reciprocal cell.

To summarise, any wavelike distortion introduced to the original primitive cell to the real-space crystal lattice corresponds to a point in reciprocal space. If this point is not related to

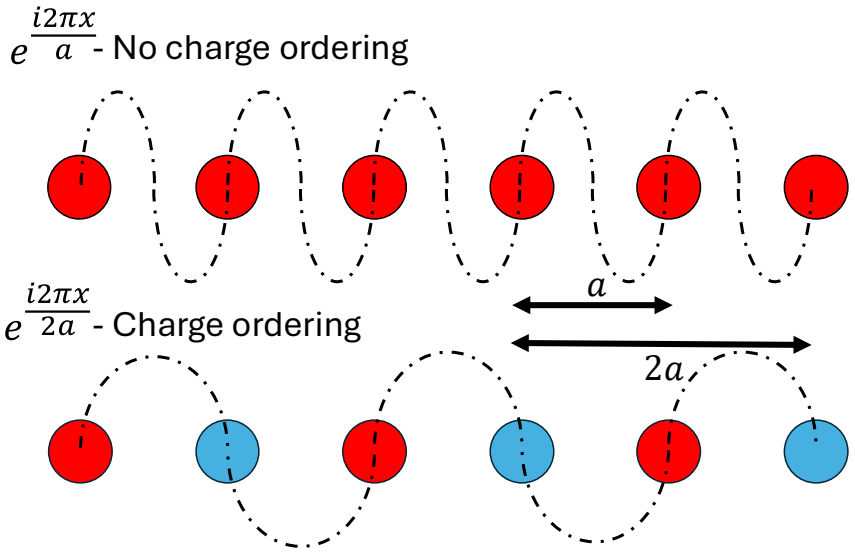

Figure 3.1: Doubling of unit cell and halving of wavenumber for a charge ordering. The charge order transforms as an irreducible representation at $k = \frac{2\pi}{2a}$. Any distortion transforming at a k-point not equivalent to a reciprocal lattice vector necessarily increases the size of the unit cell.

the origin by a reciprocal lattice vector, the unit cell of the real space cell increases its volume and the Brillioun Zone decreases.

Of course, wavelike phenomena also have a time dependence so that the full wave should properly be described as $e^{i\mathbf{k}\cdot\mathbf{r}-\omega t}$. Averaging over many time periods T averages the wave to zero so that the total distortion has no net effect on the structure. The softening of phonon modes discussed in Chapter 2 is a pertinent example of this and highlights the correspondence between reciprocal space points and changing cell sizes. Phonon modes are obviously wavelike phenomena associated with a wavevector. If $\omega^2 > 0$ the phonons are active and their average over time is zero. If $\omega^2 < 0$, the time dependence $e^{i\omega t}$ becomes $e^{-\omega t}$ (ω is imaginary) so that the phonon is damped, and no longer oscillates in time. The distortion becomes fixed at a particular reciprocal space point, and the unit cell increases.

3.1.4 Subgroups

We have classified space groups and used Neumann's Principle in determining the properties of any individual space group. Where symmetry becomes extremely powerful is through using it to understand how space groups are related to each other. This leads directly to the concept

of crystallographic (and magnetic) phase transitions. This makes symmetry a predictive instrument.

To contextualise this discussion in the context of perovskites, $BaTiO_3$ transitions from a $Pm\bar{3}m$ to a $P4mm$ symmetry at 398 K. Accompanying this transition is a breaking of symmetry elements. We have already seen that the $Pm\bar{3}m$ space group contains the inversion element and the $P4mm$ space group does not. Inversion symmetry is broken in going from the higher to the lower temperature phase. Many other symmetries are also broken - the $m\bar{3}m$ point group contains 48 symmetry elements whereas $4mm$ contains only 8. Crucially, no new symmetry elements are created. The 8 elements of $4mm$ are also contained within the 48 of $m\bar{3}m$. Therefore, $4mm$ is known as a *subgroup* of $m\bar{3}m$ (and so $P4mm$ is a subgroup of$Pm\bar{3}m$). There are many other subgroups available depending on the number of symmetry elements broken. Occasionally, the symmetry elements are broken sequentially leading to consecutive phase transitions. For $BaTiO_3$, there is another phase transition to an orthorhombic symmetry ($Amm2$) at 281 K and a final phase transition to a rhombohedral symmetry ($R3m$) at 202K [119, 122].

3.1.5 Irreducible Representations

Irreducible representations - frequently shortened to *irreps* in the literature - describe how a group can be decomposed into the smallest number of objects which transform with the symmetry elements of the group.

As shown previously, symmetry elements in a group can be represented as matrices. Both the rotation matrix and inversion matrix given above were shown to be in block diagonal form. That is, the rotation matrix could be written as

$$A_{ij,rot} = \begin{pmatrix} \cos\phi & \sin\phi & 0 \\ -\sin\phi & \cos\phi & 0 \\ 0 & 0 & 1 \end{pmatrix} = \begin{pmatrix} M_1 & 0 \\ 0 & M_2 \end{pmatrix} \tag{3.11}$$

where $M_1 = \begin{pmatrix} \cos\phi & \sin\phi \\ -\sin\phi & \cos\phi \end{pmatrix}$ and $M_2 = 1$, which is in block form. If it is possible, by the

	E	I
f_1	+1	+1
f_2	+1	-1

Table 3.1: Action of symmetry elements on even functions f_1 and odd functions f_2.

same transformation matrices, to turn all of the matrix representations of the groups symmetry elements into block diagonal form then the matrix representation is *reducible*. If it is not possible, that representation is *irreducible*.

The theory of representations is vast (see Dresselhaus, Dresselhaus and Jorio [58]) but for the purposes of this thesis, there are only a few important aspects. These can be illustrated by a simple example involving the inversion symmetry element. Consider the set of all possible functions $f(x)$ defined on the x axis. They could be linear functions, quadratics, cubics, logarithms, exponentials etc. Subject these functions to the symmetry operations E (the identity) and I (the inversion element that transforms x to $-x$) - the two elements form a mathematical group. All of these functions remain invariant when acted on by the identity so that $Ef(x) = f(x)$. Most functions, such as the exponential, do not have any particular symmetry when acted on by the inversion element. However some are *even* with respect to the inversion element so that $If_1(x) = f_1(-x) = f_1(x)$. Others are *odd* with respect to inversion so that $If_2(x) = f_2(-x) = -f_2(x)$. Each of these two functions have different eigenvalues under inversion and these eigenvalues can be used as labels. This is shown in Table 3.1. We can construct two one-dimensional vector spaces with these functions. One is formed by all vectors of the form $f = \lambda f_1$ and the other is by all vectors of the form λf_2. These vector spaces are said to be invariant with respect to $\{E, I\}$ as operating on either of the spaces with these two elements (or combinations of them) creates a vector still in the space.

The eigenvalues shown in Table 3.1 can also be interpreted as the result of *representing* the symmetry element with the eigenvalue. For example, we can interpret If_2 as being equal to $(-1)f_2$, both of which result in the same thing. Therefore, the numbers in Table 3.1 can also be seen as representations of the group itself where each symmetry element becomes a number, or alternatively, a *zero-dimensional matrix*. There is obviously no smaller subspace of functions that are also invariant with respect to the symmetry elements and so the set $\{+1, +1\}$ on the

vector space λf_1 and the set $\{+1, -1\}$ on the vector space λf_2 are the *irreducible representations* of the group $\{E, I\}$.

In this example, the 1-dimensional vectors spaces are each invariant and irreducible with respect to all symmetry elements of the group $\{E, I\}$. This can be readily extended to higher dimensions. If an m-dimensional vector space, which is spanned by m basis functions, is invariant under the applications of every symmetry element in the group G_0, and if that vector space contains no subspace that is itself invariant under all the elements of G_0, then an irreducible representation has been identified. Instead of the symmetry elements being represented by numbers (zero-dimensional matrices), they are generally represented by matrices which can be found by considering how each of the m basis functions transform into each other for each symmetry element.

If a representation of the group is not irreducible (ie. there is a smaller number of basis functions that transform only amongst each other under the symmetry operations), then it can be made so through a decomposition into irreducible representations. This procedure is outlined in great detail in the book by Dresselhaus, Dresselhaus and Jorio [58]. Such a decomposition is typically used to assess the optical activity of molecules and crystals.

Importantly, it is also possible to reduce *any* function $f(\mathbf{r})$ in terms of sets of basis functions, each set being the basis functions for an irreducible representation of the group. Mathematically, this can be written as

$$f(\mathbf{r}) = \sum_i a_i \left[\sum_k b_k \phi_k \right] \tag{3.12}$$

where ϕ_k are the basis functions of an irreducible representation Γ_k. The sum over k forms the invariant vector space describing the irrep Γ_i and the sum over i sums over all irreducible representations. I will often refer to this process as "decomposing into irreducible representations" but technically, I am decomposing into sets of basis functions.

The above relation can be easily proved for finite groups, which is very convenient seeing as we are looking at finite crystallographic point groups! To begin, we act on the arbitrary function $f(\mathbf{r})$ with each element g_i of the space group G_0. This produces a set of functions $f_i = g_i f$.

Mathematical groups are closed, meaning that the product of two elements is another element of the group ie. $g_j g_i = g_k$. Applying the the element g_j to f_i leads to $g_j f_i = g_j g_i f = g_k f = f_k$. Any function f_i is transformed into another function f_k due to the operation of any element of G_0. Therefore, the set of all f_i forms the basis functions for an invariant vector space on G_0 and is therefore associated with an irrep* Γ_k.

Being an invariant vector space, it is spanned by functions that are linear combinations of these basis functions f_k so that

$$\phi_i = \sum_k c_k f_k \tag{3.13}$$

which can be inverted to give

$$f_i = \sum_k b_k \phi_k. \tag{3.14}$$

Finally, the set f_i are linearly independent because they related only by symmetry relations and not through superpositions of each other. They are therefore complete and any function can be expanded with respect to them so that

$$f = \sum_i a_i f_i = \sum_i a_i \left[\sum_k b_k \phi_k \right]. \tag{3.15}$$

This completes the proof and demonstrates that any function can be constructed out of sets of basis functions, with each set transforming as an irreducible representation of a group G_0. Returning one more time to the inversion example, we had two vector spaces, each carrying a different irreducible representation. The first was symmetric with respect to inversion and the other was antisymmetric. After summing over the two irreps in Equation 3.15, it shows that any function can be written as a superposition of symmetric and antisymmetric parts.

If we are to reconstruct the *periodic* functions that describe the physical properties of *periodic* crystals, then a good choice of basis functions are Bloch functions

*Provided that it is irreducible. If it is instead reducible, it can be decomposed into irreducible representations.

$$\phi_{i\mathbf{k}}(\mathbf{r}) = u_{i\mathbf{k}}(\mathbf{r})e^{i\mathbf{k}\cdot\mathbf{r}} \tag{3.16}$$

where the $u_{i\mathbf{k}}$ are periodic with the lattice and the $e^{i\mathbf{k}\cdot\mathbf{r}}$ is a phase factor. They are obviously complete (otherwise Fourier expansions would not work) and it is easy to see how the symmetry operations of the space group transform the Bloch functions of Equation 3.16. Application of translation operators does not change $u_{i\mathbf{k}}$ but changes the phase factor by a multiplicative factor $e^{i\mathbf{k}\cdot\mathbf{a}}$ where $\mathbf{a}$ is the translation vector. Rotational elements transform the functions $u_{i\mathbf{k}}$ by acting on the wavevector, resulting in a new wavevector $\mathbf{k}'$. Screw axes and glide plane symmetry elements alter both of the constituent functions because of their combinations of translations and rotations. The added phase factors are unimportant and so producing the irreducible representations in this basis of Bloch functions reduces to finding how the reciprocal space vectors $\mathbf{k}$ transform under each of the symmetry operations. Therefore, each irreducible representation has an associated reciprocal space vector. There are more details to this assertion and these can be found in References [58, 123, 124].

This suggests a change of notation so that an irreducible representation is written as $(m)K_i^{(\pm)}$ where K is the label given to a high symmetry point in the Brillioun Zone for reciprocal space vectors obeying the symmetry operations of a spacegroup G_0 (describing the atomic density ρ_0 in the previous section). These points and their labels in the highest symmetry perovskite space group $Pm\bar{3}m$ are shown in Table 3.2. The irrep is either labelled + or − depending on whether it transforms with + parity or − parity under the inversion symmetry element. The label i cycles through the irreps associated with that particular $\mathbf{k}$-point. Finally, the preceding m label is only included if the irreducible representation describes a magnetic space group. In this case, the m denotes an irreducible representation that is antisymmetric with respect to the time reversal symmetry element.

3.1.6 Group-Subgroup Relations and Irrep Dimensionality

Having introduced irreducible representations, we can now define the idea of group-subgroup relationships. In a phase transition that takes a higher-symmetry group to a lower-symmetry

Label	k-points
Γ	(0,0,0)
X	(1/2,0,0),(0,1/2,0),(0,0,1/2)
M	(1/2,1/2,0),(1/2,0,1/2),(0,1/2,1/2)
R	(1/2,1/2,1/2)

Table 3.2: High symmetry points of $Pm\bar{3}m$

group, there exists a function transforming as one of the irreducible representations of the high-symmetry phase. This function is the *order parameter* (about which more will be said in the next section) and the associated irreducible representation is the *active irrep*.

Every symmetry element g of the high-symmetry group G_0 is represented by a matrix $\mathbf{M}(g)$. Applying a symmetry element to a function $\mathbf{Q}$ transforming as the active irrep (e.g the order parameter) may change the order parameter so that

$$\mathbf{M}(g)\mathbf{Q} = \mathbf{Q}'. \tag{3.17}$$

If it turns out that $\mathbf{Q}' = \mathbf{Q}$, then the symmetry element g is also a symmetry element of the irreducible representation - this is a restatement of the definition of the irreps. However, the collection of all g for which $\mathbf{M}(g)\mathbf{Q} = \mathbf{Q}$ forms an *isotropy subgroup* H of the high symmetry group G_0 under the active irrep.

This is easily demonstrated for perovskite symmetries. There are 48 symmetry operations in the $Pm\bar{3}m$ space group. There are also many possible irreducible representations, each associated with a different reciprocal space vector. Considering only active irreducible representations that do not change the volume of the cell (which means that the irrep is associated with the Γ-point), there are 32 possible isotropy subgroups; each obtained with a separate active Γ-point irrep. These can be enumerated using online tools like SUBGROUPGRAPH of the Bilbao Crystallographic Server [125, 126]. This is done in Figure 3.2.

Not all the subgroups obtained in Figure 3.2 are actually observed in perovskite materials. However, $BaTiO_3$ exhibits $Pm\bar{3}m$, $P4mm$, $Amm2$ and $R3m$ in that order when temperature is reduced. All of these symmetries are isotropy subgroups of $Pm\bar{3}m$. All three symmetries are also reached with the same active irrep, Γ_4^-. What distinguishes the three space groups is

N	HM Symbol	ITA	index	t-index	k-index
1	*P*-43*m*	215	2	2	1
2	*P*432	207	2	2	1
3	*Pm*-3	200	2	2	1
4	*P*23	195	4	4	1
5	*R*-3*m*	166	4	4	1
6	*R*3*m*	160	8	8	1
7	*R*32	155	8	8	1
8	*R*-3	148	8	8	1
9	*R*3	146	16	16	1
10	*P*4/*mmm*	123	3	3	1
11	*P*-4*m*2	115	6	6	1
12	*P*-42*m*	111	6	6	1
13	*P*4*mm*	099	6	6	1
14	*P*422	089	6	6	1
15	*P*4/*m*	083	6	6	1
16	*P*-4	081	12	12	1
17	*P*4	075	12	12	1
18	*Cmmm*	065	6	6	1
19	*Pmmm*	047	6	6	1
20	*Amm*2	038	12	12	1
21	*Cmm*2	035	12	12	1
22	*Pmm*2	025	12	12	1
23	*C*222	021	12	12	1
24	*P*222	016	12	12	1
25	*C*2/*m*	012	12	12	1
26	*P*2/*m*	010	12	12	1
27	*Cm*	008	24	24	1
28	*Pm*	006	24	24	1
29	*C*2	005	24	24	1
30	*P*2	003	24	24	1
31	*P*-1	002	24	24	1
32	*P*1	001	48	48	1

Figure 3.2: Isotropy subgroups of the $Pm\bar{3}m$ parent space group which retain the cell volume. The retention of cell volume means that the corresponding active irreducible irreps are all associated with the Γ-point. Ratio of the parent cell size to the child cell size is encapsulated by the k-index. The ratio of symmetry operations in the higher symmetry to the lower symmetry is given by the t-index and the total index is the product of the two.

that the order parameter transforming as Γ_4^- can have a selection of *order parameter directions* (OPD).

The order parameter direction is related to the dimensionality of the matrices $\mathbf{M}(g)$ forming the irrep. If the matrices $\mathbf{M}(g)$ are 3x3, as in Γ_4^-, then this can only act on a three dimensional order parameter of the form (a, b, c). The $P4mm$ symmetry is obtained from $Pm\bar{3}m$ by an active Γ_4^- with the OPD $(a, 0, 0)$, the $Amm2$ symmetry by the $(a, a, 0)$ OPD and the $R3m$ by the (a, a, a) OPD.

The dimensionality of irreps can be more than three dimensional despite describing distortions in a three dimensional crystal. For example, many irreducible representations at the X-point are formed by six-dimensional matrices. This is because the X-point is at $(1/2, 0, 0)$ in the Brillioun Zone. However, the reciprocal space vectors $(0, 1/2, 0)$ and $(0, 0, 1/2)$ are equivalent by symmetry. The three points denote the *star* of the point $(1/2, 0, 0)$. The matrices for the X_5^+ irrep are two dimensional but all points belonging to the star of the X-point must be considered and therefore, the irrep becomes six-dimensional ie. $X_5^+(a, 0; 0, 0; 0, 0)$. The semi-colons seperates the OPDs into the respective branches of the star.

It is not always possible to reach a desired symmetry with a single irreducible representation. Instead, it often takes multiple active irreps. For example, the $Pnma$ symmetry of perovskites can only be reached with two or more active irreps. It is often the case that a sequence of phase transitions is observed with each phase transition introducing a new active irrep.

To summarise the previous sections:

1. The space group is an essential tool for classifying crystal structures by their symmetries.
2. Given a space group, Neumann's Principle can be used to determine whether a particular physical property is permitted.
3. An irreducible representation is any representation of the space group with the same symmetry properties of the smallest set of basis functions that transform only amongst themselves under all the symmetry operations of the group. Any function can be expanded

into basis functions with each function transforming as an irreducible representation of the group.

4. Group-subgroup relations explore how crystallographic phases are related. The number of symmetry elements change on a phase transition and are driven by a distortion - the order parameter - which transforms with the symmetry of an irreducible representation of the high symmetry phase.

These ideas will now be combined to explore Landau's theory of phase transitions. This allows for the prediction of phase transitions and their classification. The Landau Theory concept will prove absolutely pivotal in our stated goal of finding materials in which the electric field control of magnetism is possible.

3.2 Landau Theory And Phase Transitions

With these important concepts from crystallography and group theory ready at hand, the Landau Theory of Phase Transitions [124, 127, 123] can be readily constructed.

To begin, we return to Equation 3.15 and recall that for the inversion example of the last section, one of the irreducible representations was invariant under all the symmetry elements of the (very small) group. This was the vector space formed by all even functions. The corresponding row in Table 3.1 was all "+1". The existence of this *unit representation* is generic to all decompositions into irreps. We can split this term off the sum so that

$$f = f_0 + \delta f = f_0 + \sum_{i'} a_{i'} \left[\sum_k b_k \phi_k \right] = f_0 + \sum_{i'} \sum_k \eta_{i'k} \phi_k \tag{3.18}$$

where the prime on i' denotes that the unit representation is no longer included. I have also combined the coefficients so that $\eta_{i'k} = a_{i'} b_k$. The first part f_0 is the basis function with the symmetry of the unit representation. It is symmetric with respect to all the symmetry operations of a group G_0. The symmetry of the remaining part δf is lower than that of the G_0. In fact, it must evidently be a subgroup of G_0 which I will denote G. The mathematics begin to be useful

as a model of a phase transition between two symmetries. As we aim to describe real materials, it should be clear that the quantities f and δf should have some physical interpretation. f and δf should be measurably different quantities in the two phase - the density ρ is therefore a good, intuitive choice.

If a phase transition is to happen below a particular temperature T_{C}, then the distorted density $\delta\rho$ must be $\delta\rho = 0$ above this temperature. Above this temperature, the material has symmetry G_0 and density ρ_0 whereas below, the symmetry is G and the density is $\rho = \rho_0 + \delta\rho$. Consequently, the quantities $\eta_{i'k}$ are zero above the transition point and non-zero below. They effectively describe the transition whilst also encoding the symmetry properties of the crystal on either side of the transition. A quantity with this structure is known as the *order parameter*. Referring to the definition in Equation 3.18, we see that an order parameter describes "how much" of a particular basis function (carrying a particular irreducible representation) is present in the lower symmetry part $\delta\rho$ of the atomic density. Also evident from Equation 3.18 is the fact that there could be many different order parameters.

Whether a particular material obtains the higher symmetry G_0 or the lower symmetry G is a question of thermodynamics. That is, the system displays whichever phase minimises the free energy $\mathcal{F} = \mathcal{F}(P, T, \eta_{i'k})$ which is a function of pressure P, temperature T and the coefficients $\eta_{i'k}$. Restricting ourselves to *continuous* phase transitions to begin with where $\delta\rho$ tends continuously to zero at the phase transition, the corresponding coefficients $\eta_{i'k}$ must also tend to zero at the phase transition. Thus, we can expand the free energy in a power series of these small coefficients

$$\mathcal{F} = \mathcal{F}_0 + \sum_{i'} A_{i'} \sum_{k} \eta_{i'k} + \sum_{i'} B_{i'} \left[\sum_{k} \eta_{i'k} \right]^2 + ... \tag{3.19}$$

where A, B etc are functions of P and T.

The thermodynamic free energy is a scalar physical quantity and, according to Neumann's Principle, should obey the symmetries of the space group. Crucially, it must obey the symmetries of the higher symmetry space group above the transition. Therefore, certain expressions in the free energy expansion are not permissible. For example, there can not be any linear terms. If

the space group contains the inversion element then this is obvious as acting with the inversion operator on $\eta_{i'k}$ will reverse its sign and the thermodynamic potential will not be invariant*. However, there is a more fundamental reason for the lack of a linear term. The sum over n' does not include the unit irreducible representation and so the coefficients $\eta_{i'k}$, transforming as the i'th non-unit representation must necessarily not be symmetric with respect to at least one of the symmetry operations. Therefore, a linear term in Equation 3.19 would not obey the full symmetry group G_0.

The existence of any particular term in the free energy is thus restricted to whether the whole term obeys all the symmetry operations of the group G_0. This leads to a set of easy-to-apply rules that make the construction of a Landau expansion a convenient and pragmatic procedure.

3.3 The Invariant Rules And Their Consequences

The previous section contained a lot of mathematics. This section aims to condense it into a digestible set of rules which make the construction of a Landau expansion straightforward and practical. It should be noted that this procedure is almost always carried out via the use of computational tools such as the Bilbao Crystallographic Server [125, 126] or Isotropy Software Suite [128, 129]. I try to place these results in the context of ferroelectricity in perovskites.

Given a distortion, say the in-phase octahedral tilt described in Chapter 2, we can determine the corresponding **k**-point of the irreducible representation through a consideration of how much the cell must be increased to accommodate the new distortion. For the in-phase tilt, the cell must at least be doubled along two axis, but can be kept the same size parallel to the axis of rotation. Therefore, the *supercell* has two axes that are double the length of the original cell. In contrast, the reciprocal cell now has two axes that are half as long as the original reciprocal cell. This is indicating that this distortion transforms as an irreducible representation at the $(1/2, 1/2, 0)$ point of the Brillioun zone; labelled the M-point. In this way, all of the main distortions present in perovskite materials can be mapped to their corresponding irreducible

*As the symmetry elements simply transform the basis functions of an irreducible representation amongst themselves, the transformations can be considered to be acting on the coefficients instead of the basis functions.

Distortion	Γ	X	M	R
Strain	$\Gamma_3^+;\Gamma_5^+$			
Cation Order (A Sites)		X_1^+	M_1^+	R_1^+
Cation Order (B Sites)		X_3^-	M_4^+	R_2^-
Anion Order (X Sites)		X_1^+	$M_4^+;M_5^-$	R_5^+
(Anti-) Polar (A Sites)	Γ_4^-	X_3^-	$M_3^-;M_5^-$	R_4^-
(Anti-) Polar (B Sites)	Γ_4^-	X_1^+	$M_2^-;M_5^-$	R_5^+
Jahn-Teller Modes	Γ_3^+	X_3^-	M_3^+	R_3^-
Octahedral Tilt Modes			M_2^+	R_5^-
Magnetic Order (A Sites)	$m\Gamma_4^+$	$mX_3^+;mX_5^+$	$mM_3^+;mM_5^+$	mR_4^+
Magnetic Order (B Sites)	$m\Gamma_4^+$	$mX_1^-;mX_5^-$	$mM_2^+;mM_5^+$	mR_5^-

Table 3.3: Enumeration of all distortions from Chapter 2 in ABX_3 perovskites and their associated irreducible representations.

representations. This enumeration has been done and can be found in the literature [130]. The results are reproduced in Table 3.3.

Having defined the new notation for irreducible representations, the rules for constructing invariants are simple to state. For any term in the Landau expansion to be invariant, it must:

1. Conserve crystal momentum*. Only translations by lattice vectors are symmetry elements of the high symmetry group G_0. Consequently, only translation by reciprocal lattice vectors are permitted in reciprocal space. For a term in the Landau expansion, formed as a product of two or more order parameters each transforming as an irreducible representation of the space group G_0, the combined wave-vector of the term must be a reciprocal lattice vector. The basis functions for any order parameter are Bloch functions, and the product of two Bloch functions leads to an additive combination of the associated $\mathbf{k}$ vectors. This resulting wavevector must be a member of the reciprocal lattice in order for the term to possess the same translational symmetry of G_0.

2. Preserve inversion symmetry. If the group G_0 has the inversion element, (which the high-symmetry perovskite phase does) then all the terms of the Landau expansion must respect this symmetry. A term cannot be antisymmetric with respect to inversion.

*The term "crystal momentum" is used here as the Bloch functions used as the basis are not eigenfunctions of the quantum mechanical momentum operator $-i\hbar\nabla$. Instead, momentum is only defined modulo a reciprocal lattice vector $\hbar\mathbf{G}$

3. Preserve time-reversal symmetry. If the group G_0 has time-reversal as a symmetry element (which the non-magnetic, high-symmetry perovskite phase does), then every term in the expansion must also preserve time reversal symmetry. This is practically achieved by ensuring that every term has either zero or an even number of magnetic order parameters (which break time reversal symmetry).

4. Preserve all other symmetry elements of the group. This is difficult to do by hand and so it is necessary to use a computational tool like INVARIANTS from the ISOTROPY Software Suite [131] to check.

Failure to satisfy any of the above conditions immediately eliminates the term from the Landau expansion.

3.3.1 Single Order Parameter

Suppose we only have a single order parameter P which transforms as the irreducible representation Γ_4^- of the $Pm\bar{3}m$ space group, with the order parameter direction $(a, 0, 0)^*$. The inclusion of this order parameter destroys inversion symmetry and the resulting space group is non-centrosymmetric $P4mm$. This is therefore a good model for the ferroelectric transition in $BaTiO_3$ [123].

Without considering the invariant rules, the free energy can be constructed as a power series expansion in P so that

$$\mathcal{F}(P) = \mathcal{F}_0 + aP^2 + bP^3 + cP^4 + ... \tag{3.20}$$

where the linear term has been dropped due to the fundamental reason stated in the previous section. The cubic term can also be dropped because P transforms antisymmetrically with respect to inversion symmetry and so the product P^3 would not obey inversion symmetry. In fact all odd-order terms can be dropped in this case for the same reason. I will truncate this

*In the old notation, this might look something like $\eta_{(\Gamma_4^-)}$

series at fourth order. Near to the transition temperature, the order parameter is small and so these additional terms do not add anything substantial to the analysis.

What remains can only describe the ferroelectric phase transition if the coefficients are permitted to change with temperature. a can be easily parameterised as a function of temperature by $a(T) = a_0(T - T_{\mathrm{C}})$. If $T > T_{\mathrm{C}}$, $a > 0$ and assuming that all other coefficients are positive, the minimum of the free energy is obtained by

$$\frac{\partial \mathcal{F}}{\partial P} = 2aP + 4cP^3 = 0 \rightarrow P = \pm\sqrt{\frac{-a}{2c}} \quad \text{or} \quad P = 0 \tag{3.21}$$

The first of these solutions is clearly not possible if $a > 0$ and so we are left with the result that $P = 0$. If $T < T_C$, then the first solutions do now make sense and we see two degenerate solutions (which are minima) representing the two polarisation states of $BaTiO_3$. $P = 0$ is now a metastable maximum. The energy landscape is a function of polarisation P, and how that landscape varies with dimensionless temperature $\frac{T}{T_C}$ is plotted in Figure 3.3. The temperature dependence of the coefficient a is related to the softening of phonon modes described in Chapter 2.

The phase transition just described is a *continuous* or second-order phase transition. The term "continuous" is clear when you consider the change of the order parameter with temperature $P = \pm\sqrt{\frac{-a_0(T-T_{\mathrm{C}})}{2c}}$ which shows that the order parameter grows from zero continuously as the system passes through the transition temperature. This behaviour $P \propto (T - T_{\mathrm{C}})^{1/2}$ is exactly that described in Chapter 2. In the more narrow field of ferroelectric phase transitions, this type of transition is known as a *proper* ferroelectric phase transition because it is the coefficient in front of the polar mode that changes sign or, in the language of soft phonon dynamics, it is the polar phonon that becomes imaginary and condenses.

Continuous phase transitions are also known as second order phase transitions because a continuous phase transition introduces an anomaly (either a discontinuity, a divergence or a cusp) in the *second* derivative of the free energy with respect to some quantity. For example, a second order phase transition would show a anomaly in the heat capacity (second derivative with respect to temperature) or the dielectric susceptiblity (second derivative with respect to

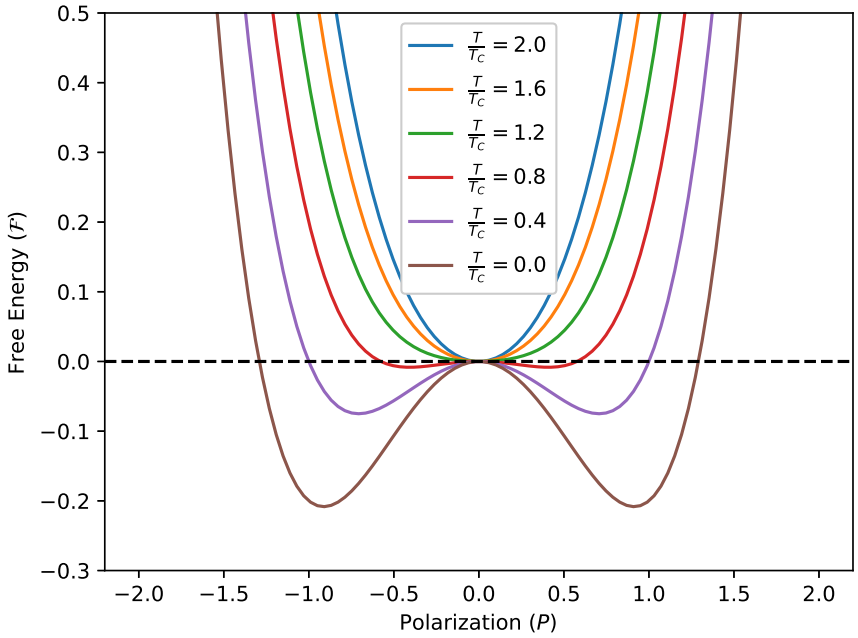

Figure 3.3: The energy landscape described by Equation 3.20 and how it varies with temperature. Below the transition temperature, a double well is formed with the minima located at $P = \pm\sqrt{\frac{-a}{2c}}$

electric field). I can easily demonstrate the latter by adding a term that couples to the electric field so that

$$\mathcal{F} = a_0(T - T_{\mathrm{C}})P^2 + cP^4 - EP \tag{3.22}$$

reveals that $P = -\frac{\partial \mathcal{F}}{\partial E}$ and

$$\frac{\partial \mathcal{F}}{\partial P} = 0 \rightarrow 2a_0(T - T_{\mathrm{C}})P + 4cP^3 = E. \tag{3.23}$$

Defining $\chi = \frac{\partial P}{\partial E} = \frac{\partial^2 \mathcal{F}}{\partial E^2}$ and differentiating Equation 3.23 with respect to E leads to

$$\chi = \frac{1}{(2a_0(T - T_{\mathrm{C}}) + 12cP^2)} \tag{3.24}$$

For $T > T_{\mathrm{C}}$, $P = 0$ so

$$\chi(T > T_{\mathrm{C}}) = \frac{1}{2a_0(T - T_{\mathrm{C}})} \tag{3.25}$$

but for $T < T_C$, $P = \pm\sqrt{\frac{-a_0(T-T_C)}{2c}}$ so that

$$\chi(T < T_C) = \frac{1}{4a_0(T_C - T)} \tag{3.26}$$

and so there is a divergence in the susceptibility with different gradients on both sides of T_C. This was stated in Chapter 1 to be a universal characteristic of continuous phase transitions and drops straight out of the Landau theory.

There are also ways in which the polarisation itself has a discontinuity. This would be a first-order phase transition because $P = -\frac{\partial \mathcal{F}}{\partial E}$. For an order parameter like P which breaks inversion symmetry, this can be achieved if the coefficient of the quartic term is allowed to be negative and a sixth order term is included. Alternatively, if the order parameter obeys the inversion symmetry so that a cubic term is permitted, this also leads to a first order transition [127]. In either of these cases, the lowest point on the free energy landscape as a function of temperature ends up jumping from $P = 0$ above T_C to a P finitely separated from 0 infinitesimally below T_C.

3.3.2 Multiple Order Parameters

Many phase transitions in perovskites involve more than one type of distortion. As a simple illustration, we consider the ferroelectric phase transition in $YMnO_3$ [85] which is an oxide closely related to perovskites and has a hexagonal symmetry. At high temperature, it does not have the cubic $Pm\bar{3}m$ like $BaTiO_3$ but instead has the hexagonal $P6_3/mmm$ space group. At lower temperatures, it transitions to the non-centrosymmetric $P6_3cm$ symmetry. The transition involves an active irreducible representation of the $P6_3/mmm$ space group attached to the $\mathbf{k} = (1/3, 1/3, 0)$ reciprocal vector. This is conventionally denoted with the letter K. Specifically, it transforms with the irreducible representation K_3 *. Importantly, a polar distortion (trans-

*The lack of a parity label in this notation is indicative that this irreducible representation has more complicated transformation properties when subject to the inversion symmetry element. The basis functions used to describe this irreducible representation are necessarily two-dimensional and so lead to a 2x2 matrix of mixed nature ie. $\begin{pmatrix} -1 & 0 \\ 0 & 1 \end{pmatrix}$. Unlike the simple example of inversion involving odd and even functions, this is clearly neither symmetric or antisymmetric and for this reason, the label is dropped. The matrix representation of the

forming as the Γ_2^- irreducible representation of the $P6_3/mmm$ space group) is also present, as is permitted in polar symmetries. How do we incorporate both of these modes into the Landau expansion?

Up to fourth order (this calculation is performed in detail in Appendix A), the expansion looks like

$$\mathcal{F}(P,K) = \mathcal{F}_0 + a_P P^2 + b_P P^4 + a_K K^2 + b_K K^4 + cP^2K^2 + \lambda PK^3 \tag{3.27}$$

where the first three terms should be familiar from the previous example. The terms $a_K K^2$ and $b_K K^4$ are the analogous terms for the K distortion. The K^2 and K^4 terms conserve crystal momentum because it is possible to add and subtract two (four) copies of (1/3,1/3,0) to get back to (0,0,0) in the K^2 (K^4) term. The mode can be treated as inversion-odd (see footnote) and so there is no K^3 term.

The interesting physics emerges from the last two terms. The first is clearly permissible in the expansion as, although both P and K carry irreps that transform as odd under inversion, they only appear with even powers. In addition, the even powers also ensure that crystal momentum is conserved. If $c > 0$, then the presence of K makes it harder to introduce P as the energy is raised if both distortions are present. If $c < 0$, the presence of K assists the formation of P. The two situations are labelled as *competitive* and *cooperative* interactions respectively. This *biquadratic* term could be combined with the term $a_P P^2$ to create $(a_P + cK^2)P^2$ so that the term cK^2 effectively renormalises the coefficient of the P^2 term. As it is this coefficient which typically carries the temperature dependence, the term cK^2 acts as a fictitious temperature. If $c << 0$, it is possible that the newly renormalised coefficient in front of P^2 becomes negative, and we obtain a phase transition similar to the $BaTiO_3$ example. This is called a *triggered* mechanism. It does not occur in $YMnO_3$ and, in fact, biquadratic interactions in perovskites tend to be strongly competitive [87].

inversion operator states that we reverse the first component and keep the second component unchanged. The order parameter direction of this particular irrep in $YMnO_3$ is in the $(a, 0)$ direction so that there is no second component. It is therefore permissible to treat this irrep as being antisymmetric under inversion.

The second term does play a significant role in the transition in $YMnO_3$. This term - a *linear-cubic* - has the interesting property that it can lower the energy irrespective of the sign of the coefficient λ, assuming that λ is not a function of P or K. Imagine that the K mode* exists and is positive, and that the P mode is non-zero but with undetermined sign. If $\lambda > 0$, then to lower the energy P can choose a sign opposite to that of K and the total free energy $\mathcal{F}$ can be lowered. The same is true for any permutation of signs - there is always a way for this term to lower the energy.

We can therefore minimise the free energy with respect to P to find the polarisation of $YMnO_3$,

$$\frac{\partial \mathcal{F}}{\partial P} = (2a_P + 2c_P K^2)P + 4b_P P^3 + 2cPK^2 + \lambda K^3 = 0. \tag{3.28}$$

As a cubic equation, this is slightly more complicated to solve analytically. However, it is not necessary to do this to realise something profound about this kind of Landau expansion. If $K \neq 0$, then this equation cannot be solved by $P = 0$. Stated differently, if the coefficient $a_K < 0$ in Eq 3.27 but $a_P > 0$ so that, without the linear-cubic coupling term, only the K mode would be non-zero, the coupling forces the P mode to also become non-zero. This is achieved without the softening of the polar phonon and the flipping of the sign of a_P. This mechanism is known as *improper ferroelectricity* [132, 133] and the ferroelectric transition in $YMnO_3$ is the prototypical example. In such an improper transition, the mode with a negative coefficient, K in this example, is known as the primary mode and the mode enforced to be non-zero is known as the secondary mode †. The free energy landscape, with different values of K is shown in Figure 3.4.

Examining Equation 3.27, reveals another way to interpret the improper transition. The term λPK^3 is analogous to an electric field term $-EP$ and so we can define an effective field $E_{\text{eff}} = -\lambda K^3$ that removes the stability of the $P = 0$ solution.

Improper ferroelectricity has important consequences for ferroelectric switching. Reversing the sign of the polarisation in Equation 3.27 does not result in a free energy that is degenerate.

*I will often use the term "mode" which is to be understood as synonymous with "order parameter"

†Occasionally described as a slave mode in the literature

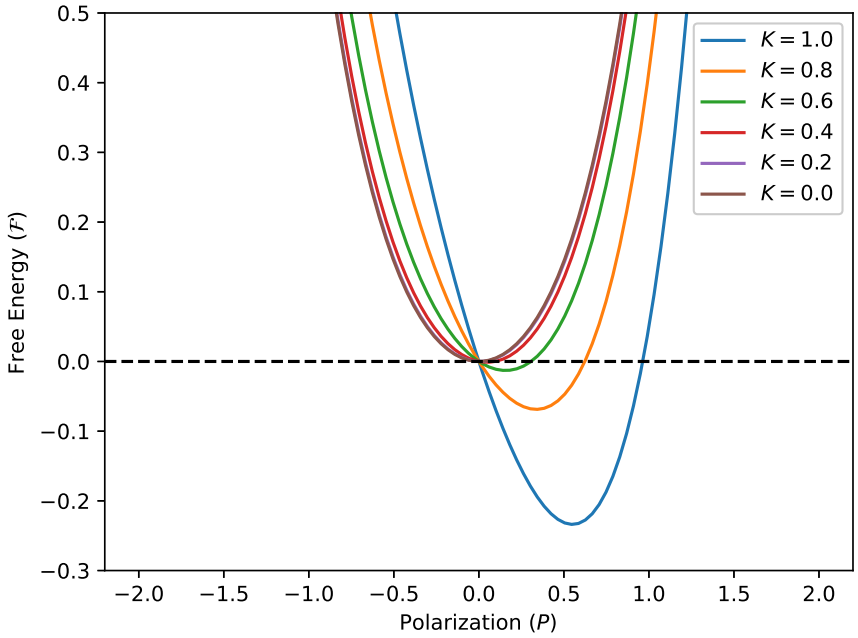

Figure 3.4: The energy landscape of an improper ferroelectric. The energy only has a minimum with a non-zero P if the K is non-zero. To obtain a sizeable P mode, K must also be large as the coefficient a_P in the P^2 term is still positive.

$\mathcal{F}(P, K) \neq \mathcal{F}(-P, K)$ because of the coupling term in which both P and K appear with odd powers. In order to be a ferroelectric with two energy degenerate minima, it is therefore necessary that K must also reverse. An applied electric field couples to P and can cause a polarisation reversal just as in an ordinary ferroelectric. But P is now coupled to K and so K must also reverse in order to attain the lowest energy state with reversed polarisation. Therefore, $YMnO_3$ allows for the electric field control of the K distortion.

There is no fundamental reason why we need to stop at two order parameters in the Landau expansion. Returning to perovskite structural polymorphs that are subgroups of the cubic $Pm\bar{3}m$ structure, we can explore the most common perovskite tilt pattern $a^-b^+a^-$ which was referred to in Chapter 2. This pattern has the $Pnma$ symmetry and contains five distortions. I can assign them to the irreducible representations describing their transformation properties. These are an $a^-b^0a^-$ antiphase (R_5^-) and an $a^0b^+a^0$ in-phase tilting pattern (M_2^+) combining to give the $a^-b^+a^-$ pattern. There are also other distortions including an antipolar motion of the A sites (X_5^-), a distinct antipolar motion of both A- and X-sites (R_4^-), and a Jahn-Teller

distortion (M_3^+).

I will not write down the full Landau expansion in this example as the terms would be too numerous but I'll discuss a few to highlight to apposite physics. Recall from Chapter 2, that for low tolerance factor perovskites, the rotation modes have the softest phonon modes and so condense first. In the language of the Landau expansion, this means that the coefficients $a_{R_5^-}$ and $a_{M_2^+}$ are the first to change sign and become negative.

Now consider the term $Q_{R_5^-}Q_{M_2^+}Q_{X_5^-}$ where Q_i are the order parameters transforming as the i^{th} irreducible representation. This term is clearly allowed via the invariant rules discussed earlier: the associated wave vectors can be made to sum to a reciprocal lattice vector; the whole term is parity-even, there are zero magnetic irreps; a final check with INVARIANTS [131] confirms that it obeys all other symmetry operations of $Pm\bar{3}m$. Therefore, this term is allowed. Like improper ferroelectricity, $Q_{X_5^-}$ will obtain whichever sign which minimises the free energy. The two tilt modes are thus all that is necessary to bring along the $Q_{X_5^-}$ mode. In some ways, this is nothing more than a simple extension of an improper transition but this mechanism now requires two primary modes. These two can be considered to be a single *hybrid mode* and consequently, this transition is labelled as a *hybrid improper* transition to distinguish it from the improper involving only one primary mode [134]. The presence of a non-zero $Q_{R_5^-}$ and $Q_{M_2^+}$ modes now means that $Q_{X_5^-}$ is also non-zero.

This unlocks a wider range of possibilities. The term $Q_{M_2^+}Q_{X_5^-}Q_{R_4^-}$ is now allowed and generates a non-zero $Q_{R_4^-}$. In addition, there is the term $Q_{R_5^-}Q_{X_5^-}Q_{M_3^+}$ which produces the distortion $Q_{M_3^+}$ (which is symmetry-equivalent to a Jahn-Teller distortion although not caused by an electronic degeneracy in this case). Even if the cations present in the perovskite do not possess degenerate d orbitals, a Jahn-Teller distortion is still permitted because of the terms present in the Landau expansion. However, the distortion is almost negligibly small as it forms as a result of consecutive improper transitions. All the distortions present in the $Pnma$ perovskites are produced by the two tilt modes acting as primary modes.

If it were possible to reverse any one of these tilt modes, the other modes would switch because of their coupled nature. For example, suppose that the $Q_{M_2^+}$ forms an alternate domain

Domain	M_2^+	R_5^-	X_5^-	R_4^-	M_3^+
1	✓	✓	✗	✓	✓
2	✓	✗	✓	✗	✓

Table 3.4: Energetically equivalent domains of *Pnma* perovskite if M_2^+ can be controlled and reversed. The second domain was discussed in text. The first domain can be obtained by choosing to reverse R_5^- in the first trilinear term and including all possible trilinear couplings. The tick denotes that the mode has been reversed and a cross denotes that the mode does not need to be reversed in the particular domain.

in materials with reversed sign. Then, due to the coupling $Q_{R_5^-}Q_{M_2^+}Q_{X_5^-}$, either $Q_{X_5^-}$ or $Q_{R_5^-}$ must reverse to force these terms to lower the free energy. Now suppose that it is $Q_{X_5^-}$ that also reverses. This conveniently satisfies the second coupling $Q_{M_2^+}Q_{X_5^-}Q_{R_4^-}$ as both $Q_{X_5^-}$ and $Q_{M_2^+}$ have been reversed. However, it does not satisfy the third coupling $Q_{R_5^-}Q_{X_5^-}Q_{M_3^+}$ which now only has one reversed mode. To fix this, $Q_{R_5^-}$ or $Q_{M_3^+}$ must be reversed. It cannot be $Q_{R_5^-}$ as that would now put three reversed modes in the first coupling $Q_{R_5^-}Q_{M_2^+}Q_{X_5^-}$ so instead it must be $Q_{M_3^+}$. This leaves all modes satisfied and illustrates the fact that reversing one mode has effects that propagate throughout all the other symmetry-adapted modes.

This argument is clearly quite difficult to follow and would be further complicated if I had included all the possible terms in the Landau expansion. Thankfully, the DOMAINS tool of ISODISTORT [135, 136, 137, 129, 138] is designed to enumerate the set of mutually reversed modes in a particular symmetry which would have the same energy, because all the terms in the Landau expansion are satisfied. Using this tool, another domain can be obtained if M_2^+ is reversed. This is listed in Table 3.4. If you could control one of the modes, it would necessarily interact with all the others.

The domain adopted by the material upon reversal of a particular mode (in this case M_2^+) is difficult to determine. As the final domains are, by definition, energetically equivalent, the path that a material takes is determined by the energy barriers required to switch individual modes. Of the two domains listed in Table 3.4, it is perhaps likely that the material would opt for Domain 2 as this doesn't reverse R_5^- which is a primary mode. However, this could only be determined *a posteriori* from the results of decades of research into the phase transitions of perovskites. From symmetry alone, it is impossible to ascertain which modes will have the lowest switching barrier. Nevertheless, one can often resort to common sense when group theory

cannot give the answer and the simulations are yet to be done. If one of the domains involved the reversal of the cation ordering, this can be almost immediately rejected; the cation mobility is typically not high enough to allow this reversal to have a low energy barrier. The rule of thumb used throughout this thesis is that, if it is not absolutely necessary, primary modes do not reverse*!

Finally, there exist hybrid improper mechanisms where it is the polarisation that is produced as a secondary mode from two primary modes. This is the case in the perovskite related Ruddlesden-Popper compounds $Ca_3Ti_2O_7$ and $Ca_3Mn_2O_7$ where the two primary modes are rotations of the octahedra [139, 140]. Ruddlesden-Popper materials do not have the same parent symmetry as perovskites but instead adopt an $I4/mmm$ symmetry at high temperatures and the non-centrosymmetric $A2_1am$ symmetry at lower temperatures. The two types of octahedral rotations transform as X_5^+ and X_5^- irreps of the $I4/mmm$ space group and the polar mode as Γ_5^-. Therefore, a hybrid improper coupling of the form $Q_{X_5^-}Q_{X_5^+}Q_{\Gamma_5^-}$ is allowed - the condensation of the octahedral tilts leads to a polarisation. Obviously, the polarisation is a mode that can be easily controlled with an external electric field, and so, because of the set of couplings, the reversal of polarisation leads to a sequence of consecutive reversals of other modes until the Landau free energy is degenerate with the original polarisation orientation.

If one can find a multiferroic in which the polarisation is caused by a hybrid improper mechanism, and one of the subsequent modes that must reverse once the polarisation has switched is the ferromagnetic order parameter, then the 180° degree reversal of magnetic dipoles with an electric field has been achieved.

3.4 Electric Field Control Of Magnetism By Design

Our aim is tantalisingly close! This short final section will therefore summarise the general strategy using everything that has been discussed so far.

In short, I need to find perovskite structural polymorphs, each of which are formed by

*With the immediate exception of the polarisation, which can be encouraged to switch by coupling to an electric field.

introducing combinations of symmetry-adapted distortions (transforming under the symmetry elements of $Pm\bar{3}m$ as irreducible representations of $Pm\bar{3}m$) so that the Landau expansion that can be constructed using these distortions ensures that the magnetisation is reversed when the polarisation is reversed.

Schematically, this can be achieved with two overlapping invariant terms in the Landau expansion. One of which is a traditional hybrid improper mechanism

$$P \cdot Q_1 \cdot Q_2, \tag{3.29}$$

and the second involves magnetic distortions

$$M \cdot Q_1 \cdot Q_{\mathrm{AFM}}. \tag{3.30}$$

A second magnetic irrep Q_{AFM} must be included to preserve time-reversal symmetry in this term. As was explored in Chapter 2, various perovskites have complicated magnetic structures labelled by their Bertault notation. They may have a dominant antiferromagnetic structure but, if the magnetic symmetry allows, can also have a ferromagnetic canting of spins. These two distortions transform as different irreducible representations of the high-symmetry phase. It is the ferromagnetic canting that takes the place of M. This mechanism of overlapping trilinear couplings is that which was most comprehensively reviewed by Senn and Bristowe [130] and will be expanded upon in the next chapter.

Importantly, the mode Q_1 appears in both terms*. If reversal of P with a field reverses Q_1 then it must reverse in the magnetic coupling too. Now one of the other two terms must reverse in this second coupling. As the couplings between the spins forming the magnetic structure is presumed to be strong, it is unlikely that the entire magnetic structure reverses and instead it seems likely that the small ferromagnetic canting reverses†. If this is the case, then the electric

*It could have been Q_2 - one of them must appear in both

†It is plausible that the overall magnetic structure could be ferromagnetic with a small *antiferromagnetic* canting. This would also satisfy a term like Equation 3.30 but the switching scheme would be unlikely to work. It would likely be the smaller antiferromagnetic canting that reverses upon reversal of P and the overall magnetisation would remain unchanged.

field has reversed the magnetisation - exactly what is needed for the next generation of memory devices. Of course, there may be many other distortions present in the material which prevent this easy scheme from working. Whether any perovskite symmetries exist in which this switching scheme is feasible is the aim of the next chapter.

Chapter 4

Electric Field Control Of Magnetism In Perovskites From Symmetry

4.1 Introduction

Chapter 2, by describing the many distortions available, established the *dramatis personae* that will play a role in the physics of perovskite materials. Treating each of the distortions as order parameters, Chapter 3 revealed how symmetry can be used to construct the Landau expansion of any particular perovskite, which determines how any given mode can interact with the others. It is these interactions that enable the electric field control of magnetism that would be so useful for future memory devices. In this first results chapter of my thesis, I begin to explore a variety of perovskite phases and establish which perovskite symmetries permit this exciting functionality.

4.2 ABO_3 Perovskites

The rapid increase in the number of symmetries obtained by introducing order parameters and permuting their order parameter directions makes their enumeration a difficult task. Therefore, I start by analyzing the symmetry of ABO_3 perovskites. I consider all possible tilt structures but allow for magnetism only on B sites. In principle, I should include A-site magnetism too but for ABO_3 materials, any magnetism on A sites is typically due to f electrons on rare earth cations

Tilt Pattern	M_2^+ OPD	R_5^- OPD	Space Group
$a^0a^0a^0$	N/A	N/A	$Pm\bar{3}m$
$a^0a^0c^+$	$(a;0;0)$	N/A	$P4/mbm$
$a^0b^+b^+$	$(a;a;0)$	N/A	$I4/mmm$
$a^+a^+a^+$	$(a;a;a)$	N/A	$Im\bar{3}$
$a^+b^+c^+$	$(a;b;c)$	N/A	$Immm$
$a^0a^0c^-$	N/A	$(a,0,0)$	$I4/mcm$
$a^0b^-b^-$	N/A	$(a,a,0)$	$Imma$
$a^-a^-a^-$	N/A	(a,a,a)	$R\bar{3}c$
$a^0b^-c^-$	N/A	$(a,b,0)$	$C2/m$
$a^-b^-b^-$	N/A	(a,a,b)	$C2/c$
$a^-b^-c^-$	N/A	(a,b,c)	$P\bar{1}$
$a^0b^+c^-$	$(a;0;0)$	$(0,0,b)$	$Cmcm$
$a^+b^-b^-$	$(a;0;0)$	$(0,b,b)$	$Pnma$
$a^+b^-c^-$	$(a;0;0)$	$(0,b,c)$	$P2_1/m$
$a^+a^+c^-$	$(a;a;0)$	$(0,b,0)$	$P4_2/nmc$

Table 4.1: All simple tilt patterns in ABO_3 perovskites. There are only 15 symmetry inequivalent patterns.

[141]. These tend to have comparatively low magnetic ordering temperatures, which make them impractical for the stated aim of designing a room-temperature multiferroic exhibiting electric field control of magnetism. I relax this restriction when I investigate cation ordered perovskites, which do allow for magnetic transition metals on the A sites.

Recapping the discussion of Chapter 2, there are 15 different simple*, symmetry inequivalent tilt patterns. These can be produced by introducing and combining the in-phase tilt irrep M_2^+ and the anti-phase tilt irrep R_5^- with varying order parameter directions (OPD). This is shown in Table 4.1.

For each of these, it is theoretically permissible for the polarisation to appear along practically any axis. This is achieved by adding in the polar Γ_4^- irrep with varying OPDs. Table 4.2 lists most of these. However, there is an extra degree of freedom available to the order parameter which is needed to complete the enumeration. For OPDs with equal magnitudes along different directions, it is possible to change the relative phase between the two components to break the symmetry in another way. Therefore, $(a,a,0) \neq (a,-a,0)$ etc. The remaining symmetries are obtained in Table 4.3.

*By "simple", I mean tilt patterns in which there is no superposition between antiphase and inphase tilts along the same axis. Such a tilt pattern cannot be described by Glazer notation.

	Γ_4^- Order Parameter Direction									
Tilt Pattern	$(a,0,0)$	$(0,a,0)$	$(0,0,a)$	$(a,a,0)$	$(a,0,a)$	$(0,a,a)$	(a,a,a)	$(a,b,0)$	$(a,0,b)$	$(0,a,b)$	(a,b,c)
$a^0a^0a^0$	$P4mm$	$P4mm$	$P4mm$	$Amm2$	$Amm2$	$Amm2$	$R3m$	Pm	Pm	Pm	$P1$
$a^0a^0c^+$	$Amm2$	$Amm2$	$P4bm$	$Pmc2_1$	Cm	Cm	Pc	Pm	Cm	Cm	$P1$
$a^0b^+b^+$	$I4mm$	$Imm2$	$Imm2$	Cm	Cm	$Fmm2$	Cm	Cm	Cm	Cm	$P1$
$a^+a^+a^+$	$Imm2$	$Imm2$	$Imm2$	Cm	Cm	Cm	$R3$	Cm	Cm	Cm	$P1$
$a^+b^+c^+$	$Imm2$	$Imm2$	$Imm2$	Cm	Cm	Cm	$P1$	Cm	Cm	Cm	$P1$
$a^0a^0c^-$	$Fmm2$	$Fmm2$	$I4cm$	$Ima2$	Cm	Cm	Cc	Cm	Cm	Cm	$P1$
$a^0b^-b^-$	Cm	$Ima2$	Cm	$P1$	$Ima2$	$P1$	Cc	$P1$	Cm	$P1$	$P1$
$a^-a^-a^-$	Cc	Cc	Cc	Cc	Cc	Cc	$R3c$	$P1$	$P1$	$P1$	$P1$
$a^0b^-c^-$	Cm	$C2$	Cm	$P1$	Cm	$P1$	$P1$	$P1$	Cm	$P1$	$P1$
$a^-b^-b^-$	$P1$	Cc	$P1$	$P1$	Cc	$P1$	Cc	$P1$	$P1$	$P1$	$P1$
$a^-b^-c^-$	$P1$	$P1$	$P1$	$P1$	$P1$	$P1$	$P1$	$P1$	$P1$	$P1$	$P1$
$a^0b^+c^-$	$Ama2$	$Amm2$	$Cmc2_1$	Pm	Cc	Cm	$P1$	Pm	Cc	Cm	$P1$
$a^+b^-b^-$	Pm	Pm	$Pna2_1$	$Pmc2_1$	$P1$	$P1$	Pc	Pm	$P1$	$P1$	$P1$
$a^+b^-c^-$	Pm	Pm	$P2_1$	Pm	$P1$	$P1$	$P1$	Pm	$P1$	$P1$	$P1$
$a^+a^+c^-$	$P4_2mc$	$Pmn2_1$	$Pmn2_1$	Pm	Pm	$Aba2$	Cc	Pm	Pm	Pc	$P1$

Table 4.2: Symmetry lowering by adding the polar Γ_4^- mode with various OPDs to each tilt pattern.

	Γ_4^- Order Parameter Direction					
Tilt Pattern	$(a,-a,0)$	$(a,0,-a)$	$(0,a,-a)$	$(a,-a,-a)$	$(-a,a,-a)$	$(-a,-a,a)$
$a^0a^0a^0$	$Amm2$	$Amm2$	$Amm2$	$R3m$	$R3m$	$R3m$
$a^0a^0c^+$	$Pmc2_1$	Cm	Cm	Pc	Pc	Pc
$a^0b^+b^+$	Cm	Cm	$Fmm2$	Cm	Cm	Cm
$a^+a^+a^+$	Cm	Cm	Cm	$R3$	$R3$	$R3$
$a^+b^+c^+$	Cm	Cm	Cm	$P1$	$P1$	$P1$
$a^0a^0c^-$	$Ima2$	Cm	Cm	Cc	Cc	Cc
$a^0b^-b^-$	$P1$	$Imm2$	$P1$	Cm	Cc	Cm
$a^-a^-a^-$	$C2$	$C2$	$C2$	Cc	Cc	Cc
$a^0b^-c^-$	$P1$	Cm	$P1$	$P1$	$P1$	$P1$
$a^-b^-b^-$	$P1$	$C2$	$P1$	$P1$	Cc	$P1$
$a^-b^-c^-$	$P1$	$P1$	$P1$	$P1$	$P1$	$P1$
$a^0b^+c^-$	Pm	Cc	Cm	$P1$	$P1$	$P1$
$a^+b^-b^-$	$Pmn2_1$	$P1$	$P1$	Pc	Pc	Pc
$a^+b^-c^-$	Pm	$P1$	$P1$	$P1$	$P1$	$P1$
$a^+a^+c^-$	Pm	Pm	$Aba2$	Cc	Cc	Cc

Table 4.3: Symmetry lowering by adding the polar Γ_4^- mode with additional OPDs to each tilt pattern.

Some features of Tables 4.2 and 4.3 should be noted. Firstly, an identical space group does not necessarily mean that the two crystal structures are the same. For example, the $Pmc2_1$ symmetry can be obtained from a $a^0a^0c^+$ tilt pattern and a Γ_4^- mode along $(a,a,0)$. It can also be obtained through an $a^+b^-b^-$ tilt pattern with Γ_4^- mode along $(a,a,0)$. The additional polarisation does not enforce the additional tilts. Evidently, these crystal structures are not equivalent due to the manifestly different tilt patterns yet share the same symmetry elements. In contrast, introducing the polar mode can relax restrictions on the tilt pattern so that two tilt patterns become equivalent - this is reflected in identical space groups. For example, the Cm space group achieved in the $a^0a^0c^+$ and $a^0b^+b^+$ rows are genuinely the same crystallographic structure; the polar mode and associated OPD allows the appearance of a second in-phase tilt. Frustratingly then, sometimes identical space groups denote similar crystal structures, and

sometimes they do not.

In addition, the $P1$ symmetry is the lowest symmetry space group, containing only the identity symmetry element. I will not focus on any material with this space group because every non-trivial symmetry element in $Pm\bar{3}m$ has been broken. The irreps in the space group are too numerous to work with and a group theoretical analysis becomes distinctly less enlightening than with higher symmetry subgroups.

Most of the crystallographic symmetries explored in Tables 4.2 and 4.3 are physically unattainable because of the considerations listed in Chapter 2. Introducing any magnetic cation significantly reduces the tolerance factor of the perovskite material and introduces tilts. We can therefore safely ignore any untilted perovskite structure (or those with a small number of tilts). In fact, the vast majority of ABO_3 perovskites take up the $a^+b^-b^-$ tilt pattern and so I focus on that symmetry. A great deal of work has been conducted to engineer polar distortions in this common tilt pattern and typically, the polar distortion is in highly symmetrical directions.

Similar rules of thumb apply to magnetism. The full range of magnetic symmetries are not explored by perovskites. Indeed, perovskite magnetism is usually relatively simple [27], with easy axes along pseudocubic axes.

4.2.1 $a^+b^-b^-$ Perovskites

Tables 4.2 and 4.3 list five distinct symmetries* for different polarisation directions superimposed onto the $a^+b^-b^-$ tilt pattern. These were Pm : $(a,0,0)$ and $(0,a,0)$, $Pmc2_1$: $(a,a,0)$, $Pmn2_1$: $(a,-a,0)$, $Pna2_1$: $(0,0,a)$ and finally Pc : (a,a,a). As an example of the equivalence of different order parameter direction, $(a,0,0)$ and $(0,a,0)$ are subsumed into $(a,b,0)$ and both result in Pm symmetry. The immediate result of this is that I only need to investigate either the $(a,0,0)$ or $(0,a,0)$ OPD.

For each of these symmetries, I insert a collinear magnetic structure described by one of the magnetic irreps and then for each magnetic irrep I choose OPDs along the pseudocubic directions. For the three dimensional irreps, this is $(a,0,0),(0,a,0)$ and $(0,0,a)$. For the six-dimensional

*Not including $P1$.

	B-site Magnetism				
Γ_4^- OPD	mX_1^-	mX_5^-	mM_2^+	mM_5^+	mR_5^-
$(a,0,0)$	$(0;0;a)$	$(0,0;0,0;a,b)$	$(a;0;0)$	$(a,b;0,0;0,0)$	$(a,0,0)$ $(0,a,b)$
$(0,0,a)$	$(0;0;a)$	$(0,0;0,0;a,b)$	N/A	$(a,b;0,0;0,0)$	$(a,0,0)$ $(0,a,b)$
$(a,a,0)$	$(0;0;a)$	$(0,0;0,0;a,b)$	N/A	$(a,b;0,0;0,0)$	$(a,0,0)$ $(0,a,b)$
(a,a,a)	$(0;0;a)$	$(0,0;0,0;a,b)$	$(a;0;0)$	$(a,b;0,0;0,0)$	(a,b,b) (a,b,c)
$(a,-a,0)$	$(0;0;a)$	$(0,0;0,0;a,b)$	N/A	$(a,b;0,0;0,0)$	$(a,0,0)$ $(0,a,b)$

Table 4.4: Magnetic structures allowing for weak ferromagnetism in polar subgroups of ABO_3 perovskites with $a^+c^-c^-$ tilt patterns. Entries are the magnetic irrep OPDs that result on symmetries that allow for the wFM irrep $m\Gamma_4^+$

magnetic irreps*, these are all the permutations of $(a,0;0,0;0,0)$. I then use ISODISTORT to see if these magnetic structures, when superimposed on the polar structure, allow for weak ferromagnetism which transforms as the $m\Gamma_4^+$ irrep. The results of this analysis are shown in Table 4.4.

Each entry in Table 4.4 is the OPD of the magnetic irrep allowing for wFM. Both X and M point modes only allow for wFM in particular directions whereas mR_5^- allows for wFM with any simple easy axis (the $(0,a,0)$ and $(0,0,a)$ OPDs are symmetry equivalent and both reduce to $(0,a,b)$). Typically, the same magnetic structure creates wFM irrespective of the polar direction but this is not true for the mM_2^+ where the polar direction can kill wFM. This is because a coupling like $Q_{mM_2^+}Q_{M_2^+}Q_{m\Gamma_4^+}$, which creates the wFM, does not satisfy all the point group operations for certain wFM OPDs.

Weak ferromagnetism is therefore a fairly generic feature of $a^+c^-c^-$ tilts for almost any polarisation direction, especially if the perovskite has a G-type antiferromagnetic structure. The question to answer now is whether any of these polar, weakly ferromagnetic structures allow for the electric field control of magnetism.

*Six-dimensional order parameters can be understood to be a combination of lower dimensional order parameters. For example, the semi-colon in the notation $(a,0;0,0;0,0)$ separates the six-dimensional order parameter into three, two dimensional order parameters, which correspond to magnetic moments that are able to rotate within three mutually perpendicular planes.

For Pm symmetry, with the polar mode along the $(a, 0, 0)$ OPD, all collinear structures allow for wFM. However, when I compute all of the possible domains reached by reversing the primary modes, as is done in Tables B.1, B.2, B.3, B.4 and B.5, there always exists a domain in which the polar mode Γ_4^- is the only primary mode that must reverse. As this reverses the fewest number of primary modes, it is likely that such a domain would have the lowest energy barrier.

I have also explicitly calculated the domain structure for all magnetic structures in $Pna2_1$ (Tables B.6, B.7 and B.8) and $Pmc2_1$ (Tables B.9, B.10 and B.11) and obtain the same result. For the sake of space, the $Pmn2_1$ and Pc symmetries are not included but suffer from the same negative conclusion.

In Table B.8, I have also included domains in which the weak ferromagnetism rotates by 90 degrees rather than reverses completely. This is allowed whenever the wFM has an OPD with two components. I've belaboured this point because it has been reported in the literature that $Pna2_1$ allows for this rotation of wFM with reversal of polarisation [142]. This is indeed true but it seems very unlikely to be observed because there is always a favoured domain without any magnetoelectric response at all. Any discussion of alternative domains was absent from Reference [142].

It could be argued that the conditions I have imposed here to determine the "lowest energy barrier" between the original state and a domain with some modes reversed is overly simplistic. This is true - ferroelectric switching normally takes place via the nucleation of the reversed domain at a defect, and then the motion of domain walls and the subsequent growth of domains [143, 144]. This entire chain of events is known as the Kolmogorov-Avrami-Ishibashi process. The domain wall motion is also strongly dependent on the domain wall pinning. Furthermore, considerations of the dielectric breakdown of any particular material must be made. If the field required to switch is larger than the critical field that destroys the insulating state, then obviously no electrically induced ferroelectric switching is possible. All of these conditions make for a far more accurate description of ferroelectric switching, but it is also necessarily much more complicated, especially as the ferroelectric switching in any particular material is dependent on idiosyncratic features of that same material and a proper study of any one of them would require

years of work and become a PhD project by itself.

Instead, the approach taken here in reducing the complex domain wall dynamics to a more simplified situation in which there is a homogeneous reversal of modes, and then ordering their likelihood based on the number of reversing primary modes, acts as a zeroth-order approximation. It may be crude but as has been demonstrated in this section, it is very easily scalable to many symmetries at once. This makes a high-throughput discussion of many perovskites possible. Besides, these simple considerations of "lowest energy switching barrier" may not be as rudimentary as they seem. Previous studies have actually seen this kind of homogeneous switching [145, 146] (albeit under special conditions) and more recent work [147] has shown that nucleation can be important even in defect free crystals. Moreover, it is not unreasonable to assume that domain wall motion occurs via a local mode reversal. To zeroth order, this would mimic the discussion given here.

The real advantage of our simplified method here is that we can almost immediately rule out certain perovskite symmetries as candidates for the electric field control of magnetism, as was possible for $a^-a^-c^+$ single perovskites. This was because the polar irrep Γ_4^- was not coupled directly to any other primary mode. In order to have large magnetoelectric couplings, we need an improper ferroelectric.

We can create ABO_3 single perovskite structures that do allow for the electric field control of magnetism through an improper mechanism if we allow for magnetism on the A-site. Consider a material with $a^+c^-c^-$ (R_5^- and M_2^+) tilts and also A-type spins on both the A-site and the B site (mX_3^+ and mX_1^- respectively). Then a weak ferromagnetic moment can be produced through a coupling like

$$Q_{m\Gamma_4^+}Q_{mX_1^-}Q_{M_2^+}Q_{R_5^-} \tag{4.1}$$

and a polarisation can be formed through the spin-driven (Type II), improper mechanism

$$Q_{\Gamma_4^-}Q_{mX_1^-}Q_{mX_3^+} \tag{4.2}$$

so that if it is preferable to switch the magnetism on the B-site over the magnetism on the A-sites, and the weak ferromagnetism is preferred over the tilts (extraordinarily likely), then the electric field control of magnetism would be achieved using only primary modes.

	Irrep Reversal					
Domain	Γ_4^-	$m\Gamma_4^+$	M_2^+	R_5^-	mX_1^-	mX_3^+
1	✓	✓	✓	✗	✗	✓
2	✓	✓	✓	✓	✓	✗
3	✓	✓	✗	✓	✗	✓
4	✓	✓	✗	✗	✓	✗
5	✓	✗	✓	✓	✗	✓
6	✓	✗	✓	✗	✓	✗
7	✓	✗	✗	✗	✗	✓
8	✓	✗	✗	✓	✓	✗

Table 4.5: Domain structure of hypothetical perovskite with a collinear A-type magnetic structure on both A and B sites. Electric field switching of magnetisation can be achieved if the switching of magnetism on A-sites is engineered to be harder than switching the magnetism on B-sites.

To confirm, adding the tilt pattern, mX_1^- and mX_3^+ (both magnetic modes with OPD $(0, 0, a)$) leads to a $Pna2_1$ symmetry which is both polar and allows for wFM. The domain structure for this hypothetical material is shown in Table 4.5.

Alternatively, I can do the same thing for G-type spins on both the A and B sites because a coupling like

$$Q_{\Gamma_4^-} Q_{mR_5^-} Q_{mR_4^+} \tag{4.3}$$

would produce the ferroelectricity and then a coupling like

$$Q_{m\Gamma_4^+} Q_{mR_5^-} Q_{R_5^-} \tag{4.4}$$

establishes the weak ferromagnetism. We again need a system in which it is easier to switch the B spins than the A spins. Checking with ISODISTORT, this again results in a $Pna2_1$ symmetry with a weak ferromagnetic moment. The domain structure in Table 4.6 would also allow for the electric field control of magnetism.

The conclusion here is that the electric field control of magnetism is certainly a theoretical possibility in perovskites with simple tilt patterns, but it requires unusual magnetic orderings. If we allow for realistic ion ordering, this extra degree of freedom allows greater flexibility and makes the electric field control of magnetism a serious possibility in real materials.

	Irrep Reversal					
Domain	Γ_4^-	$m\Gamma_4^+$	M_2^+	R_5^-	mR_4^+	mR_5^-
1	✓	✓	✓	✓	✓	✗
2	✓	✓	✓	✗	✗	✓
3	✓	✓	✗	✗	✗	✓
4	✓	✓	✗	✓	✓	✗
5	✓	✗	✓	✗	✓	✗
6	✓	✗	✓	✓	✗	✓
7	✓	✗	✗	✓	✗	✓
8	✓	✗	✗	✗	✓	✗

Table 4.6: Domain structure of hypothetical perovskite with a collinear G-type magnetic structure on both A and B sites. Electric field switching of magnetisation can be achieved if the switching of magnetism on A-sites is engineered to be harder than switching the magnetism on B-sites.

4.3 Ion Ordered Perovskites

The previous section investigated how symmetry breakings may permit the electric field control of magnetism in perovskites without cation order ie. ABO_3 perovskite materials. In the following, I allow for the additional symmetry breaking associated with cation order and investigate whether this will be more fruitful.

The previous subsection also tried to be somewhat comprehensive in the symmetry analysis. Such an approach is certainly enlightening but in practice, there were too many degrees of freedom to be exhaustive. With the new focus on cation-order in perovskite materials, we restrict the symmetry analysis to structural polymorphs that could potentially be synthesized.

This effectively reduces our symmetry analysis to simple cation orderings and tilt patterns. From Chapter 2, the simplest cation orderings include rocksalt ordering (transforming as an R-point irrep (R_2^-)), columnar ordering (transforming as an M-point irrep M_4^+) and layered ordering (transforming as an X-point irrep X_3^-) but others will also be investigated. The primary advantage associated with introducing cation orderings is that the energy barrier to reverse such an ordering is enormously large because of the relatively low cation mobility and so I can ignore any domains that are reached via a reversal in cation order.

4.3.1 $A_2BB'O_6$ Perovskites

We begin with perovskites with ordered B-sites. The standard reference for B-site ordering in perovskites is the extensive review by Vasala and Karpinnen [59]. This reviews the literature of $A_2BB'O_6$ perovskites, listing various physical properties of which the space group and the B-site ordering are the most important for our present purposes.

Interestingly, there is not a single example of columnar ordered B-sites. King and Woodward [60], explained that cation ordering is strongly dependent on the difference in oxidation states and the strain caused by cation size-mismatch. B-site columnar ordering has only been observed in charge-ordered Mn compounds where the additional strain from the first-order Jahn-Teller distortion of the Mn^{3+} increases the propensity towards cation ordering. As the review only focuses on materials with two *distinct* B-sites, these materials are omitted.

The enumeration of space groups is also useful. The review states that of the 540 materials with rocksalt ordered B-sites, 310 of them have the $a^-a^-c^+$ tilt pattern giving a $P2_1/n$ space group. This reflects the general fact that such a tilt pattern is generally favoured in perovskites because of the additional energy lowering gained by the $Q_{X_5^-}Q_{M_2^+}Q_{R_5^-}$ trilinear coupling. I will focus on this tilt pattern.

There are no examples of transition metals on the A-sites when the B-sites are rocksalt ordered, and so magnetism on these A-sites can be neglected.

Very few $A_2BB'O_6$ perovskites are polar, which presents a huge problem if we intend to use this structure to couple the polarisation to the magnetism. $A_2BB'O_6$ with A=Pb can frequently be made to be polar after applying an electric field because of the Pb lone-pairs but this would describe an antiferroelectric. Only $Pb_2ScB'O_6$ with B'=Nb,Ta results in a polar space group ($R3$) without any applied field [148]. Of course, Nb^{5+} and Ta^{5+} are non-magnetic. It thus appears that obtaining a proper Type-I multiferroic from BB' ordering is not possible. Is it possible to obtain a Type-II multiferroic through the simultaneous appearance of a polarisation with the magnetic structure and if so, does this allow for the electric field control of magnetism?

To answer this, I introduce the rocksalt ordering R_2^- to the $a^-a^-c^+$ symmetry as well as

	mX_1^-	mM_2^+	R_5^-
Polar?	N/A	N/A	N/A
wFM?	$(0;0;a)$ $(0;a;a)$ $(0;a;-a)$ $(a;b;c)$	$(a;0;0)$ $(a;b;c)$	$(a,0,0)$ $(0,a,0)$ $(0,a,0)$ $(a,a,0)$ $(0,a,a)$ (a,b,b) (a,b,c)

Table 4.7: Properties enabled by the introduction of different collinear structures on the BB' sites of cation ordered $A_2BB'O_6$ perovskites with $a^-a^-c^+$ tilt patterns.

	X_1^+ OPD		
	$(a;0;0)$	$(0;a;0)$	$(0;0;a)$
Space Group	$P2_1/m$	$P2_1/m$	$Pmc2_1$

Table 4.8: Symmetries obtained by layering the cations along different directions. Only the $(0;0;a)$ OPD leads to a polarisation.

various magnetic structures. The results of the symmetry analysis are included in Table 4.7. There are many OPDs producing weak ferromagnetism but there are none that break the centre of symmetry.

Repeating the analysis with columnar (M_4^+) or layered (X_3^-) cation order instead leads to similar results. Just superposing cation order and magnetism does not break inversion symmetry but frequently allows for wFM. The combination of magnetism and cation ordering on the B-site is therefore not a fruitful approach in designing materials which permit the electric field control of magnetism, at least not for the most common tilt pattern.

4.3.2 $AA'B_2O_6$ Perovskites

What about ordering the A-sites instead? As mentioned in Chapter 2 and discussed in the review by King and Woodward [60], layered ordering is preferred on the A-site. Combining the various magnetic structures with A-site layering (X_1^+) with the the $a^-a^-c^+$ tilt pattern (formed by M_2^+ with OPD $(a,0,0)$ and R_5^- with OPD $(0,a,a)$) leads to several possibilities. This is demonstrated in Table 4.8.

Table 4.9: Magnetic irreps and their OPDs that also allow for the wFM irrep $m\Gamma_4^+$.

B-Site Magnetism				
mX_1^-	mX_5^-	mM_2^+	mM_5^+	mR_5^-
$(0;0;a)$ $(a;b;c)$	$(0,0;0,0;a,b)$	$(a;b;c)$	$(a,b;0,0;0,0)$	$(a,0,0)$ $(0,a,b)$ (a,b,c)

For the OPD $(0;0;a)^*$, the space group is the non-centrosymmetric $Pmc2_1$. The combinations of $a^-a^-c^+$ and cation layering breaks the centre of symmetry and leads to a polar crystal structure. This is due to the appearance of a trilinear coupling

$$E = \lambda Q_{X_5^-} Q_{X_1^+} Q_{\Gamma_4^-} \tag{4.5}$$

between the cation ordering, the antipolar motions of the A sites (X_5^-) and the polar mode Γ_4^-. Both $Q_{X_5^+}$ (because it is in the high symmetry structure and coupled to tilts) and $Q_{X_1^+}$ (being a cation ordering) would have large amplitudes and $Q_{\Gamma_4^-}$ would adopt a sign that reduces the overall energy irrespective of the sign of the coefficient λ.

The next step is to check simple magnetic structures for wFM, and if this is permitted, to check whether the polarisation and wFM are coupled in the desired way. Again, I only consider magnetic orderings on the B-site. The OPDs of the magnetic irreps that allow for wFM are listed in Table 4.9. There are only three simple configurations I need to consider further and calculate their domains. These are $mX_1^-(0;0;a)$, $mR_5^-(a,0,0)$ and $mM_5^+(a,b;0,0;0,0)$ which are now considered primary distortions along with $X_1^+(0;0;a)$, $M_2^+(a;0;0)$ and $R_5^-(0,a,a)$. The domains for these three magnetic structures are shown in Tables 4.10, 4.11, 4.12. For all of these magnetic structures, we see a domain in which only the polarisation and the cation order is switched. We assume that such a domain is unfavourable because of the enormous energy barriers to reversing a cation order. For the mX_1^- structure, the domain that reverses the second fewest number of modes (either domain 1 or 2) is a magnetoelectric domain in which the wFM has also reversed. It is due to the cation order that a domain of this kind is favourable. However, this domain still requires the switching of one of the tilt modes.

*In real space, this is a cation layering in which the normal to the layers is parallel to the in phase tilt axis.

$mX_1^-(0;0;a)$	Primary Irrep Reversal					
Domain	Γ_4^-	$m\Gamma_4^+$	M_2^+	R_5^-	X_1^+	mX_1^-
1	✓	✓	✗	✓	✗	✗
2	✓	✓	✓	✗	✗	✗
3	✓	✓	✗	✗	✓	✓
4	✓	✓	✓	✓	✓	✓
5	✓	✗	✗	✓	✗	✓
6	✓	✗	✓	✗	✗	✓
7	✓	✗	✗	✗	✓	✗
8	✓	✗	✓	✓	✓	✗

Table 4.10: Domains for layered A-site perovskite with $a^-a^-c^+$ tilts and a magnetic structure transforming as the $mX_1^-(0;0;a)$ irrep.

$mR_5^-(a,0,0)$	Primary Irrep Reversal					
Domain	Γ_4^-	$m\Gamma_4^+$	M_2^+	R_5^-	X_1^+	mR_5^-
1	✓	✓	✗	✓	✗	✗
2	✓	✓	✓	✗	✗	✓
3	✓	✓	✗	✗	✓	✓
4	✓	✓	✓	✓	✓	✗
5	✓	✗	✓	✗	✗	✗
6	✓	✗	✗	✓	✗	✓
7	✓	✗	✓	✓	✓	✓
8	✓	✗	✗	✗	✓	✗

Table 4.11: Domains for layered A-site perovskite with $a^-a^-c^+$ tilts and a magnetic structure transforming as the $mR_5^-(a,0,0)$ irrep.

For the mR_5^- structure, the most favourable domain is the ferroelectric domain in which the polarisation is switched with the in-phase tilt. For the mM_5^+ structure, the situation is more subtle. The lowest energy domain obtained after switching the polarisation would depend on whether the combined switching of $m\Gamma_4^+$ and M_2^+ is favoured over switching just R_5^-.

To summarise, a layered perovskite with $a^-a^-c^+$ tilts and a magnetic structure transforming as mX_1^- would allow for the electric field control of magnetism if we assume that the cation ordering is immutable. The properties of a candidate material with this symmetry is explored in Chapter 7 through computer simulation. The mM_5^+ and mR_5^- structures may also allow for the effect.

$mM_5^+(a,b;0,0;0,0)$	Primary Irrep Reversal					
Domain	Γ_4^-	$m\Gamma_4^+$	M_2^+	R_5^-	X_1^+	mM_5^+
1	✓	✓	✗	✓	✗	✓
2	✓	✓	✗	✗	✓	✓
3	✓	✓	✓	✗	✗	✗
4	✓	✓	✓	✓	✓	✗
5	✓	✗	✗	✓	✗	✗
6	✓	✗	✗	✗	✓	✗
7	✓	✗	✓	✗	✗	✓
8	✓	✗	✓	✓	✓	✓

Table 4.12: Domains for layered A-site perovskite with $a^-a^-c^+$ tilts and a magnetic structure transforming as the $mM_5^+(a,b;0,0;0,0)$ irrep.

4.3.3 $A_3BB'_2O_9$ Triple Perovksites

Triple perovskites with $A_3BB'_2O_9$ were first observed in the 1960s with for the $Ba_3SrTa_2O_9$ composition [149]. The Sr and Ta occupy the B sites in 1:2 layers that are ordered along the [111] direction of the pseudocubic 5-atom perovskite cell. This family of materials was quickly extended to include many materials with a $A_3^{2+}B^{2+}B_2'^{5+}O_9$ [150, 151] composition when A=Ca, Sr, Ba; B=Mg,Ca,Sr,Mn,Fe,Co,Ni,Cu,Zn; and B'= Nb,Ta. Importantly, it was noticed that the 1:2 ordering only takes place when the difference in cation radii for the two B sites are substantially different [150]. Therefore Ca and Nb order successfully but Fe and Nb do not. In fact, none of the magnetic transition cations order. Nevertheless, the resulting symmetry after cation order is still centrosymmetric and so would not permit the necessary polarisation.

It was later found that other magnetic cations could be included in the B' site and that the B sites would continue to order in the 1:2 state. Therefore $Sr_3CaRu_2O_9$, [152, 153], $Sr_3CaIr_2O_9$ [154], $Sr_3CaOs_2O_9$ [155] all order successfully. The Os composition is especially interesting due to the extremely high magnetic ordering temperature (T_N = 385K). The Ru compound also shows impressive magnetic ordering temperatures (T_N = 190K) whereas the Ir compound is paramagnetic. All of these compounds also show the familiar $a^-a^-c^+$ tilt pattern which combines with the cation order to produce a monoclinic $P2_1/c$ symmetry.

This symmetry is stil centrosymmetric. How can inversion be broken? I looked for examples of the 1:2 B site order with additional ordering on the A-site. There is a single reported

example - $(Na_{\frac{1}{2}}La_{\frac{1}{2}})(Mg_{\frac{1}{3}}Nb_{\frac{2}{3}})O_3$ [156]. This has the A-sites layered along the [001] direction of the pseudocubic in addition to the 1:2 ordering of the B-sites*. This material also has the $a^-a^-c^+$ tilt pattern. Combining the tilts and the two cation orders reduces the symmetry to Pc - a polar space group. However, the original study [156], did not conduct any experiments to test whether the material is a ferroelectric with a switchable polarisation.

The natural course of action to take would be to try and combine the high magnetic ordering temperature of $Sr_3CaOs_2O_9$ with the polar crystal structure of $(Na_{\frac{1}{2}}La_{\frac{1}{2}})(Mg_{\frac{1}{3}}Nb_{\frac{2}{3}})O_3$. We therefore propose either $(Na_{\frac{1}{2}}La_{\frac{1}{2}})(Ca_{\frac{1}{3}}Os_{\frac{2}{3}})O_3$ or $(Na_{\frac{1}{2}}La_{\frac{1}{2}})(Ca_{\frac{1}{3}}Ru_{\frac{2}{3}})O_3$. The new materials have similar tolerance factors to the originals (for example $t_{\mathrm{NLMN}} = 0.958$ and $t_{\mathrm{NLCR}} = 0.939$), and we do not suspect that the magnetic structure of Os will be affected by the small distortions induced by the slightly different change in tolerance factor. It seems likely that $(Na_{\frac{1}{2}}La_{\frac{1}{2}})(Ca_{\frac{1}{3}}Os_{\frac{2}{3}})O_3$ would therefore be a multiferroic† with an above room temperature Neel temperature.

Using ISODISTORT, we analyse the symmetry of this proposed triple perovskite, with the magnetic structure of the Os compound, using the 5-atom perovskite $Pm\bar{3}m$ as the parent structure. The resulting decomposition into symmetry-adapted modes is incredibly complicated, with 32 separate irreps involves. The primary modes are the two tilt modes M_2^+ and R_5^-, a combination of $m\Lambda_2$ and $m\Lambda_3$ (Λ is at the $\boldsymbol{k} = (\frac{1}{3}, \frac{1}{3}, \frac{1}{3})$ point) modes that describe the magnetic structure, a Λ_1 mode that describes the cation order of the B sites and the familiar X_1^+ mode for the cation order in the A-sites.

For secondary modes, we have an allowed polarisation mode Γ_4^- directed with an (a, b, b) OPD. This suggests that the polarisation is predominantly along the [111] direction but also allows for some canting because $a \neq b$ by symmetry. In addition, there is the crucial $m\Gamma_4^+$ ferromagnetic mode describing the ferromagnetic canting with a (a, b, b) OPD. Therefore, all the necessary ingredients are present.

As the Λ modes are at $\boldsymbol{k} = (\frac{1}{3}, \frac{1}{3}, \frac{1}{3})$, they allow for the interesting possibility of electric field

*Technically, this is no longer a *triple perovskite* but is instead now a *sextuple perovskite* because when the chemical formula is expanded, it becomes $Na_3La_3Ca_2Os_4O_{18}$

†In the broad sense of the word in which there is a polarisation and a long ranged magnetic structure

control of magnetism through a single coupling in the Landau expansion rather than the two overlapping couplings discussed at the end of Chapter 3. Checking on INVARIANTS reveals a term of the form

$$Q_{\Gamma_4^-}Q^3_{m\Lambda_1}Q_{m\Gamma_4^+}. \tag{4.6}$$

Being a fifth order term that is odd in all of the constituent modes, it acts analogously to trilinear terms. Assuming that $Q^3_{m\Lambda_1}$ is the large magnetic structure that is unlikely to switch, then a reversal of $Q_{\Gamma_4^-}$ with an electric field results in a reversal of the ferromagnetic canting $Q_{m\Gamma_4^+}$. If this were the only term involved, the electric field control of magnetism would be achieved.

However, there are a great many other terms that may play a role. Due to the sheer number of secondary modes and the complexity of the structure, I change tactic when computing all allowed invariants in the Landau expansion and the energy degenerate domains. Instead of using the $Pm\bar{3}m$ cell as my parent structure, I instead use a cell with the ordered A and B sites already present. The central assumption in the previous section when investigating $AA'B_2O_6$ perovskites is that cation order does not change in any switching process. If this is true, and the low mobility of cations in perovskites suggest that it is, I can ignore this additional degree of freedom. The new parent structure has a $C2/m$ symmetry.

Decomposing the full structure with the tilts and the magnetic structure as symmetry adapted modes of this $C2/m$ parent simplifies matters. There are now only 8 irreps to deal with. These are Γ_1^+, Γ_2^- (which describes the ferroelectric distortion), $m\Gamma_2^+$ (the ferromagnetic canting), $m\Gamma_1^-$ (the primary magnetic structure), Y_2^+ and Y_1^- (the octahedral tilts) with mY_1^+ and mY_2^- describing symmetry allowed antiferromagnetic canting. What are these Y modes which ISODISTORT reports as being at the $(0, 1, 0)$ point? Isn't this just equivalent to the Γ point? In fact, $(0, 1, 0)$ is not actually a point in the reciprocal lattice at all. This can be seen by recognising that a C-centered lattice possesses an extra lattice point within the face perpendicular to the $\mathbf{c}$ lattice. With respect to the conventional cell lattice vectors $(\mathbf{a}, \mathbf{b}, \mathbf{c})$, the primitive lattice vectors $(\mathbf{a}', \mathbf{b}', \mathbf{c}')$ could be (the choice is not unique but the conclusions would be unchanged)

$$\mathbf{a}' = -\frac{1}{2}\mathbf{a} + \frac{1}{2}\mathbf{b},$$

$$\mathbf{b}' = \frac{1}{2}\mathbf{a} + \frac{1}{2}\mathbf{b},$$

and

$$\mathbf{c}' = \mathbf{c}.$$

These expressions can be used to find the transformation matrix $\mathbf{Q}$ between the conventional, centered cell and the primitive by constructing the matrix $\mathbf{P}$ with these primitive lattice vectors as columns, and then transposing it so that

$$\mathbf{Q} = \mathbf{P}^{\mathrm{T}} = \begin{pmatrix} -\frac{1}{2} & \frac{1}{2} & 0 \\ \frac{1}{2} & \frac{1}{2} & 0 \\ 0 & 0 & 1 \end{pmatrix}^{\mathrm{T}} = \begin{pmatrix} -\frac{1}{2} & \frac{1}{2} & 0 \\ \frac{1}{2} & \frac{1}{2} & 0 \\ 0 & 0 & 1 \end{pmatrix}.$$

We can then apply this transformation to the conventional point $(0, 1, 0)$ to get

$$\begin{pmatrix} -\frac{1}{2} & \frac{1}{2} & 0 \\ \frac{1}{2} & \frac{1}{2} & 0 \\ 0 & 0 & 1 \end{pmatrix} \begin{pmatrix} 0 \\ 1 \\ 0 \end{pmatrix} = \begin{pmatrix} \frac{1}{2} \\ \frac{1}{2} \\ 0 \end{pmatrix}$$

which is clearly not a lattice point. Another nice detail of this calculation is that it can be repeated for an arbitrary point (hkl) in the conventional cell so that

$$\begin{pmatrix} -\frac{1}{2} & \frac{1}{2} & 0 \\ \frac{1}{2} & \frac{1}{2} & 0 \\ 0 & 0 & 1 \end{pmatrix} \begin{pmatrix} h \\ k \\ l \end{pmatrix} = \begin{pmatrix} \frac{1}{2}(-h + k) \\ \frac{1}{2}(h + k) \\ l \end{pmatrix}$$

and it becomes clear that a point in the reciprocal conventional cell is only a lattice point if $h + k = 2n$ or $h - k = 2n$. These are systematic absences. With respect to the primitive cell then, Y modes are actually zone boundary modes which increase the volume of the primitive cell*.

*Thank you to Branton Campbell of Brigham Young University for explaining this to me.

	Irrep Reversal							
Domain	Γ_1^+	Γ_2^-	$m\Gamma_2^+$	$m\Gamma_1^-$	Y_2^+	Y_1^-	mY_1^+	mY_2^-
1	✗	✓	✓	✗	✓	✗	✗	✓
2	✗	✓	✓	✗	✗	✓	✓	✗
3	✗	✓	✗	✓	✗	✓	✗	✓
4	✗	✓	✗	✓	✓	✗	✓	✗

Table 4.13: Energy equivalent domains in the Pc phase of $(Na_{\frac{1}{2}}La_{\frac{1}{2}})(Ca_{\frac{1}{3}}Os_{\frac{2}{3}})O_3$ specified by which irreps must be switched to reach the domain. Irreps describe symmetry breakings from the $C2/m$ parent symmetry which has the cation ordering frozen in.

I used INVARIANTS to calculate all couplings between these new modes, and then the allowed domains, which are summarised in Table 4.13. These are the only domains available when the polarisation is reversed.

From Table 4.13, we can see immediately that the electric field reversal of magnetism will be allowed in this material because Domains 1 and 2 are clearly favoured over Domains 3 and 4. Domains 1 and 2 do not reverse the overall magnetic structure whereas the other two do. In all domains, reversing the polarisation must reverse at least one of the tilt modes and one antiferromagnetic canting. With this collection of modes, it is highly likely that this material would possess the electric field control of magnetism. In the context of the new parent cell, the relevant term in the Landau expansion is

$$Q_{\Gamma_2^-}Q_{m\Gamma_1^-}Q_{m\Gamma_2^+}. \tag{4.7}$$

The physics is the same as before, but the coupling term now takes on a much simpler form.

I note that there have been other reports of multiferroic triple perovskites [157, 158] but these are only formed at extremely low temperatures ($T \approx 4$K) and are due to the hexagonal symmetry producing a non-collinear spin structure that breaks the symmetry. This makes the materials Type-II multiferroics. $(Na_{\frac{1}{2}}La_{\frac{1}{2}})(Ca_{\frac{1}{3}}Os_{\frac{2}{3}})O_3$ would instead be a Type-I multiferroic with a very high magnetic transition temperature.

4.3.4 $AA'_3B_4\mathbf{O}_{12}$ Perovskites

$AA'_3B_4O_{12}$ are quadruple perovskites, deduced from the O_{12} in the chemical formula. This structure can be obtained for a perovskite with an $a^+a^+a^+$ tilt pattern when A is a large cation and A' is a smaller, transition metal cation. The A' cations are far too small for their site and so the octahedra undergo especially large tilts to accomodate this - the B-O-B angle between neighbouring cations is about 140° [66]. These huge tilts result in the A' sites having a square-planar coordination environment, which can be contrasted with the standard 12-coordinated, cubo-octahedral environment inhabited by the A sites in ABO_3 perovskites. As such, the A-site is usually occupied by cations that allow for strong Jahn-Teller distortions such as Cu^{2+} and Mn^{3+} [67]. In the extreme limit of a Jahn-Teller distortion, four anions move closer to the central cation and two move further away, forming the square.

I analysed the symmetry of these materials using a $Pm\bar{3}m$ parent structure. The $a^+a^+a^+$ tilt pattern is described by the M_2^+ irrep and the cation ordering on the A-site is the M_1^+ with the (a, a, a) OPD.

We begin the analysis by seeing whether any simple collinear magnetic structures can break the symmetry and produce a Type II multiferroic.

I look at simple magnetic structures on the B-sites. Using ISODISTORT, I find that for both the A-type magnetic irreps mX_1^- and mX_5^-, none of the resulting space groups are non-centrosymmetric. This is also the case for the two C-type magnetic irreps, mM_2^+ and mM_5^+. To complete the set, the G-type magnetic irrep mR_5^- also doesn't break inversion symmetry. The system remains centrosymmetric for all simple magnetic structures if we also allow for the B-site rocksalt ordering (R_2^-) which is occasionally observed in these materials [159, 160].

I introduce a polar mode Γ_4^-, so that we model a Type-I multiferroic. I use $BiMn_3Cr_3O_{12}$ as a model system to explore the possibilities [161]. This is known to undergo a sequence of phase transitions, the first introducing a polar distortion along the [001] direction of the pseudocubic cell and reducing the symmetry from $Im\bar{3}$ to $Imm2$. This is due to the ordering of the lone pairs on the Bi^{3+} cation. The second introduces G-type magnetism to the B-sites. The third introduces an antiferromagnetic spin-structure on the A'-site, which produces a second

	Irrep Reversal				
Domain	Γ_4^-	$m\Gamma_4^+$	M_1^+	M_2^+	mM_5^+
1	✓	✓	✗	✗	✓
2	✓	✓	✓(109°)	✓(109°)	✓(90°)
3	✓	✓	✓(109°)	✓(109°)	✓(−90°)
4	✓	✓	✓(109°)	✓(109°)	✗
5	✓	✗	✗	✗	✗
6	✓	✗	✓(109°)	✓(109°)	✓(−90°)
7	✓	✗	✓(109°)	✓(109°)	✓(90°)
8	✓	✗	✓(109°)	✓(109°)	✓

Table 4.14: Energy equivalent domains in the $Imm2$ phase of $AA'_3B_4O_{12}$ perovskites with a polar mode introduced along the [001] direction and C-type magnetism.

polarisation along the [111] direction. This is an additional spin-driven ferroelectricity which is also the only source of macroscopic polarisation in $LaMn_3Cr_3O_{12}$.

I start by adding various magnetic structures to the polar phase with a polarisation along the [001] direction. Adding the experimentally observed G-type structure, for all OPDs, doesn't result in a magnetic space group that allows for wFM. This is the same for the two A-type irreps mX_1^- and mX_5^-. However, for the C-type irrep mM_5^+, weak ferromagnetism is allowed. It is perhaps no surprise that these mM^+ modes can induce weak ferromagnetism in a material dominated by other M point irreps. For example, one of the allowed couplings here is $Q_{M_2^+}Q_{mM_5^+}Q_{m\Gamma_4^+}$ so that the combination of the in-phase tilts and the magnetic structure produce a weak ferromagnetic moment. Does the switching of the polar mode necessitate the switching of the weak ferromagnetism in this system? As there is a domain that can be achieved by reversing only the polar mode, which would presumably be the domain with the lowest energy barrier, it is unlikely that this combination of distortions will allow for the electric field control of magnetism. These domains are enumerated in Table 4.14.

Other authors [162] contend that the polarisation after the first transition in $BiMn_3Cr_3O_{12}$ is actually along the $[1\bar{1}0]$ direction which produces a Cm symmetry. In this situation, weak ferromagnetism is again only allowed for C-type magnetism. However, there is also a domain in which only the polarisation is reversed, The same result arises for the hypothetical situation where the polar mode is along the [111] direction. Therefore, $BiMn_3Cr_3O_{12}$ or any other quadruple perovskite with the same symmetry, does not allow for the electric field control of

magnetism below the first polar transition.

Before introducing A-site magnetism, I check whether a rocksalt ordered B-site analogue of $BiMn_3Cr_4O_{12}$ ($BiMn_3B_2B'_2O_{12}$) changes this conclusion. Rocksalt ordering the B-sites while retaining the overall G-type magnetic structure does allow for a ferromagnetic mode. However, this is not a weak ferromagnetic mode but is instead a *ferrimagnetic* mode. As the rocksalt order splits the magnetic sites, the two become inequivalent and the spins no longer have to exactly cancel and this causes the appearance of a ferromagnetic mode. In fact, just introducing the rocksalt order R_2^- and the magnetic order mR_5^- to the $Pm\bar{3}m$ produces a ferrimagnetic moment through this mechanism. From the perspective of Landau theory, the ferrimagnetic moment is produced by a coupling of the form $Q_{R_2^-}Q_{mR_5^-}Q_{m\Gamma_4^+}$. As the cation order does not change, this means that whenever we wish to reverse the ferrimagnetic moment, we have to also reverse the dominating antiferromagnetic structure too. Any domain that doesn't do this describes a continuous increase of spin on one magnetic site and a decrease on the other. This is unphysical.

With this in mind, I examined the domains of $BiMn_3B_2B'_2O_{12}$ with G-type magnetism and rocksalt order on the B sites. There still exists a single domain in which only the polar mode needs to be switched. The additional rocksalt order does not change matters, and this is another demonstration that in order to guarantee that the polar mode reversal will also reverse the magnetisation, the polar mode must be caused via a coupling to other modes in the system.

To introduce A-site magnetism and model the second transition in $BiMn_3Cr_3O_{12}$, or the ferroelectricity of $LaMn_3Cr_3O_{12}$, the symmetry adapted modes describing the magnetism are in fact a superposition of three modes; the mR_4^+ describing G-type magnetism on the A and A' sites which puts erroneous spins on the non-magnetic A sites, and then a combination of mX_3^+ and mX_5^+ which cancel these erroneous spins. In general, a magnetic structure of a material on sites that are split by a cation order must be a superposition of multiple magnetic order parameters.

I will now restrict myself to magnetic structures that have actually been observed or else the possibilities become intractably large. Decomposing the A-site magnetic structure observed in $BiMn_3Cr_3O_{12}$ and $LaMn_3Cr_3O_{12}$, into symmetry adapted modes reveals that no weak ferromag-

	Irrep Reversal						
Domain	Γ_4^-	$m\Gamma_4^+$	M_1^+	M_2^+	R_2^-	mR_4^+	mR_5^-
1	✓	✓	✗	✓	✓	✓	✗
2	✓	✓	✓(71°)	✓(109°)	✗	✗	✓
3	✓	✓	✓(71°)	✓(109°)	✗	✗	✓
4	✓	✓	✓(71°)	✓(109°)	✓	✓	✗
5	✓	✓	✓(71°)	✓(109°)	✗	✗	✓
6	✓	✓	✓(71°)	✓(109°)	✓	✓	✗
7	✓	✓	✓(71°)	✓(109°)	✓	✓	✗
8	✓	✓	✗	✓	✗	✗	✓
9	✓	✗	✓(71°)	✗	✓	✗	✓
10	✓	✗	✓(71°)	✓(71°)	✗	✓	✗
11	✓	✗	✓(71°)	✓(71°)	✗	✓	✗
12	✓	✗	✓(71°)	✓(71°)	✓	✗	✓
13	✓	✗	✓(71°)	✓(71°)	✗	✓	✗
14	✓	✗	✓(71°)	✓(71°)	✓	✗	✓
15	✓	✗	✓(71°)	✓(71°)	✓	✗	✓
16	✓	✗	✗	✗	✗	✓	✗

Table 4.15: Domains in the $R3$ phase of $AA'_3B_2B'_2O_{12}$ perovskites with nearest neigbour magnetism on both the A' and B sites, with all spins pointing along the [111] direction. Rocksalt order is also included on the B sites.

netism is allowed. In addition, it does not make the system polar. Reinserting the B-site G-type spins (mR_5^-) does produce a secondary polar distortion. This is the origin of the ferroelectricity in $BiMn_3Cr_3O_{12}$ and $LaMn_3Cr_3O_{12}$ below their magnetic transition temperatures - it is caused by a spin-induced symmetry breaking but only when these spins appear on both A and B sites, and when they are overlayed on the $a^+a^+a^+$ tilt pattern and the cation order. Specifically, the polarisation is due to a coupling of the form $Q_{mR_5^-}Q_{mR_4^+}Q_{\Gamma_4^-}$ which is only allowed when all three terms have the (a, a, a) OPD.

However, this does not allow for any ferromagnetic mode but, as we have seen, reinserting the B-site rocksalt order brings about the ferrimagnetic mode. The resulting domain structure is shown in Table 4.15.

To estimate which of these domains may have the lowest barrier in a switching scheme, we can immediately eliminate any domain in which the cation orders reverse. Interestingly, this leaves only two domains! Domain 8 is the structure we wish to obtain when we reverse the polarisation as it also reverses the ferrimagnetic moment. Domain 16 reverses the magnetism on the A' sites. I have only displayed the primary irreps here but it is obvious that other secondary

modes will also need to switch. For example, Domain 16 involves the reversal of the mR_4^+ magnetic mode, but I have already stated that this is only one part of the A' site magnetic structure. The two mX modes must also switch to counter the unphysical A spins that would arise from mR_4^+ reversing. As a result, small X point structural irreps must also reverse. In Domain 8, it is clear that other irreps must also reverse because Γ_4^-, $m\Gamma_4^+$ and M_2^+ and mR_5^- do not form closed sets of couplings with each other without violating either preservation of parity or crystal momentum.

I therefore conclude that quadruple perovskites with chemical formula $AA'_3B_2B'_2O_{12}$ could potentially be used to engineer the electric field control of magnetism, but I have unfortunately reached the limit of what symmetry alone can tell me. The switching mechanism would be complicated and the energy barriers between leading to either Domain 8 or Domain 16 can only be determined with computational methods.

The antiferromagnetic nearest neighbour interaction is one possible collinear A'-site magnetic structure. Another is analogous to C-type in that it has columns of magnetic moments with parallel alignment. Neighbouring columns are antiferromagnetically aligned. This sort of magnetic structure is found in the AMn$_7$O$_{12}$ materials [68], which is due to a charge disproportionation on the Mn site. The above analysis could be extended to this family of materials too.

4.3.5 A bottom-up approach

An interesting corollary of the work on $BiMn_3Cr_4O_{12}$, is that the tilts or cation order are not essential to create a polarisation. The $Q_{mR_5^-}Q_{mR_4^+}Q_{\Gamma_4^-}$ coupling would also exist in a $Pm\bar{3}m$ symmetry without the tilts or the cation order. If it were possible to engineer a cubic, untilted perovskite with G-type spins on both the A and B sites, then that would be polar. I investigated this result further, and used ISODISTORT to confirm that this is true but only for particular OPDs for the two magnetic irreps. For example, if the spins on both sites align along [111], this produces a polarisation in exact analogy to $LaMn_3Cr_3O_{12}$. Unfortunately, no weak ferromagnetism is allowed, but this is due to a lack of positive parity R^+ modes that could form a coupling like $Q_{R^+}Q_{mR_4^+}Q_{m\Gamma_4^+}$ or a negative parity R^- mode to form a coupling

	Irrep Reversal				
Domain	Γ_4^-	$m\Gamma_4^+$	mR_4^-	mR_5^-	R_5^-
1	✓	✓	✗	✓	✗
2	✓	✓	✓	✗	✓
3	✓	✗	✓	✗	✗
4	✓	✗	✗	✓	✓

Table 4.16: Domains in the ABO_3 perovskites with G-type magnetism on both the A' and B sites, and a single antiphase tilt parallel to the spin-induced polarisation.

like $Q_{R^-}Q_{mR_5^-}Q_{m\Gamma_4^+}$. Referring to Table 3.3, we see that R_5^- or R_3^- describe octahedral tilts and Jahn-Teller distortions respectively and these two modes could be used to create the weak ferromagnetism.

The simplest hypothetical structure I can find which permits this involves a collinear magnetic structure in which G-type exist on both the A and the B sites with an easy axis along the [110] direction of the pseudocubic cell. This produces a polarisation perpendicular to this easy axis. Adding a single antiphase tilt along about this polarisation axis would allow for weak ferromagnetism. Furthermore, this weak ferromagnetism is potentially switchable by reversing the polarisation. This is made clear from looking at the four domains in Table 4.16 that can be reached from switching the polarisation. It is not at all obvious which of these domains would possess the lowest switching barrier. If we could engineer a system in which it is extremely hard to reverse the single antiphase tilt and the A-site magnetism, then a domain allowing for the electric field control of magnetism would be favoured. Of course, this is all very hypothetical, I am not able to find any perovskites with this combination of modes in any structural database or in the literature. In fact, it would be extremely difficult to engineer because the magnetic cations needed for magnetism on both cation sites would drastically change the tolerance factor and result in a much more complex tilt pattern.

It is clear that I've essentially reached the same conclusion as I did when I added A-type spins to $a^+c^-c^-$ tilts. However, I see that initial discussion as being part of a "top down" approach in which I already knew which kind of tilt patterns are likely in perovskites and then investigated which distortions could be added to create the desired effects. The current discussion is more of a "bottom up" strategy in which I looked for the minimum number of irreducible representations that result in the electric field control of magnetism.

I've taken this philosophical digression because the "bottom up" and "top down" approaches are the two different strategies I could have taken to complete this project. The "bottom up" approach is advantageous because extra complexity is added progressively, but it is not clear whether each added distortion is physically realistic. You would need to check every distortion against the literature or through simulation to make sure it makes sense. In contrast, the "top down" approach starts with a complicated structure, decomposes that into its symmetry adapted modes and then asks "What is missing to allow for electric field control of magnetism?". It takes a material as complex as $BiMn_3Cr_4O_{12}$ to make use of the simple observation that we need spins on both sublattices, as well as an additional R-point mode (cation ordering in the case of quadruple perovskites) to have any hope of electric-field control of magnetism. Typically, I've preferred the "top-down" approach because it is inherently grounded in the existing literature. Taking the triple perovskite cation ordering as an example, I would have very likely discarded the 1:2 layering of cations as a serious possibility if I was building up, but because I had found this structure in the literature, it immediately seems like a useful avenue to explore.

4.4 Summary

This chapter has attempted to explore the symmetries of common perovskite polymorphs in a systematic manner. For perovskites without cation order and with the ubiquitous $a^-a^-c^+$ tilt pattern, few structures allow for the electric field control of magnetism, because there are relatively few mechanisms to create improper ferroelectricity. Nevertheless, Chapter 6 will identify a slightly different kind of electric field control of magnetism in these materials, which has not previously been described in the literature.

Including cation order increases the flexibility of perovskite materials. It is much easier to create a polarisation through an improper mechanism with these additional degrees of freedom. I have shown that layered A-site cations are one route to create the electric field control of magnetism. This will be investigated in more detail for a candidate material in Chapter 7. Furthermore, I have suggested that both triple and quadruple perovskites may be amenable to hosting the same effect but for different reasons. In the triple perovskite, the ferroelectricity

is again due to a layering of cations whereas in the quadruple perovskite, it is due to a spin ordering.

Chapter 5

Density Functional Theory And Quantum Mechanical Simulation

The previous chapter outlined how we can predict various material properties from a symmetry analysis alone. This proved to be a very powerful methodology but it is not complete. As I stated, a symmetry analysis can be decisive in determining what type of physics is possible but is unable to estimate the magnitudes of the symmetry-allowed effects.

The magnitudes of these effects are encoded within the Schrödinger Equation which determines the energy and time-evolution of the multidimensional ($3N$ dimensions for N particles) *wave function* Ψ. The wavefunction completely describes any non-relativistic quantum system. Famously, Paul Dirac stated that "The underlying physical laws necessary for the mathematical theory of a large part of physics and the whole of chemistry are thus completely known, and the difficulty is only that the exact application of these laws leads to equations much too complicated to be soluble" [163].

This chapter describes a methodology that reformulates the Schrodinger Equation into a form that is tractable using computational methods. The trick involves converting the Schrodinger equation, which depends on the wavefunction, into an equation that depends only on the density of electrons. *Density functional theory* (DFT), in the formulation by Kohn and Sham (KS), is an *exact* reformulation of the ground-state interacting many-body Schrodinger Equation into a system of equations describing fictitious non-interacting particles. The electronic ground state

density assumes centre stage in DFT because the energy is computed as a functional of the density. Being a 3-dimensional quantity, the density takes up substantially less memory than the wavefunction, and is therefore easier to work with and store. How the Schrodinger Equation is transformed into a density functional is explored in this chapter.

DFT may be exact in principle but sadly, that exact formulation is still beyond the reach of theorists. In applications, the exact ground state functional must instead be approximated. The number of approximations are vast and so I focus only on those which I have used during the work described in this thesis.

In addition to the fundamental approximations that must be made in constructing the density functional, various other approximations are routinely made to make the calculation of the energy tractable. Furthermore, there exists extensions to the original formulation of DFT so that it becomes more useful to slightly more non-trivial quantum systems - spin-DFT and strongly correlated corrections being the two that I use extensively in my work.

DFT is fundamentally a theory for the ground state of a quantum system. Therefore, it's applicability at any temperature above 0K should be called into question. Nevertheless, DFT is often very good at describing real materials at non-zero temperatures. This is because the relevant energy scales in materials are typically far higher than the temperatures encountered in everyday life. As an illustrative example, the band gap for excitation in Si is 1.12 eV. This corresponds to temperatures of approximately 13000K, well above any normal operating conditions. Therefore, the conclusions drawn from DFT are typically representative of materials but the restriction to 0K must always be kept in mind.

5.1 From Schrodinger To Kohn-Sham

To obtain the wavefunction and energies of a quantum system made of nuclei and electrons, it is necessary to solve the time independent Schrodinger equation [164, 165]

$$\hat{H}\Psi(\mathbf{r}_1, \mathbf{r}_2, ..., \mathbf{r}_N) = E\Psi(\mathbf{r}_1, \mathbf{r}_2, ..., \mathbf{r}_N). \tag{5.1}$$

This is an eigenvalue equation with the energy E and wavefunction Ψ playing the roles of eigenvalue and eigenfunction, respectively. The Hamiltonian $\hat{H}$ acts upon the wavefunction and returns the energy. For a system of nuclei and electrons, the Hamiltonian takes the form

$$\begin{aligned}\hat{H} = &-\sum_{i}^{N}\frac{\hbar^2}{2m_e}\nabla_i^2 - \sum_{I}^{M}\frac{\hbar^2}{2M_I}\nabla_I^2 + \frac{1}{2}\sum_{i\neq j}\frac{e^2}{4\pi\epsilon_0}\frac{1}{|\mathbf{r}_i-\mathbf{r}_j|}\\ &+\frac{1}{2}\sum_{I\neq J}\frac{e^2}{4\pi\epsilon_0}\frac{Z_I Z_J}{|\mathbf{R}_I-\mathbf{R}_J|} - \sum_{i,I}\frac{e^2}{4\pi\epsilon_0}\frac{Z_I}{|\mathbf{r}_i-\mathbf{R}_I|},\end{aligned} \tag{5.2}$$

where uppercase indices run over nuclear degrees of freedom, lowercase indices run over electronic degrees of freedom, m_e and M_I are the electronic and nuclear masses respectively and $\frac{e^2}{4\pi\epsilon_0}$ is the usual constant found in Coulomb interactions. The complexity of this Hamiltonian is the primary cause of difficulty in quantum mechanical simulations (as pithily stated by Dirac) but it is simple to understand by treating each term individually:

- The first term is the kinetic energy of the electrons, expressed in standard operator form.
- The second term is the kinetic energy of the nuclei.
- The third is the repulsive Coulomb interaction of the electrons. This term causes the greatest difficulty in the solution of this eigenvalue equation because the wavefunction cannot be split into individual electron wave functions.
- This fourth term is the Coulomb repulsion between the nuclei.
- This final term is the electrical attraction of the negatively charged electrons to the positively charged nuclei.

This Hamiltonian can be immediately simplified by invoking the *clamped nuclei approximation* which is valid because $m_e \lll M_I$ - the nuclear kinetic term is considerably smaller than the electronic kinetic and can be safely dropped. Physically, this can be interpreted as the electronic and nuclear dynamics occuring on two different timescales. The change in the electronic wavefunction is faster than the changing nuclear wavefunction and so, for any electronic motion,

the nuclei are essentially fixed. A more sophisticated and mathematically rigourous approach is the *adiabatic* or *Born-Oppenheimer* approximation.

Due to the clamped nuclei approximation, the nuclear repulsion can also be dropped because this simply adds an arbitrary constant to the energy. The nuclei are thus reduced to providing a positively charged potential to the electrons so that the electronic Hamiltonian becomes

$$\hat{H} = -\frac{1}{2}\sum_{i}^{N}\nabla_i^2 - \sum_{i,I}\frac{Z_I}{|\mathbf{r}_i - \mathbf{R}_I|} + \frac{1}{2}\sum_{i\neq j}\frac{1}{|\mathbf{r}_i - \mathbf{r}_j|}. \tag{5.3}$$

Use has been made of *atomic* or *Hartree* units in which distances are measured in Bohr radii a_0, energies are measured in hartrees (Ha) and masses in units of m_e.

This Hamiltonian remains far too complex to solve. The electronic repulsion term prevents a separable solution and so the wavefunction must remain a function of $3N$ variables. Instead, further approximations must be made to remove the electronic repulsion term and deal with *independent electrons*.

If the electronic interactions were a small perturbation, the electronic repulsion term could simply be dropped as a first approximation. This would result in the wavefunction assuming a product form of non-interacting particles so that

$$\Psi(\mathbf{r}_1, \mathbf{r}_2, ..., \mathbf{r}_N) = \phi_1(\mathbf{r}_1)\phi_2(\mathbf{r}_2)\phi_3(\mathbf{r}_3)...\phi_N(\mathbf{r}_N), \tag{5.4}$$

with each wave function ϕ_i satisfying independent particle Hamiltonians

$$\left[-\frac{1}{2}\nabla_i^2 - \sum_{I}\frac{Z_I}{|\mathbf{r}_i - \mathbf{R}_I|}\right]\phi_i(\mathbf{r_i}) = \epsilon_i\phi_i(\mathbf{r_i}) \tag{5.5}$$

and the energies becomes a sum of independent particle energies

$$E = \epsilon_1 + \epsilon_2 + \epsilon_3 + ... + \epsilon_N. \tag{5.6}$$

Unfortunately, the electronic repulsion is not a small perturbation and so this is an extremely crude and inaccurate approximation. Any serious attempt at approximating the Hamiltonian must retain some form of interaction. In addition, the above approximation ignores the fermionic nature of electrons which requires that the total wavefunction must be antisymmetric with

respect to particle exchange. The easiest way to reintroduce particle statistics is to write the wavefunction in the form of a *Slater determinant*

$$\Psi(\mathbf{r}_1, \mathbf{r}_2, ..., \mathbf{r}_N) = \frac{1}{\sqrt{N!}} \begin{vmatrix} \phi_1(\mathbf{r}_1) & \phi_1(\mathbf{r}_2) & ... & \phi_1(\mathbf{r}_N) \\ \phi_2(\mathbf{r}_1) & \phi_2(\mathbf{r}_2) & ... & \phi_2(\mathbf{r}_N) \\ ... & ... & ... & ... \\ \phi_N(\mathbf{r}_1) & \phi_N(\mathbf{r}_2) & ... & \phi_N(\mathbf{r}_N) \end{vmatrix} \tag{5.7}$$

which enforces the correct exchange symmetry due to the rules of determinants [77]. The spin of the electrons has been omitted in this expression. It should be clear that the exchange symmetry would affect the energy of the state. Two fermions are prohibited from occupying the same state and there is an energy cost from this criterion whenever two electrons come close together. For now, this effect will be added as a *local* function $V_x(\mathbf{r})$ to the Hamiltonian and a discussion reserved until later in this section. Therefore we have

$$\left[-\frac{1}{2}\nabla_i^2 - \sum_I \frac{Z_I}{|\mathbf{r}_i - \mathbf{R}_I|} + V_x(\mathbf{r}_i) \right] \phi_i(\mathbf{r}_i) = \epsilon_i \phi_i(\mathbf{r}_i). \tag{5.8}$$

In addition, eigenfunctions of an Hermitian operator such as the Hamiltonian are orthogonal and satisfy:

$$\int_\infty^\infty d\mathbf{r} \phi_i^*(\mathbf{r}) \phi_j(\mathbf{r}) = \delta_{ij}. \tag{5.9}$$

This fact proves useful when defining the density of electrons as

$$n(\mathbf{r}) = N \int |\Psi(\mathbf{r}, \mathbf{r}_2, ..., \mathbf{r}_N)|^2 d\mathbf{r}_2 d\mathbf{r}_3 ... d\mathbf{r}_N, \tag{5.10}$$

which reduces to

$$n(\mathbf{r}) = \sum_i |\phi_i(\mathbf{r})|^2 \tag{5.11}$$

when (5.9) is used.

This density is crucial to reintroducing interactions. Instead of treating each electron as experiencing a point particle repulsion from every other electron, it is possible to treat each electron as experiencing an effective field from a background made up of the other particles. From electrostatic theory, a charge density $n(\mathbf{r})$ produces a electrical potential through Poisson's equation [49]:

$$\nabla^2 V_{\mathrm{H}}(\mathbf{r}) = -4\pi n(\mathbf{r}). \tag{5.12}$$

This has the solution

$$V_{\mathrm{H}}(\mathbf{r}) = \int d\mathbf{r}' \frac{n(\mathbf{r}')}{|\mathbf{r} - \mathbf{r}'|} \tag{5.13}$$

and is known as the *Hartree potential*.

With this step, we have reintroduced interactions to the independent electron approximation and each electron wavefunction now satisfies

$$\left[-\frac{1}{2}\nabla_i^2 - \sum_I \frac{Z_I}{|\mathbf{r}_i - \mathbf{R}_I|} + V_{\mathrm{H}}(\mathbf{r}) + V_x(\mathbf{r}) \right] \phi_i(\mathbf{r_i}) = \epsilon_i \phi_i(\mathbf{r_i}), \tag{5.14}$$

$$V_{\mathrm{H}}(\mathbf{r}) = \int d\mathbf{r}' \frac{n(\mathbf{r}')}{|\mathbf{r} - \mathbf{r}'|}, \tag{5.15}$$

$$n(\mathbf{r}) = \sum_i |\phi_i(\mathbf{r})|^2. \tag{5.16}$$

This very nearly completes the construction of the mean-field, independent electron Hamiltonian. This has reduced the original Hamiltonian operating on a wavefunction with $3N$ variables to one which acts on N three dimensional functions. However, the three above equations are now coupled. To solve for the wavefunctions, knowledge of the density is needed, which requires knowledge of the wavefunctions. This circular situation can only be solved via a *self consistent* solution to the equations so that an initial guess of the density is made, the wavefunctions are calculated and the density recomputed. If the new density is equal to the original density (to within a reasonable tolerance), self consistency has been reached.

As the final step in the construction, some addition must be made to go beyond the mean-field approach. This is accomplished in an ad hoc manner by adding a *correlation potential* V_c which catches any deviations from the mean-field Hartree interactions resulting from electron interactions that are also not the result of exchange symmetry. Like the exchange potential V_x, its determination is left for later.

So finally, the independent electron Hamiltonian is

$$\boxed{\left[-\frac{1}{2}\nabla_i^2 + V_{\mathrm{N}}(\mathbf{r}) + V_{\mathrm{H}}(\mathbf{r}) + V_x(\mathbf{r}) + V_c(\mathbf{r}) \right] \phi_i(\mathbf{r_i}) = \epsilon_i \phi_i(\mathbf{r_i})} \tag{5.17}$$

where V_{N} is the nuclear attraction from above. The problem is considered solved if the orbitals and energies are determined.

For periodic potentials, we can use translational symmetry to derive Bloch's theorem so that

$$\phi_{j\boldsymbol{k}}(\boldsymbol{r}_j) = u_{j\boldsymbol{k}} e^{i\boldsymbol{k}\cdot\boldsymbol{r}} \tag{5.18}$$

and every solution can be decomposed into a function $u_{i\boldsymbol{k}}$ obeying translational symmetry and a modulating wave $e^{i\boldsymbol{k}\cdot\boldsymbol{r}}$. Every solution is associated with a wavevector $\boldsymbol{k}$ within the Brillioun zone. Periodic boundary conditions mean that there are a finite number of $\boldsymbol{k}$ but for a large enough system, with a large enough number of cells, the spacing between $\boldsymbol{k}$ tends to zero.

The energies also pick up this new k index so that they are written $\epsilon_{i\boldsymbol{k}}$. For a given i, the $\boldsymbol{k}$ produce a continuum of energies. This is an energy band. Therefore the index i is known as the band index. This is analogous to the energy levels in isolated atoms.

If electrons occupy the bands so that a band is left partly occupied, this defines a metal. Alternatively, if electrons occupy lower bands completely and are seperated from empty bands by a gap, this defines an insulator*.

5.2 The Hohenberg-Kohn Theorems And The Kohn-Sham Scheme

The most widely used approach to tackling Equation (5.17) is density functional theory (DFT). To introduce this method, we rewrite the many body Hamiltonian present in the Schrödinger equation as

$$\hat{H} = \hat{T} + \sum_i V_N(\mathbf{r}_i) + \hat{W}, \tag{5.19}$$

with $\hat{T}$ and $\hat{W}$ as the first and third terms of (5.3) respectively, covering the kinetic energy and mutual repulsion of electrons. The energy of this hamiltonian is thus

$$E = \langle\Psi|\hat{H}|\Psi\rangle = \langle\Psi|\sum_i V_N(\mathbf{r}_i)|\Psi\rangle + \langle\Psi|\hat{T} + \hat{W}|\Psi\rangle \tag{5.20}$$

*The energy eigenvalues in the Kohn-Sham scheme do not accurately describe the gap because the band gap is actually an excited state property and DFT only describes the ground state - this is mathematically captured by the concept of the derivative discontinuity. Nevertheless, the Kohn-Sham scheme is frequently used to describe the gaps in insulators but this proviso must be kept in mind. I do not have space to discuss this in detail. [166]

The first term can be written as

$$\langle\Psi|\sum_i V_N(\mathbf{r}_i)|\Psi\rangle = \sum_i \int V_N(\mathbf{r}_i)|\Psi|^2 d\mathbf{r}_1 d\mathbf{r}_2 d\mathbf{r}_3 ... d\mathbf{r}_\mathrm{N} = \int V_N(\mathbf{r}) n(\mathbf{r}) d\mathbf{r}, \tag{5.21}$$

where the final step has been made as every element of the sum is the same and so the definition of the density can be employed. This form of the energy allows two very useful theorems to be proved [167]:

1st Theorem Of Hohenberg and Kohn: The external potential (and hence the total energy), is a unique functional of the electron density.

Proof: This is a proof by contradiction. Suppose that there are two external potentials V_1 and V_2 that produce the same ground state density n. Then we assume that the two corresponding Hamiltonians H_1 and H_2 have two different ground states Ψ_1 and Ψ_2. Ψ_2 is not the ground state of H_1 so that

$$\langle\Psi_1|H_1|\Psi_1\rangle < \langle\Psi_2|H_1|\Psi_2\rangle = \langle\Psi_2|H_2|\Psi_2\rangle + \langle\Psi_2|H_1 - H_2|\Psi_2\rangle \tag{5.22}$$

or

$$E_1 < E_2 + \int d\mathbf{r}\,[V_1(\mathbf{r}) - V_2(\mathbf{r})]\,n(\mathbf{r}), \tag{5.23}$$

but the argument could have worked the other way round so that

$$E_2 < E_1 + \int d\mathbf{r}\,[V_2(\mathbf{r}) - V_1(\mathbf{r})]\,n(\mathbf{r}), \tag{5.24}$$

and adding them both together gets the contradictory results that $0 < 0$. So there cannot be two external potentials that produce the same density.

The corollary of this theorem is that, since the Hamiltonian is fully described by a given density, then the entire wavefunction is also described by this density which from we can make the final assertion that all ground state properties are completely described by the density.

I mentioned that "we assume that the two corresponding Hamiltonians H_1 and H_2 have two different ground states Ψ_1 and Ψ_2". This assumption sounds straight forward but is in fact difficult to justify. In fact, when spins are included, this assumption is much more tricky to make [168]. Nevertheless, spin-DFT has been shown to have sound theoretical foundation [169].

2^{nd} Theorem Of Hohenberg and Kohn: A universal functional for the energy $\mathcal{F}[n]$ in terms of the density $n(\mathbf{r})$ can be defined, valid for any external potential $V(\mathbf{r})$. For any particular external potential $V(\mathbf{r})$, the exact ground-state energy of the system is the global minimum value of the functional

$$E[n] = \int V_N(\mathbf{r})n(\mathbf{r}) + \mathcal{F}[n], \tag{5.25}$$

and the density $n(\mathbf{r})$ that minimizes the functional is the exact ground-state density $n(\mathbf{r})$.

This statement does not need such a formal proof (although one is available in [164]) as it is almost self evident. Via the first theorem, knowledge of the density determines the potential and the Hamiltonian. Knowledge of the potential allows for the determination of the wavefunction, and the wavefunction and Hamiltonian are all that are required to know the energy via the functional in Equation (5.20). Thus the ground state energy should be completely specified by a functional of the density.

The difficulty is now to construct this energy functional. It can quite easily be written as

$$E[n] = \int V_N(\mathbf{r})n(\mathbf{r}) + \mathcal{F}[n] = \int V_N(\mathbf{r})n(\mathbf{r}) + \langle \Psi[n]|\hat{T} + \hat{W}|\Psi[n]\rangle\,, \tag{5.26}$$

where the dependence on the density is explicit in the first term but implicit through the wavefunctions, via the Hohenberg-Kohn theorems, in the other terms. If this dependence were known exactly, then every ground state property could be determined exactly. This is sadly not the case and approximations must be made to develop the functional. As was seen above in (5.17), the simplest procedure is often to recast the problem in terms of independent electrons and this is exactly the approach taken by Kohn and Sham [170]. They crafted a functional of the density, including the kinetic energy and Coulomb repulsion terms, that would reproduce the independent electron Hamiltonian (5.17). Their functional takes the form

$$E[n] = \int V_N(\mathbf{r})n(\mathbf{r}) - \frac{1}{2}\sum_i \int d\mathbf{r}\phi_i^*(\mathbf{r})\nabla^2\phi_i(\mathbf{r}) + \frac{1}{2}\int\int d\mathbf{r}d\mathbf{r}'\frac{n(\mathbf{r})n(\mathbf{r}')}{|\mathbf{r}-\mathbf{r}'|} + E_{xc}[n], \tag{5.27}$$

where the first term is the energy due to the attraction between the electronic density and the fixed nuclei, the second term is the kinetic energy of independent electrons, the third term is the mean field Hartree repulsion between electrons and the final term is a yet to be determined functional of the density that captures the effects of fermionic exchange properties and electron

correlations beyond the Hartree approximation. This final term is called the *exchange-correlation energy functional* and combines these two contributions in a single functional rather than separating them. This energy functional is explicitly constructed to reproduce single particle dynamics which can be seen by taking a functional derivative

$$\frac{\delta E}{\delta n} = 0. \tag{5.28}$$

The density $n(\mathbf{r})$ that satisfies this condition completely describes the ground state functional and all ground state properties can be calculated from it. The functional derivative leads to the following familiar equation of motion for the independent electron wavefunctions ϕ_i:

$$\left[-\frac{1}{2}\nabla_i^2 + V_N(\mathbf{r}) + V_{\mathrm{H}}(\mathbf{r}) + V_{xc}(\mathbf{r})\right]\phi_i(\mathbf{r_i}) = \epsilon_i\phi_i(\mathbf{r_i}), \tag{5.29}$$

where

$$V_N(\mathbf{r}) = -\sum_I \frac{Z_I}{|\mathbf{r}_i - \mathbf{R}_I|}, \tag{5.30}$$

$$V_{\mathrm{H}}(\mathbf{r}) = \int d\mathbf{r}' \frac{n(\mathbf{r}')}{|\mathbf{r} - \mathbf{r}'|}, \tag{5.31}$$

$$n(\mathbf{r}) = \sum_i |\phi_i(\mathbf{r})|^2, \tag{5.32}$$

$$V_{xc}(\mathbf{r}) = \frac{\delta E_{xc}[n]}{\delta n}. \tag{5.33}$$

These are the *Kohn-Sham equations* and provide the method for determining an approximation to the energy of a system, given the elements, positions and valencies of the nuclei. As these are the only parameters, Kohn-Sham DFT is unquestionably an *ab initio* (first principles) method and requires no empirical data to make useful predictions. Unfortunately, the Kohn-Sham scheme still makes explicit reference to the Kohn-Sham orbitals. The Hohenberg-Kohn theorems state that it is theoretically possible to construct the energy functional as an explicit function of the density only, doing away with the orbital dependence entirely. An orbital free DFT of this kind is much vaunted because of its superior scaling properties [171], and is currently attracting much attention from the world's pre-eminent solid state theorists [172].

As with Hartree-Fock, the Kohn-Sham equations must be solved self consistently but crucially, the inclusion of the exchange-correlation energy as a *local* function $E_{xc}(\mathbf{r})$ makes this self consistent calculation significantly quicker. The downside is clearly that the accuracy of the energy is now dependent on the suitability of the choice of E_{xc}.

In order to keep the simulation free from empirical parameters, the standard choice of free energy functional is to use the *local density approximation* (LDA) in determining the V_{xc} functional. For a system of interacting electrons, immersed in a constant positive charge density, it is possible to construct the exchange and correlation energies analytically [173], with both being explicit functions of the density. LDA then simply maps the exchange-correlation energies for this homogeneous electron gas to that of the real system based on the density of electrons at any point. This approach is useful as no parameters are needed but obviously, a homogeneous electron gas cannot be expected to be a perfectly accurate description of real crystal.

Therefore, we have completed the first step in the simulation of materials; we can calculate the energy of a system using the Kohn-Sham formulation of DFT under the LDA. The next step requires a procedure to move the nuclei into their lowest energy configuration and then analysing this state for the relevant irreps.

5.3 Density Functional Theory In Practice

The above section is rather abstract. What kind of computational methodologies are included in a software package like the Vienna Ab-Initio Software Package (VASP) that can be used to calculate energies?

5.3.1 Exchange-Correlation Potentials

LDA is a rudimentary approximation to real systems and to accurately model systems, more sophisticated methods must be utilised. Within LDA, the exchange and correlation energies are calculated only from the density n itself. Considerably more accurate results can be obtained if the gradient of the density is included as well. This forms the basis of the generalised gradient

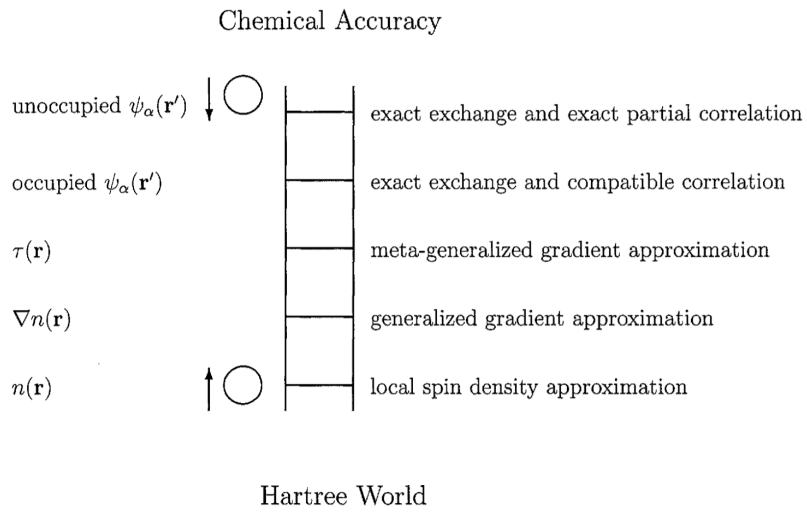

Figure 5.1: Jacob's Ladder Of exchange-correlation calculations in DFT. Each rung adds increased complexity and computational cost whilst producing more accurate predictions of material properties. Taken from [176].

approximation (GGA). Unlike LDA, GGA is not unique and there are thus many methods which incorporate density gradients in their exchange-correlation functionals and each are adapted to perform better in particular systems. A suitable choice of a GGA can produce more accurate results than LDA and so they are widely used. One such popular option was produced by Perdew, Burke and Ermenzhof (PBE) and revised for solids in an extension named PBEsol [174, 175].

There are further extensions to exchange-correlation functionals which are of note [176]. In meta-GGA functionals, the second derivative of the density is taken into account (in a kinetic energy term). This is more computationally taxing than GGA methods but can be suitable in some situations. In hybrid functionals, the exchange portion of the exchange-correlation functional is split between a contribution coming from GGA methods and another contribution in which exchange is explicitly calculated using non-local Hartree-Fock. This adds complexity to any calculation but is useful in producing more accurate bandstructures. Each step up a rung in Figure 5.1 adds additional computational cost but seeks to get closer to the holy grail of "chemical accuracy". Sensible choices of exchange correlation should thus be made to match the system being investigated.

5.3.2 Plane Wave Expansions and Monkhorst-Pack Grids

The electronic wavefunction in the periodic potential of crystal lattice is the key quantity in Kohn-Sham DFT. Solving the Kohn-Sham equations permits the determination of the electronic wavefunction and the electronic density can be trivially calculated from this. Eigenfunctions of Hamiltonians (such as Equation (5.17) if the nuclear attraction represents a periodic crystal) in periodic potentials are represented in terms of Bloch functions [79]:

$$\phi_{\mathbf{k}}(\mathbf{r}) = e^{i\mathbf{k}\cdot\mathbf{r}} u_{\mathbf{k}}(\mathbf{r}). \tag{5.34}$$

This describes the eigenfunction as being the product of a plane wave and a function $u_{\mathbf{k}}(\mathbf{r})$ with the periodicity of the potential. The wavefunction is now parameterised by the crystal momentum $\mathbf{k}$ of the electron. Various properties require a summation over all electrons in a crystal and this condition is now easily converted into a summation over all values of $\mathbf{k}$. Any function $\bar{f}$ which is calculated via averaging over electron states can now be written as

$$\bar{f} = \frac{1}{N_{\mathbf{k}}} \sum_{\mathbf{k}} f(\mathbf{k}) = \frac{V}{(2\pi)^3} \int_{\mathrm{BZ}} f(\mathbf{k}) d\mathbf{k} \tag{5.35}$$

where the second equality is obtained by converting the sum over discrete k points into an integral over infinitesimally close k points. The conversion of a sum to an integral is permissible if the size of the crystal under study is much larger than the dimensions of a single unit cell. In this regime, the k-points within the Brillioun Zone which must be integrated over form a continuum.

For real calculations, this is not practicable. To calculate a quantity such as Eq 5.35 on a computer requires a finite number of k points which provide a representative sample of the Brillioun Zone. This is most readily achieved via the application of a *Monkhorst-Pack grid* [164, 177] defined in three dimensions as

$$\mathbf{k} = \sum_{i}^{3} \frac{2n_i - N_i - 1}{2N_i} \mathbf{b}_i, \tag{5.36}$$

where the $\mathbf{b}_i$ are reciprocal lattice vectors, n_i ranges from 0 to N_i and the N_i is number of points that are selected along each reciprocal lattice vector to sample the Brillioun Zone. In fact, the

method can be made more efficient by not sampling the whole Brillioun Zone but instead only sampling the symmetry inequivalent points - the irreducible Brillioun zone. The rest of the zone can be reconstructed via the symmetry operations of the cell.

What about the function $u_{\mathbf{k}}(\mathbf{r})$? As this object is periodic with the crystal lattice, it can be expanded as a complete set of its Fourier components [77] so that

$$u_{\mathbf{k}}(\mathbf{r}) = \sum_{\mathbf{G}} c_{\mathbf{k},\mathbf{G}} e^{i\mathbf{G}\cdot\mathbf{r}}. \tag{5.37}$$

In order to have a completely accurate representation of the wavefunction, an infinite number of $\mathbf{G}$ vectors must be included but again, this is impracticable. Instead, the expansion is truncated. Rapidly fluctuating functions contain a greater number of Fourier modes and require a larger basis set to accurately model. Usually, the number of $\mathbf{G}$ vectors is parameterised by stating a *cutoff energy*, defined as $\frac{\hbar^2 G^2}{2m_e}$, with only vectors with a corresponding energy below this being admitted into the expansion.

The choice of Monkhorst-Pack k-grid and $\mathbf{G}$-vector basis set is thus up to the choice of the DFT user but rigourous testing should be done. The properties of a system may not be accurately modelled with a small Monkhorst-Pack grid or basis set and so *convergence testing* is critical to produce accurate results. A range of grids and basis sets should be tested and the properties of the simulated material recorded. If the properties do not change considerably when the k grid or basis set is adapted, then a good combination of k points and basis set have been chosen.

5.3.3 Pseudopotentials

The wavefunction of an electron bounded to an atom is analogous to that of an electron in a box. The wavefunction has an oscillatory behaviour which can have many nodes. This kind of rapidly oscillating function contains many harmonics and, following the discussion of the previous subsection, must be represented by a large plane wave basis set.

In contrast, the wavefunction in the free space between ions is quite well described by a small number of Bloch plane waves as they are distant from the potential of the ions. This leads quite naturally to the separation of electronic wavefunctions into two regimes :

$$\psi_{\boldsymbol{k}}(\boldsymbol{r}) = \begin{cases} e^{i\mathbf{k}\cdot\mathbf{r}} & \text{for} \quad |\mathbf{r}| > R_0. \\ \text{Atomic Orbital} & \text{for} \quad |\mathbf{r}| < R_0, \end{cases} \tag{5.38}$$

where R_0 is the measure of the atomic radius. This is the augmented plane wave method [79] and separates the complicated behaviour of an electron near an ion from the more placid and calm plane waves that lie in between.

The wavefunction for the atomic orbital region still requires a large basis set to model accurately but this difficulty is relieved via the use of pseudopotentials [164, 178]. These alter the form of the ionic potential to take a less pathological form. This is often achieved by placing electrons of lower quantum number n into the core, screening the ionic potential and refocusing the dynamics on high n electrons. This is often justified for tightly bound electrons but care must be taken as higher orbitals are considered.

5.3.4 Hellman-Feynman Forces and Phonons

Now that we have the energy of a system with a particular arrangement of ions, it is necessary to see how changes in the positions of ions effect the energy of the system as a whole. When this is done, it should be possible to find the state of the system which minimises the energy.

This is easily done by finding the forces on ions. Any force on a ion will cause it to move to a state of lower energy (just like a ball rolling down the hill) and so a minimum is reached whenever all ionic forces are zero. The calculation of forces is simple. Force is defined as the negative gradient of the energy so that

$$\begin{aligned} \mathbf{F}_I &= -\frac{\partial E}{\partial \mathbf{R}_I} = -\frac{\partial}{\partial \mathbf{R}_I}\langle\Psi|\hat{H}|\Psi\rangle \\ &= -\langle\frac{\partial\Psi}{\partial \mathbf{R}_I}|\hat{H}|\Psi\rangle - \langle\Psi|\frac{\partial\hat{H}}{\partial \mathbf{R}_I}|\Psi\rangle - \langle\Psi|\hat{H}|\frac{\partial\Psi}{\partial \mathbf{R}_I}\rangle \\ &= -\langle\Psi|\frac{\partial\hat{H}}{\partial \mathbf{R}_I}|\Psi\rangle - E\langle\frac{\partial\Psi}{\partial \mathbf{R}_I}|\Psi\rangle - E\langle\Psi|\frac{\partial\Psi}{\partial \mathbf{R}_I}\rangle \\ &= -\langle\Psi|\frac{\partial\hat{H}}{\partial \mathbf{R}_I}|\Psi\rangle - E\frac{\partial}{\partial \mathbf{R}_I}\langle\Psi|\Psi\rangle \\ &= -\langle\Psi|\frac{\partial\hat{H}}{\partial \mathbf{R}_I}|\Psi\rangle . \end{aligned} \tag{5.39}$$

This result is the *Hellman-Feynman theorem* [179] and could be considered as an example of Ehrenfest's theorem [180] - that operator expectation values obey classical laws. If the Hamiltonian (5.19) includes the rewriting of the electron-nuclei term as (5.21) and reinserts the nuclear-nuclear Coulomb repulsion, then the only terms that depends explicitly on the atomic positions $\mathbf{R}_I$ are those that include V_N and the reinstated nuclear repulsion term so that

$$\mathbf{F}_I = Z_I \left[\int d\mathbf{r} n(\mathbf{r}) \frac{\mathbf{r} - \mathbf{R}_I}{|\mathbf{r} - \mathbf{R}_I|^3} - \sum_{J \neq I} Z_J \frac{\mathbf{R}_J - \mathbf{R}_I}{|\mathbf{R}_J - \mathbf{R}_I|^3} \right]. \tag{5.40}$$

Miraculously, the term in square brackets is simply the classical electrostatic field produced by the electron density and all other nuclear charges.

Therefore, after the Kohn-Sham equations have been solved self-consistently for a particular configuration of atoms, that calculated density can then be used immediately to calculate the forces on all the ions. The system can then be evolved under influence of these forces until it reaches a situation in which all the atomic forces vanish. There are multiple methods for doing this with varying efficiencies but, however the system is evolved, all methods find a minimum [164]. Each minimisation algorithm aims to find the *global* minimum.

Notice that the above equation is only valid as it was assumed that the Kohn-Sham wavefunctions do not depend on the atomic positions. This is true whenever plane waves are being used to represent the wavefunctions. If instead, the wavefunctions were constructed via a linear combination of atomic orbitals, the wavefunctions would have a dependence on the nuclear positions and there would be an additional contribution to the forces, known as *Pulay forces* [165], which makes the calculation of forces slightly more involved.

It is usually useful to restrict relaxations to retain the symmetry of the material under investigation. In that situation, the algorithm only allows for displacements that do not break any space group symmetries.

This is the basis of structural relaxation in atomistic simulations using DFT. The energies of a particular configuration are calculated via a self-consistent solution to the Kohn-Sham equations and the electron density is calculated. The density permits a calculation of the force on all ions which can then be evolved to a new position, the Kohn-Sham equations solved again

and the new density used to calculated the new forces. This procedure is continued until all forces and stresses vanish.

Occasionally, it is necessary to relax a system in such a way that stresses along certain directions are not changed. This results in certain lattice vectors retaining their lengths throughout. This situation is very useful for simulating a material constrained to grow on an epitaxial substrate of fixed lattice constant. Relaxations of this type are used in Chapter 6.

Once the Hellmann-Feynman forces on all the ions are determined, it is possible to obtain the force constant matrix. Finding the eigenvalues and eigenvectors of this matrix leads to the allowed phonon frequencies and modes. As stated in Chapter 2, imaginary phonon frequencies denote soft modes and suggest structural instabilities.

5.3.5 Spin DFT And Non-Collinear Magnetism

Introducing collinear magnetism is straightforward in any DFT code. The density is simply split into spin-dependent parts so that

$$n_\sigma(\boldsymbol{r}) = \sum_i^N |\phi_{\sigma i}(\boldsymbol{r})|^2 \tag{5.41}$$

I've shown in Chapter 2 that magnetic interactions find their origin in exchange interactions so that the exchange-correlation energy also picks up a spin dependence *.

$$V_\sigma^{xc}(\boldsymbol{r}) = \frac{\delta E_{xc}[n_\uparrow, n_\downarrow]}{\delta n_\sigma} \tag{5.42}$$

and so the non-interacting equations take the form

$$\left[-\frac{1}{2}\nabla_i^2 + V_{\mathrm{N}}(\mathbf{r}) + V_{\mathrm{H}}(\mathbf{r}) + V_\uparrow^{xc}(\mathbf{r})\right]\phi_{\uparrow i}(\mathbf{r_i}) = \epsilon_i\phi_{\uparrow i}(\mathbf{r_i}), \tag{5.43}$$

$$\left[-\frac{1}{2}\nabla_i^2 + V_{\mathrm{N}}(\mathbf{r}) + V_{\mathrm{H}}(\mathbf{r}) + V_\downarrow^{xc}(\mathbf{r})\right]\phi_{\downarrow i}(\mathbf{r_i}) = \epsilon_i\phi_{\downarrow i}(\mathbf{r_i}), \tag{5.44}$$

*Obviously the kinetic energy, attraction due to nuclei, repulsion from other electrons depends only on the mass and charge of the electron and not the spin.

The introduction of spins is almost as if there are two different species of electrons in the system. However, they do interact indirectly because of the dependence of the exchange-correlation energy on the density of both.

To allow for non-collinear interactions, Kohn-Sham DFT is extended to incorporate the full spinor nature of the electron. The density becomes a matrix

$$n_{\sigma'\sigma} = \sum_{i}^{N} \phi_{\sigma' i}(\boldsymbol{r})\phi_{\sigma i}(\boldsymbol{r}), \tag{5.45}$$

as does the potential

$$V^{\text{eff}}_{\sigma'\sigma} = V^{\text{ext}}_{\sigma'\sigma}(\mathbf{r}) + \delta_{\sigma'\sigma}V_H(\mathbf{r}) + V^{xc}_{\sigma'\sigma}(\mathbf{r}) \tag{5.46}$$

The term V_{N} has been generalised to allow for external fields too. This could represent the the interaction between the electrons spin and the field produced as it orbit around the atom - the spin-orbit coupling. The final Kohn-Sham equations become

$$\sum_{\sigma} \left[-\frac{1}{2}\delta_{\sigma'\sigma}\nabla_i^2 + V^{\text{eff}}_{\sigma'\sigma} \right] \phi_{\sigma i} = \epsilon_{\sigma' i}\phi_{\sigma' i}. \tag{5.47}$$

The equations are now coupled because of off-diagonal elements in potential. This and the fact that everything must be manipulated as matrices, makes non-collinear equations much more costly to solve.

5.3.6 Correlation Effects, Hubbard Model and DFT+U

The magnetism present in multiferroic materials arises from unpaired electrons in strongly localised d or f orbitals. It is often the case with these materials that a naive application of band theory, which does not properly take electron interactions into account, would predict these materials to be metals whereas the strong Coulomb repulsion between electrons in these strongly correlated orbitals prevents them from becomes delocalised - a necessity for metallicity. These materials are termed *Mott insulators* [26, 181] and the strongly correlated electrons are said to be experiencing *Mott localisation*. Often, LDA approximations would not pick up on this

subtlety*. Extensions such as meta-GGAs or hybrid functionals would fare better but they are computationally expensive. A much cheaper, though less rigourous, method would be to add this Coulomb repulsion as an additional contribution to the energy and this is exactly what is done in DFT+U methods [184, 185].

DFT+U is based upon the Hubbard model of field theory, in which there is an energy cost U to doubly occupy electrons on the same site. In the DFT+U formulation, this energy penalty is incorporated through

$$\begin{aligned} E_{\mathrm{DFT}+U} = E_{\mathrm{DFT}} + \frac{1}{2} \sum_{i,m,m',\sigma} U(n_{im\sigma} - n_0)(n_{im'-\sigma} - n_0) \\ + \frac{1}{2} \sum_{i,m\neq m',\sigma} (U-J)(n_{im\sigma} - n_0)(n_{im'\sigma} - n_0). \end{aligned} \tag{5.48}$$

This equation is easy to interpret. It simply states that there is an energy cost to have two electrons on the same site i. The occupancy of an electron at site i, with angular momentum m and spin σ is $n_{im\sigma}$ and the average occupancy of that orbital is n_0. If the occupancy of the orbital varies at all from n^0, this Hubbard term penalizes that state. The first correction deals with electrons with opposite spins and the second involves those with parallel spins (which is why $m \neq m'$ in the sum or Pauli's exclusion principle would be violated). The parallel spin term has a weaker correction $U - J$ because Hund's rules prefer aligned spins - a result of exchange symmetry. These terms penalise fractional occupancy and so are therefore also effectively penalising the metallic state. This leads to the opening of band gaps.

Importantly, the expression relies on the occupancy of *localised* orbitals. This can be computed from the delocalised Kohn-Sham orbitals $\phi_{\mathbf{k}v\sigma}$ with wavevector $\mathbf{k}$ and band index v, by projection onto a localised orbital Φ_{im} on site i and with orbital momentum m, so that

$$n_{im\sigma} = \sum_{k,v} f_{kv\sigma} \langle \phi_{\mathbf{k}v\sigma} | \Phi_{im} \rangle \langle \Phi_{im} | \phi_{\mathbf{k}v\sigma} \rangle \tag{5.49}$$

*There is debate in the literature into the role of symmetry in opening up band-gaps. Allowing for more symmetry breaking by simulating a larger cell may open up band gaps and turn a material that is predicted to be a metal in a small cell into an insulator [182]. Nevertheless, this cannot be the whole truth as it is a fact that higher levels of theory also provide gapping mechanisms without symmetry breaking.[183]

where f is the Fermi-Dirac function. These localised orbitals could be either atomic orbitals or Wannier functions. A localised orbital description is also essential in the proper formulation of the theory of polarisation, which I discuss next.

5.3.7 The Modern Theory Of Polarisation

If we are to study the polarisation of ferroelectrics, we need some manner in which to calculate that polarisation. The simplistic model of polarisation as a sum of dipoles within a unit cell seems fundamentally flawed because the value for the polarisation depends on that specific choice of unit cell. Taking various sized cells [54] leads to different values of the polarisation but interestingly, the different values are always separated by integer multiples of the polarisation quantum

$$P_i^0 = \frac{e}{V} a_i \tag{5.50}$$

for a calculation of the polarisation along the ith direction. a_i is the length of the ith lattice vector. There are other methods to calculate the polarisation [56] such as using a charge current $\boldsymbol{J}(\lambda)$ with some parameter λ, to add charge to a region and changing the polarisation by

$$\Delta \boldsymbol{P} = \int_{t_i}^{t_f} \boldsymbol{J}(\lambda) d\lambda. \tag{5.51}$$

This would suggest that a cyclic process would result in $\Delta \boldsymbol{P} = \oint \boldsymbol{J}(\lambda) d\lambda = 0$. However, when this calculation is done by changing the parameter λ adiabatically, the cycle results in a change in polarisation by a quantum. Stated simply, polarisation is only defined in a bulk material modulo a quantum. An easy extension to this idea is the concept of a polarisation lattice which are all the values of polarisation that can be connected to any other via adding or subtracting integer multiples of a quantum.

This leads to interesting results when trying to calculate the polarisation of perovskite materials. For the five-atom cubic phase of perovskites, the polarisation along any direction can

be calculated by summing up charges. Take $K^{1+}Nb^{5+}O_3^{2-}$ and calculate the polarisation along any direction (I use z), when the A-site is at the origin via

$$P_z = \frac{e}{V}\sum_i Z_i z = \frac{e}{V}\left[(+1)(0) + (+5)(\frac{a}{2}) + (-2)(\frac{a}{2}) + (-2)(\frac{a}{2}) + (-2)(0)\right] = \frac{e}{V}\frac{a}{2} \tag{5.52}$$

which should really be written as $\frac{ea}{V}(\frac{1}{2} + n)$ where n denotes any number of polarisation quanta. This centrosymmetric perovskite has infinitely many values of polarisation, and none of them are zero! If we had studied $Ba^{2+}Ti^{4+}O_3^{2-}$ instead, I would have got a polarisation lattice centered on 0.

Importantly, the polarisation lattice in either case is symmetric about 0. This is generic for all centrosymmetric materials and highlights the fact that the polarisation in a bulk material is only defined up to a quantum.

What is well defined are *changes* in polarisation, provided that we focus on the same point in the polarisation lattice. Adding a ferrodistortive mode to $BaTiO_3$ would shift all points of the polarisation lattice away from their original position, so that the lattice is no longer symmetric about the origin and tracking the change of any one point from its original position leads to a well defined value for the change in polarisation. Remaining on the correct branch of the polarisation lattice is vital, and care was taken to do this in Chapters 6 and 7.

How do we calculate polarisation of the density in an ab-initio, quantum mechanical simulation? As polarisation is described as the motion of localised charges, it is helpful to move away from the delocalised Bloch function description of electrons $\phi_{i\boldsymbol{k}}(\boldsymbol{r}_i) = u_{i\boldsymbol{k}}e^{i\boldsymbol{k}\cdot\boldsymbol{r}}$ and transform to localised Wannier functions

$$w_i(\boldsymbol{r} - \boldsymbol{R}) = \frac{V}{(2\pi)^3}\int_{BZ} d^3\boldsymbol{k} e^{i\boldsymbol{k}\cdot(\boldsymbol{r}-\boldsymbol{R})}u_{i\boldsymbol{k}} \tag{5.53}$$

which is localised about $\boldsymbol{R}$. We can then work out the average position of electrons described by a Wannier function

$$\bar{\boldsymbol{r}}_i = \int w_i^* \boldsymbol{r} w_i d^3\boldsymbol{r} \tag{5.54}$$

which, by substituting the definition of the Wannier functions and remembering that the position operator can be written as a momentum derivative $\boldsymbol{r} = -i\frac{\partial}{\partial \boldsymbol{k}}$

$$\bar{\boldsymbol{r}}_i = i\frac{V}{(2\pi)^3}\int_{BZ} d^3\boldsymbol{k} e^{-i\boldsymbol{k}\cdot\boldsymbol{R}} \langle u_{i\boldsymbol{k}}|\frac{\partial u_{i\boldsymbol{k}}}{\partial \boldsymbol{k}}\rangle \,. \tag{5.55}$$

The electronic contribution to the polarisation is then given by

$$\boldsymbol{P}_{\text{elec}} = \frac{1}{V}\sum_i^{\text{occ}} q_i \bar{\boldsymbol{r}}_i = -\frac{2ie}{(2\pi)^3}\int_{BZ} d^3\boldsymbol{k} e^{-i\boldsymbol{k}\cdot\boldsymbol{R}} \langle u_{i\boldsymbol{k}}|\frac{\partial u_{i\boldsymbol{k}}}{\partial \boldsymbol{k}}\rangle \,. \tag{5.56}$$

because each filled level holds two electrons of charge $-2e$. This description of electronic polarisation in this manner is an example of a Berry (or geometric) phase - these occur whenever a quantum system is moved in a closed loop through in phase space. The Aharanov-Bohm effect, where an electron can be affected by electromagnetic field even if the electron is in a region where the field is zero, is another prominent phenomena described by Berry Phases. Berry phases are described in more detail in Reference [56]. One point worth mentioning is the non-uniqueness of Wannier functions. Bloch functions can always be multiplied by a k-dependent phase factor $e^{-i\beta(\mathbf{k})}$. Obviously this *gauge freedom* will be reflected in the Wannier functions that are constructed from the Bloch functions but importantly, Equation 5.56 is *gauge* invariant* - the value of polarisation does not depend on the choice of gauge.

To actually perform the calculation in a density functional theory code, the electronic structure is solved to obtain the Bloch functions. Equation 5.56 can then be used. The integral over the Brillioun zone is performed by sampling the zone using a Monkhorst-Pack grid. The Berry phase expression (Equation 5.56) contains gradients, and these are obtained by calculating the $\langle u_{i\boldsymbol{k}}|\frac{\partial u_{i\boldsymbol{k}}}{\partial \boldsymbol{k}}\rangle$ along strings of k points, obtaining more points in the strings by moving the sampling slice up and down until the full zone is reasonably covered with points. This would calculate the polarisation along the direction of the strings.

*A nice proof is given in Reference [56]

Chapter 6

Single Perovskites

6.1 Introduction

Chapter 4 revealed that the common symmetries of single perovskites with an ABO_3 chemical formula are not good candidates to explore the particular kind of magnetoelectricity that enables the electric field controlled reversal of magnetisation. This was because there were too few degrees of freedom to play with and there was not an easy way to introduce ferroelectric distortion that were strongly coupled to other primary modes in the material.

All is not lost as the current chapter reveals an alternative, and highly unexpected, form of magnetoelectricity in which certain highly distorted forms of ABO_3 perovskites with $a^-a^-c^+$ tilts can undergo electric-field induced phase transitions to convert a paraelectric antiferromagnetic into a ferroelectric ferromagnet.

I shall explain how this highly non-linear form of magnetoelectricity is a direct result of the couplings between distortions, but to fully understand the physics, it is necessary to consider even-order terms rather than the odd order terms I have been focusing on until now.

6.2 Computational Details

All simulations in this chapter are performed using density functional theory (DFT) as implemented in the Vienna Ab-Initio Software Package (VASP) Version 6.3.2 [186, 187, 188, 189].

I use the Perdew-Burke-Ernzerhof exchange correlation functional for solids (PBESol)[175]. I used a high plane wave cutoff energy of 800 eV to ensure convergence for all systems studied as well as a 7x5x7 Monkhorst-Pack k-grid for the $\sqrt{2}\times2\times\sqrt{2}$ 20-atom supercell. Self consistent field calculations were continued until differences in energies were within a tolerance of 10^{-8} eV. Geometry relaxations were continued until the smallest Hellman-Feynman force was less than 10^{-3} eV/Å. I used projector augmented wave pseudopotentials in all our calculations. To better approximate the effect of electron localization and correlation, we use the rotationally invariant formulation of the onsite Hubbard-U parameter [190]. I used a consistent value of $U = 4$ eV for all materials with unpaired d electrons and $U = 0$ eV for those without. This is also the methodology employed in previous computational screening studies [191]. As will be demonstrated later, the results are not qualitatively affected by the choice of U.

6.3 $Pna2_1$ Symmetry Through Strain

I explored the dynamical stability of $ScCrO_3$ which is observed to have, when synthesised under high pressure, a $Pnma$ symmetry with a C-type magnetic structure [192, 193]. C-type magnetism is unusual in perovskites [194, 195] but, as established in Chapter 4, does not allow for the electric field control of magnetism for any direction of polar distortion. Motivated largely by academic curiosity over potential applicability to multiferroic memories, I explored whether an applied strain would be able to induce a polar distortion and result in a multiferroic with C-type magnetism.

As discussed in Chapter 2, epitaxial strain strongly couples to the zone-centered optical phonons, softening them and eventually causing transitions to polar structures. A tensile epitaxial strain preferentially softens the in-plane polar phonon while compressive strain softens the out-of-plane polar phonon. Typically, the polar distortion emerges in the direction that is increased by strain.

This viewpoint is widespread in the literature [90] and so, when simulating the application of *tensile* epitaxial strain to C-type $Pnma$ $ScCrO_3$, I expected to see the softening (and hopefully freezing) of a phonon producing an in-plane polarisation and resulting in a $Pmc2_1$ or $Pmn2_1$

space group. To begin, I fully relaxed a $Pnma$ symmetry $ScCrO_3$ and averaged the two short lattice vectors to produce the in-plane lattice vectors $\bar{a} = \frac{a+b}{2}$. The epitaxial strain η is then defined as

$$\eta = \frac{a_{IP} - \bar{a}}{\bar{a}}, \tag{6.1}$$

so that I am simulating the growth on a cubic substrate with a variable lattice parameter a_{IP}. This calculation is performed using VASP with the IOPTCELL [196] patch installed to constrain the in-plane lattice vectors during relaxation.

As shown in Figure 6.1, we observe the condensation of a phonon with a B_{2u}* irrep. Including this frozen phonon in the structure results in a $Pna2_1$ symmetry which has a polarisation *out-of-plane*. Somehow, a tensile epitaxial strain appears to lead to a out-of-plane polarisation. This is in sharp distinction to the existing literature.

Figure 6.1 also contains further mysteries. Firstly, the C-type phonon frequency softens with increasing tensile strain but then, beyond about 4%, suddenly reversing direction and begins hardening again. To the best of my knowledge, this kind of behaviour has never been observed in the literature. Furthermore, switching the magnetic structure to ferromagnetic, approximately doubles the softening of the polar phonon and hints towards very strong spin-phonon coupling present in the material.

To verify this effect, we performed further first-principles calculations using VASP in which we relaxed both the $Pnma$ and $Pna2_1$ symmetries for each strain and plotted the resulting final energies. The result for this computational experiment is presented in Figure 6.2. We also see a prominent dip the $Pna2_1$ energy so that this phase becomes favoured in the same range of tensile strains that the polar phonons are frozen. The two sets of calculations both point to the same conclusion - tensile strain seems to favour an out-of-plane polarisation but strangely only within a small strain window.

*This is an alternative way to label irreps which is preferred in the Raman spectroscopy community. The software package used to perform this phonon frequency calculation - *phonopy* - adopts it. It simply describes a zone-centered phonon with odd parity - the subscript u is short for the German *ungerade* meaning odd or uneven. It is equivalent to Γ_4^- with an $(0, 0, a)$ OPD.

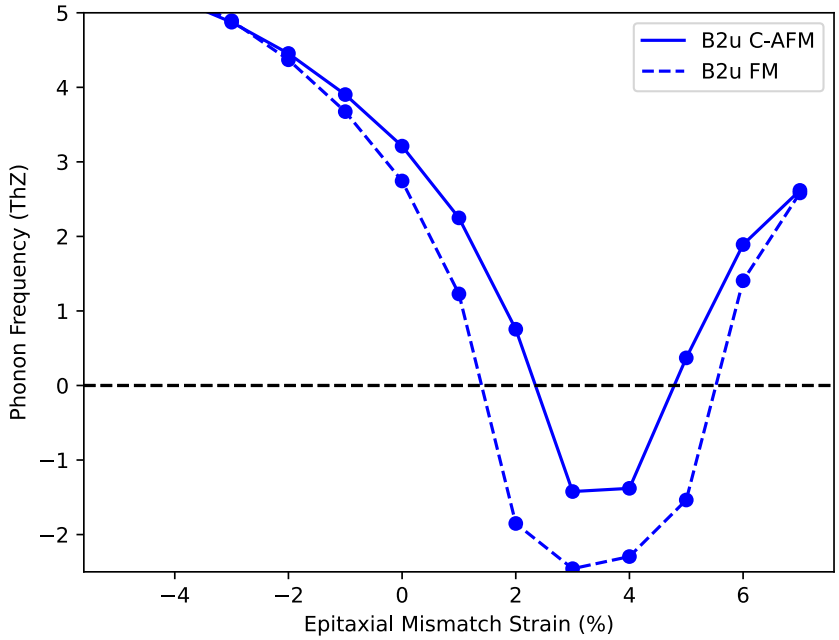

Figure 6.1: Γ point phonon frequencies of the *Pnma* phase as a function of tensile strain. A negative frequency is actually denoting an imaginary, soft phonon mode. The B_{2u} phonon is polar. Changing the experimentally observed *C*-type magnetic structure to FM softens this phonon further.

6.4 The Origins Of The $Pna2_1$ Symmetry

Captivated by this completely unexpected and exciting result, I began to think about what could be causing this physics. It seemed reasonable to assume that the unusually low tolerance factor $t = 0.754$ (which was the reason why high pressures had to be used to synthesise the material[192, 193]) could be the cause and so we repeated the energy calculation* for a range of materials with similar tolerance factors. The resulting energy plots are shown in Figure 6.3.

Some of these materials have been synthesised in the *Pnma* symmetry [192, 197, 198] and others are purely hypothetical. I selected the materials in Figure 6.3 because they effectively span a large range of the periodic table and include different combinations of *p*, *d* and *f* block elements. Many choices possess magnetic cations which are known to prohibit the second order Jahn-

*We only performed the energy calculation because it much cheaper computationally. As seen from the $ScCrO_3$ example, it is expected that the phonon plots would corroborate the findings.

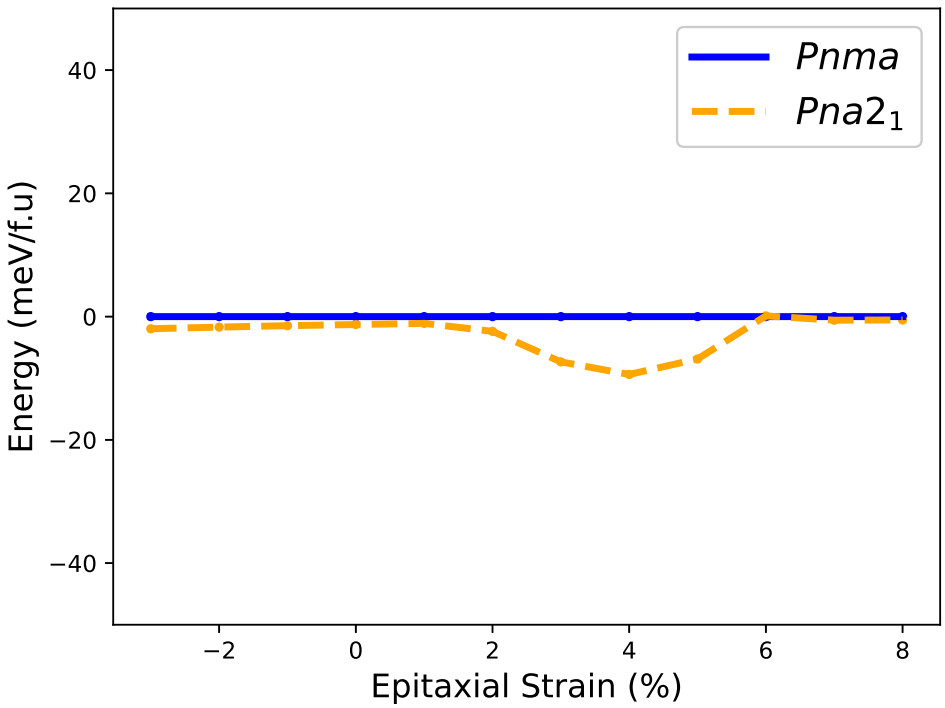

Figure 6.2: Energies of the $Pna2_1$ phase (dashed orange) and the $Pnma$ structure (solid blue) of $ScCrO_3$ when subject to epitaxial strain. The $Pna2_1$ symmetry with an out-of-plane polarisation is lower in energy between 2% and 6% - a rare prediction of out-of-plane polarisation with tensile strain.

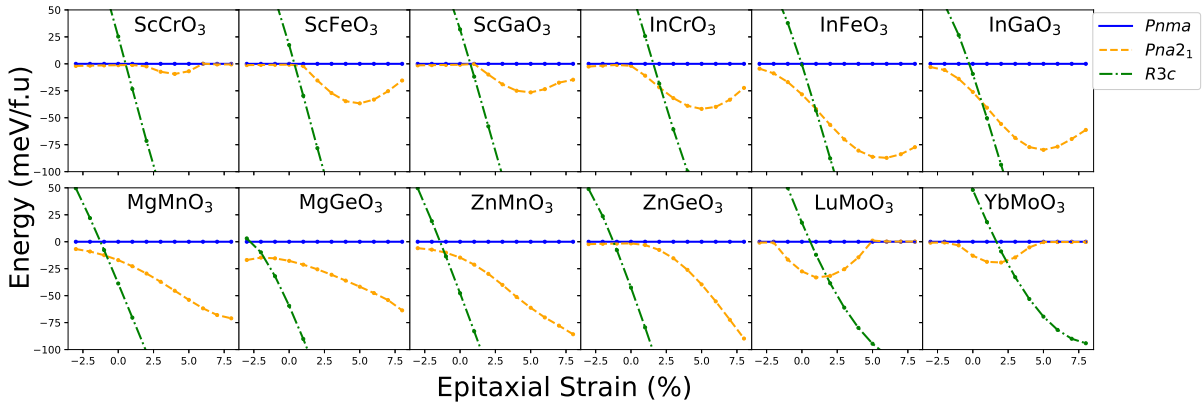

Figure 6.3: Energies of the $Pnma$,$Pna2_1$ and $R3c$ symmetries of various ABO_3 materials. In all cases, I observe that $Pna2_1$ is always stabilised over $Pnma$, at least for some strain range.

Teller mechanism. Others contain magnetic rare-earth elements. Irrespective of the chemical composition, we always observe that the $Pna2_1$ phase (orange plot) is favoured in a range of strains; in the top row and the rare-earths, the difference between $Pna2_1$ and $Pnma$ is maximised and some particular strain whereas for Mg and Zn materials the energy difference continues to increase.

Importantly, Fujita *et al* [198] demonstrated that $InFeO_3$ can also be stabilized in a rhombohedral $R3c$ symmetry. This symmetry was also included in the energy plots of Figure 6.3 and are represented by green dashed-dotted lines. We see that for most of these materials, it is actually the $R3c$ phase which is thermodynamically stable for most strains*. There are some notable exceptions to this. $InCrO_3$ and $InFeO_3$, which have been observed in $Pnma$ and $R3c$ symmetries respectively have a region of strain where $Pna2_1$ might be observable. Similarly, $MgMnO_3$ also has a region but in the compressive regime. These materials seem the most promising because of their common chemical compositions and potentially high magnetic transition temperatures due to presence of $3d$ elements.

Figure 6.3 poses three essential questions. Firstly, what is driving the condensation of the out-of-plane polarisation? Secondly, why is it that for some materials there is a maximum energy difference between $Pnma$ and $Pna2_1$ and why not for other materials? Finally, what are the consequences of this polar instability and does it have any technological applications?

I begin by addressing the second question : why is it that for some materials that there is a maximum energy difference between $Pnma$ and $Pna2_1$? To begin to address this, I compared the relative sizes of the distortions present in $Pnma$ $InCrO_3$ and investigated how they are changed with epitaxial strain. This was done using ISODISTORT [128] and the results are compiled in the top panel of Figure 6.4.

Understandably, the two tilt distortions forming the $a^-a^-c^+$ tilt pattern R_5^- and M_2^+ are the largest. These modes change in opposite fashion with increasing tensile strain, so that the product of the two stays approximately constant. X_5^- is also large because of the hybrid

*Although I stated that the $InFeO_3$ is observed to have $R3c$ symmetry, Figure 6.3 shows that at 0% strain, it is the $Pna2_1$ phase which is lowest in energy. This is because the strains are being defined with respect to the $Pnma$ lattice vectors. If instead, the strain was defined with respect to the larger $R3c$ lattice vectors, all the x-axes would be shifted to the right.

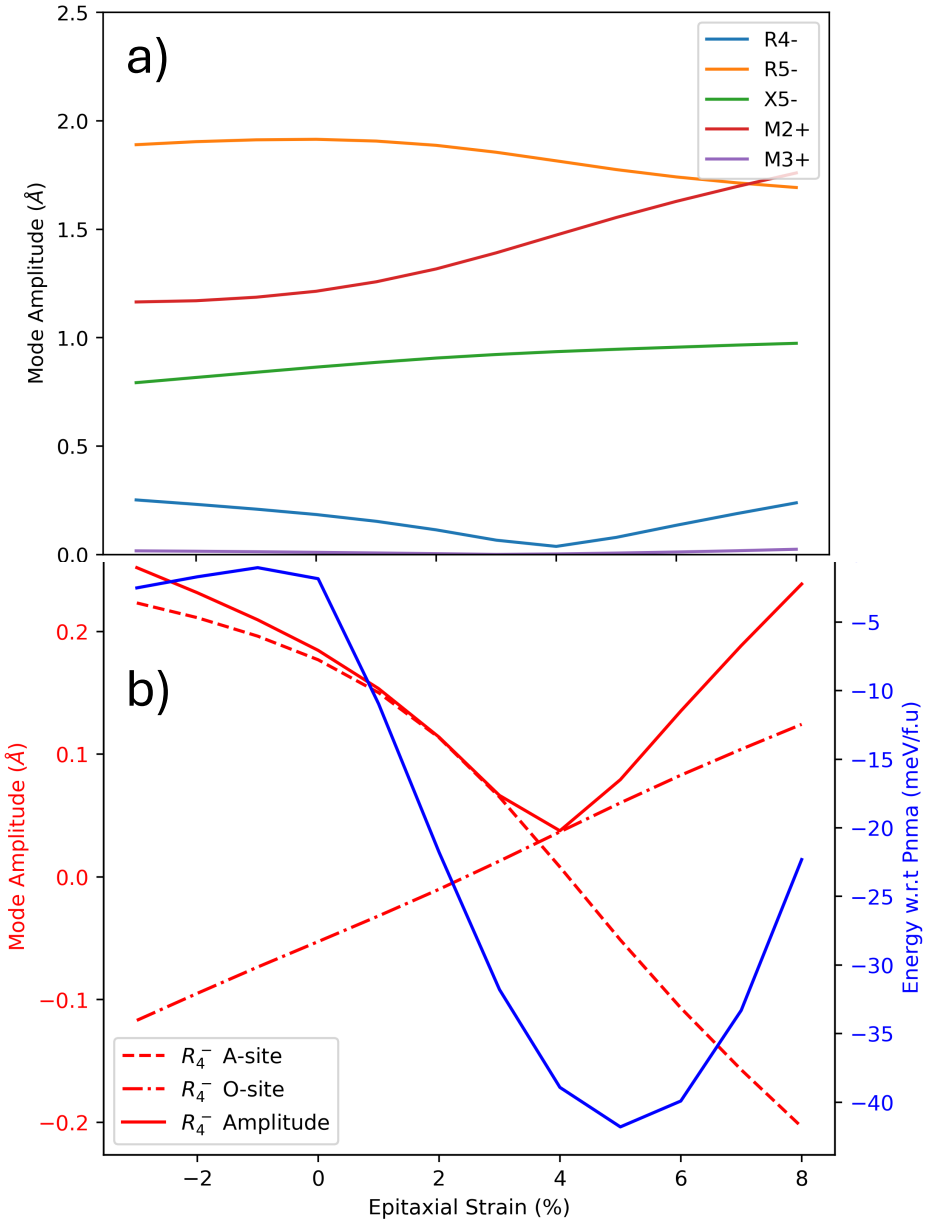

Figure 6.4: Variation of modes with strain in $InCrO_3$. a) Variation of all averaged *Pnma* modes with epitaxial strain. The averaging is performed by taking the root-mean-square displacement of all atoms moved by each order parameter The R_4^- mode shows a prominent minimum. b) the R_4^- mode minimum is due to the decomposition of the mode into a component that affects only the *A*-site and one that affects only the O site. These behave oppositely under strain, resulting in a minimum.

improper mechanism $Q_{X_5^-}Q_{M_2^+}Q_{R_5^-}$ coupling this mode to the two tilts. The symmetry allowed Jahn-Teller mode M_3^+ is negligibly small. The remaining R_4^- mode, is an antipolar motion affecting both the *A*-site and the *O*-site, shows a distinctive dip in amplitude at around 4%, which is the same strain at which the energy also has its minimum. Why should the R_4^- mode have a minima? The lower panel of Figure 6.4 reveals that the two components of this distortion behave oppositely under applied tensile strain and each pass through zero. When combining the two modes into a total amplitude, this results in a minimum. I have overlayed the energy of the $Pna2_1$ phase in blue on top of the R_4^- mode amplitude to show the alignment of the two minima.

This alignment of minima is too tantalising to be cheaply dismissed as a coincidence, so I investigated further by studying the strain effects on the modes of the other materials included in Figure 6.3. This is presented in Figure 6.5.

This fascinating result is plainly indicating that the strain-induced decrease of the R_4^- mode is central to the stabilisation of the $Pna2_1$ phase. The minimum of the $Pna2_1$ energies in $ScCrO_3$, $ScFeO_3$, $ScGaO_3$, $InCrO_3$, $InCrO_3$,$InGaO_3$, $LuMoO_3$ and $YbMoO_3$ overlap well with the minima of the R_4^- distortion which lends credence to the idea that the R_4^- mode is controlling the energy of the $Pna2_1$ phase. However, this hypothesis does not explain the behaviour of $MgMnO_3$, $MgGeO_3$, $ZnMnO_3$ and $ZnGeO_3$. In these materials, R_4^- still possesses a minimum but the energy appears to be smoothly decreasing with tensile strain. Inspecting Figure 6.5 offers some clues which address this discrepancy. The highest R_4^- amplitude reached for the Zn and Mg series is approximately 0.2 Å whereas the other materials obtain values of 0.3 Å or higher. The size of the R_4^- reflects the relative tolerance factors of these materials. $LuMoO_3$ has the smallest with $t = 0.766$ and, as a t far from 1 indicates a propensity for distortion, has a correspondingly large R_4^- amplitude whereas $ZnGeO_3$ has the largest tolerance factor $t = 0.786$ and the smallest R_4^- mode amplitude.

A large R_4^- mode therefore clearly suppresses an out-of-plane polarisation and the gradual decrease in R_4^- with strain lessens this effect so that the polar phase can break through. In the Mg and Zn series, the suppressing influence of smaller R_4^- is never large enough so that the $Pna2_1$ phase is always preferred over the centrosymmetric *Pnma*.

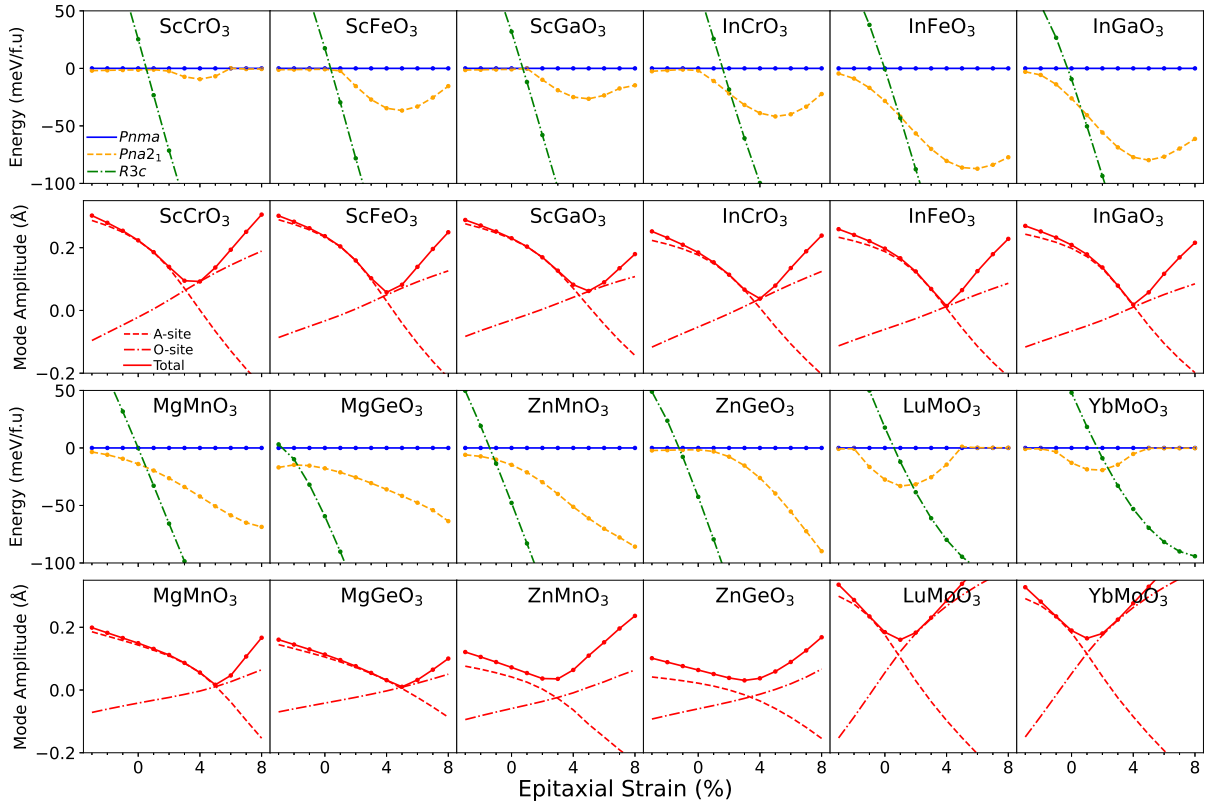

Figure 6.5: First and third rows: Energies of the $Pnma$,$Pna2_1$ and $R3c$ symmetries of various ABO_3 materials. In all cases, I observe that $Pna2_1$ is always stabilised over $Pnma$, at least for some strain range. Second and fourth rows: amplitude of the antipolar motions on the A and O site described by the R_4^- irrep. The minima in R_4^- typically aligns withe the $Pna2_1$ energy minima.

The suppression of polarisation by R_4^- has in fact already been noted in the literature. Referred to in Chapter 2, "Why are there so few ferroelectric perovskites" by Benedek and Fennie [87] explored the suppressive effect that the tilts M_2^+ and R_5^- have on the polar distortion. Large tilts in $Pnma$ lead to hard polar phonon frequencies. Similarly, they found that the antipolar motion of the A-site (X_5^-) also hardened the polar phonon. They suggested searching for ferroelectricity in perovskites with a tilt pattern that does not allow for this secondary motion of cations brought about by a hybrid improper mechanism. In fact, they suggested that $R3c$ materials with an $a^-a^-a^-$ tilt pattern would be one such symmetry. This is one reason why the non-centrosymmetric $R3c$ is one of the only polar space groups available to low tolerance factor perovskites - it is only the tilts that are suppressing the polarisation and not the A-site motion.

Benedek and Fennie also mentioned that the R_4^- also strongly hardens any polar phonons

but, because the mode tends to be small, is perhaps less significant when compared to the tilts and the A-site motions. What my work has demonstrated is that the R_4^- mode is indeed very important because it behaves so uniquely under strain. In effect, my work has extended Benedek and Fennie's to lower tolerance factor perovskites where the R_4^- mode is larger in amplitude.

The suppression of one mode by another is best captured by including biquadratic terms like those in Chapter 2 in the Landau expansion

$$\Delta E_{\text{biquadratic}} = \sum_i a_{i,\Gamma_4^-} Q_i^2 Q_{\Gamma_4^-}^2, \tag{6.2}$$

which changes the energy of the system by $\Delta E_{\text{biquadratic}}$ and the index i cycles over all the $Pnma$ modes (R_5^-, M_2^+, X_5^-, R_4^-, M_3^+). Benedek and Fennie showed that the coefficients a_{i,Γ_4^-} coupling each of these modes to the polar mode are strongly positive. This means that the energy of the system can be lowered if the polarisation is reduced to zero. The sum of all these terms are in competition with other terms which favour a non-zero polarisation and the balance of power in that competition can be adjusted by applying strain to weaken R_4^- - the polarisation-favouring terms begin to dominate and a $Pna2_1$ phase results. Clearly these low-tolerance factor, orthorhombic perovskites are extremely finely balanced between polar and non-polar symmetries.

What are these other terms that favour a non-zero polarisation and compete with the polarisation-suppressing biquadratics? One possibility is that they result from higher order even terms. In $R3c$ materials, which have extremely large tilts in a $a^-a^-a^-$ pattern, it is not possible to neglect the higher order terms in the Landau expansion because the order parameters are not necessarily small. If these higher terms are included, one comes across a term of the form

$$\Delta_E = bQ_{R_5^-}^4 Q_{\Gamma_4^-}^2. \tag{6.3}$$

The $a^-a^-a^-$ tilt pattern is constructed exclusively by antiphase tilts and can therefore be described by a single irrep R_5^- with the (a,a,a) OPD. If the coefficient $b > 0$, then this term

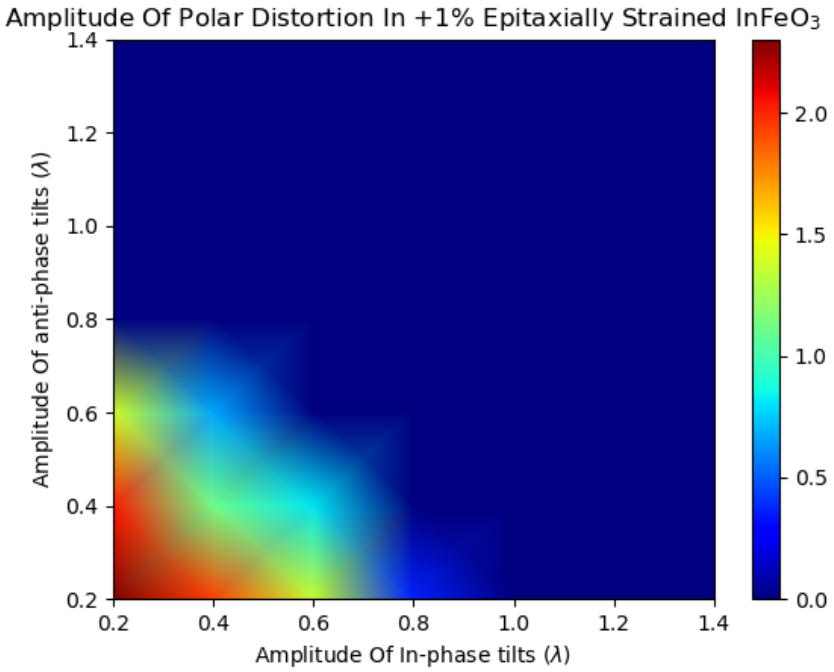

Figure 6.6: Demonstration of a competitive interaction between large tilts and polar modes in 1% strained $InFeO_3$. The colour denotes the amplitude of polarisation that minimizes the free energy. For very large tilts, the energy is minimised for zero polarisation. This is in contrast to the cooperative interaction in $R3c$ materials found in Reference [199].

behaves identically to a competitive biquadratic term and suppresses ferroelectricity. However, if $b < 0$, then this term actually favours ferroelectricity. This is exactly what happens in $R3c$ materials [199] like $ZnSnO_3$ so that for extremely large tilts, polarisation can actually become favoured. This is another reason why $R3c$ is favoured at low tolerance factors. It is the best example of a *triggered* mechanism mentioned in Chapter 2.

This sixth order mechanism is therefore the first thing we checked in the $Pna2_1$ phase. This is slightly more complicated than the $R3c$ system as the $a^-a^-c^+$ tilt pattern is formed of both antiphase and in-phase tilts and so the energy landscape has a greater dimension. We scaled the tilts $\lambda Q_{M_2^+}$ and $\lambda Q_{R_5^-}$ using a scaling parameter λ. For each combination of in-phase and antiphase tilts, we computed the energy associated with a polar distortion by scaling the out-of-plane polar mode and locating the value of the polarisation that minimises the energy. The results for $InFeO_3$ are shown as a polarisation landscape in Figure 6.6. No other distortions are included in the numerical experiment apart from the two tilts and the polarisation.

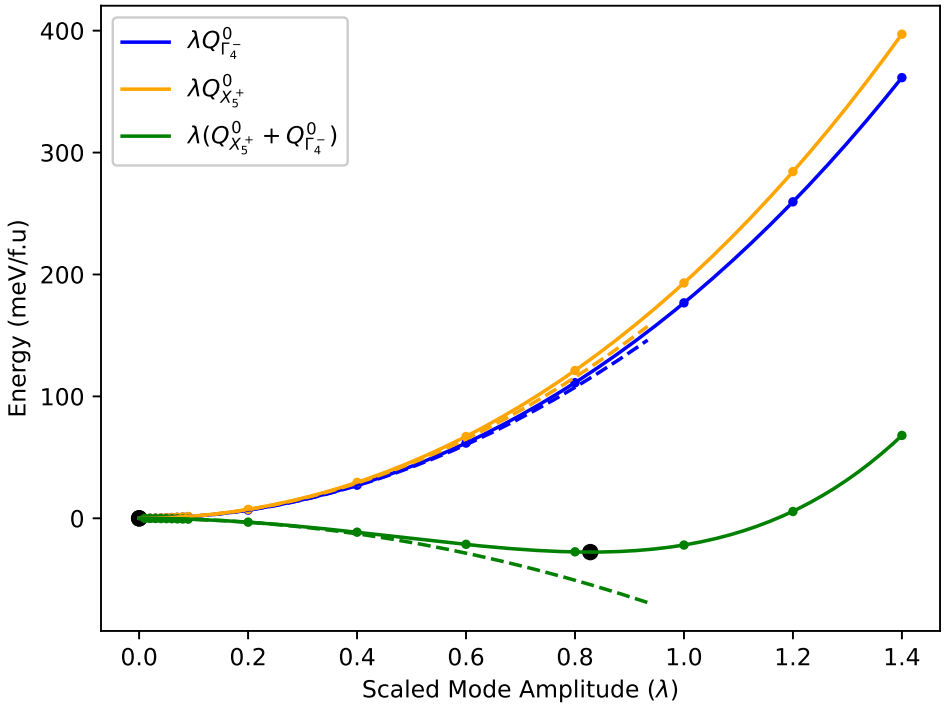

Figure 6.7: Energy wells formed by introducing the polar mode Γ_4^-, the antipolar B-site motions (X_5^+), and then both modes together to the $Pnma$ symmetry. Energy is only gained when both modes are introduced together.

The colour bar indicates the value of the polarisation that minimises the energy. We see that only non-zero values of polarisation are obtained for small tilts. This indicates that the mechanisms driving the transition to $Pna2_1$ is wholly distinct from that in $R3c$ materials and that the coefficient in the sixth order term is indeed positive.

We gained some additional insight into the possible mechanism by adding each of the modes that appear once the symmetry is broken to $Pna2_1$. This obviously includes the Γ_4^- polar distortion with the $(0, 0, a)$ OPD but the allowed antipolar motion of the B-sites described by an X_5^+ irrep is also important. There is also a R_5^+ antipolar mode but, like the M_3^+ Jahn-Teller mode, is too small to contribute much. We took the two mode amplitudes obtained from a $Pna2_1$ geometry relaxation as fixed constants $Q_{\Gamma_4^-,0}$ and $Q_{X_5^+,0}$ and then introduced them to the $Pnma$ structures by scaling their value with a scaling parameter λ so that $Q_{\Gamma_4^-} = \lambda Q_{\Gamma_4^-,0}$ and $Q_{X_5^+} = \lambda Q_{X_5^+,0}$. We also introduced them simultaneously so that the combined mode was $Q = \lambda(Q_{\Gamma_4^-,0} + Q_{X_5^+,0})$. The changes to the energy of the structure are presented in Figure 6.7.

This intriguing result suggests that neither Γ_4^- or X_5^+ are unstable by themselves. In the language of phonons, the frozen phonon is of hybrid character and mixes the zone centre distortion with the zone-boundary* Only when both of the modes are present does the energy decrease†. Any theory constructed to explain this phase transition must be able to describe this simultaneous condensation of order parameters.

The first candidate Landau theory that could have some potential returns to the familiar biquadratic terms in a triggered ferroelectric mechanism. As a reminder from Chapter 4, this occurs when the coefficient in front of the biquadratic is negative so that a term like

$$\Delta E = cQ_{X_5^+}^2 Q_{\Gamma_4^-}^2 \tag{6.4}$$

with $c < 0$ would decrease the energy of the system and prefer the existence of X_5^+ if Γ_4^- appears. While a tempting solution, it is clearly insufficient. The triggering mechanism relies on at least one of the order parameters to be non-zero but Figure 6.7 patently shows that neither X_5^+ or Γ_4^- can spontaneously appear. Furthermore, explicit calculation by adding only the X_5^+ and Γ_4^- modes to the highest symmetry $Pm\bar{3}m$ in $InCrO_3$ shows that adding the polar mode with a non-zero X_5^+ mode reduces the energy gain that would have been obtained if just Γ_4^- were introduced by itself. Therefore, the coefficient c is strongly positive and rules out the triggered mechanism. Of course, this newly determined competitive biquadratic interaction only adds to the barrier that the actual mechanism needs to fight through.

Before discussing what terms could be driving the simultaneous appearance of the polarisation and the antipolar X_5^+ mode, I note that I repeated the calculation of Figure 6.7 on all materials studied in Figure 6.3. This is shown in Figure 6.9. Identical behaviour is observed in each and so the mechanism must have universal applicability.

While the terms of even powers in the Landau expansion are acting to suppress the polarisation, it is the odd powers that are driving the polarisation. Specifically, we can form combinations of order parameters

*This is not entirely surprising. After condensing in the tilts from $Pm\bar{3}m$ to get $Pnma$, the original X-point in the $Pm\bar{3}m$ Brillioun zone has been folded onto the zone centre of the $Pnma$ Brillioun zone.

†The minimum of the combined mode is not at $\lambda = 1$. This is because Γ_4^- and X_5^+ are being introduced to the $Pnma$ structure which has slightly different mode amplitudes to the fully relaxed $Pna2_1$ structure.

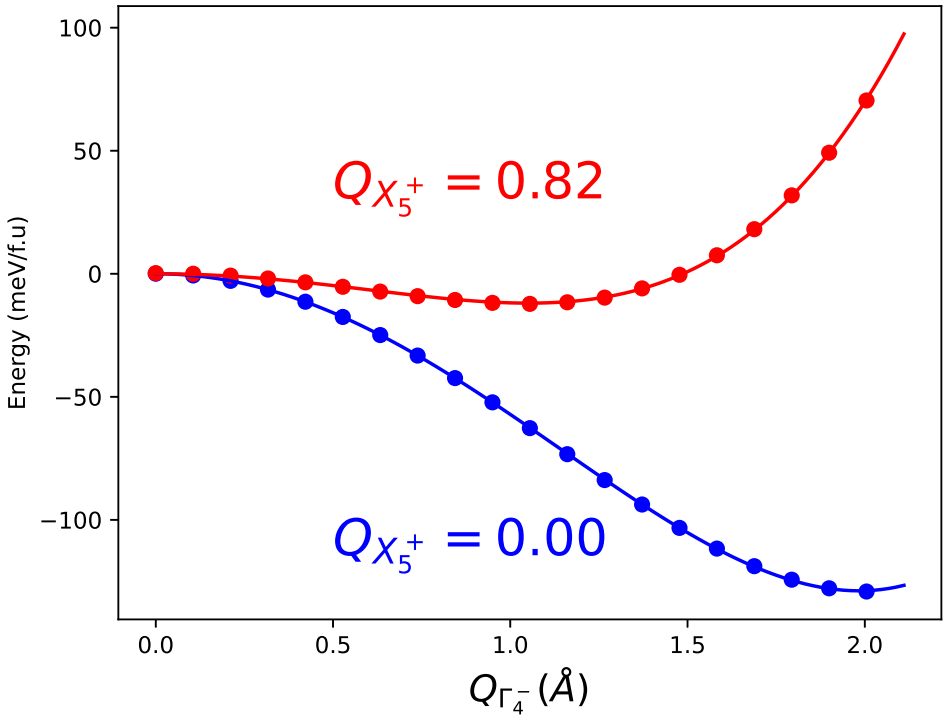

Figure 6.8: Energy wells formed by introducing the polar mode to the highest symmetry $Pm\bar{3}m$ structure alone (blue) and then introducing it with a fixed amplitude of antipolar B-site motions (red). The energy gain is greatest without the antipolar motion of B-sites. This suggests a competitive biquadratic interaction and rules out the possibility of a triggered mechanism.

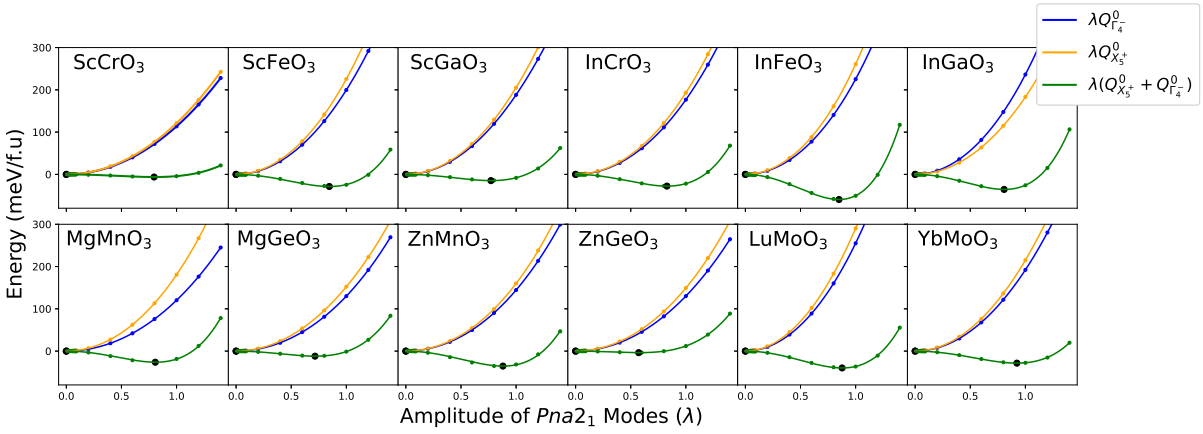

Figure 6.9: Simultaneous appearance of antipolar B-site and polar distortions in all materials studied.

$$\Delta E_{\text{odd}} = c_1 Q_{X_5^+} Q_{X_5^-} Q_{\Gamma_4^-} + c_2 Q_{X_5^+} Q_{R_5^-} Q_{M_2^+} Q_{\Gamma_4^-} + c_3 Q_{X_5^+} Q_{R_4^-} Q_{M_2^+} Q_{\Gamma_4^-} + c_4 Q_{X_5^+} Q_{R_5^-} Q_{M_3^+} Q_{\Gamma_4^-}, \tag{6.5}$$

which couple the order parameters X_5^+ and Γ_4^- to modes that already exist in the *Pnma* structure. These terms were constructed using the rules established in Chapter 3 and checked with INVARIANTS [131]. Taking these terms one at a time, the first term $c_1 Q_{X_5^+} Q_{X_5^-} Q_{\Gamma_4^-}$ extends the concept of hybrid improper couplings. This is because in a hybrid improper mechanism, two frozen modes form a hybrid mode that induces the appearance of the third - think of the two frozen tilts inducing the X_5^- antipolar motion in *Pnma* perovskites. $c_1 Q_{X_5^+} Q_{X_5^-} Q_{\Gamma_4^-}$ implies something very different. Only $Q_{X_5^-}$ is a frozen mode that already exists in the structure. This term encourages both X_5^+ and Γ_4^- to condense if X_5^- is already present; the new order parameters will adopt signs so that this term reduces the overall energy of the system. In this term, one mode induces two others.

The next term $c_2 Q_{X_5^+} Q_{R_5^-} Q_{M_2^+} Q_{\Gamma_4^-}$ couples the polar mode and X_5^+ to the enormous tilt modes. The larger the tilts, the larger the push to introduce the two new modes. The product of tilts does not vary much with strain in these materials and so we can expect this term to be a constant pressure towards polarisation at all strains. In Figure 6.10, we see this constant product.

The next term couples the two new terms to R_4^- and M_2^+. From Figure 6.4, we see that M_2^+ increases with strain while R_4^- has that characteristic dip. In Figure 6.10, we see that the change in R_4^-, dominates the product so it also has that same characteristic dip. I conclude that this term has its maximum effect at either very low or very high strains.

Finally, we have a coupling to the tiny Jahn-Teller mode which is negligibly small. This whole term is therefore largely unimportant. The huge fluctations in this term shown in Figure 6.10 is largely due to tiny changes M_3^+, potentially due to noise, having a outsized effect on the product.

So it appears that the first two terms are the most important in driving the polarisation and the third term, already small due to the smaller R_4^- mode, becomes less important as the strain

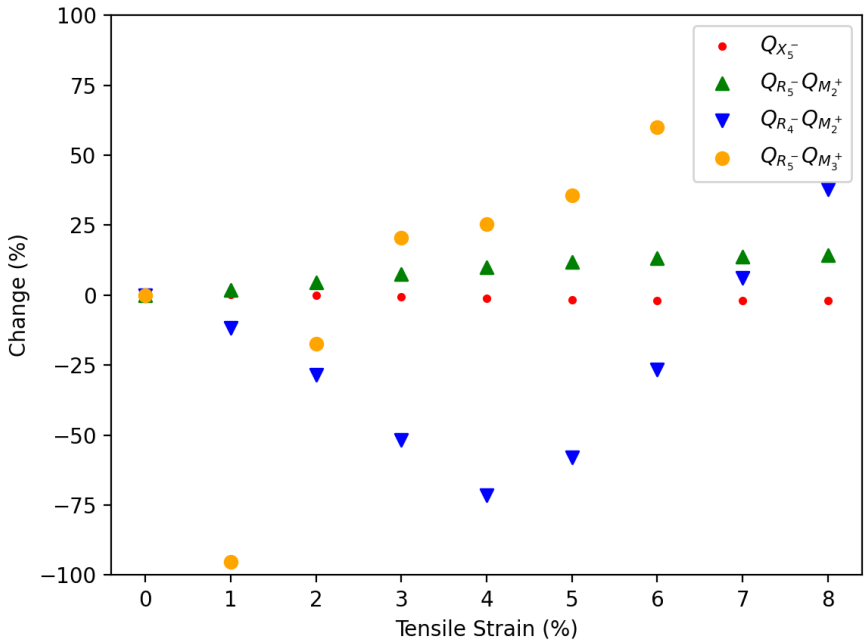

Figure 6.10: Products of mode amplitudes that play a role in the odd-order coupling terms of Equation 6.5. We see that the role of the tilts and antipolar A-sites remain constant for the entire strain range. However, the other modes, which were already small, have changing significance with increasing strain.

is increased, at least up to a point.

These terms are immediately reminiscent of the avalanche transitions studied in Aurivillius compounds [200, 201, 202]. The idea here is that the specific couplings in these materials could potentially allow for two modes to appear simultaneously and therefore skip a phase in which only one mode is present. This classification is non-specific and so could be caused by either triggered mechanism or the extended hybrid improper mechanisms that seem to be at play in these $Pna2_1$ materials. Although the condensation of the X_5^+ and Γ_4^- are certainly simultaneous, it is not clear whether this should be called a avalanche transition as it's not obvious if any intermediate symmetry is skipped. For example, the first two terms suggest that large tilts would also bring X_5^+ and Γ_4^-, but would these two secondary modes appear simultaneously with the tilts or develop only after the material has cooled and the tilt magnitudes have strengthened?

The couplings above also explain why it is only the $Pna2_1$ phase which can be obtained in this way. The alternative strain-induced polar phases $Pmc2_1$ and $Pmn2_1$ do not allow for this

Symmetry Adapted Modes	$Pnma$	$Pna2_1$	$Pmn2_1$	$Pmc2_1$	$R3c$
R_5^-	(a,a,0)	(a,0,a)	(0,a,-a)	(0,a,a)	(a,a,a)
M_2^+	(0;a;0)	(0;0;a)	(a;0;0)	(a;0,0)	N/A
X_5^-	(a,a;0,0;a,a)	(0,0;a;a,0,0)	(0,0;0,0;a,-a)	(0,0;0,0;a,a)	N/A
R_4^-	(a,-a,0)	(a,0,-a)	(0,a,a)	(0,a,-a)	N/A
M_3^+	(0;a;0)	(0;0;a)	(a;0;0)	(a;0,0)	N/A
Γ_4^-	N/A	(a,0,0)	(a,a,0)	(a,a,0)	(a,a,a)
X_5^+	N/A	(0,0;a,-a;0,0)	N/A	N/A	N/A
R_5^+	N/A	(a,0,-a)	(a,0,0)	N/A	N/A
X_2^+	N/A	N/A	(0;0;a)	N/A	N/A
Γ_5^-	N/A	N/A	(0,a,-a)	(0,a,-a)	N/A
M_5^-	N/A	N/A	(a,-a;0,0;0,0)	(a,-a;0,0;0,0)	N/A
X_1^+	N/A	N/A	N/A	(0;0;a)	N/A

Table 6.1: Symmetry adapted modes of space groups studied. Entries denote the order parameter direction of the individual modes. Order parameter directions should not be confused with real space directions of a distortion. For example, the polar mode Γ_4^- of $Pna2_1$ is along the same real space direction as the M_2^+ rotation axis. In $Pmc2_1$, the polar mode is perpendicular to this tilt axis and in $Pmn2_1$, the polar mode is along the third mutually perpendicular direction. $Pnma$,$Pmc2_1$, $Pmn2_1$ and $Pna2_1$ have the octahedral tilt pattern $a^-c^+a^-$ (or equivalent in the different standard settings) whereas $R3c$ has the $a^-a^-a^-$ pattern. All modes can be visualised using ISODISTORT.

additional X_5^+ motion of the B-sites and so the above couplings would not exist. An enumeration of the modes present in each of the symmetries considered is presented in Table 6.1.

The couplings also have profound consequences for the switching of the polar mode. The odd order terms in the Landau expansion mean that Γ_4^- is not able to reverse unless X_5^+ also reverses simultaneously. This is demonstrated explicitly in Figure 6.11 which is actually just an extension of Figure 6.7. Here, the energy degenerate state can only be obtained if the both the polarisation and the antipolar B-sites are reversed together.

Finally, we discuss whether any alternative orientations may be preferred in this epitaxial strain geometry. There are two ways to position a $Pnma$ perovskite on top of a cubic substrate. The first, and the one that I have been considering exclusively up until now, is to position the short axes parallel to the substrate and have the long axis perpendicular. The second involves the long axis being in the plane. We restricted ourselves to the first orientation because previous research demonstrated that tensile strain favours this orientation [93] for materials like $CaTiO_3$. However, we cannot assume this is still the case for the materials studied here with extremely low tolerance factors. We fully relaxed all of the materials without constraining any lattice

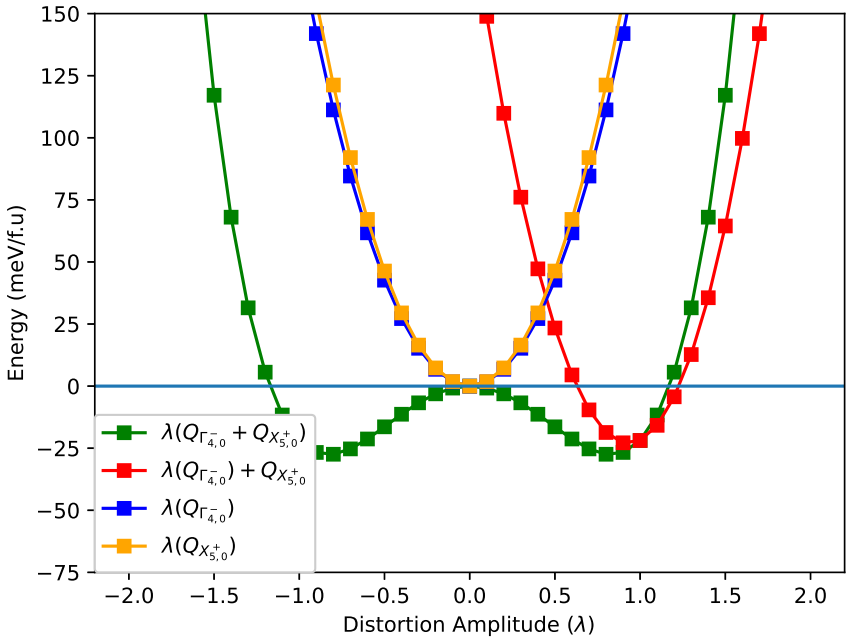

Figure 6.11: Energy wells demonstrating the coupled switching in $InCrO_3$. The degenerate minima can only be obtained by switching both the polar mode and the antipolar motion of B-sites.

vectors and then in Table 6.2, we computed the areas of the face in contact with the substrate for the geometry in which the long axis is perpendicular to the substrate and also when the long axis is parallel to the surface. Applying tensile strain should favour the orientation with the larger surface area. We see that for $CaTiO_3$, the perpendicular orientation has the larger area which supports previous work. However for all the remaining materials except $LuMoO_3$, the parallel orientation maximises the area. This suggests it is this alternative orientation that would be preferred with increasing tensile strain.

This is confirmed in Figure 6.12 for $InFeO_3$. The bold black line shows that the alternative orientation for *Pnma* quickly becomes stable with tensile strain. Interestingly, there is also an alternative orientation to the $Pna2_1$ phase which is also lower in energy so that the polar instability persists even with this new orientation. However, for small strains around 0%, the polar instability on top of the *Pnma* symmetry oriented with the long axis out of the plane is still the lowest energy structure and so we would still expect to see an out of plane polarisation for low enough strains. In fact, we would not expect to see the alternative orientation at all as

Material	a	b	c	$A_\perp$	$A_\parallel$
$ScCrO_3$	5.370	7.421	5.033	27.030	27.311
$ScFeO_3$	5.364	7.516	5.018	26.915	27.603
$ScGaO_3$	5.338	7.497	5.011	26.745	27.444
$InCrO_3$	5.387	7.599	5.194	27.977	28.431
$InFeO_3$	5.392	7.692	5.168	27.867	28.726
$InGaO_3$	5.355	7.681	5.152	27.585	28.537
$MgMnO_3$	5.169	7.211	4.940	25.537	25.781
$MgGeO_3$	5.143	7.253	4.963	25.526	25.920
$ZnMnO_3$	5.111	7.295	5.007	25.593	26.100
$ZnGeO_3$	5.078	7.349	5.014	25.464	26.223
$YbMoO_3$	5.721	7.825	5.342	30.565	30.626
$LuMoO_3$	5.719	7.718	5.335	30.510	30.181
$CaTiO_3$	5.442	7.639	5.377	29.266	29.221

Table 6.2: Fully relaxed $Pnma$ materials and their corresponding lattice constants. $A_\perp$ and $A_\parallel$ are the areas of face in contact with the surface and are obtained by $A_\perp = ac$ and $A_\parallel = \frac{b}{2}\sqrt{a^2+c^2}$.

it is the $R3c$ phase which actually becomes stable with increasing strain.

6.5 Applications Of The $Pna2_1$ Symmetry

The stabilisation of $Pna2_1$ symmetry over $Pnma$ and $R3c$ has immediate technological consequences. The out-of-plane polarisation is tempting for device physics because, to construct a device, the ferroelectric must be sandwiched between two metallic electrodes. If the ferroelectric has an out-of-plane polarisation, this would interact very strongly with the electric field emanating from the electrodes and realise low voltage ferroelectric switching*. The well studied ferroelectric $BiFeO_3$ has a polarisation of around 90 $\mu C/cm^2$ but this is along the [111] direction. The component along the out-of-plane direction would therefore be approximately 60 $\mu C/cm^2$ - this value forms the benchmark of what a competitive out-of-plane polarisation is.

We begin by calculating the polarisation of the $InFeO_3$ $Pna2_1$ symmetry. We see from Figure 6.3 that the $Pna2_1$ symmetry is stabilised over both the $Pnma$ and $R3c$ symmetry at 0% strain and so it is at this strain that we calculate all material properties. The polarisation is calculated

*The larger out-of-plane polarisation would also create a larger surface charge and hence a larger depolarizing field the suppresses the polar distortion. We can negate this effect by assuming that the electrodes are sufficiently metallic to screen the surface charge and that the epitaxial film is thick enough that any residual surface charge does not produce such a large depolarizing field.

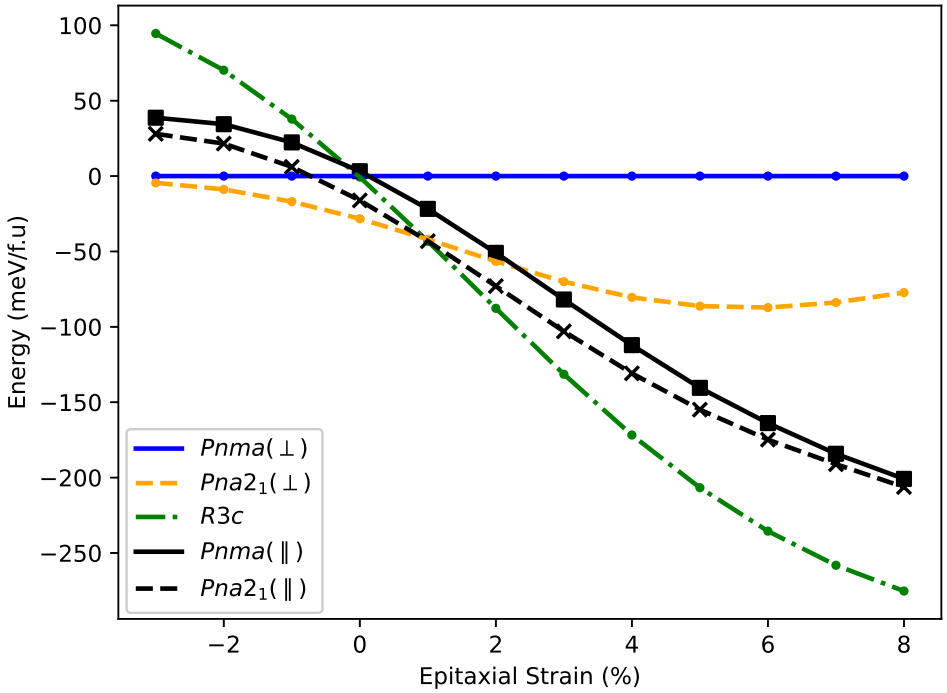

Figure 6.12: Energies of all studied crystallographic phases with G-type AFM. I have included the two possible growth orientations that have been observed in $Pnma$ perovskites. We see that the perpendicular arrangement, which will have an out-of-plane polarisation, is favoured for small strains. Interestingly, the same polar instability occurs for both growth orientations.

using the Modern Theory Of polarisation and so, being a quantity that is defined only modulo a quantum of polarisation, there are multiple polarisation branches to contend with. This is shown in Figure 6.13. One of these branches includes the point $P = 0$ when the amplitude of the polar distortion is zero. Following this branch upwards with increasing polar distortion leads to a fully relaxed polarisation of $P = 22.42\ \mu\text{C/cm}^2$. This is smaller than $BiFeO_3$ but still of the same order of magnitude.

Another quantity related to the polarisation is the Born effective charges tensor. As discussed in Chapter 2, this quantity measures the disparity between the nominal valence state of the ions in a purely ionic description of the material to the actual change in polarisation obtained when charges are moved. In effect, it describes how much of the electronic charge density are also dragged along with the ion as it is displaced. A huge disparity in the nominal and Born effective charges indicate that the polarisation is being driven by electronic effects such as the second order Jahn-Teller distortion. In $InFeO_3$, all Born effective charges are roughly equal to the

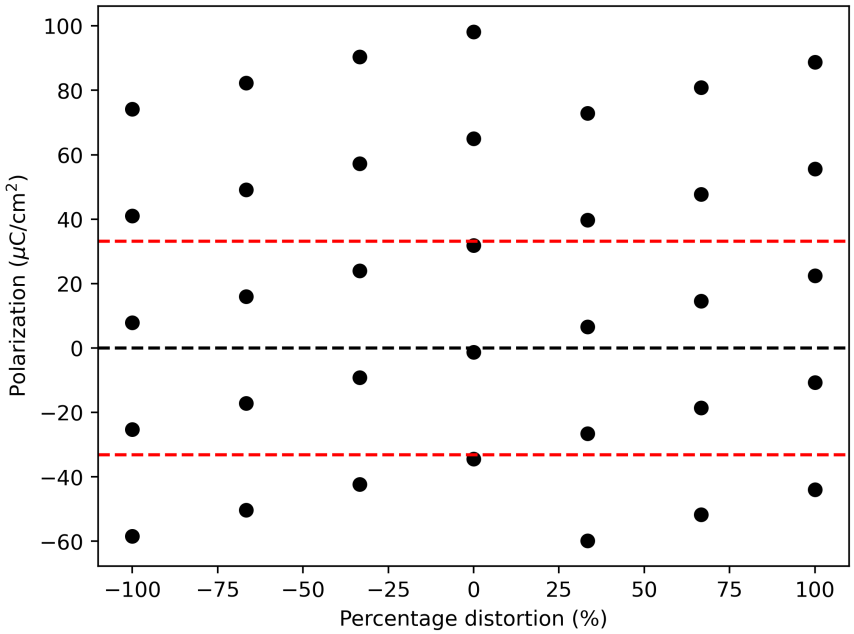

Figure 6.13: Multiple polarisation branches of $Pna2_1$ $InFeO_3$ and how they are changed as I alter the amplitude of the Γ_4^- mode as a percentage. The centrosymmetric structure should be centered on zero through classical arguments. The quoted polarisation is obtained as the difference between a 100% distortion and a 0% distortion *while remaining on the same branch*. The red dashed lines indicate polarisation quanta.

nominal ionic values. For example, the Born effective charge for the Fe^{3+} ion is about +3.7. In contrast, for a material like $BaTiO_3$ where the second order Jahn-Teller effect is known to play a dominant role in driving the polarisation, the Born effective charge for the nominally Ti^{4+} ion is about +7 - a huge contrast. The similarity between the Born effective charges and the nominal charges in $InFeO_3$ is not surprising, we have shown that in the previous section that the polarisation emerges from a symmetry dictated coupling between crystallographic modes. A ferroelectric with nominal Born effective charges is known as *geometric*.

Moving on to the magnetic properties of $InFeO_3$, we include the four most common magnetic structures of ABO_3 perovskites: A, C, G and FM and investigate how these change with strain. This is done in Figure 6.14. The bold lines denote the $Pnma$ structure, the dashed lines the $Pna2_1$ and the dashed-dotted line the $R3c$. Experimentally, $InFeO_3$ is a G-type antiferromagnet [198] and so it is reassuring that this magnetic structure is always substantially lower in energy

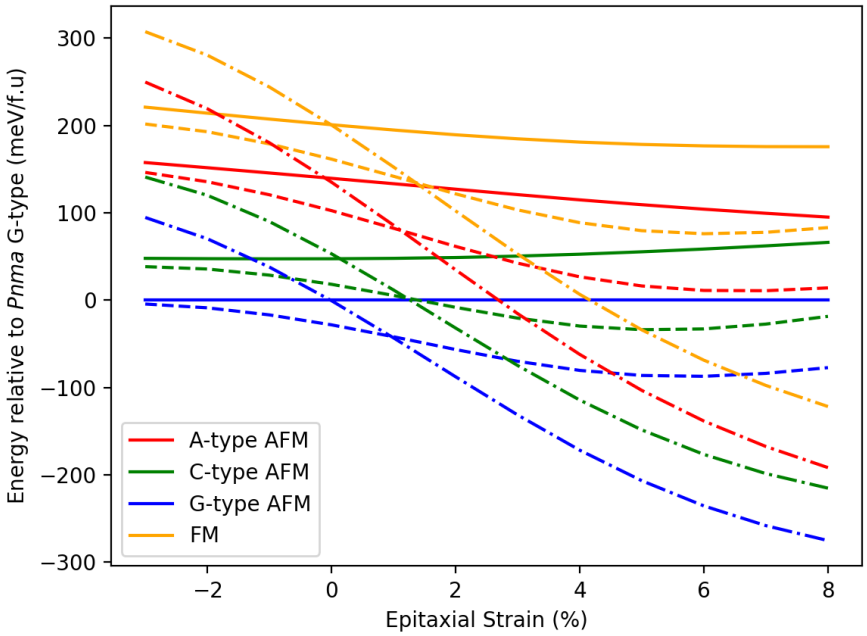

Figure 6.14: Energies of crystallographic and magnetic structures in $InCrO_3$ as a function of epitaxial strain. I observe a region between -2% and 1% strain for which a G-type AFM $Pna2_1$ phase is thermodynamically stable. Solid, dashed and dashed-dotted lines are the energies of $Pnma$, $Pna2_1$ and $R3c$ symmetries respectively.

than the others in Figure 6.14. Furthermore, the G-type structure permits a weak ferromagnetic moment, which I calculated through a non-collinear spin calculation, to have a value of $0.021\mu_B$. This is comparable to the weak ferromagnetic moment in other ferrite perovskites [27]. The magnetic easy axis is within the plane and perpendicular to the polarisation.

It is important to contrast the energy difference between the $Pnma$ and $Pna2_1$ symmetries, and the $R3c$ and $R\bar{3}c$ (not shown on Figure 6.14) symmetries. This is because the centrosymmetric symmetries $Pnma$ and $R\bar{3}c$ would presumably form a good model for the paraelectric phase and so the energy between the orthorhombic phases $\Delta E_O = E_{Pnma} - E_{Pna2_1}$ or rhombohedral phases $\Delta E_R = E_{R\bar{3}c} - E_{R3c}$ can be used as a rudimentary proxy for switching barriers. For $InFeO_3$, $\Delta E_O = 28.30$ meV/f.u and $\Delta E_R = 252.96$ meV/f.u. This suggests that the ferroelectric switching is potentially easier in the orthorhombic materials and therefore circumvents the high switching barriers present in $R3c$ materials [203, 204].

The electronic structure of $InFeO_3$ is explored in Figure 6.15. We see that the material is

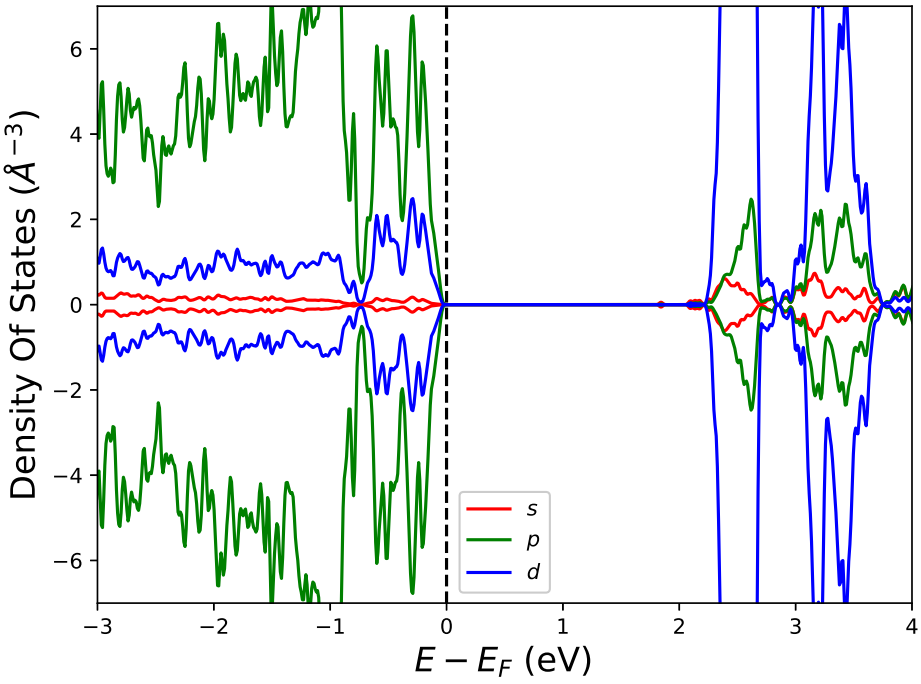

Figure 6.15: Density of states for the G-type AFM $Pna2_1$ phase of $InFeO_3$ at 0% strain, demonstrating the insulating character.

clearly insulating with a band gap of 1.81 eV. The gap persists with all choices of Hubbard-U.

Figure 6.16 explores how the choice of Hubbard-U affects the magnetic structure and the polar instability at 0%. We see that for all values of U, the polar instability persists but the energy differences between $Pna2_1$ and $Pnma$ decreases with increasing U.

Turning to $InCrO_3$ at 1% strain, the polarisation is also sizeable at 11.15 $\mu C/cm^2$ and like $InFeO_3$, the Born effective charges are nominal. In addition ΔE_O = 29.70 meV/f.u and ΔE_R = 317.40 meV/f.u. The relative energies of the various magnetic structures in Figure 6.17 show some interesting features. The experimentally observed C-type magnetic structure is the lowest for the $Pnma$ symmetry but once the polar instability forms, the ferromagnetic magnetic structure becomes the lowest energy $Pna2_1$ structure. In fact, the ferromagnetic $Pna2_1$ structure is the lowest energy structure overall between 0 and 2% epitaxial strain. The cause of this change can be seen from Figure 6.17: the polar instability happens at a lower strain (around -1%) for the FM and A-type magnetic structures than for the G- or C-types. This earlier onset of polarisation means that, in the region where $Pna2_1$ is stable, it is these magnetic structures

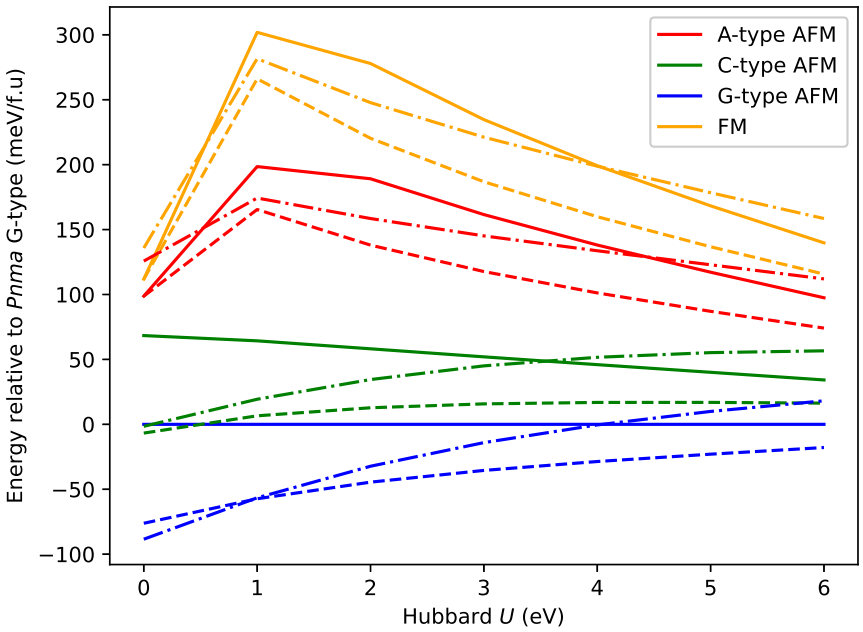

Figure 6.16: Energies of crystallographic and magnetic structures in $InFeO_3$ at 0% strain, as a function of the Hubbard-U parameter. The ground state is always G-type but could be either $Pna2_1$ or $R3c$ symmetry depending on U. However, the value of U leading to an $R3c$ symmetry is unrealistically small. Solid, dashed and dashed-dotted lines are the energies of $Pnma$, $Pna2_1$ and $R3c$ symmetries respectively.

that are lower in energy.

For FM and A-type spins, the intralayer interactions are ferromagnetic. For G and C, the intralayer interactions are antiferromagnetic. We saw in the previous section that the polar instability is driven by a coupling to the antipolar motion to the *magnetic* B-sites. This antipolar motion is also directed within the planes and so it is clear that ferromagnetic alignment of intralayer spins increases this distortion and leads to a stronger coupling between Γ_4^- and X_5^+. Antiferromagnetic spins have a weaker coupling. This explains the strange strengthening of the polar phonon when the magnetic structure was switched to FM in $ScCrO_3$ in Figure 6.1. The introduction of the antipolar X_5^+ mode is not only crucial for controlling the polar distortion but it is also clearly very important for determining the magnetic structure.

This unexpected result leads to two exciting possibilities. Applying an electric field to $InCrO_3$ strained at just below 0% would lower the energies of the non-centrosymmetric structures

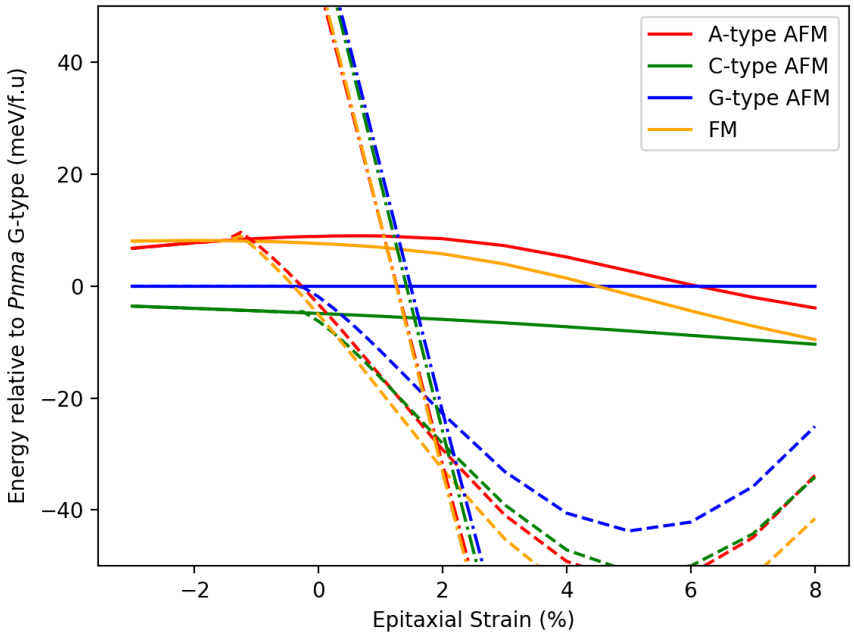

Figure 6.17: Energies of crystallographic and magnetic structures in $InCrO_3$ as a function of epitaxial strain. I observe a region between 0% and 2% strain for which a $Pna2_1$ phase is thermodynamically stable. For most of this region, I also observe a rare ferromagnetic structure. Solid, dashed and dashed-dotted lines are the energies of $Pnma$, $Pna2_1$ and $R3c$ symmetries respectively.

by roughly equal amounts. This could make the FM $Pna2_1$ symmetry the thermodynamic ground state and thus achieve the electric field control of magnetism, albeit not quite in the same form discussed in Chapter 4. The application of the electric field could turn a C-type antiferromagnetic into a polar ferromagnet. The presence or vanishing of a net magnetisation could be the two states needed for a memory device *.

Alternatively, applying a magnetic field at the same strain would lower only the ferromagnetic energies. A large enough field would result in the ferromagnetic polar structure being the lowest energy overall. If such an effect were possible, this would be a kind of magnetic field control of polarisation.

Given the exciting possibilities enabled by a ferroelectric ferromagnet, it is important to

*Once in the polar ferromagnet phase, it is not yet clear to me whether the reversal of polarisation also results in the reversal of the magnetisation due to the necessary reversal of the X_5^+ which clearly has an effect on the magnetism. If the magnetisation does not need to reverse, then this material could actually be the basis of a 4-state memory.

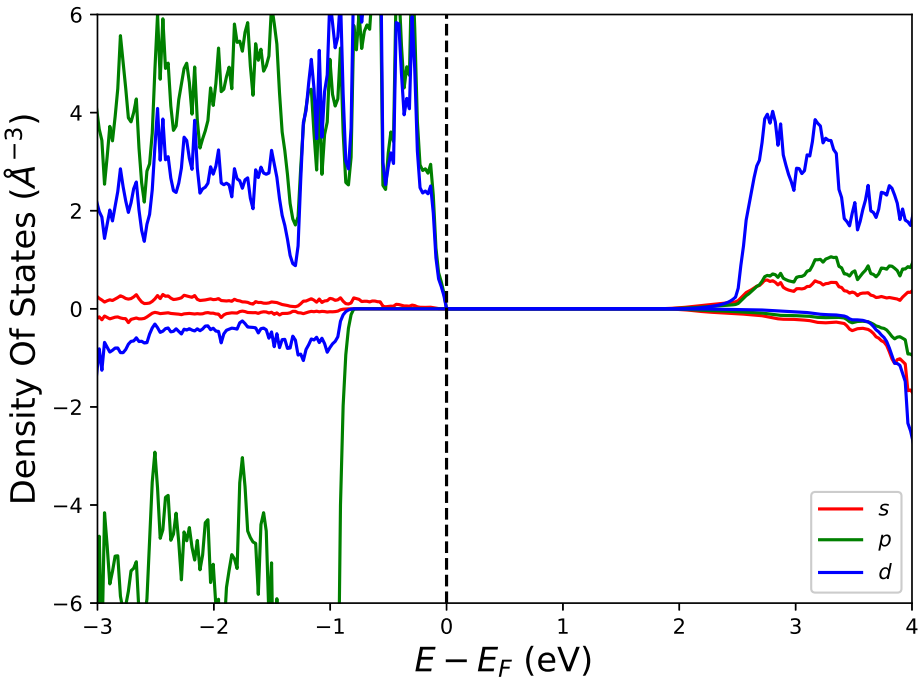

Figure 6.18: Density of states for the FM $Pna2_1$ phase of $InCrO_3$ at 1% strain, demonstrating the insulating character.

check if the material is insulating. Figure 6.18 confirms this and reveals a band gap of 1.84 eV. Figure 6.19 also reveals that for higher values of U, we can expect to see a FM ground state whereas for lower U we obtain a C-type $Pna2_1$ phase. However the huge energy difference between $Pnma$ and $Pna2_1$ A-type and FM magnetic structures persists so that the potential for physical applications remains robust to the choice of U.

Finally, $MgMnO_3$ at 0% strain has a polarisation of $P = 15.49\mu C/cm^2$ and nominal Born effective charges with $\Delta E_O = 13.95$ meV/f.u and $\Delta E_R = 331.01$ meV/f.u. Due to the identical d^3 filling in both, the behaviour of the magnetic structure is analogous to $InCrO_3$. We again see the early onset of polarisation for A-type and FM magnetic structures in Figure 6.20 and see insulating behaviour (although with a reduced band gap of 0.85 eV) in Figure 6.21 and the material exhibits a similar dependence on Hubbard-U. A summary of all material properties is given in Table 6.3.

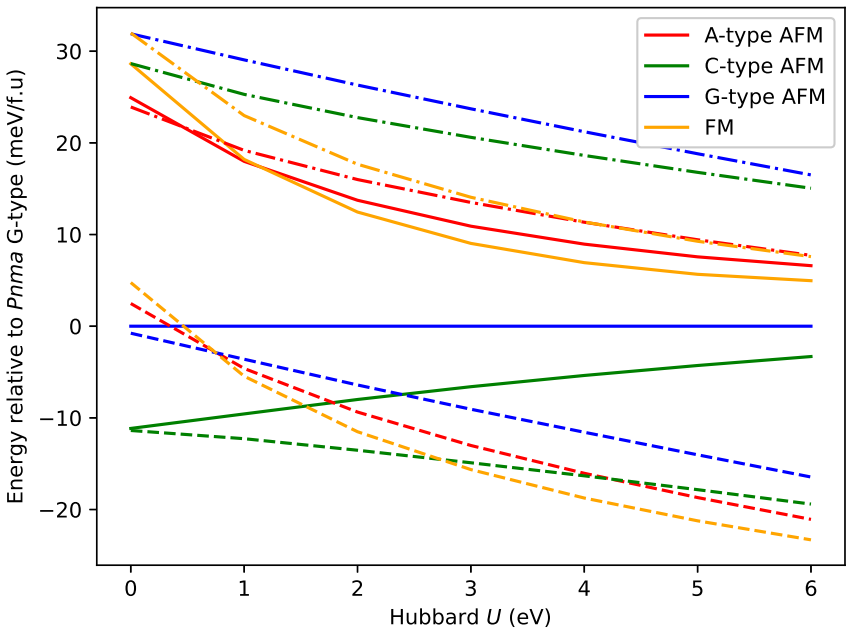

Figure 6.19: Energies of crystallographic and magnetic structures in $InCrO_3$ at 1% strain, as a function of the Hubbard-U parameter. The ground state is either ferromagnetic and of $Pna2_1$ symmetry or C-type and also of $Pna2_1$ symmetry. Solid, dashed and dashed-dotted lines are the energies of $Pnma$, $Pna2_1$ and $R3c$ symmetries respectively.

Material	Strain (%)	polarisation ($\mu C/cm^2$)	Magnetic Structure	Easy Axis	Band Gap (eV)	ΔE_0 (meV/f.u)	ΔE_R (meV/f.u)
$InCrO_3$	1	11.15	FM	[100]	1.84	29.70	317.40
$InFeO_3$	0	22.42	G-AFM*	[010]	1.81	28.30	252.96
$MgMnO_3$	0	15.49	FM	[010]	0.85	13.95	331.01

Table 6.3: Properties of candidate materials at specified strains. $InFeO_3$ is a G-type antiferromagnetic - the asterisk denotes a magnetic point group allowing for a wFM moment. This has a calculated magnitude of $0.021\mu_B$. ΔE_O and ΔE_R are the difference in energies between the two orthorhombic structures ($Pnma$ and $Pna2_1$) and the two rhombohedral structures ($R\bar{3}c$ and $R3c$) respectively. We use these values as a proxy for ferroelectric switching barrier height. Note that the ilmenite phase is not considered in the current study. Calculations on this phase in $InFeO_3$ reveal the ilmenite structure to be 502 meV/f.u higher in energy than the $Pnma$ phase.

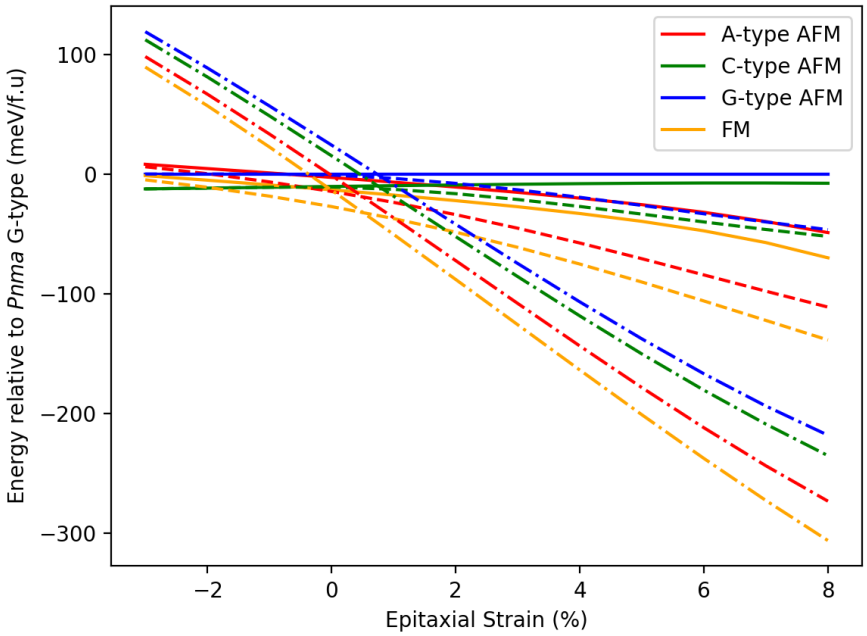

Figure 6.20: Energies of crystallographic and magnetic structures in $MgMnO_3$ as a function of epitaxial strain. I observe a small region $\approx 0\%$ strain for which a ferromagnetic $Pna2_1$ phase is thermodynamically stable. Solid, dashed and dashed-dotted lines are the energies of $Pnma$, $Pna2_1$ and $R3c$ symmetries respectively.

6.6 Contextualising the $Pna2_1$ Symmetry

To position our work in the context of the existing literature, the $Pna2_1$ phase is relatively rare in perovskite oxides and there is currently much debate into the causes. The phase has been observed in lone-pair systems like $BiInO_3$ [205], $PbRuO_3$ [206] and predicted in $PbCoO_3$ [142] (which also identified one of the terms in the odd power Landau expansion). It has similarly been identified in various d^0 materials like $CdTiO_3$ [207, 208, 209]. In fact, Reference [209], predicted that strain could be used to enable phase control between $R3c$, $Pna2_1$ and $Pnma$ in $ZnSnO_3$, although this was not known to me when I first created Figure 6.1. We have repeated the work of Reference [209] and found that it is always the $R3c$ phase which is energetically favourable. Our repeated calculations are shown in Figure 6.23 which should be compared to Figure 9 of their paper.

$Pna2_1$ symmetry has also been observed in rare earth orthoferrites and orthochromates

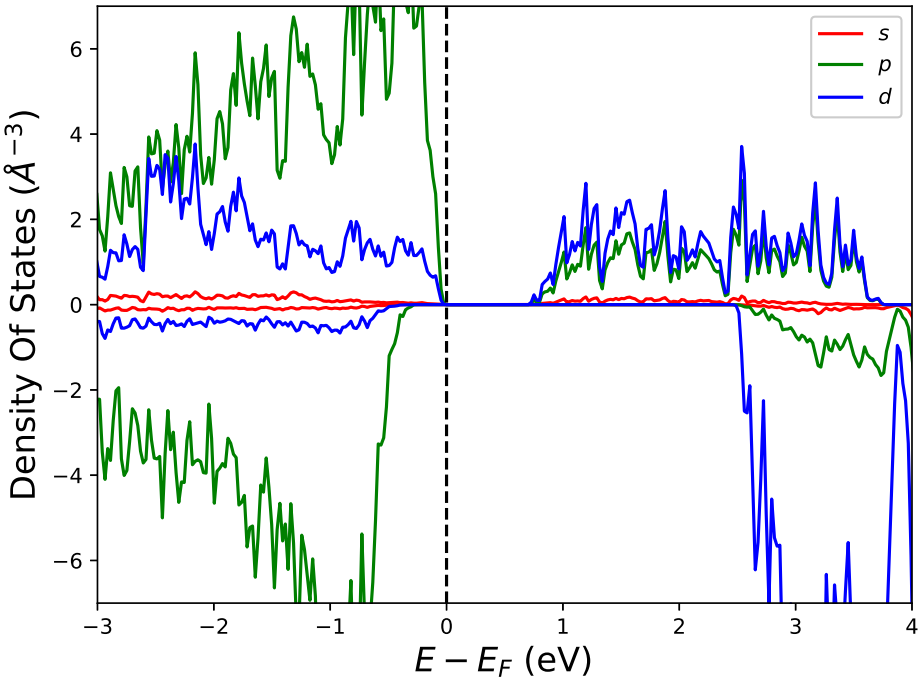

Figure 6.21: Density of states for the FM $Pna2_1$ phase of $MgMnO_3$ at 0 strain, demonstrating the insulating character.

[210, 191] but is usually ascribed to a spin-driven symmetry breaking, although conflicting reports of the $Pna2_1$ symmetry appearing at a much higher temperature than the rare earth T_N also exist [211]. While lone-pair, d^0 and spin-driven effects might be important in certain cases, I argue that the mechanism presented in the present study must also be important and is universal to all low-t systems since it depends solely on the symmetry of the parent phase.

6.7 Summary

This chapter has explored novel polar instabilities in highly orthorhombic perovskite materials. I demonstrated that the construction of a Landau Theory was essential to explain their unusual properties. The polarisation is suppressed by the strong biquadratic coupling to the R_4^- antipolar distortions. With increasing strain, this coupling is lessened so that the polar distortion, which is driven by extended hybrid improper terms in the energy expansion, can appear. This polar transition is avalanche-like in that the polar distortion can only appear simultaneously with the

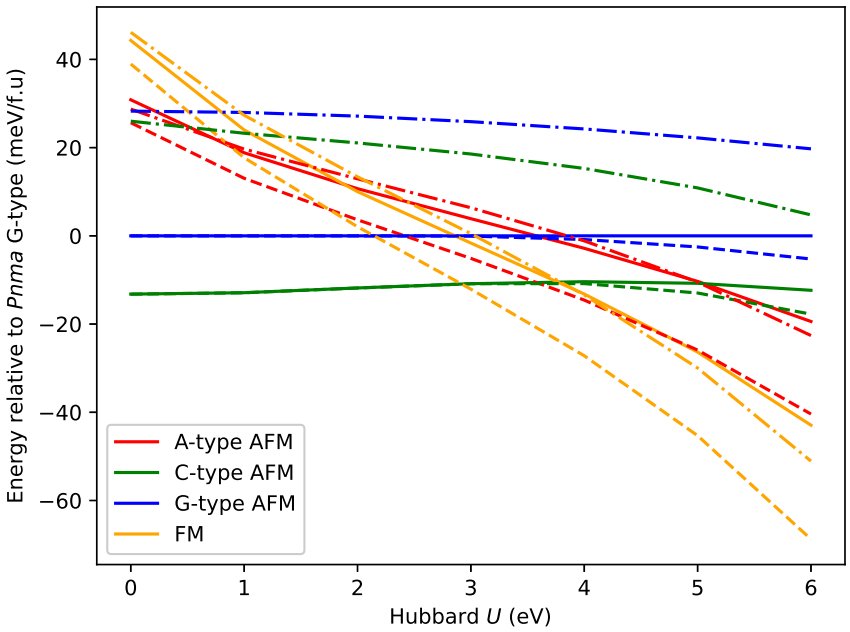

Figure 6.22: Energies of crystallographic and magnetic structures in $MgMnO_3$ at 0% strain, as a function of the Hubbard-U parameter. The ground state is either ferromagnetic and polar or C-type and non-polar.Solid, dashed and dashed-dotted lines are the energies of $Pnma$, $Pna2_1$ and $R3c$ symmetries respectively.

X_5^+ mode.

This X_5^+ is pivotal to the magnetic properties because the magnitude of this mode is altered by the type of magnetic interaction. The changing strength of the coupling between the polar mode and the X_5^+ mode with magnetic structure results in polar, ferromagnetic insulators becoming the thermodynamic ground states. In these materials, exciting effects such as the electric field control of magnetism can be theoretically achieved although not in the form that was the basis of the discussion in Chapter 4.

To extend this project, it would be interesting to explore just how universal this effect is. I already have some preliminary results suggesting that materials of the form $AScO_3$ would also show these instabilities. Alternatively, it would also be interesting to zoom in on a particular material such as $InCrO_3$ and determine the coefficients in the Landau expansion to work out which effects are truly dominant here.

It is not clear whether this mechanism would be useful in the original goal of memory devices.

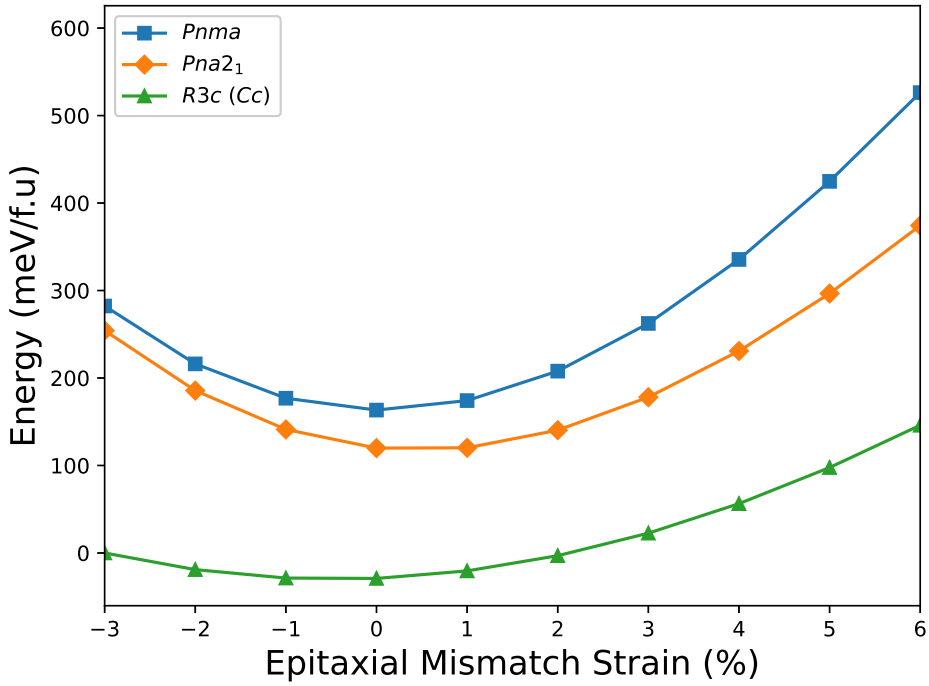

Figure 6.23: Energy of three competing polymorphs of $ZnSnO_3$ as a function of epitaxial strain. In contrast to [209], we observe that the $R3c$ is always the ground state.

It is true that the application of an electric field, in a region of strain, would convert a paraelectric antiferromagnet to a ferroelectric ferromagnet and so a material like $InCrO_3$ would show a degree of electric field control of magnetisation. The write operation could be performed with an electric field and the change from an AFM to a FM could be read in the read operation. However, once the electric field is released, the material would return to its paraelectric state. As a result, this mechanism would only be useful for a volatile memory device. Its interesting to note that the mechanism identified in this chapter makes use of a fully ferromagnetic state and not just a wFM canting. It would be considerably easier to interact with this larger magnetisation.

This work of this chapter were published in The Journal Of The American Chemical Society as "Universal Polar Instability In Highly Orthorhombic Perovskites" [212].

Chapter 7

Double Perovskites

Chapter 4 revealed that a A-site layered double perovskite with a $a^-a^-c^+$ tilt pattern and a magnetic structure described by an mX_1^- irreducible representation permits the electric field control of magnetism provided that both the normal to the layered cation planes and the antiferromagnetic easy axis is parallel to the in-phase tilt axis.

This chapter uses density functional theory (DFT) to simulate a candidate material possessing this exact symmetry - $CeBaMn_2O_6$.

Portions of this chapter form the basis of the computational half of 'Symmetry-informed design of magnetoelectric coupling in the manganite perovskite $CeBaMn_2O_6$' published in *The Journal Of Materials Chemistry C* [213].

7.1 $CeBaMn_2O_6$

Why should $CeBaMn_2O_6$ form the double perovskite with $a^-a^-c^+$ tilts and an X-point magnetic structure[†]? Furthermore, would $CeBaMn_2O_6$ have the insulating electronic structure required to allow ferroelectric switching?

Before starting to use any DFT at all, we can be fairly confident that $CeBaMn_2O_6$ will satisfy this criteria. To begin with, we hope that $CeBaMn_2O_6$ is simply a cation ordered variant of $LaMnO_3$. This material is well studied [214, 215, 216, 26, 217, 218]. It has the required $a^-a^-c^+$

[†]Also known as an A-type magnetic structure. I use the two terms synonymously.

tilt pattern and a X-point magnetic structure with the easy axis parallel to the in-phase tilt axis.

The valence states are $La^{(3+)}Mn^{(3+)}O_3^{(2-)}$ and, from this we can work out the tolerance factor of $LaMnO_3$ through

$$t_{LaMnO_3} = \frac{1}{\sqrt{2}} \frac{R_{La^{3+}} + R_{O^{2-}}}{R_{Mn^{3+}} + R_{O^{2-}}} = 0.961 \tag{7.1}$$

where the values of $R_{La^{3+}}$, $R_{Mn^{3+}}$, and $R_{O^{2-}}$ are taken from Shannon's compilation of ionic radii [219]. Assuming that the A-sites become ordered with Ce^{4+} and Ba^{2+} - an assumption that will be verified later - then the tolerance factor of $CeBaMn_2O_6$ is

$$t_{CeBaMn_2O_6} = \frac{1}{\sqrt{2}} \frac{\frac{1}{2}(R_{Ce^{4+}} + R_{Ba^{2+}}) + R_{O^{2-}}}{R_{Mn^{3+}} + R_{O^{2-}}} = 0.966 \tag{7.2}$$

and these two tolerance factors are relatively close. It is the tolerance factor that controls the tilt pattern and the similarity of the two suggests that $CeBaMn_2O_6$ will have the same $a^-a^-c^+$ tilt pattern as $LaMnO_3$.

In fact, the similarity in tolerance factors is the primary reason why Ce and Ba were selected to form the double perovksite. In addition, the $2+/4+$ charge states and the differing cation radii are also supposed to favour cation ordering [60].

The magnetism and electronic structure of $LaMnO_3$ are determined by the Jahn-Teller active Mn^{3+} cation. The d^4 filling of the d orbitals within the crystal field splitting of the octahedral anion environment (Chapter 2), leads to a degeneracy in the e_g states. This degeneracy is lifted through a Jahn-Teller (JT) distortion compressing two of the Mn-O bonds and extending the third. Now a particular e_g orbital is occupied, breaking the octahedral symmetry of the degenerate e_g states and causing the single e_g electron to occupy the orbital of lower energy. This is an orbital directed along the octahedral axis. This causes a local strain to which all other orbitals must collectively order to reduce this strain. Kugel and Khomskii [220] describe the process as a close packing of these cigar-shaped e_g orbitals and determine the resulting orbital ordering of e_g in $LaMnO_3$ is presented in Figure 7.1.

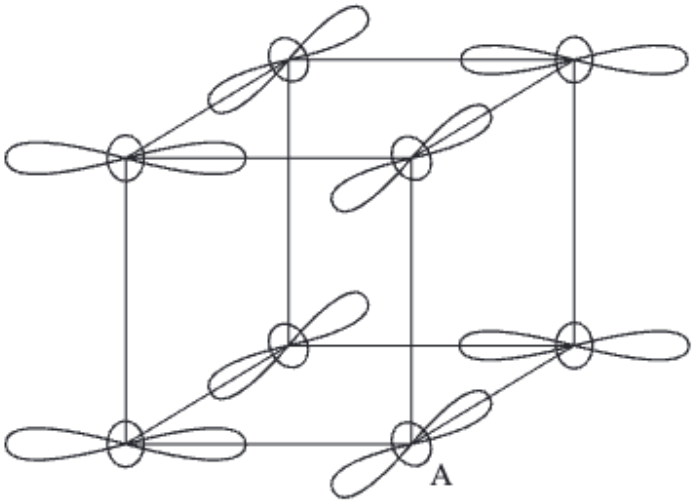

Figure 7.1: Orbital ordering of e_g orbitals in $LaMnO_3$ caused by a cooperative Jahn-Teller distortion of the MnO_6 octahedra (not shown). Taken from [26]

.

In the language of irreps, such a distortion is clearly described by an M-point irrep because the two basal axes in Figure 7.1 must be doubled to accomodate it. In fact, this is the M_3^+ irrep and is already permitted as a secondary order parameter in the *Pnma* symmetry. It is caused by the trilinear coupling

$$Q_{R_5^-} Q_{X_5^-} Q_{M_3^+} \tag{7.3}$$

involving antiphase tilts $Q_{R_5^-}$ and the secondary antipolar La motions $Q_{X_5^-}$. Being caused by a coupling to an already small secondary mode, the JT distortion is usually negligible in this symmetry (see Chapter 6) but obtains a sizeable magnitude without breaking the symmetry further for JT active Mn^{3+}.

Having established the orbital ordering, the magnetic structure can also be guessed at without recourse to simulation. The occupied e_g orbitals alternate in orientation within the xz plane * and the empty e_g orbitals on each site are orthogonal. This leads to a situation in which half-filled e_g orbitals on one site are overlapping with empty e_g orbitals on the next site. From the Goodenough-Kanamori-Anderson rules for superexchange interactions, this results in ferromagnetically ordering xy planes of Mn^{3+} cations. This should be weighed against the overlapping half-filled t_{2g} orbitals on every site which would favour antiferromagnetic arrangements between

*The *Pnma* setting has $\hat{\mathbf{y}}$ parallel to the long axis.

all neighbouring cations. Within the xz planes, the ferromagnetic interaction wins because the overlap between e_g orbitals (in a σ bond) is greater than that between t_{2g} (in a π bond). Along the y direction, there is practically no overlap between e_g orbitals and so AFM interactions dominate. The resulting structure is one with ferromagnetic interactions within each layer with antiferromagnetic interactions between layers - the exact X-point magnetic distortion (mX_1^-) required for the electric field reversal of magnetism to work.

We have seen that, replacing the A-site with ordered Ce/Ba would not substantially change the tilts. Even if it did, previous work [221] has demonstrated that altering the tilts do not substantially change the magnetic properties. Similarly, the intralayer orbital overlaps will hardly be affected as the A-sites are not within these layers. The interlayer overlap may be altered with the A-site layering but, as the π bond overlap remains the only serious superexchange mechanism, there is no reason to suppose that the magnetic structure will change once Ce/Ba layers are introduced.

7.1.1 Computational Details

We performed all subsequent computational simulation using density functional theory (DFT) as implemented in the Vienna Ab-Initio Software Package (VASP) [187, 188, 189, 186]. To compute the electronic structure and the Hellman-Feynman forces required to relax the geometry, we used projected augmented wave (PAW) pseudopotentials in which the following electrons are treated as valence: Ce - $5s^2 5p^6 4f^1 5d^1 6s^2$, Ba - $5s^2 5p^2 6s^2$, Mn - $3p^6 3d^5 4s^2$, O - $2s^2 2p^4$. All the other electrons were frozen to the atomic cores. For my exchange-correlation functional, I opt for a generalised gradient approximation using the Perdew-Burke-Enzerhof parameterization for solids (PBESol)[174].

As mentioned in Chapter 5, the d and f electrons have a small spatial extent but cannot be treated as core electrons because their energies are similar to the O p states. The small spatial extent increases the intrasite repulsion between these localised electrons; an effect which is not easily captured within standard DFT. This necessitates correction terms U and J modelling the repulsion and exchange respectively, of two d (or f) electrons occupying the same site.

Previous computational work has found that $U = 5$eV and $J = 1.5$eV are appropriate values to use for the Mn^{3+} ion in $LaMnO_3$ [222, 223]. We also use values $U = 10$eV and $J = 0$eV for the strongly localised Ce f states.

Energies and Hellman-Feynman forces were converged to less than 0.1 meV and 0.5 meVÅ^{-1} respectively, requiring a 1000 eV plane wave energy cutoff and a 4x3x4 Monkhorst-Pack k-point integration mesh.

7.1.2 Ground State Crystallographic, Electronic and Magnetic Structure

We begin by performing a geometry optimization on both $CeBaMn_2O_6$ and $LaMnO_3$ to compare the two resulting crystallographic structures. After the geometry relaxation is completed, we decompose the structures into their symmetry adapted distortions, each of which transforms as a seperate irreducible representation of the $Pm\bar{3}m$ parent symmetry. In addition, we decomposed an experimental, low-temperature $LaMnO_3$ structure refinement [218] to provide a benchmark for our computational relaxation. Importantly, we normalise the amplitude of these symmetry adapted modes to the volume of the 5-atom $Pm\bar{3}m$ cell so that we can directly compare between $LaMnO_3$ and $CeBaMn_2O_6$*. This analysis was carried out using ISODISTORT [128, 129] and the results tabuled in Table 7.1.

Two conclusions can be drawn from this table. The first is that our simulations faithfully reproduce the $LaMnO_3$ structure as the lattice constants and irrep magnitudes are quite similar in both the data obtained through x-ray diffraction and our simulated structure. Secondly, the cation layering does not substantially alter the amplitude of the modes in the structure. Of course, the additional layering of cations does not leave the structure entirely unchanged. The long b axis is noticeably lengthened after cation ordering, and the antiphase tilts R_5^- are weakened. Due to the $a^-b^+a^-$ tilt patterns, the antiphase tilts are about axes that are perpendicular to the direction of cation layering. This means that the apical oxygens translated by these tilts move within the A-O layers and a changing A-site environment, such as through the

*Such a normalisation is not strictly necessary in this case because the distorted cells of $Pnma$ and $Pmc2_1$ symmetry obtained from $Pm\bar{3}m$ are of the same size - the additional cation layering does not require a further increase in cell size.

Property	Experimental $LaMnO_3$ (Å)	Simulated $LaMnO_3$ (Å)	Simulated $CeBaMn_2O_6$ (Å)
a	5.746	5.799	5.818
b	7.664	7.610	7.738
c	5.533	5.505	5.523
$Q_{\Gamma_4^-}$	N/A	N/A	0.517
$Q_{R_4^-}$	0.112	0.117	0.081
$Q_{R_5^-}$	1.274	1.314	0.975
$Q_{X_1^+}$	N/A	N/A	0.697
$Q_{X_5^-}$	0.605	0.683	0.592
$Q_{M_2^+}$	0.971	1.106	1.010
$Q_{M_3^+}$	0.353	0.377	0.358
$Q_{M_5^-}$	N/A	N/A	0.338

Table 7.1: Comparison of irrep amplitudes between experimentally determined $LaMnO_3$ [218] structural modes, a relaxed $LaMnO_3$ cell obtained in the present investigation and the A-site layered $CeBaMn_2O_6$ structure. The irrep amplitudes (Q) have been normalised with respect to the parent $Pm\bar{3}m$ structure (parameter A_p in ISODISTORT)

cation ordering, will clearly have an effect. In contrast, the in-phase modes rotate oxygens in between these A-O layers and so the effect of cation ordering is negligible. This can also be seen from Table 7.1. Unlike the ABO_3 systems studied in Chapter 6, $CeBaMn_2O_6$ has Mn^{3+} which is Jahn-Teller active. This results in a non-negligible M_3^+ mode.

Therefore, we are relatively safe in our assumption that the crystal structure of $CeBaMn_2O_6$ is similar to $LaMnO_3$. This was necessary in our hypothesis that $CeBaMn_2O_6$ may exhibit the same magnetic structure as $LaMnO_3$ which was controlled by a particular Jahn-Teller induced orbital ordering, leading to ferromagnetic superexchange interactions within each BO_2 plane and an antiferromagnetic interaction perpendicular to the plane. The resulting magnetic structure is A-type (transforming as a mX_1^- irrep.) We confirm that this magnetic structure is indeed the ground state for a wide range of $U_{\text{eff}} = U - J$ in Figure 7.2. We find that for a $3eV < U_{\text{eff}} < 6eV$ on the Mn d orbitals, the A-type magnetic structure is stable. In all future calculations, we use $U_{\text{eff}} = 3.5$ eV which is known to be appropriate for $LaMnO_3$. With this choice of U_{eff}, we calculate the magnetic moment on each Mn ion to be $3.71\mu_B$. This value, along with the sizeable Jahn-Teller mode, lends credence to the assignment of a Mn^{4+} state and therefore a Ce^{4+} oxidation state. Thus, the necessary magnetic structure for the electric field control of

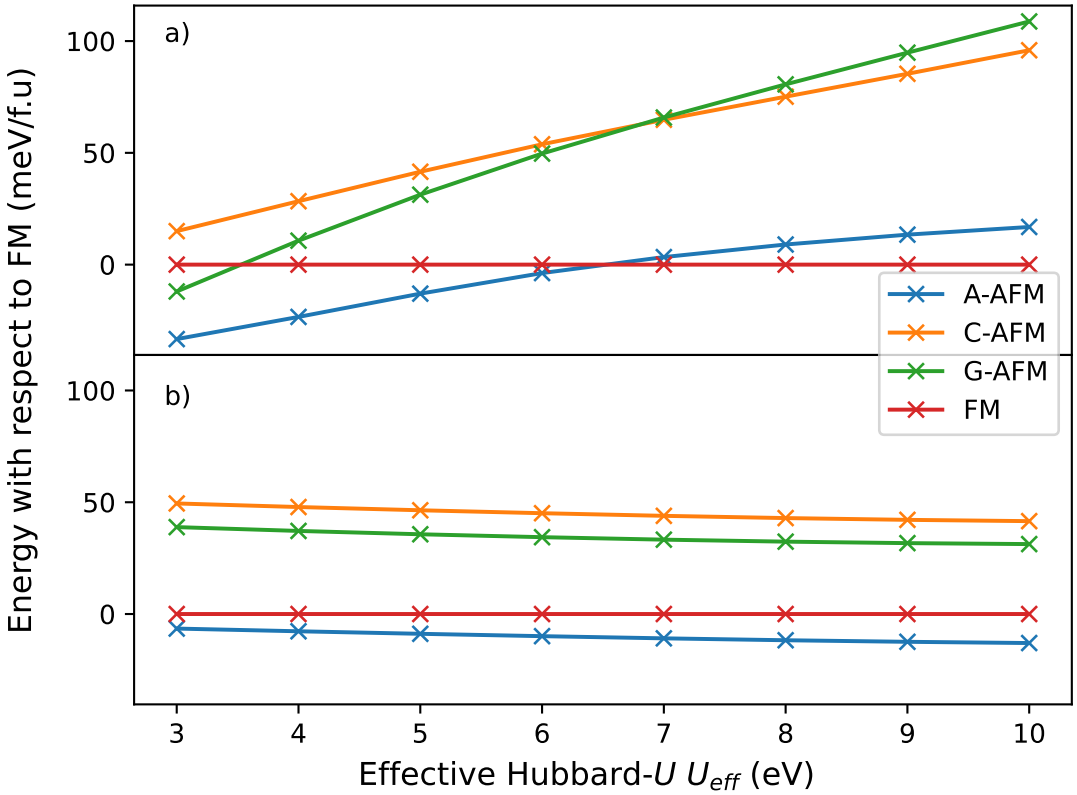

Figure 7.2: Variation of magnetic energies with Hubbard-U. a) Variation of magnetic energies when varying the effective U on the Mn ions. Variation of the magnetic structure when varying on the Ce site.

magnetism in $CeBaMn_2O_6$ is obtained.

Given this magnetic structure, we also require a magnetic easy axis that allow for a weak ferromagnetic moment. Table 7.2 details the results of our relativistic non-collinear calculations including spin-orbit coupling to determine the magnetocrystalline anisotropy of A-type $CeBaMn_2O_6$. We see that that the energy is lowest when the spins are directed parallel and antiparallel to the the [100] direction - along the a axis of the $CeBaMn_2O_6$ $Pnma$ cell. This is exactly the same direction that has been experimentally determined for $LaMnO_3$ and so we can conclude that the magnetic structure is not changed at all after cation ordering. Like $LaMnO_3$, $CeBaMn_2O_6$ also posessess a weak ferromagnetic moment which we calculate to be $0.029\mu_B$ per Mn along the b direction. This is a similar value to other magnetic perovskite oxides [27].

Quantisation Axis	Energy (meV/f.u)	Magnetic Moment (μ_B/Mn)
[001]	1.4	(0.000,0.000,0.000)
[100]	0.0	(0.000,0.029,0.000)
[010]	1.9	(0.001,0.000,0.000)
[101]	0.7	(0.000,0.000,0.004)
[011]	1.5	(0.001,0.000,0.001)
[010]	1.0	(0.000,0.000,0.003)
[111]	1.4	(0.000,0.000,0.000)

Table 7.2: Magnetocrystalline anisotropy energy and magnetic moments of various easy axes in A-type A-site layered $CeBaMn_2O_6$. Obtained non-self-consistently by freezing the charge density of the collinear self-consistent calculation and then rotating the easy axis. The quantisation axes and magnetic moments are listed with respect to the $Pnma$ setting of the $LaMnO_3$ structure.

A $a^-b^+a^-$ tilt pattern, an A-site layering, a magnetic structure transforming as an mX_1^- irrep with an OPD allowing for wFM is all that is necessary by symmetry for the 180° reversal of wFM with reversal of polarisation to work. However, the material must still be insulating in order to have a macroscopic polarisation. We confirm this in Figure 7.3 by calculating the bandstructure and density-of-states of $CeBaMn_2O_6$.

We obtain an indirect band gap of about 0.98 eV - smaller than the 1.7 eV measured in $LaMnO_3$ [224]. Figure 7.3 also shows that the lowest energy excitations are between hybridised O-p and Mn-d levels and importantly, we see that the Ce-f states are empty. This provides further validation of the Ce^{4+} oxidation state.

From this data, we can also confirm that $CeBaMn_2O_6$ has the same orbital ordering as $LaMnO_3$. Figure 7.4 plots the square of Kohn-Sham orbital of the highest occupied band at $k = (0, 0, 0)$, Γ-point, in real space and we can clearly see that the ordering of charge density near the Mn ions is akin to that in Figure 7.1. We see approximately orthogonal charge density on neighbouring cations and then significant charge density on the O anions which reflects the dp hybridisation of this highest occupied band.

Finally as we have confirmed an insulating electronic structure, we compute the polarisation of the $CeBaMn_2O_6$ using the Modern Theory Of Polarisation. In Figure 7.5, we only show one branch of the polarisation ladder as the hybrid mode is varied. The hybrid mode is all of the modes that must be switched in order to obtain the reversed domain. In this case, the main

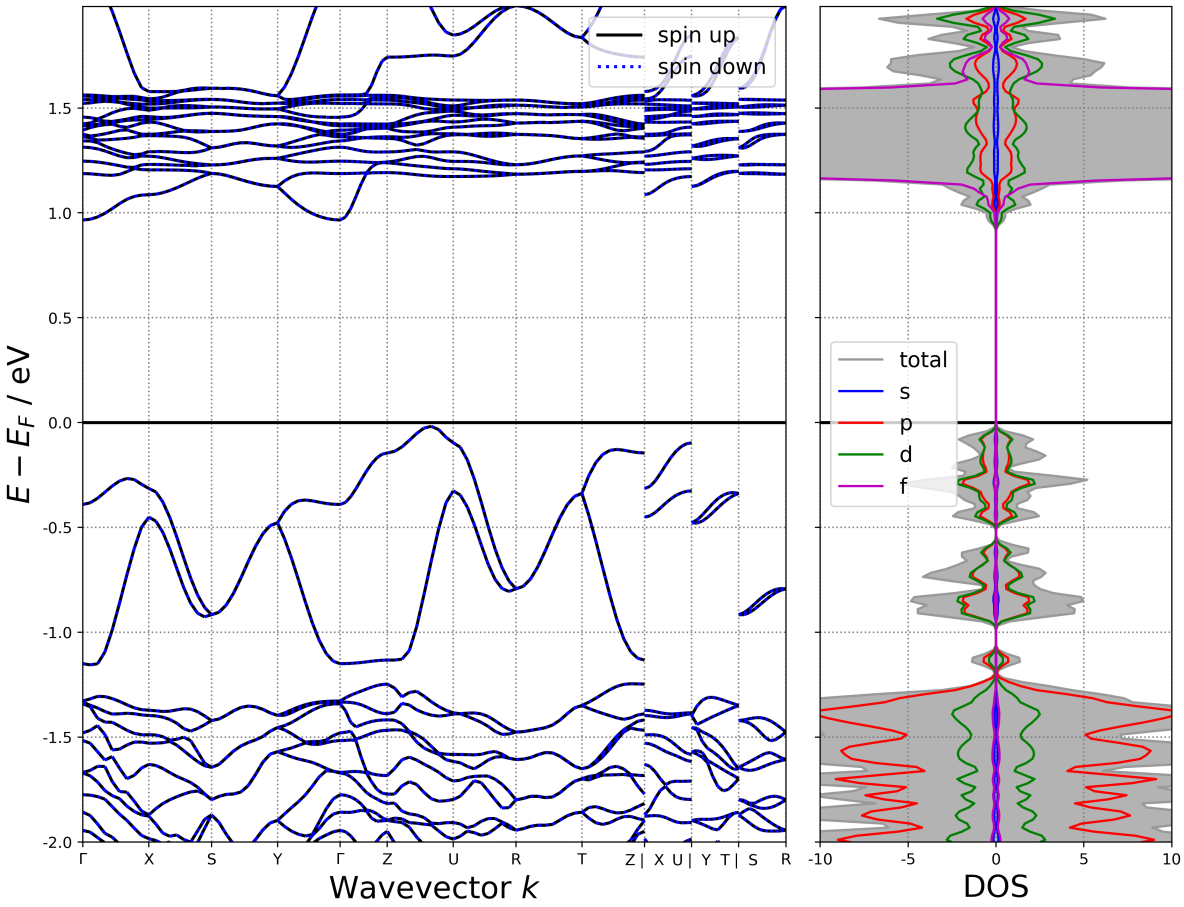

Figure 7.3: Band structure and density of states for $CeBaMn_2O_6$. I observe an band gap of 0.98 eV, traversed by excitations from the hybridised $d-p$ valence to the empty d conduction states.

modes to switch are the polarisation Γ_4^-, the inphase tilt M_2^+ and the antiphase tilts X_5^- (see Chapter 4). All of these modes are scaled linearly and the polarisation calculated at every point. The polarisation at the end points denote the macroscopic polarisation - a value of $\pm 9.9 \mu C/cm^2$. This is similar in magnitude to other improper ferroelectrics like $YMnO_3$ ($\pm 6.5 \mu C/cm^2$) [86].

7.1.3 Alternative Ground States

As the precise cation order is so central in determining whether the electric field control of magnetism is permissible, we compute the energies of several other candidate cation orderings and compare them with the energy of the required cation ordering. To do this, we create a supercell of the $a^-b^+a^-$ tilt pattern (so that the cell is now a 2x2x2 supercell of the $Pm\bar{3}m$

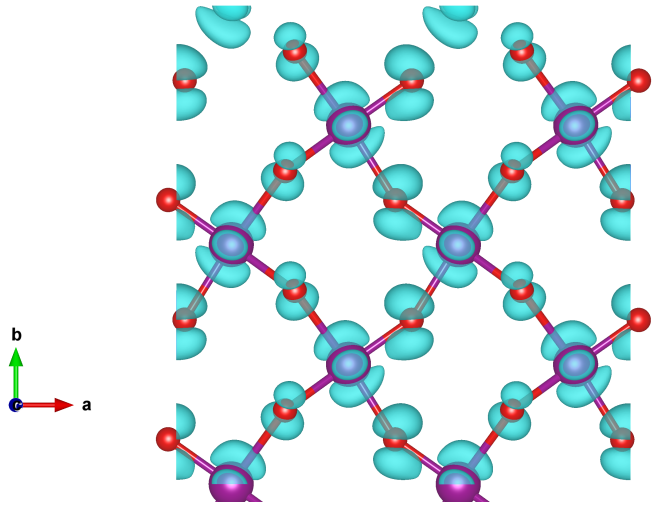

Figure 7.4: Charge density $\phi^*\phi$ of the highest occupied band at the Γ-point. This is the density for up-spin bands and which only has significant density on a single BO_2 layer. The layer below has an identical orbital ordering which accounts for the A-type antiferromagnetic structure through the rules of superexchange. The plot is produced for a different crystallographic setting where the long axis is now c.

structure), and order the cations in various ways. For each ordering, we perform a geometry relaxation and calculate the final energy. The results of this calculation are presented in Tables 7.3 and 7.4.

Surprisingly, we do not find the expected cation order, with alternating Ce/Ba layers along the long axis of the cell, to be the ground state. Instead a cation ordering in which the layering is perpendicular to the long axis is the ground state. The next lowest in energy are columnar ordered A-site which, in some sense, can almost be considered to be in-between the two lowest energy layered configurations; a 45° rotation of the cation layers in the lowest energy ordered structures results in the columnar structure. These new lower energy layerings do not result in the same symmetry as the intended layering. The two other layerings are symmetry equivalent and have $P2_1/m$ symmetry. This was noted in the symmetry analysis of Chapter 4. It is not generally true that identical symmetries result in identical energies, but it is clear why these two materials have similar energies; the normals to the cation layers in both of the $P2_1/m$ structures are orthogonal to the in-phase tilt axis and it is the $a^-a^-c^+$ tilt pattern that introduces most of the anisotropy to this crystal structure.

The similar energies to layered configurations with cation layers perpendicular to the anti-

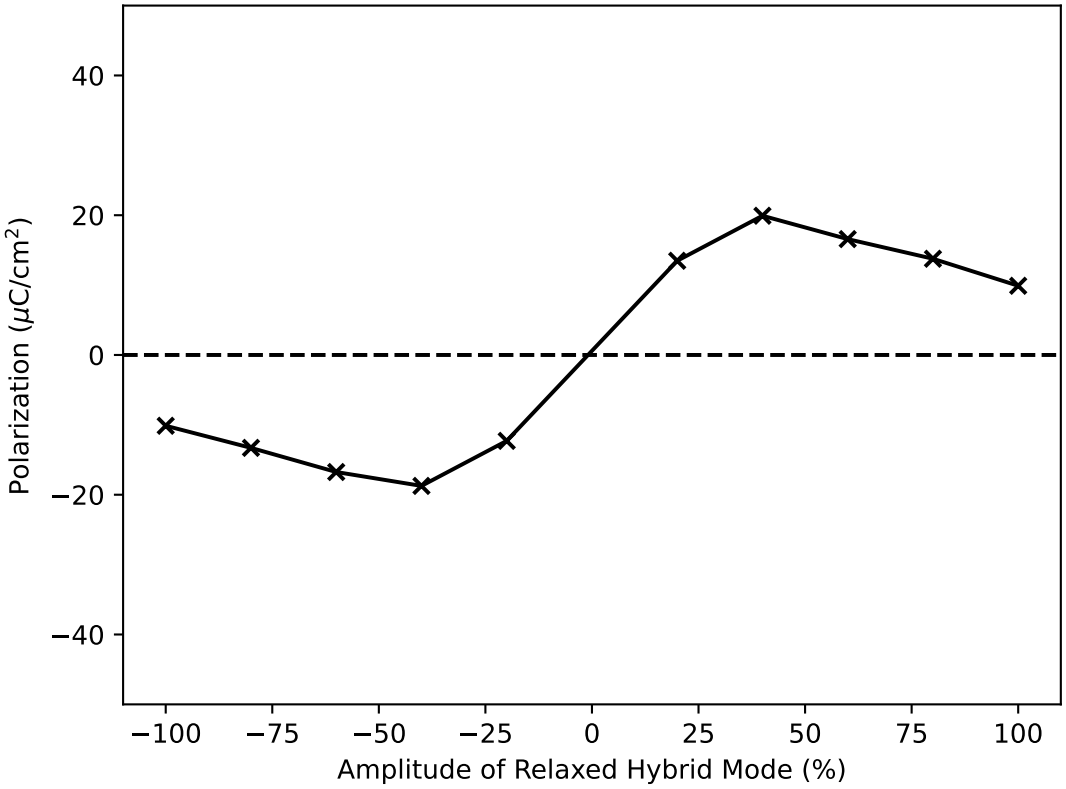

Figure 7.5: Single polarisation branch in $CeBaMn_2O_6$ as the total mode necessary to switch is reversed. This hybrid mode, from 4, involves antipolar A-site motions and at least one tilt mode.

phase tilt axis suggests strong competition between the two. In any attempts to sythesise these materials, it will thus be difficult to observe the required cation ordering.

7.2 Summary

Chapter 4 identified $AA'B_2O_6$ perovskites with an $a^-b^+a^-$ tilt pattern, A-type magnetism and layered A-sites as a material which would demonstrate the electric field control of magnetism. This chapter has confirmed that replacing the La layers in $LaMnO_3$ with alternating layers of Ce and Ba creates a materials with just the required properties.

However, the existence of alternative cation layerings demonstrates that the required cation

Ordering	Space Group	Energy (meV/f.u)	Irrep
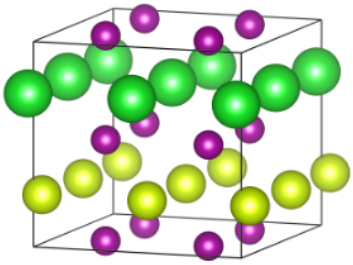 [010] Layered	$Pmc2_1$	119.7	$X_1^+(0;a;0)$
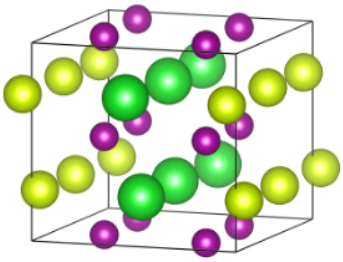 [100] Layered	$P2_1/m$	0.0	$X_1^+(0;a;b)$
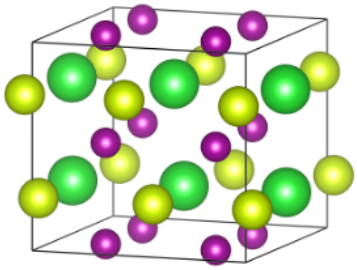 [001] Layered	$P2_1/m$	0.0	$X_1^+(a;b;0)$
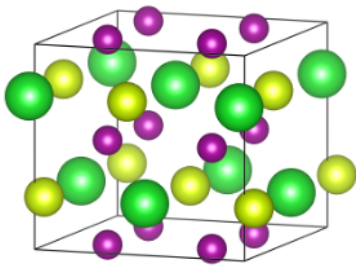 Rocksalt	Pm	314.0	$R_1^+(a)$

Table 7.3: Alternative cation schemes. Each cation layered was added to the relaxed CeBaMn2O6 structure and then allowed to relax further. The resulting space groups are listed along with the irrep for the particular cation order.

layering will be difficult to synthesise, as was demonstrated through an experimental collaboration based on the theoretical predictions of this chapter [213].

Future work will focus on how to stabilize the required layering with epitaxial strain or

Ordering	Space Group	Energy (meV/f.u)	Irrep
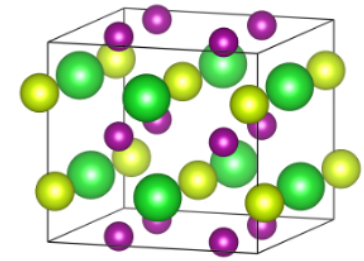 Columnar	$P2_1/m$	77.4	$M_1^+(0;a;0)$
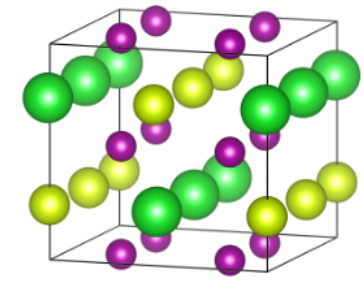 Alternative Columnar	Pm	219.7	$M_1^+(a;b;c)$ $R_1^+(a)$ $X_1^+(a;b;c)$
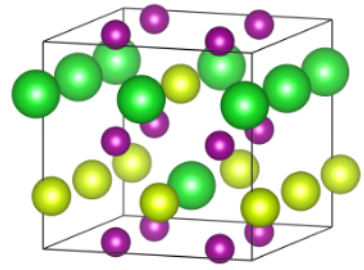 Single substitution	Pm	277.4	$M_1^+(a;b;c)$ $R_1^+(a)$ $X_1^+(a;b;c)$
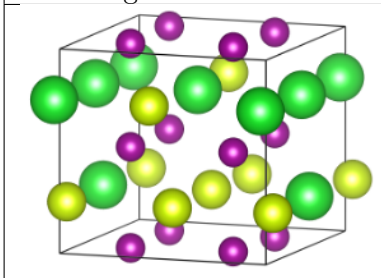 Double Substitution	Pm	107.0	$R_1^+(a)$ $X_1^+(a;b;c)$

Table 7.4: Additional alternative cation order schemes. Each cation layered was added to the relaxed $CeBaMn_2O_6$ structure and then allowed to relax further. Energies are given with respect to the lowest energy orderings. The resulting space groups are listed along with the irrep for the particular cation order.

pressure being the obvious mechanisms to do this. As a preliminary example of such an investigation, I modelled the three layered structures as epitaxial films, with the inphase tilt axis perpendicular to the surface. These simulations are analogous to those performed in Chapter

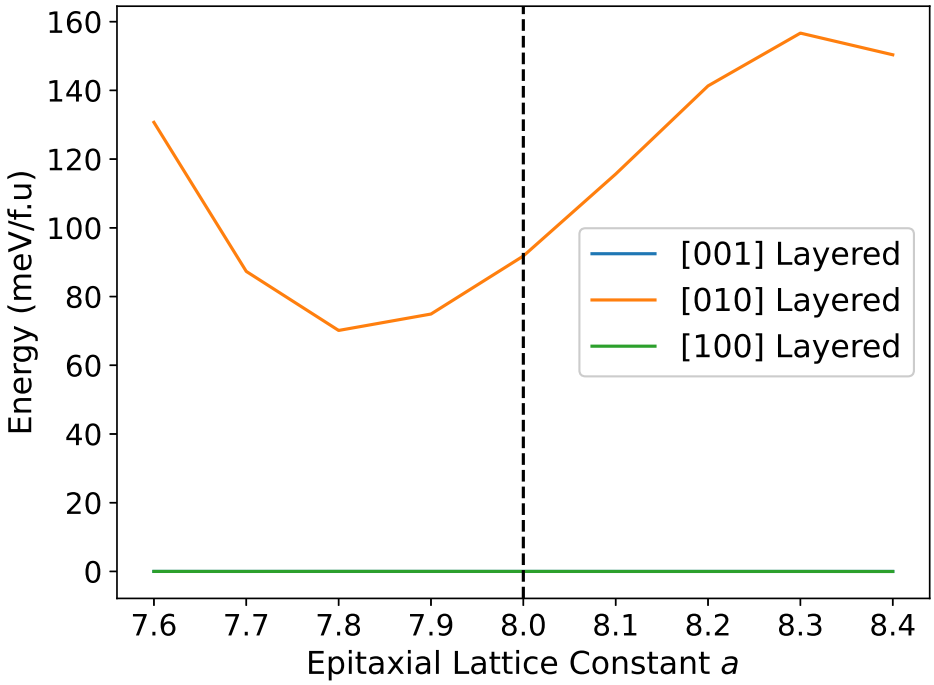

Figure 7.6: Energy of the three layered cation orderings as a function of epitaxial strain. A mild compressive strain makes the desired layering more favourable.

6. I observe that mild compressive strains do make the desired layering more favourable, but not by enough to make it the thermodynamically stable ground state. It would be interesting to see how external fields can control cation order, because we have seen that cation ordering is an efficient way to control the symmetry of materials.

Chapter 8

Conclusion

As stated in the Introduction, the primary goal of this thesis has been to explore whether the 180° reversal of the magnetisation via a coupling to the electric field induced 180° reversal of polarisation is possible in perovskite materials. In Chapter 4, I have shown that such a switching is a definite theoretical possibility in virtually all perovskite materials, and have identified domains with reversed polarisations that, as a consequence of maintaining energetic degeneracy, must also have a reversed weak ferromagnetic canting (and other reversed secondary modes in addition). Due to the high-symmetry parent phase of perovskites, such domains are ubiquitous.

The incredible flexibility attributed to the high-symmetry of perovskites is also a curse. Other combinations of modes lead to energetically equivalent, but structurally distinct ferroelectric domains in which it is not a necessity for the weak ferromagnetic canting to reverse. As demonstrated numerous times in Chapter 4, this leads to a wide number of competing domains. The only way to ascertain which is likely to be found in a ferroelectric switching experiment is to estimate the switching barrier in some way between the positve polarisation and negative dipole domains. Using computational quantum mechanical calculations like DFT would have been one way to do this but the calculations would have been frustratingly tedious.

Instead, Chapter 4 leaned heavily on the group theoretical results and, after sprinkling in some of the physical intuition obtained from Chapter 2, I was able to determine structures in which the *only* domain that can be obtained from a ferroelectric switching experiment was one with the weak ferromagnetic canting also reversed. This was done by identifying the importance

of *improper* ferroelectrics - the polarisation only arises from a coupling to other structural modes in the perovskite. With this idea in mind, we can immediately see that a hypothetical, cubic perovskite with spins on both the A and B sites would allow for the electric field control of magnetism because it is an improper ferroelectric driven by the collinear magnetic structure*. In a more realistic context, we showed that various forms of ion-ordering is also sufficient to break symmetries and create a material in which the magnetic moment can be controlled via a reversal of the polarisation. $CeBaMn_2O_6$, identified in Chapter 4 and studied in detail in Chapter 7, was one example of this idea. The $A_3BB'_2O_9$ perovskites with 1:2 cation order on the B sites were another.

Something omitted from Chapter 4 was any consideration of incommensurate magnetic or crystallographic structures. In principle, there is nothing stopping me from extending the ideas of reversable domains to incommensurate structures; the necessary irreps would just be at irrational k-points. This might make it difficult to find couplings in the Landau theory that preserve translation symmetry but other than that, there is no reason why these could not have been explored from a group theoretical perspective. The major challenge with incommensurate structures are in their quantum mechanical simulation. To be mathematically precise, they would require infinite sized cells. To get a decent approximation, the cell would have to be enormous. This was well beyond the scope of the project but it is possible that recent advances in machine-learned force fields would make the accurate simulation of these large cells a definite possibility in the near future.

The majority of Chapter 4 focused on using the $Pm\bar{3}m$ structure as the high-symmetry parent. This allowed a simple decomposition of a complicated perovskite structure into a collection of physically intuitive symmetry-adapted modes. However, the resulting symmetry was often so low that there were an intractable number of modes to contend with. In my analysis of $A_3BB'_2O_9$ perovskites, I circumvented this issue by choosing to work with a lower symmetry structure, namely, the perovskite with the A and B site cation ordering already included. This reduced the number of modes necessary to work with but also made the problem more phys-

*Again, some would say a Type-II multiferroic which is really just a more precise term for an improper ferroelectric in which the polarisation is couplied to magnetic, and not structural, modes.

ically meaningful. Since I was working on the assumption that long-range cation order (as a large amplitude primary mode) cannot be reversed, it makes sense to freeze out this degree of freedom. As I showed in Chapter 4, this made the symmetry analysis easier and demonstrated that the reversal of the magnetisation is feasible. As the parent cell is the same size as the distorted cell, this transforms all symmetry modes onto the Γ-point of the Brillouin zone and consequently, I refer to this procedure as "constructing a Γ-point scheme".

Γ-point schemes are therefore a useful trick for calculational purposes. However, they are also essential if we are to extend the methodology presented in this thesis to materials beyond perovskites where it is not clear what structure to use as the high-symmetry aristotype. This has been done previously for layered oxides with chemical formula $A_4B_3O_9$ [225]. The ideas of this thesis can be quite readily extended beyond perovskites in this manner.

Although the central question of this thesis was whether the possibility of electric field control of magnetism can be ascertained through group-theoretical methods, I am perhaps most proud of the work presented in Chapter 6 in which I demonstrate that although the terms in the Landau Expansion do not allow for the desired magnetoelectric consequences, considering the effect that each of the terms have on the energy of the system leads to exciting and related effects. In fact, I showed in Chapter 4, that it is very unlikely that the reversal of polarisation would lead to a reversal of magnetisation in $Pna2_1$ perovskites, but in Chapter 6, I show that you can easily convert an AFM $Pna2_1$ perovskite to a FM $Pna2_1$ perovskite under the application of an electric field; this is a different kind of magnetoelectricity but potentially useful nonetheless. This effect would not have been possible to predict from the symmetry alone, but on the other hand, the understanding of this magnetoelectric effect would have been impossible without first constructing the Landau expansion from a consideration of the symmetry adapted modes. This project synthesised both approaches, revealing new insights that would have been obscured if either the symmetry or the energetics were treated in isolation. I believe that this project was a powerful demonstration of the capabilities of the Landau expansion, clearly showing its utility in explaining the nature of unusual phase transitions.

To conclude, I believe that the prospect of using perovskites to observe the electric field control of magnetism rests on a solid foundation of existing literature, to which I have tried to

contribute something. In this thesis, I have restricted myself to perovskite materials which seem likely to be synthesisable through current methods. This clearly does not exhaust all theoretical possibilities. For example, I only seriously considered $a^-a^-c^+$ tilt patterns which may be the most likely tilt pattern for low tolerance magnetic perovskites but are certainly not the *only* tilt pattern. In addition, the diversity of structures that could be obtained through tuning the cation-ordering degree of freedom (which includes vacancy ordering) is theoretically infinite, and I have shown that any material in which an ordering of this kind breaks centrosymmetry would be a strong candidate for the electric-field reversal of magnetisation, so that the question becomes "Which kinds of unusual long-range order are actually possible to create?". In addition, if we also consider how the symmetry adapted modes affect the energies of the simplest perovskite structures, unusual physics can still be found - as Chapter 6 demonstrated. There is plenty of room at the bottom of perovskite physics and I hope that this thesis has demonstrated that considerations of symmetry and the Landau theory of phase transitions provide the tools to exploring it.

Appendix A

Construction Of Invariants

In this short appendix, I review how to construct the allowed invariants between two modes, one transforming as Γ_2^- and the other as a K_3 mode. This allows the construction of a Landau-like free energy for a material with distortions transforming as these two irreducible representation ie. the $P6_3/mmc$ to $P6_3cm$ transition in $YMnO_3$.

However, this method is much more general and forms the basis of how a software tool like INVARIANTS in the ISOTROPY Software Suite actually operates.

In Chapter 3, I constructed a Landau expression for Γ_2^- (one-dimensional irrep at $k = (0, 0, 0)$) and K_3 (two-dimensional irrep at $k = (\frac{1}{3}, \frac{1}{3}, 0)$) modes with the specific OPDs for the transition in $YMnO_3$. However, I could have maintained full generality and kept all possible degrees of freedom. Therefore, $\mathbf{P} = (P_1)$ and $\mathbf{K} = (K_1, K_2)$. The fully general Landau expansion, up to fourth order would then be

$$\begin{aligned} F(P_1, K_1, K_2) =& P_1 + K_1 + K_2 + P_1^2 + K_1^2 + K_2^2 + P_1K_1 + P_1K_2 + K_1K_2 \\ & P_1^3 + K_1^3 + K_2^3 + P_1^2K_1 + P_1^2K_2 + P_1K_1^2 + P_1K_2^2 + P_1K_1K_2 \\ & K_1^2K_1 + K_1K_2^2 + P_1^4 + K_1^4 + K_2^4 + P_1^3K_1 + P_1^3K_2 + P_1^2K_1^2 \\ & P_1^2K_2^2 + P_1^2K_1K_2 + P_1K_1^3 + P_1K_2^3 + P_1K_1^2K_2 + P_1K_1K_2^2 \\ & K_1^3K_2 + K_1^2K_2^2 + K_1K_2^3. \end{aligned} \tag{A.1}$$

Coefficients have been dropped for simplicity. We first look at translation symmetry and check

whether the various products of P_1, K_1 and K_2 sum to a reciprocal lattice vector. This is easy to do because we can always add a Γ point mode to any product and K modes can only survive products containing even powers of K (because it is always possible to do $(\frac{1}{3},\frac{1}{3},0)) - (\frac{1}{3},\frac{1}{3},0))$ to get to a reciprocal lattice vector) or products containing a multiple $3n$ K modes. This kills many of the terms in the Landau expansion so that

$$\begin{aligned} F(P_1,K_1,K_2) =& P_1 + P_1^2 + K_1^2 + K_2^2 + K_1K_2 + P_1^3 + K_1^3 + K_2^3 + P_1K_1^2 + P_1K_2^2 + P_1K_1K_2 + \\ & K_1^2K_1 + K_1K_2^2 + P_1^4 + K_1^4 + K_2^4 + P_1^2K_1^2 + P_1^2K_2^2 + P_1^2K_1K_2 + P_1K_1^3 + \\ & P_1K_2^3 + P_1K_1^2K_2 + P_1K_1K_2^2 + K_1^3K_2 + K_1^2K_2^2 + K_1K_2^3. \end{aligned} \tag{A.2}$$

This is now simpler but can be reduced further by looking at point symmetries. It is always simplest to begin with inversion and the matrix representation of this operation in the Γ_2^- and K_3 irreducible representation of the $P6_3/mmc$ space group are $\begin{bmatrix} -1 \end{bmatrix}$ and $\begin{bmatrix} -1 & 0 \\ 0 & 1 \end{bmatrix}$ respectively. Under inversion, $P_1 \rightarrow -P_1$, $K_1 \rightarrow -K_1$ and $K_2 \rightarrow K_2$. Therefore, we can eliminate term containing odd multiples of P_1 and K_1, reducing it to

$$\begin{aligned} F(P_1,K_1,K_2) =& P_1^2 + K_1^2 + K_2^2 + K_2^3 + P_1K_1K_2 + P_1^4 + K_1^4 + K_2^4 + \\ & P_1^2K_1^2 + P_1^2K_2^2 + P_1K_1^3 + P_1K_1K_2^2 + K_1^2K_2^2. \end{aligned} \tag{A.3}$$

This can be repeated for all other point group operations. For example, there is the two fold rotation axis along the [001] direction; this has matrices $\begin{bmatrix} 1 \end{bmatrix}$ and $\begin{bmatrix} 1 & 0 \\ 0 & -1 \end{bmatrix}$ and so we can eliminate any terms that have odd-order powers of K_2. This finally reduces the expansion to

$$\begin{aligned} F(P_1,K_1,K_2) =& P_1^2 + K_1^2 + K_2^2 + P_1^4 + K_1^4 + K_2^4 + \\ & P_1^2K_1^2 + P_1^2K_2^2 + P_1K_1^3 + P_1K_1K_2^2 + K_1^2K_2^2. \end{aligned} \tag{A.4}$$

No other symmetry operation reduces this expansion any further. The experimentally observed order parameter directions are $\mathbf{P} = (P_1)$ and $\mathbf{K} = (K_1, 0)$ and so we can remove any

terms that contain K_2. This reproduces the expression given in Chapter 3. However, the term $P_1K_1K_2^2$ would provide a further mechanism to further lower the energy. The fact that K_2 is not observed in experiment is an indication that the competitive interactions between all three modes are large enough to prevent any K_2 mode appearing.

Appendix B

Domain Structures

	Irrep Reversal				
Domain	Γ_4^-	$m\Gamma_4^+$	M_2^+	R_5^-	mX_1^-
1	✓	✓	✗	✓	✗
2	✓	✓	✗	✗	✓
3	✓	✓	✓	✗	✗
4	✓	✓	✓	✓	✓
5	✓	✗	✗	✓	✓
6	✓	✗	✗	✗	✗
7	✓	✗	✓	✗	✓
8	✓	✗	✓	✓	✗

Table B.1: Domain structure of Pm perovskites with a magnetic structure described by the mX_1^- irrep. Domain 6 has no magnetoelectric effects.

	Irrep Reversal				
Domain	Γ_4^-	$m\Gamma_4^+$	M_5^+	R_5^-	mX_5^-
1	✓	✓	✗	✓	✗
2	✓	✓	✗	✗	✓
3	✓	✓	✓	✗	✗
4	✓	✓	✓	✓	✓
5	✓	✗	✗	✓	✓
6	✓	✗	✗	✗	✗
7	✓	✗	✓	✗	✓
8	✓	✗	✓	✓	✗

Table B.2: Domain structure of Pm perovskites with a magnetic structure described by the mX_5^- irrep. Domain 6 has no magnetoelectric effects.

	Irrep Reversal				
Domain	Γ_4^-	$m\Gamma_4^+$	M_2^+	R_5^-	mM_2^+
1	✓	✓	✗	✓	✓
2	✓	✓	✗	✗	✓
3	✓	✓	✓	✗	✗
4	✓	✓	✓	✓	✗
5	✓	✗	✗	✓	✗
6	✓	✗	✗	✗	✗
7	✓	✗	✓	✗	✓
8	✓	✗	✓	✓	✓

Table B.3: Domain structure of Pm perovskites with a magnetic structure described by the mM_2^+ irrep. Domain 6 has no magnetoelectric effects.

	Irrep Reversal				
Domain	Γ_4^-	$m\Gamma_4^+$	M_2^+	R_5^-	mM_2^+
1	✓	✓	✗	✓	✓
2	✓	✓	✗	✗	✓
3	✓	✓	✓	✗	✗
4	✓	✓	✓	✓	✗
5	✓	✗	✗	✓	✗
6	✓	✗	✗	✗	✗
7	✓	✗	✓	✗	✓
8	✓	✗	✓	✓	✓

Table B.4: Domain structure of Pm perovskites with a magnetic structure described by the mM_5^+ irrep. Domain 6 has no magnetoelectric effects.

	Irrep Reversal				
Domain	Γ_4^-	$m\Gamma_4^+$	M_2^+	R_5^-	mR_5^-
1	✓	✓	✗	✓	✗
2	✓	✓	✗	✗	✓
3	✓	✓	✓	✗	✓
4	✓	✓	✓	✓	✗
5	✓	✗	✗	✓	✓
6	✓	✗	✗	✗	✗
7	✓	✗	✓	✗	✗
8	✓	✗	✓	✓	✓

Table B.5: Domain structure of Pm perovskites with a magnetic structure described by the mR_5^- irrep for both the $(a, 0, 0)$ and $(0, a, b)$ OPD. Domain 6 has no magnetoelectric effects.

	Irrep Reversal				
Domain	Γ_4^-	$m\Gamma_4^+$	M_2^+	R_5^-	mX^-
1	✓	✓	✗	✓	✗
2	✓	✓	✗	✗	✓
3	✓	✓	✓	✗	✗
4	✓	✓	✓	✓	✓
5	✓	✗	✗	✓	✓
6	✓	✗	✗	✗	✗
7	✓	✗	✓	✗	✓
8	✓	✗	✓	✓	✗

Table B.6: Domain structure of $Pna2_1$ perovskites with a magnetic structure described by either the mX_1^- or mX_5^- irrep. Domain 6 has no magnetoelectric effects.

	Irrep Reversal				
Domain	Γ_4^-	$m\Gamma_4^+$	M_2^+	R_5^-	mM_5^+
1	✓	✓	✗	✗	✓
2	✓	✓	✗	✓	✓
3	✓	✓	✓	✓	✗
4	✓	✓	✓	✗	✗
5	✓	✗	✗	✓	✗
6	✓	✗	✗	✗	✗
7	✓	✗	✓	✗	✓
8	✓	✗	✓	✓	✓

Table B.7: Domain structure of $Pna2_1$ perovskites with a magnetic structure described by the mM_5^+ irrep. Domain 6 has no magnetoelectric effects.

	Irrep Reversal				
Domain	Γ_4^-	$m\Gamma_4^+$	M_2^+	R_5^-	mR_5^-
1	✓	✓	✓	✓	✗
2	✓	✓	✓	✗	✓
3	✓	✓	✗	✗	✓
4	✓	✓	✗	✓	✗
5	✓	✗	✓	✗	✗
6	✓	✗	✓	✓	✓
7	✓	✗	✗	✓	✓
8	✓	✗	✗	✗	✗
9	✓	✓(90°)	✗	✓(90°)	✓
10	✓	✓(90°)	✗	✓(−90°)	✗
11	✓	✓(90°)	✓	✓(−90°)	✗
12	✓	✓(90°)	✓	✓(90°)	✓
13	✓	✓(−90°)	✗	✓(−90°)	✓
14	✓	✓(−90°)	✗	✓(90°)	✗
15	✓	✓(−90°)	✓	✓(90°)	✗
16	✓	✓(−90°)	✓	✓(−90°)	✓

Table B.8: Domain structure of $Pna2_1$ perovskites with a magnetic structure described by the mR_5^- irrep for both the $(a, 0, 0)$ and $(0, a, b)$ OPD. Domain 8 has no magnetoelectric effects.

	Irrep Reversal				
Domain	Γ_4^-	$m\Gamma_4^+$	M_2^+	R_5^-	mX_1^-
1	✓	✓	✗	✓	✗
2	✓	✓	✓	✗	✗
3	✓	✓	✗	✗	✓
4	✓	✓	✓	✓	✓
5	✓	✗	✗	✓	✓
6	✓	✗	✓	✗	✓
7	✓	✗	✗	✗	✗
8	✓	✗	✓	✓	✗

Table B.9: Domain structure of $Pmc2_1$ perovskites with a magnetic structure described by the mX^- irreps. Domain 7 has no magnetoelectric effects.

	Irrep Reversal				
Domain	Γ_4^-	$m\Gamma_4^+$	M_2^+	R_5^-	mM_5^+
1	✓	✓	✗	✓	✓
2	✓	✓	✗	✗	✓
3	✓	✓	✓	✗	✗
4	✓	✓	✓	✓	✗
5	✓	✗	✗	✓	✗
6	✓	✗	✗	✗	✗
7	✓	✗	✓	✗	✓
8	✓	✗	✓	✓	✗

Table B.10: Domain structure of $Pmc2_1$ perovskites with a magnetic structure described by the mM_5^+ irrep. Domain 7 has no magnetoelectric effects.

	Irrep Reversal				
Domain	Γ_4^-	$m\Gamma_4^+$	M_2^+	R_5^-	mR_5^-
1	✓	✓	✗	✓	✗
2	✓	✓	✓	✗	✓
3	✓	✓	✗	✗	✓
4	✓	✓	✓	✓	✗
5	✓	✗	✓	✗	✗
6	✓	✗	✗	✓	✓
7	✓	✗	✓	✓	✓
8	✓	✗	✗	✗	✗

Table B.11: Domain structure of $Pmc2_1$ perovskites with a magnetic structure described by both OPDs of the mR_5^- irrep. Domain 8 has no magnetoelectric effects.

Bibliography

[1] John Bardeen and Walter Hauser Brattain. The transistor, a semi-conductor triode. *Physical Review*, 74(2):230, 1948.

[2] Julius E Lilienfeld. Electric current control mechanism. *Canadian patent CA*, 272437(19):07, 1927.

[3] Robert R Schaller. Moore's law: past, present and future. *IEEE spectrum*, 34(6):52–59, 1997.

[4] Simon Min Sze. *Semiconductor devices: physics and technology*. John wiley & sons, 2008.

[5] Anders SG Andrae and Tomas Edler. On global electricity usage of communication technology: trends to 2030. *Challenges*, 6(1):117–157, 2015.

[6] Vaclav Smil. *Energy and Civilization: A History*. MIT press, 2018.

[7] Hannah Ritchie and Pablo Rosado. Electricity mix. *Our World in Data*, 2020. https://ourworldindata.org/electricity-mix.

[8] Miyuru Dayarathna, Yonggang Wen, and Rui Fan. Data center energy consumption modeling: A survey. *IEEE Communications surveys & tutorials*, 18(1):732–794, 2015.

[9] James F Annett. *Superconductivity, superfluids and condensates*, volume 5. Oxford University Press, 2004.

[10] Kriti Sharma, Anmol Arora, Surya Kant Tripathi, et al. Review of supercapacitors: Materials and devices. *Journal of Energy Storage*, 21:801–825, 2019.

[11] An Chen. A review of emerging non-volatile memory (NVM) technologies and applications. *Solid-State Electronics*, 125:25–38, 2016.

[12] W A Wulf and Sally A McKee. Hitting the memory wall: Implications of the obvious. *ACM SIGARCH Computer Architecture News*, 23(1):20–24, 1995.

[13] Yuan Taur and Tak H Ning. *Fundamentals of modern VLSI devices*. Cambridge University Press, 2021.

[14] Yoshio Nishi and Blanka Magyari-Kope. *Advances in non-volatile memory and storage technology*. Woodhead Publishing, 2019.

[15] Nigel Goldenfeld. *Lectures on phase transitions and the renormalization group*. CRC Press, 2018.

[16] Javier Junquera, Yousra Nahas, Sergei Prokhorenko, Laurent Bellaiche, Jorge Íñiguez, Darrell G Schlom, Long-Qing Chen, Sayeef Salahuddin, David A Muller, Lane W Martin, et al. Topological phases in polar oxide nanostructures. *Reviews of Modern Physics*, 95(2):025001, 2023.

[17] Guillaume F Nataf, Sebastian Volz, Jose Ordonez-Miranda, Jorge Íñiguez-González, Riccardo Rurali, and Brahim Dkhil. Using oxides to compute with heat. *Nature Reviews Materials*, pages 1–2, 2024.

[18] Stephen Blundell. *Magnetism in condensed matter*. OUP Oxford, 2001.

[19] M.E. Lines and A.M. Glass. *Principles and Applications of Ferroelectrics and Related Materials*. International series of monographs on physics. OUP Oxford, 2001.

[20] Charles Kittel and Paul McEuen. *Introduction to solid state physics*. John Wiley & Sons, 2018.

[21] Karin M Rabe, Charles H Ahn, and Jean-Marc Triscone. *Physics of ferroelectrics: a modern perspective*, volume 105. Springer Science & Business Media, 2007.

[22] J.F. Scott. *Ferroelectric Memories*. Advanced microelectronics. Springer, 2000.

[23] Orlando Auciello, James F Scott, and Ramamoorthy Ramesh. The physics of ferroelectric memories. *Physics today*, 51(7):22–27, 1998.

[24] Nicola A Spaldin. Analogies and differences between ferroelectrics and ferromagnets. In *Physics of Ferroelectrics: A Modern Perspective*, pages 175–218. Springer, 2007.

[25] S Chikazumi. *Physics of ferromagnetism*, volume 506. Oxford University Press, 1997.

[26] Daniel I Khomskii. *Transition metal compounds*. Cambridge University Press, 2014.

[27] Eric Bousquet and Andrés Cano. Non-collinear magnetism in multiferroic perovskites. *Journal of Physics: Condensed Matter*, 28(12):123001, 2016.

[28] Lane W Martin, Ying-Hao Chu, and R Ramesh. Emerging multiferroic memories. In *Emerging Non-Volatile Memories*, pages 103–166. Springer, 2014.

[29] S Ikeda, K Miura, H Yamamoto, K Mizunuma, HD Gan, M Endo, Sl Kanai, J Hayakawa, F Matsukura, and H Ohno. A perpendicular-anisotropy CoFeB–MgO magnetic tunnel junction. *Nature materials*, 9(9):721–724, 2010.

[30] Yizhe Jiang, Eric Parsonnet, Alexander Qualls, Wenbo Zhao, Sandhya Susarla, David Pesquera, Arvind Dasgupta, Megha Acharya, Hongrui Zhang, Tanay Gosavi, et al. Enabling ultra-low-voltage switching in $BaTiO_3$. *Nature materials*, 21(7):779–785, 2022.

[31] Wilma Eerenstein, ND Mathur, and James F Scott. Multiferroic and magnetoelectric materials. *nature*, 442(7104):759–765, 2006.

[32] Nicola A Spaldin and Manfred Fiebig. The renaissance of magnetoelectric multiferroics. *Science*, 309(5733):391–392, 2005.

[33] Bas B Van Aken, Jean-Pierre Rivera, Hans Schmid, and Manfred Fiebig. Observation of ferrotoroidic domains. *Nature*, 449(7163):702–705, 2007.

[34] Daniel Khomskii. Classifying multiferroics: Mechanisms and effects. *Physics*, 2:20, 2009.

[35] Ravi Shankar PN, Swarnamayee Mishra, and Sundaresan Athinarayanan. Polar magnetic oxides from chemical ordering: A new class of multiferroics. *APL Materials*, 8(4), 2020.

[36] Alexei A Belik. Hybrid multiferroic behavior in the double perovskite ($Ca_{0.5}Mn_{1.5}MnWO_6$). *Chemistry of Materials*, 36(15):7604–7609, 2024.

[37] Manfred Fiebig. Revival of the magnetoelectric effect. *Journal of physics D: applied physics*, 38(8):R123, 2005.

[38] Edgar Ascher, Hans Schmid, and D Tar. Dielectric properties of boracites and evidence for ferroelectricity. *Solid State Communications*, 2(2):45–49, 1964.

[39] JBNJ Wang, JB Neaton, H Zheng, V Nagarajan, SB Ogale, B Liu, D Viehland, V Vaithyanathan, DG Schlom, UV Waghmare, et al. Epitaxial $BiFeO_3$ multiferroic thin film heterostructures. *Science*, 299(5613):1719–1722, 2003.

[40] Daniel Sando, A Barthélémy, and M Bibes. $BiFeO_3$ epitaxial thin films and devices: past, present and future. *Journal of Physics: Condensed Matter*, 26(47):473201, 2014.

[41] JT Heron, JL Bosse, Q He, Y Gao, Morgan Trassin, L Ye, JD Clarkson, C Wang, Jian Liu, S Salahuddin, et al. Deterministic switching of ferromagnetism at room temperature using an electric field. *Nature*, 516(7531):370–373, 2014.

[42] J Silva, A Reyes, Hilda Esparza, H Camacho, and L Fuentes. $BiFeO_3$: a review on synthesis, doping and crystal structure. *Integrated Ferroelectrics*, 126(1):47–59, 2011.

[43] Albert Fert, Ramamoorthy Ramesh, Vincent Garcia, Fèlix Casanova, and Manuel Bibes. Electrical control of magnetism by electric field and current-induced torques. *arXiv preprint arXiv:2311.11724*, 2023.

[44] Richard JD Tilley. *Perovskites: structure-property relationships*. John Wiley & Sons, 2016.

[45] Patrick M Woodward, Pavel Karen, John SO Evans, and Thomas Vogt. *Solid state materials chemistry*. Cambridge University Press, 2021.

[46] Anthony M Glazer. The classification of tilted octahedra in perovskites. *Acta Crystallographica Section B: Structural Crystallography and Crystal Chemistry*, 28(11):3384–3392, 1972.

[47] AM Glazer. Simple ways of determining perovskite structures. *Acta Crystallographica Section A: Crystal Physics, Diffraction, Theoretical and General Crystallography*, 31(6):756–762, 1975.

[48] Patrick M Woodward. Octahedral tilting in perovskites. I. Geometrical considerations. *Acta Crystallographica Section B: Structural Science*, 53(1):32–43, 1997.

[49] David J Griffiths. *Introduction to electrodynamics*. Cambridge University Press, 2023.

[50] RR Mehta, BD Silverman, and JT Jacobs. Depolarization fields in thin ferroelectric films. *Journal of Applied Physics*, 44(8):3379–3385, 1973.

[51] Javier Junquera and Philippe Ghosez. Critical thickness for ferroelectricity in perovskite ultrathin films. *Nature*, 422(6931):506–509, 2003.

[52] P W Anderson and EI Blount. Symmetry considerations on martensitic transformations:" ferroelectric" metals? *Physical Review Letters*, 14(7):217, 1965.

[53] Sayantika Bhowal and Nicola A Spaldin. Polar metals: principles and prospects. *Annual Review of Materials Research*, 53(1):53–79, 2023.

[54] Nicola A Spaldin. A beginner's guide to the modern theory of polarization. *Journal of Solid State Chemistry*, 195:2–10, 2012.

[55] RD King-Smith and David Vanderbilt. Theory of polarization of crystalline solids. *Physical Review B*, 47(3):1651, 1993.

[56] David Vanderbilt. *Berry phases in electronic structure theory: electric polarization, orbital magnetization and topological insulators*. Cambridge University Press, 2018.

[57] Michael W Lufaso and Patrick M Woodward. Jahn-Teller distortions, cation ordering and octahedral tilting in perovskites. *Acta Crystallographica Section B: Structural Science*, 60(1):10–20, 2004.

[58] Mildred S Dresselhaus, Gene Dresselhaus, and Ado Jorio. *Group theory: application to the physics of condensed matter*. Springer Science & Business Media, 2007.

[59] Sami Vasala and Maarit Karppinen. $A_2B'B"O_6$ perovskites: a review. *Progress in solid state chemistry*, 43(1-2):1–36, 2015.

[60] Graham King and Patrick M Woodward. Cation ordering in perovskites. *Journal of Materials Chemistry*, 20(28):5785–5796, 2010.

[61] Mark T Anderson, Kevin B Greenwood, Gregg A Taylor, and Kenneth R Poeppelmeier. B-cation arrangements in double perovskites. *Progress in solid state chemistry*, 22(3):197–233, 1993.

[62] Meghan C Knapp and Patrick M Woodward. A-site cation ordering in $AA'BB'O_6$ perovskites. *Journal of Solid State Chemistry*, 179(4):1076–1085, 2006.

[63] Padraig Kearins, Elena Solana-Madruga, Kunlang Ji, Clemens Ritter, and J Paul Attfield. Cluster spin glass formation in the double double perovskite $CaMnFeTaO_6$. *The Journal of Physical Chemistry C*, 125(17):9550–9555, 2021.

[64] Santanu De, Mahima M Kurian, Leelashree Solaiappan, Arun Kumar, Shipra Das, Sourav Samanta, Yasar K Arafath, and Santhosh P Nagappan Nair. Chemistry and physics of triple perovskite oxides: A topical review. *Chemistry of Materials*, 36(19):9207–9233, 2024.

[65] Valeska Ting, Yun Liu, Lasse Norén, RL Withers, DJ Goossens, Michael James, and C Ferraris. A structure, conductivity and dielectric properties investigation of $A_3CoNb_2O_9$ ($a = Ca^{2+}$, Sr^{2+}, Ba^{2+}) triple perovskites. *Journal of Solid State Chemistry*, 177(12):4428–4442, 2004.

[66] Youwen Long. A-site ordered quadruple perovskite oxides. *Chinese Physics B*, 25(7):078108, 2016.

[67] Jie Ding and Xinhua Zhu. Research progress of quadruple perovskite oxides. *Journal of Materials Chemistry C*, 2024.

[68] Alexei A Belik, Roger D Johnson, and Dmitry D Khalyavin. The rich physics of a-site-ordered quadruple perovskite manganites $A\mathrm{Mn_7O_{12}}$. *Dalton Transactions*, 50(43):15458–15472, 2021.

[69] Alexei A Belik. Rise of a-site columnar-ordered $A_2A'A''B_4\mathrm{O_{12}}$ quadruple perovskites with intrinsic triple order. *Dalton Transactions*, 47(10):3209–3217, 2018.

[70] Y Tsujimoto, CI Sathish, Y Matsushita, K Yamaura, and T Uchikoshi. New members of layered oxychloride perovskites with square planar coordination: $\mathrm{Sr_2}M\mathrm{O_2Cl_2}$ (M= Mn, Ni) and $\mathrm{Ba_2PdO_2Cl_2}$. *Chemical Communications*, 50(44):5915–5918, 2014.

[71] Hai-Chen Wang, Jonathan Schmidt, Silvana Botti, and Miguel AL Marques. A high-throughput study of oxynitride, oxyfluoride and nitrofluoride perovskites. *Journal of Materials Chemistry A*, 9(13):8501–8513, 2021.

[72] Minghui Yang, Judith Oró-Solé, Jennifer A Rodgers, Ana Belén Jorge, Amparo Fuertes, and J Paul Attfield. Anion order in perovskite oxynitrides. *Nature chemistry*, 3(1):47–52, 2011.

[73] Ghanshyam Pilania, Ayana Ghosh, Steven T Hartman, Rohan Mishra, Christopher R Stanek, and Blas P Uberuaga. Anion order in oxysulfide perovskites: origins and implications. *npj Computational Materials*, 6(1):71, 2020.

[74] MV Talanov, VB Shirokov, and VM Talanov. Anion order in perovskites: a group-theoretical analysis. *Acta Crystallographica Section A: Foundations and Advances*, 72(2):222–235, 2016.

[75] J Paul Attfield. Principles and applications of anion order in solid oxynitrides. *Crystal growth & design*, 13(10):4623–4629, 2013.

[76] Nenian Charles, Richard J Saballos, and James M Rondinelli. Structural diversity from anion order in heteroanionic materials. *Chemistry of Materials*, 30(10):3528–3537, 2018.

[77] Kenneth Franklin Riley, Michael Paul Hobson, and Stephen John Bence. *Mathematical methods for physics and engineering: a comprehensive guide*. Cambridge university press, 2006.

[78] W Cochran. Crystal stability and the theory of ferroelectricity. *Advances in Physics*, 9(36):387–423, 1960.

[79] N.W. Ashcroft and N.D. Mermin. *Solid State Physics*. Cengage Learning, 2011.

[80] Aron Walsh and Graeme W Watson. The origin of the stereochemically active Pb (II) lone pair: DFT calculations on PbO and PbS. *Journal of Solid State Chemistry*, 178(5):1422–1428, 2005.

[81] Walter A Harrison. *Electronic structure and the properties of solids: the physics of the chemical bond*. Courier Corporation, 2012.

[82] James M Rondinelli, Aaron S Eidelson, and Nicola A Spaldin. Non-d^0 Mn-driven ferroelectricity in antiferromagnetic $BaMnO_3$. *Physical Review B—Condensed Matter and Materials Physics*, 79(20):205119, 2009.

[83] Ralph G Pearson. The second-order Jahn-Teller effect. *Journal of Molecular Structure: THEOCHEM*, 103:25–34, 1983.

[84] Isaac B Bersuker. Modern aspects of the Jahn-Teller effect theory and applications to molecular problems. *Chemical reviews*, 101(4):1067–1114, 2001.

[85] Bas B Van Aken, Thomas TM Palstra, Alessio Filippetti, and Nicola A Spaldin. The origin of ferroelectricity in magnetoelectric $YMnO_3$. *Nature materials*, 3(3):164–170, 2004.

[86] Craig J Fennie and Karin M Rabe. Ferroelectric transition in $YMnO_3$ from first principles. *Physical Review B—Condensed Matter and Materials Physics*, 72(10):100103, 2005.

[87] Nicole A Benedek and Craig J Fennie. Why are there so few perovskite ferroelectrics? *The Journal of Physical Chemistry C*, 117(26):13339–13349, 2013.

[88] Marin Alexe, Michael Ziese, Dietrich Hesse, Pablo Esquinazi, Kunihiko Yamauchi, Tetsuya Fukushima, Silvia Picozzi, and Ulrich Gösele. Ferroelectric switching in multiferroic magnetite (Fe_3O_4) thin films. *Advanced Materials*, 21(44):4452–4455, 2009.

[89] Jeroen Van Den Brink and Daniel I Khomskii. Multiferroicity due to charge ordering. *Journal of Physics: Condensed Matter*, 20(43):434217, 2008.

[90] Darrell G Schlom, Long-Qing Chen, Chang-Beom Eom, Karin M Rabe, Stephen K Streiffer, and Jean-Marc Triscone. Strain tuning of ferroelectric thin films. *Annu. Rev. Mater. Res.*, 37(1):589–626, 2007.

[91] Jun Hee Lee and Karin M Rabe. Epitaxial-strain-induced multiferroicity in $SrMnO_3$ from first principles. *Physical review letters*, 104(20):207204, 2010.

[92] Oswaldo Diéguez, Karin M Rabe, and David Vanderbilt. First-principles study of epitaxial strain in perovskites. *Physical Review B—Condensed Matter and Materials Physics*, 72(14):144101, 2005.

[93] C-J Eklund, CJ Fennie, and KM Rabe. Strain-induced ferroelectricity in orthorhombic $CaTiO_3$ from first principles. *Physical Review B—Condensed Matter and Materials Physics*, 79(22):220101, 2009.

[94] John B Goodenough. Goodenough-kanamori rule. *Scholarpedia*, 3(10):7382, 2008.

[95] Philip W Anderson. Antiferromagnetism. theory of superexchange interaction. *Physical Review*, 79(2):350, 1950.

[96] John B Goodenough. Theory of the role of covalence in the perovskite-type manganites [La, M(II)] MnO_3. *Physical Review*, 100(2):564, 1955.

[97] Junjiro Kanamori. Superexchange interaction and symmetry properties of electron orbitals. *Journal of Physics and Chemistry of Solids*, 10(2-3):87–98, 1959.

[98] Catriona A Crawford, Craig I Hiley, Cameron AM Scott, Clemens Ritter, Martin R Lees, Nicholas C Bristowe, Richard I Walton, and Mark S Senn. The interplay of electronic

configuration and anion ordering on the magnetic behavior of hydroxyfluoride diaspores. *Inorganic Chemistry*, 2024.

[99] JT Zhang, C Ji, JL Wang, WS Xia, XM Lu, and JS Zhu. Stabilization of E-type magnetic order caused by epitaxial strain in perovskite manganites. *Physical Review B*, 97(8):085124, 2018.

[100] Myron B Salamon and Marcelo Jaime. The physics of manganites: Structure and transport. *Reviews of modern physics*, 73(3):583, 2001.

[101] Tôru Moriya. Anisotropic superexchange interaction and weak ferromagnetism. *Physical review*, 120(1):91, 1960.

[102] Igor Dzyaloshinsky. A thermodynamic theory of "weak" ferromagnetism of antiferromagnetics. *Journal of physics and chemistry of solids*, 4(4):241–255, 1958.

[103] Toshiyuki Atou, H Chiba, K Ohoyama, Y Yamaguchi, and Y Syono. Structure determination of ferromagnetic perovskite $BiMnO_3$. *Journal of Solid State Chemistry*, 145(2):639–642, 1999.

[104] Roman V Shpanchenko, Viktoria V Chernaya, Alexander A Tsirlin, Pavel S Chizhov, Dmitry E Sklovsky, Evgeny V Antipov, Evgeny P Khlybov, Vladimir Pomjakushin, Anatoly M Balagurov, Julia E Medvedeva, et al. Synthesis, structure, and properties of new perovskite $PbVO_3$. *Chemistry of materials*, 16(17):3267–3273, 2004.

[105] Satadeep Bhattacharjee, Eric Bousquet, and Philippe Ghosez. Engineering multiferroism in $CaMnO_3$. *Physical review letters*, 102(11):117602, 2009.

[106] T Günter, Eric Bousquet, A David, Ph Boullay, Ph Ghosez, Wilfrid Prellier, and Manfred Fiebig. Incipient ferroelectricity in 2.3% tensile-strained $CaMnO_3$ films. *Physical Review B—Condensed Matter and Materials Physics*, 85(21):214120, 2012.

[107] JW Guo, PS Wang, Y Yuan, Q He, JL Lu, TZ Chen, SZ Yang, YJ Wang, R Erni, MD Rossell, et al. Strain-induced ferroelectricity and spin-lattice coupling in $SrMnO_3$ thin films. *Physical Review B*, 97(23):235135, 2018.

[108] Andrés Camilo Garcia-Castro, Nicola A Spaldin, AH Romero, and Eric Bousquet. Geometric ferroelectricity in fluoroperovskites. *Physical Review B*, 89(10):104107, 2014.

[109] Andrés Camilo Garcia-Castro, Aldo H Romero, and Eric Bousquet. Strain-engineered multiferroicity in *pnma* $NaMnF_3$ fluoroperovskite. *Physical Review Letters*, 116(11):117202, 2016.

[110] Michel Kenzelmann, A Brooks Harris, S Jonas, C Broholm, Jürg Schefer, SB Kim, CL Zhang, <? format?> S-W Cheong, Owen P Vajk, and Jeffrey W Lynn. Magnetic inversion symmetry breaking and ferroelectricity in $TbMnO_3$. *Physical review letters*, 95(8):087206, 2005.

[111] Tsuyoshi Kimura, T Goto, H Shintani, K Ishizaka, T-h Arima, and Y Tokura. Magnetic control of ferroelectric polarization. *nature*, 426(6962):55–58, 2003.

[112] William Lawrence Bragg. The structure of some crystals as indicated by their diffraction of X-rays. *Proceedings of the Royal Society of London. Series A, Containing papers of a mathematical and physical character*, 89(610):248–277, 1913.

[113] Satoshi Sasaki, Kiyoshi Fujino, and Yoshio Takéuchi. X-ray determination of electron-density distributions in oxides, MgO, MnO, Coo, and Nio, and atomic scattering factors of their constituent atoms. *Proceedings of the Japan Academy, Series B*, 55(2):43–48, 1979.

[114] Theo Hahn, Uri Shmueli, and JC Wilson Arthur. *International tables for crystallography*, volume 1. Reidel Dordrecht, 1983.

[115] Paolo Radaelli. *Symmetry in crystallography: understanding the international tables*, volume 17. Oxford University Press, 2011.

[116] Helen D Megaw. Crystal structure of double oxides of the perovskite type. *Proceedings of the Physical Society*, 58(2):133, 1946.

[117] F Neumann. Vorlesungen über die theorie der elastizität der festen körper und des lichtäthers, edited by oe meyer. *Leipzig: BG Teubner-Verlag*, 1885.

[118] Robert E Newnham. *Properties of materials: anisotropy, symmetry, structure*. Oxford university press, 2005.

[119] YL Li and LQ Chen. Temperature-strain phase diagram for $BaTiO_3$ thin films. *Applied physics letters*, 88(7), 2006.

[120] DB Litvin. Tables of crystallographic properties of magnetic space groups. *Acta Crystallographica Section A: Foundations of Crystallography*, 64(3):419–424, 2008.

[121] Daniel B Litvin. Magnetic group tables. *International Union of Crystallography*, 10:9780955360220001, 2013.

[122] Jingtong Zhang, Louis Bastogne, Xu He, Gang Tang, Yajun Zhang, Philippe Ghosez, and Jie Wang. Structural phase transitions and dielectric properties of $BaTiO_3$ from a second-principles method. *Physical Review B*, 108(13):134117, 2023.

[123] Pierre Toledano and Jean-claude Toledano. *Landau Theory Of Phase Transitions, The: Application To Structural, Incommensurate, Magnetic And Liquid Crystal Systems*, volume 3. World Scientific Publishing Company, 1987.

[124] L.D. Landau, E.M. Lifshitz, E.M. Lifshits, and L.P. Pitaevskii. *Statistical Physics: Theory of the Condensed State*. Course of theoretical physics. Elsevier Science, 1980.

[125] Mois Ilia Aroyo, Juan Manuel Perez-Mato, Cesar Capillas, Eli Kroumova, Svetoslav Ivantchev, Gotzon Madariaga, Asen Kirov, and Hans Wondratschek. Bilbao crystallographic server: I. databases and crystallographic computing programs. *Zeitschrift für Kristallographie-Crystalline Materials*, 221(1):15–27, 2006.

[126] Mois I Aroyo, Asen Kirov, Cesar Capillas, JM Perez-Mato, and Hans Wondratschek. Bilbao crystallographic server. II. representations of crystallographic point groups and space groups. *Acta Crystallographica Section A: Foundations of Crystallography*, 62(2):115–128, 2006.

[127] Daniel I Khomskii. *Basic aspects of the quantum theory of solids: order and elementary excitations*. Cambridge university press, 2010.

[128] Harold T Stokes, Dorian M Hatch, and Branton J Campbell. ISODISTORT. iso.byu.edu.

[129] Branton J Campbell, Harold T Stokes, David E Tanner, and Dorian M Hatch. ISODISPLACE: a web-based tool for exploring structural distortions. *Journal of Applied Crystallography*, 39(4):607–614, 2006.

[130] Mark S Senn and Nicholas C Bristowe. A group-theoretical approach to enumerating magnetoelectric and multiferroic couplings in perovskites. *Acta Crystallographica Section A: Foundations and Advances*, 74(4):308–321, 2018.

[131] Dorian M Hatch and Harold T Stokes. INVARIANTS: program for obtaining a list of invariant polynomials of the order-parameter components associated with irreducible representations of a space group. *Journal of applied crystallography*, 36(3):951–952, 2003.

[132] V Dvořák. A thermodynamic theory of gadolinium molybdate. *physica status solidi (b)*, 46(2):763–772, 1971.

[133] Arkadii Petrovich Levanyuk and Daniil G Sannikov. Improper ferroelectrics. *Soviet Physics Uspekhi*, 17(2):199, 1974.

[134] Nicole A Benedek and Michael A Hayward. Hybrid improper ferroelectricity: a theoretical, computational, and synthetic perspective. *Annual Review of Materials Research*, 52(1):331–355, 2022.

[135] James W Lewis, Julia L Payne, Ivana Radosavljevic Evans, Harold T Stokes, Branton J Campbell, and John SO Evans. An exhaustive symmetry approach to structure determination: phase transitions in $Bi_2Sn_2O_7$. *Journal of the American Chemical Society*, 138(25):8031–8042, 2016.

[136] Melanie Müller, Robert E Dinnebier, A-C Dippel, Harold T Stokes, and Branton J Campbell. A symmetry-mode description of rigid-body rotations in crystalline solids: a case study of $Mg(H_2O)_6RbBr_3$. *Journal of Applied Crystallography*, 47(2):532–538, 2014.

[137] Sean Kerman, Branton J Campbell, Kiran K Satyavarapu, Harold T Stokes, Francesca Perselli, and John SO Evans. The superstructure determination of displacive distortions via symmetry-mode analysis. *Acta Crystallographica Section A: Foundations of Crystallography*, 68(2):222–234, 2012.

[138] Branton J Campbell, John SO Evans, Francesca Perselli, and Harold T Stokes. Rietveld refinement of structural distortion-mode amplitudes. *IUCr Comput. Comm. Newsl*, 8:81–95, 2007.

[139] Nicole A Benedek and Craig J Fennie. Hybrid improper ferroelectricity: A mechanism for controllable polarization-magnetization coupling. *Physical review letters*, 106(10):107204, 2011.

[140] Yoon Seok Oh, Xuan Luo, Fei-Ting Huang, Yazhong Wang, and Sang-Wook Cheong. Experimental demonstration of hybrid improper ferroelectricity and the presence of abundant charged walls in (Ca, Sr)$_3$Ti$_2$O$_7$ crystals. *Nature materials*, 14(4):407–413, 2015.

[141] Maria Luisa Medarde. Structural, magnetic and electronic properties of perovskites (r= rare earth). *Journal of Physics: Condensed Matter*, 9(8):1679, 1997.

[142] Feng Lou, Wei Luo, Junsheng Feng, and Hongjun Xiang. Genetic algorithm prediction of pressure-induced multiferroicity in the perovskite PbCoO$_3$. *Physical Review B*, 99(20):205104, 2019.

[143] Shi Liu, Ilya Grinberg, and Andrew M Rappe. Intrinsic ferroelectric switching from first principles. *Nature*, 534(7607):360–363, 2016.

[144] JF Scott. A review of ferroelectric switching. *Ferroelectrics*, 503(1):117–132, 2016.

[145] Matthew J Highland, Timothy T Fister, Marie-Ingrid Richard, Dillon D Fong, Paul H Fuoss, Carol Thompson, Jeffrey A Eastman, Stephen K Streiffer, and G Brian Stephenson. Polarization switching without domain formation at the intrinsic coercive field in ultrathin ferroelectric PbTiO$_3$. *Physical review letters*, 105(16):167601, 2010.

[146] YW Li, JF Scott, DN Fang, and FX Li. 90-degree polarization switching in $BaTiO_3$ crystals without domain wall motion. *Applied Physics Letters*, 103(23), 2013.

[147] Vishal Boddu, Florian Endres, and Paul Steinmann. Molecular dynamics study of ferroelectric domain nucleation and domain switching dynamics. *Scientific reports*, 7(1):806, 2017.

[148] KZ Baba-Kishi, PM Woodward, and K Knight. The crystal structures of Pb_2ScTaO_6 and Pb_2ScNbO_6 in the paraelectric and ferroelectric states. *Ferroelectrics*, 261(1):21–26, 2001.

[149] Francis Galasso, James R Barrante, and Lewis Katz. Alkaline earth-tantalum-oxygen phases including the crystal structure of an ordered perovskite compound, $Ba_3SrTa_2O_9$. *Journal of the American Chemical Society*, 83(13):2830–2832, 1961.

[150] Francis Galasso and Jane Pyle. Ordering in compounds of the $A(B'_{0.33}Ta_{0.67})O_3$ type. *Inorganic Chemistry*, 2(3):482–484, 1963.

[151] Francis Galasso and Jane Pyle. Preparation and study of ordering in $A(B'_{0.33}Nb_{0.67})O_3$ perovskite-type compounds. *Journal of Physical Chemistry*, 67(7):1561–1562, 1963.

[152] Job T Rijssenbeek, Takashi Saito, Sylvie Malo, Masaki Azuma, Mikio Takano, and Kenneth R Poeppelmeier. Effect of explicit cationic size and valence constraints on the phase stability of 1: 2 B-site-ordered perovskite ruthenates. *Journal of the American Chemical Society*, 127(2):675–681, 2005.

[153] Job T Rijssenbeek, Sylvie Malo, Vincent Caignaert, and Kenneth R Poeppelmeier. Site and oxidation-state specificity yielding dimensional control in perovskite ruthenates. *Journal of the American Chemical Society*, 124(10):2090–2091, 2002.

[154] David C Wallace and Tyrel M McQueen. New honeycomb iridium (V) oxides: $NaIrO_3$ and $Sr_3CaIr_2O_9$. *Dalton Transactions*, 44(47):20344–20351, 2015.

[155] Gohil S Thakur, Thomas C Hansen, Walter Schnelle, Shuping Guo, Oleg Janson, Jeroen Van Den Brink, Claudia Felser, and Martin Jansen. Buckled honeycomb lattice compound

$Sr_3CaOs_2O_9$ exhibiting antiferromagnetism above room temperature. *Chemistry of Materials*, 34(10):4741–4750, 2022.

[156] Rachel Tarvin and Peter K Davies. *A*-site and *B*-site order in $(Na_{1/2}La_{1/2})(Mg_{1/3}Nb_{2/3})O_3$ perovskite. *Journal of the American Ceramic Society*, 87(5):859–863, 2004.

[157] J Hwang, ES Choi, F Ye, CR Dela Cruz, Y Xin, HD Zhou, and P Schlottmann. Successive magnetic phase transitions and multiferroicity in the spin-one triangular-lattice antiferromagnet $Ba_3NiNb_2O_9$. *Physical review letters*, 109(25):257205, 2012.

[158] M Lee, ES Choi, X Huang, J Ma, CR Dela Cruz, M Matsuda, W Tian, ZL Dun, S Dong, and HD Zhou. Magnetic phase diagram and multiferroicity of $Ba_3MnNb_2O_9$: A spin-5/2 triangular lattice antiferromagnet with weak easy-axis anisotropy. *Physical Review B*, 90(22):224402, 2014.

[159] Wei-tin Chen, Masaichiro Mizumaki, Hayato Seki, Mark S Senn, Takashi Saito, Daisuke Kan, J Paul Attfield, and Yuichi Shimakawa. A half-metallic *A*-and *B*-site-ordered quadruple perovskite oxide $CaCu_3Fe_2Re_2O_{12}$ with large magnetization and a high transition temperature. *Nature Communications*, 5(1):3909, 2014.

[160] Duo Wang, Monirul Shaikh, Saurabh Ghosh, and Biplab Sanyal. Prediction of half-metallic ferrimagnetic quadruple perovskites $ACu_3Fe_2Re_2O_{12}$ (A= Ca, Sr, Ba, Pb, Sc, Y, La) with high Curie temperatures. *Physical Review Materials*, 5(5):054405, 2021.

[161] Long Zhou, Jianhong Dai, Yisheng Chai, Huimin Zhang, Shuai Dong, Huibo Cao, Stuart Calder, Yunyu Yin, Xiao Wang, Xudong Shen, et al. Realization of large electric polarization and strong magnetoelectric coupling in $BiMn_3Cr_4O_{12}$. *Advanced Materials*, 29(44):1703435, 2017.

[162] Jian-Qing Dai and Chang-Chang Zhang. Ferroelectricity driven by soft phonon and spin order in multiferroic $BiMn_3Cr_4O_{12}$. *Journal of the American Ceramic Society*, 102(10):6048–6059, 2019.

[163] Paul Adrien Maurice Dirac. Quantum mechanics of many-electron systems. *Proceedings of the Royal Society of London. Series A, Containing Papers of a Mathematical and Physical Character*, 123(792):714–733, 1929.

[164] Richard M Martin. *Electronic structure: basic theory and practical methods*. Cambridge university press, 2020.

[165] Feliciano Giustino. *Materials modelling using density functional theory: properties and predictions*. Oxford University Press, 2014.

[166] John P Perdew. Density functional theory and the band gap problem. *International Journal of Quantum Chemistry*, 28(S19):497–523, 1985.

[167] Pierre Hohenberg and Walter Kohn. Inhomogeneous electron gas. *Physical review*, 136(3B):B864, 1964.

[168] Klaus Capelle and Giovanni Vignale. Nonuniqueness of the potentials of spin-density-functional theory. *Physical Review Letters*, 86(24):5546, 2001.

[169] Nikitas I Gidopoulos. Potential in spin-density-functional theory of noncollinear magnetism determined by the many-electron ground state. *Physical Review B—Condensed Matter and Materials Physics*, 75(13):134408, 2007.

[170] Walter Kohn and Lu Jeu Sham. Self-consistent equations including exchange and correlation effects. *Physical review*, 140(4A):A1133, 1965.

[171] Wenhui Mi, Kai Luo, SB Trickey, and Michele Pavanello. Orbital-free density functional theory: An attractive electronic structure method for large-scale first-principles simulations. *Chemical Reviews*, 123(21):12039–12104, 2023.

[172] Private communication with Dr Nikitas Gidopolous.

[173] Charles Kittel and Ching-yao Fong. *Quantum theory of solids*, volume 5. Wiley New York, 1963.

[174] John P Perdew, Kieron Burke, and Matthias Ernzerhof. Generalized gradient approximation made simple. *Physical review letters*, 77(18):3865, 1996.

[175] John P Perdew, Adrienn Ruzsinszky, Gábor I Csonka, Oleg A Vydrov, Gustavo E Scuseria, Lucian A Constantin, Xiaolan Zhou, and Kieron Burke. Restoring the density-gradient expansion for exchange in solids and surfaces. *Physical review letters*, 100(13):136406, 2008.

[176] John P Perdew and Karla Schmidt. Jacob's ladder of density functional approximations for the exchange-correlation energy. In *AIP Conference Proceedings*, volume 577, pages 1–20. American Institute of Physics, 2001.

[177] Hendrik J Monkhorst and James D Pack. Special points for Brillouin-zone integrations. *Physical review B*, 13(12):5188, 1976.

[178] David Vanderbilt. Soft self-consistent pseudopotentials in a generalized eigenvalue formalism. *Physical review B*, 41(11):7892, 1990.

[179] Richard Phillips Feynman. Forces in molecules. *Physical review*, 56(4):340, 1939.

[180] Ramamurti Shankar. *Principles of quantum mechanics*. Springer Science & Business Media, 2012.

[181] Masatoshi Imada, Atsushi Fujimori, and Yoshinori Tokura. Metal-insulator transitions. *Reviews of modern physics*, 70(4):1039, 1998.

[182] Julien Varignon, Manuel Bibes, and Alex Zunger. Origin of band gaps in 3d perovskite oxides. *Nature communications*, 10(1):1658, 2019.

[183] Richard M Martin, Lucia Reining, and David M Ceperley. *Interacting electrons*. Cambridge University Press, 2016.

[184] Burak Himmetoglu, Andrea Floris, Stefano De Gironcoli, and Matteo Cococcioni. Hubbard-corrected dft energy functionals: The lda+u description of correlated systems. *International Journal of Quantum Chemistry*, 114(1):14–49, 2014.

[185] Vladimir I Anisimov, Jan Zaanen, and Ole K Andersen. Band theory and mott insulators: Hubbard u instead of stoner i. *Physical Review B*, 44(3):943, 1991.

[186] Peter E Blöchl. Projector augmented-wave method. *Physical review B*, 50(24):17953, 1994.

[187] Georg Kresse and Jürgen Furthmüller. Efficiency of ab-initio total energy calculations for metals and semiconductors using a plane-wave basis set. *Computational materials science*, 6(1):15–50, 1996.

[188] Georg Kresse and Jürgen Furthmüller. Efficient iterative schemes for ab initio total-energy calculations using a plane-wave basis set. *Physical review B*, 54(16):11169, 1996.

[189] Georg Kresse and Daniel Joubert. From ultrasoft pseudopotentials to the projector augmented-wave method. *Physical review b*, 59(3):1758, 1999.

[190] Sergei L Dudarev, Gianluigi A Botton, Sergey Y Savrasov, CJ Humphreys, and Adrian P Sutton. Electron-energy-loss spectra and the structural stability of nickel oxide: An LSDA+ u study. *Physical Review B*, 57(3):1505, 1998.

[191] Hong Jian Zhao, Laurent Bellaiche, and Jorge Íñiguez. First-principles screening of ABO_3 oxides with two magnetic sublattices. *Physical Review Materials*, 3(6):064406, 2019.

[192] Alexei A Belik, Yoshitaka Matsushita, Masahiko Tanaka, and Eiji Takayama-Muromachi. Crystal structures and properties of perovskites $ScCrO_3$ and $InCrO_3$ with small ions at the A site. *Chemistry of Materials*, 24(11):2197–2203, 2012.

[193] Lei Ding, Pascal Manuel, Dmitry D Khalyavin, Fabio Orlandi, Yu Kumagai, Fumiyasu Oba, Wei Yi, and Alexei A Belik. Unusual magnetic structure of the high-pressure synthesized perovskites $ACrO_3$ (A= Sc, In, Tl). *Physical Review B*, 95(5):054432, 2017.

[194] SV Streltsov, MA Korotin, VI Anisimov, and DI Khomskii. Band versus localized electron magnetism in $CaCrO_3$. *Physical Review B—Condensed Matter and Materials Physics*, 78(5):054425, 2008.

[195] Yuanhui Xu, Zhenhong Tan, Wei-Tin Chen, Chung-Kai Chang, Yu-Chun Chuang, Masato Goto, and Yuichi Shimakawa. High-pressure synthesized perovskite $CdMnO_3$ with C-type antiferromagnetic spin configuration. *Inorganic Chemistry*, 61(51):21011–21015, 2022.

[196] Chengcheng Xiao. VASP_OPT_AXIS. https://github.com/Chengcheng-Xiao/VASP_OPT_AXIS, 2022. Accessed: 2024-04-22.

[197] Alexei A Belik and Wei Yi. High-pressure synthesis, crystal chemistry and physics of perovskites with small cations at the *A* site. *Journal of Physics: Condensed Matter*, 26(16):163201, 2014.

[198] Koji Fujita, Takahiro Kawamoto, Ikuya Yamada, Olivier Hernandez, Naoaki Hayashi, Hirofumi Akamatsu, William Lafargue-Dit-Hauret, Xavier Rocquefelte, Masafumi Fukuzumi, Pascal Manuel, et al. $LiNbO_3$-type $InFeO_3$: room-temperature polar magnet without second-order Jahn-Teller active ions. *Chemistry of Materials*, 28(18):6644–6655, 2016.

[199] Teng Gu, Timothy Scarbrough, Yurong Yang, Jorge Íñiguez, L Bellaiche, and HJ Xiang. Cooperative couplings between octahedral rotations and ferroelectricity in perovskites and related materials. *Physical review letters*, 120(19):197602, 2018.

[200] JM Perez-Mato, M Aroyo, Alberto García, Peter Blaha, Karlheinz Schwarz, Johannes Schweifer, and K Parlinski. Competing structural instabilities in the ferroelectric aurivillius compound $SrBi_2Ta_2O_9$. *Physical Review B*, 70(21):214111, 2004.

[201] JM Perez-Mato, Peter Blaha, Karlheinz Schwarz, M Aroyo, D Orobengoa, I Etxebarria, and Alberto García. Multiple instabilities in $Bi_4Ti_3O_{12}$: A ferroelectric beyond the soft-mode paradigm. *Physical Review B*, 77(18):184104, 2008.

[202] Urko Petralanda, Jirka Hlinka, and I Etxebarria. Influence of epitaxial strain on multiple-mode compounds: The case of $SrBi_2Nb_2O_9$. *Physical Review B*, 96(14):144112, 2017.

[203] Meng Ye and David Vanderbilt. Ferroelectricity in corundum derivatives. *Physical Review B*, 93(13):134303, 2016.

[204] Meng Ye and David Vanderbilt. Domain walls and ferroelectric reversal in corundum derivatives. *Physical Review B*, 95(1):014105, 2017.

[205] Alexei A Belik, Sergey Yu Stefanovich, Bogdan I Lazoryak, and Eiji Takayama-Muromachi. Biino3: A polar oxide with $GdFeO_3$-type perovskite structure. *Chemistry of materials*, 18(7):1964–1968, 2006.

[206] J-G Cheng, KE Kweon, J-S Zhou, JA Alonso, P-P Kong, Y Liu, Changqing Jin, Junjie Wu, Jung-Fu Lin, Sebastian Alberto Larregola, et al. Anomalous perovskite $PbRuO_3$ stabilized under high pressure. *Proceedings of the National Academy of Sciences*, 110(50):20003–20007, 2013.

[207] Pai-Hsuan Sun, Tetsuro Nakamura, Yue Jin Shan, Yoshiyuki Inaguma, and Mitsuru Itoh. The study on the dielectric property and structure of perovskite titanate $CdTiO_3$. *Ferroelectrics*, 217(1):137–145, 1998.

[208] Hiroki Moriwake, Akihide Kuwabara, Craig AJ Fisher, Hiroki Taniguchi, Mitsuru Itoh, and Isao Tanaka. First-principles calculations of lattice dynamics in $CdTiO_3$ and $CaTiO_3$: Phase stability and ferroelectricity. *Physical Review B*, 84(10):104114, 2011.

[209] Sung Gu Kang. First-principles examination of low tolerance factor perovskites. *International Journal of Quantum Chemistry*, 117(19):e25420, 2017.

[210] GNP Oliveira, RC Teixeira, RP Moreira, JG Correia, JP Araújo, and AML Lopes. Local inhomogeneous state in multiferroic $SmCrO_3$. *Scientific reports*, 10(1):4686, 2020.

[211] Suryakanta Mishra, Krishna Rudrapal, Biswajit Jana, Kazi Parvez Islam, Archna Sagdeo, Ayan Roy Chaudhuri, Venimadhav Adyam, Debraj Choudhury, et al. Structural origin of room-temperature ferroelectricity in spark-plasma sintered $DyCrO_3$ and $LaCrO_3$. *Physical Review B*, 107(21):214104, 2023.

[212] Cameron AM Scott and Nicholas C Bristowe. Universal polar instability in highly orthorhombic perovskites. *Journal of the American Chemical Society*, 2024.

[213] Struan Simpson, Cameron AM Scott, Fernando Pomiro, Jeremiah P Tidey, Urmimala Dey, Fabio Orlandi, Pascal Manuel, Martin R Lees, Zih-Mei Hong, Wei-tin Chen, et al. Symmetry-informed design of magnetoelectric coupling in the manganite perovskite $CeBaMn_2O_6$. *Journal of Materials Chemistry C*, 12(37):15058–15069, 2024.

[214] Gen Matsumoto. Study of $(La_{1-x}Ca_x)MnO_3$. I. magnetic structure of $LaMnO_3$. *Journal of the Physical Society of Japan*, 29(3):606–615, 1970.

[215] V Skumryev, F Ott, JMD Coey, A Anane, J P Renard, L Pinsard-Gaudart, and A Revcolevschi. Weak ferromagnetism in $LaMnO_3$. *The European Physical Journal B-Condensed Matter and Complex Systems*, 11:401–406, 1999.

[216] P Norby, IG Krogh Andersen, E Krogh Andersen, and NH Andersen. The crystal structure of lanthanum manganate (III), $LaMnO_3$, at room temperature and at 1273 K under N_2. *Journal of solid state chemistry*, 119(1):191–196, 1995.

[217] MN Iliev, MV Abrashev, H-G Lee, VN Popov, YY Sun, Ch Thomsen, RL Meng, and CW Chu. Raman spectroscopy of orthorhombic perovskitelike $YMnO_3$ and $LaMnO_3$. *Physical Review B*, 57(5):2872, 1998.

[218] EO Wollan and WC Koehler. Neutron diffraction study of the magnetic properties of the series of perovskite-type compounds $[(1-x)$ La, x Ca$]$ MnO_3. *Physical Review*, 100(2):545, 1955.

[219] Robert D Shannon. Revised effective ionic radii and systematic studies of interatomic distances in halides and chalcogenides. *Foundations of Crystallography*, 32(5):751–767, 1976.

[220] DI Khomskii and KI Kugel. Elastic interactions and superstructures in manganites and other Jahn-Teller systems. *Physical Review B*, 67(13):134401, 2003.

[221] J-S Zhou and JB Goodenough. Unusual evolution of the magnetic interactions versus structural distortions in $R$$MnO_3$ perovskites. *Physical review letters*, 96(24):247202, 2006.

[222] Seung Woo Jang, Siheon Ryee, Hongkee Yoon, and Myung Joon Han. Charge density functional plus u theory of $LaMnO_3$: Phase diagram, electronic structure, and magnetic interaction. *Physical Review B*, 98(12):125126, 2018.

[223] Michael Marcus Schmitt, Yajun Zhang, Alain Mercy, and Philippe Ghosez. Electron-lattice interplay in $LaMnO_3$ from canonical Jahn-Teller distortion notations. *Physical Review B*, 101(21):214304, 2020.

[224] T Arima, Y Tokura, and JB Torrance. Variation of optical gaps in perovskite-type $3d$ transition-metal oxides. *Physical Review B*, 48(23):17006, 1993.

[225] Urmimala Dey, Emma E McCabe, and Nicholas C Bristowe. Prediction of room-temperature electric field reversal of magnetization in the family of $A_4B_3O_9$ layered oxides. *arXiv preprint arXiv:2405.01307*, 2024.

Colophon

This thesis is based on a template developed by Matthew Townson and Andrew Reeves. It was typeset with LaTeX 2_ε. It was created using the *memoir* package, maintained by Lars Madsen, with the *madsen* chapter style. The font used is Latin Modern, derived from fonts designed by Donald E. Knuth.